Fully-Photonic Digital Radio Over Fibre for Future Super-Broadband Access Network Applications

Seyedreza Abdollahi

A Thesis Submitted in fulfilment of the requirements
For the Degree of Doctor of Philosophy (PhD)

Electronic and Computer Engineering
School of Engineering and Design
Brunel University, London
United Kingdom

-August 2012-

Abstract

In this thesis a Fully-Photonic DRoF (FP-DRoF) system is proposed for deploying of future super-broadband access networks. Digital Radio over Fibre (DRoF) is more independent of the fibre network impairments and the length of fibre than the ARoF link. In order for fully optical deployment of the signal conversion techniques in the FP-DRoF architecture, two key components an Analogue-to-Digital Converter (ADC) and a Digital-to-Analogue Converter (DAC)) for data conversion are designed and their performance are investigated whereas the physical functionality is evaluated.

The system simulation results of the proposed pipelined Photonic ADC (PADC) show that the PADC has 10 GHz bandwidth around 60 GHz of sampling rate. Furthermore, by changing the bandwidth of the optical bandpass filter, switching to another band of sampling frequency provides optimised performance condition of the PADC. The PADC has low changes on the Effective Number of Bit (ENOB) response versus analogue RF input from 1 GHz up to 22 GHz for 60 GHz sampling frequency. The proposed 8-Bit pipelined PADC performance in terms of ENOB is evaluated at 60 Gigasample/s which is about 4.1.

Recently, different methods have been reported by researchers to implement Photonic DACs (PDACs), but their aim was to convert digital electrical signals to the corresponding analogue signal by assisting the optical techniques. In this thesis, a Binary Weighted PDAC (BW-PDAC) is proposed. In this BW-PDAC, optical digital signals are fully optically converted to an analogue signal. The spurious free dynamic range at the output of the PDAC in a back-to-back deployment of the PADC and the PDAC was 26.6 dBc. For further improvement in the system performance, a 3R (Retiming, Reshaping and Reamplifying) regeneration system is proposed in this thesis. Simulation results show that for an ultra-short RZ pulse with a 5% duty cycle at 65 Gbit/s using the proposed 3R regeneration system on a link reduces rms timing jitter by 90% while the regenerated pulse eye opening height is improved by 65%.

Finally, in this thesis the proposed FP-DRoF functionality is evaluated whereas its performance is investigated through a dedicated and shared fibre links. The simulation results show (in the case of low level signal to noise ratio, in comparison with ARoF through a dedicated fibre link) that the FP-DRoF has better BER performance than the ARoF in the order of 10^{-20}. Furthermore, in order to realize a BER about 10^{-25} for the ARoF, the power penalty is about 4 dBm higher than the FP-DRoF link. The simulation results demonstrate that by considering 0.2 dB/km attenuation of a standard single mode fibre, the dedicated fibre length for the FP-DRoF link can be increased to about 20 km more than the ARoF link. Moreover, for performance assessment of the proposed FP-DRoF in a shared fibre link, the BER of the FP-DRoF link is about 10^{-10} magnitude less than the ARoF link for -19 dBm launched power into the fibre and the power penalty of the ARoF system is 10 dBm more than the FP-DRoF link. It is significant to increase the fibre link's length of the FP-DRoF access network using common infrastructure. In addition, the simulation results are demonstrated that the FP-DRoF with non-uniform Wavelength Division Multiplexing (WDM) is more robust against four wave mixing impairment than the conventional WDM technique with uniform wavelength allocation and has better performance in terms of BER. It is clearly verified that the lunched power penalty at CS for DRoF link with uniform WDM techniques is about 2 dB higher than non-uniform WDM technique. Furthermore, uniform WDM method requires more bandwidth than non-uniform scheme which depends on the total number of channels and channels spacing.

In the name of God

To My Wife Alieh

and

My Son SeyedAli

and

My daughter SeyedehTasnim

Acknowledgments

First of all, I would like to express my appreciation and gratefulness to my brothers Seyed Saeid and Seyed Ehsan for supporting me during my PhD study.

I would like to thank my supervisor Professor Hamed Al-Raweshidy for his valuable advices and guidance during the PhD period. He has been very helpful and supportive for all these years.

I am thankful to my second supervisor Dr. Rajagopal Nilavalan and Dr. Thomas Owens for their encouragement and support. My gratitude goes to my colleagues in the Wireless Networks and Communications Centre (WNCC), who have been supportive throughout this period. I would like to acknowledge the great attitude of all the staff members that I have interacted with at Brunel University and specifically in the department of Electronic and Computer Engineering.

Finally, to my father and my mother, who have always been my main inspiration and always urged me to pursue higher level of education and complete my PhD studies.

Table of contents

List of Figures

List of Tables

Abbreviation

ADC:	Analogue-to-Digital converter
AFL:	Amplified Feedback DFB Laser
AM:	Amplitude Modulation
APD:	Avalanche Photo Diode
ASE:	Amplified Spontaneous Emission
BA:	Brillouin Amplifier
BB:	BaseBand
BER:	Bit Error Rate
BS:	Base Station
BW:	Bandwidth
CAGR:	Compound Annual Growth Rate
CCSL:	Coupled-Cavity Semiconductor Laser
CNR:	Carrier to Noise Ratio
CO:	Central Office
CPSS:	Constant Phase-Shift Step
CW:	Continuous wave
DAC:	Digital-to-Analogue converter
DAS:	Distributed Antenna System
DCM:	Directional Coupler Modulator
DCSMF:	Dispersion Compensated standard SMF
DCU:	Dispersion Compensation Unit
DFB:	Distributed Feed Back
DLI:	Delay-Line Interferometers
DNL:	Differential NonLinearity
DR:	Data Recovery
DRoF:	Digital Radio over Fibre
DVB2:	Digital Video Broadcasting 2
DWDM:	Dense WDM
E/O:	Electric-to-Optic Converter
EADC:	Electronic ADC
EAM:	Electro-Absorption Modulator
EDAC:	Electronic DAC
EDFA:	Erbium-Doped Fibre Amplifier
EMI:	Electromagnetic Interference
ENOB:	Effective Number Of Bit
EOM:	Electro Optical Modulator
ESA:	Electrical Spectrum Analyzer
FBG:	Fibre Bragg Grating
FFT:	Fast Fourier Transform
Fi-Wi:	Fibre and Wireless
FM:	Frequency Modulation
FoM:	Figure of Merit
FP:	Fabry-Perot
FP-DRoF:	Fully-Photonic Digital Radio over Fibre
FPF:	Fabry-Perot Filter
FSR:	Free Spectral Range
FTTH:	Fibre-to-the-home
FWHM:	Full Width at Half Maximum
FWM:	Four Waves Mixing

GLPF:	Gaussian Low Pass Filter
GVD:	Group Velocity Dispersion
HDTV:	High-Definition Television
HDWDM:	Highly DWDM
HL:	Hard Limiter
HNLF:	Highly NonLinear Fibre
IF:	Intermediate Frequency
IM:	Intensity Modulation
IMD:	InterModulation Distortion
IMDD:	Intensity-Modulation Direct- Detection
INL:	Integral Nonlinearity
IP:	Internet Protocol
ISI:	InterSymbol Interferences
ISP:	Internet Service Provider
ITS:	Intelligent Transportation System
ITU:	International Telecommunication Union
LAN:	Local Area Network
LD:	Laser Diode
LED:	Light-Emitting Diodes
LiNbO3:	Lithium Niobate
LNA:	Low Noise Amplifier
LSB:	Least Significant Bit
LTE:	Long Term Evolution
M2M:	Machine-to-Machine
MLL:	Mode-Locked Laser
MLLD:	Mode-Locked Laser Diode
MMF:	Multi-Mode Fibre
mm-Wave:	Millimetre Wave
MSB:	Most Significant Bit
MSR:	Mode-Suppression Ratio
MZI:	Mach-Zehnder Interferometer
MZM:	Mach-Zehnder interferometer Modulator
NA:	Numerical Aperture
NF:	Noise Figure
NRZ:	NonReturn-to-Zero
O/E:	Optic-to-Electric Converter
OBPF:	Optical Bandpass Filter
OCDMA:	Optical Code Division Multiple Access
OCR:	Optical Clock Recovery
ODQPSK:	Optical Differential Quadrature Phase Shift Keying
OGF:	Optical Gaussian Filter
OGR:	Optical Golomb Ruler
OHL:	Optical Hard Limiter
OLT:	Optical Line Terminations
ONU:	Optical Network Unit
OPA:	Optical Parametric Amplifier
OS:	Optical Sampling
OSNR:	Optical Signal-to-Noise Ratio
OWC:	Optical Wavelength Conversion
PADC:	Photonic ADC
P-CMP:	Phase Comparators

PD:	Photo Diode
PDAC:	Photonic DAC
PDAS:	Photonic Distributed Antenna System
PM:	Phase Modulation
PMD:	Polarization Mode Dispersion
PON:	Passive Optical Network
PPG:	Periodic Pulse Generator
PSTN:	Public Switched Telephone Network
P-to-MP:	Point-to-Multi-Point
P-to-P:	Point-to-Point
PWM:	Pulse Width Modulator
QoT:	Quality of Transmission
RAP:	Radio Access Point
RBS:	Remote Base Station
RF:	Radio Frequency
RFI:	Radio Frequency Interference
RIN:	Relative Intensity Noise
RMS:	Root-Mean Square
ROA:	Raman Optical Amplifier
RoF:	Radio over Fibre
RZ:	Return to Zero
SAR:	Successive Approximation Register
SBS:	Stimulated Brillouin Scattering
SCMA:	SubCarrier Multiple Access
SDSAR:	Spatially Distributed Successive Approximation Register
SFDR:	Spurious Free Dynamic Range
SHDTV:	Super-High-Definition Television
SMF:	Single Mode Fibre
SNDR:	Signal-to-Noise and Distortion Ratio
SNR:	Signal to Noise Ratio
SOA:	Semiconductor Optical Amplifier
SoI:	Signal of Interest
SP-DFBL:	Self-Pulsating DFB Laser
SPM:	Self-Phase Modulation
SRS:	Stimulated Raman Scattering
SSH:	Spatial-Spectral Holographic
Tbps:	Tera-bit per second
TDMA:	Time Division Multiple Access
THD:	Total Harmonic Distortion
TOPS:	Tuneable Optical Phase Shifter
TS-DFBL:	Two different Sections Distributed Feedback Laser
UHDTV:	Ultra High Definition Television
UI:	Unit Interval
UV:	Ultra Violet
VCSEL:	Vertical-Cavity Surface Emitting Laser
WAN:	Wide Area Network
WC:	Wavelength Conversion
WDD:	Wavelength Division De-multiplexing
WDM:	Wavelength division multiplexing
WDMA:	Wavelength Division Multiple Access

WiMAX: Worldwide Interoperability for Microwave Access
WiFi: Wireless Fidelity
XAM: Cross-Absorption Modulation
XGM: Cross-Gain Modulation
XPM: Cross Phase Modulation

Chapter 1

Introduction

1.1. Background

Today's communication network deployment is driven by the requirement to send, receive, hand over, and deliver voice, video, and data communications from one end-user to another. Current deployment strategies result in end-to-end networks composed of the interconnection of networks each of which can be classified as falling into one of three main categories of network: core, metropolitan and access network. Each component network of the end-to-end communication network performs different roles.

Nowadays, the increase in the number and size of access networks is the biggest contributor to the rapid expansion of communication networks that transport information such as voice, video and data from one end-user to another one via wired, wireless, or converged wired and wireless technologies. Such services are commonly marketed collectively as a triple play service, a term which typically refers to the provision of high-speed Internet access, cable television, and telephone services over a single broadband connection. The metropolitan networks perform a key role in triple play service provision in delivering the service traffic to a multiplicity of access networks that provide service coverage across a clearly defined geographical area such as a city over fibre or wireless infrastructure. The core networks or long haul networks are those parts of the end-to-end communication network that interconnect the metropolitan area networks. The core network infrastructure includes optical routers, switches, multiplexers and demultiplexers, used to deliver triple play service traffic to the metropolitan networks and route traffic from one metropolitan network to another.

Figure 1-1, shows a simplified diagram of network connecting triple play service providers to end-users of the service. In this network, the uplink traffic from the end-

users is input to the network via wireless or wired access network connections in the user's home. The packets associated with this traffic are multiplexed together and forwarded to the local metropolitan network for delivery to a long haul network for transporting to the service providers' access network and hence to the service provider. The downlink traffic from different service providers which is typically traffic corresponding to requested services is input to the network via local access network connections in the service provider premises. The downlink traffic from a particular access network is multiplexed together and delivered to the local metropolitan network for forwarding to a core network (or in some cases another metropolitan network) and hence to the end-users access networks for delivery to the end users.

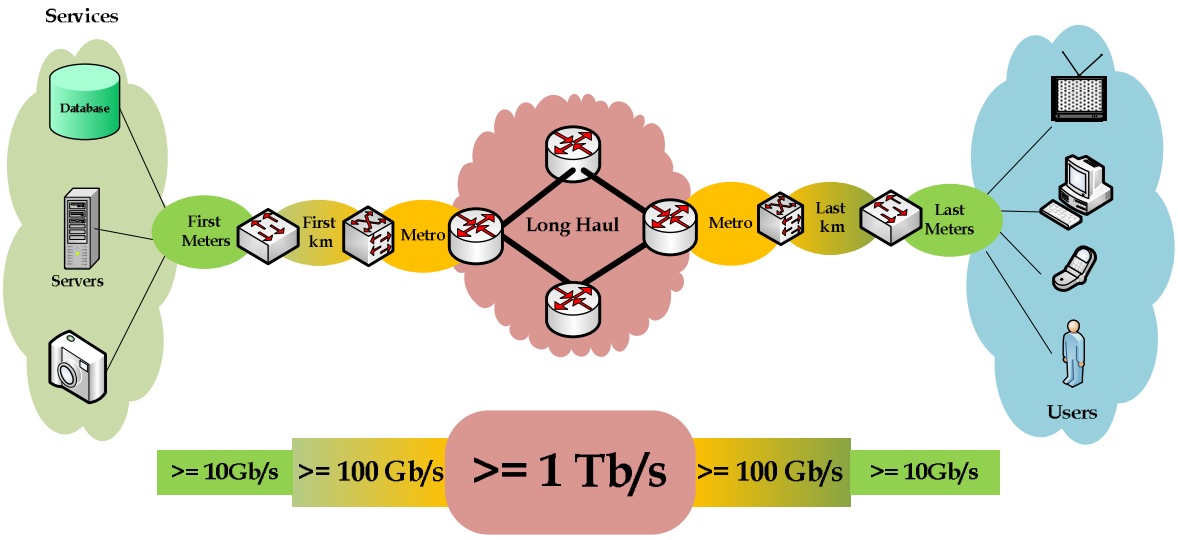

Figure 1-1: Near term future network capacity requirements.

As many access networks are connected to a metropolitan network the traffic data rates throughout a metropolitan network are significantly higher than those throughout an access network. As many metropolitan networks feed traffic into a core network the traffic handling capabilities of a core network are significantly higher than those of a metropolitan network. The network traffic on core networks is expected to reach the order of ten exabytes in the near future [1]. The rapidly changing face of networked communications has seen a continued growth in the need to transfer enormous amounts of information across large distances. A consequence of this is that technologies that are used extensively for transferring

information such as coaxial cable, satellite, and microwave radio are rapidly running out of spare capacity [2].

Therefore, transportation of the traffic volumes that will be demanded by users in the near future will require significantly greater network transmission bandwidth than that provided by the current infrastructure. Consequently, in the near term each category of component network of existing end-to-end networks will face different and increasingly difficult challenges with respect to transmission speed, cost, interference, reliability, and delivery of the demanded traffic to or from end-users. However, super-broadband penetration and the on-going growth in the internet traffic to and from business and home users are placing a huge bandwidth demand on the existing infrastructure.

Broadband wireless sits at the confluence of two of the most remarkable growth stories of the telecommunication industry in recent years. Wireless and broadband have each enjoyed rapid mass-market adoption. Wireless mobile services grew from 11 million subscribers worldwide in 1990 to more than 6.2 billion by the end of first quarter of 2012. Moreover, it is forecasted to reach 9 billion by 2017 while about 5 billion are mobile broadband subscribers [3]. Fixed broadband subscribers numbered only 57,000 in 1998 is projected to exceed 720 million by 2015 [4][5]. The growth in the numbers of mobile telephone subscribers, broadband and internet users over the last decade and the projections for the growth in these numbers are depicted in Figure 1-2.

It follows that the demand for use of the available radio spectrum is very high, with terrestrial mobile phone and broadband internet systems being just one of many types of access technology competing for bandwidth. Mobile telephony and internet applications require the systems that support them to operate reliably in non-line-of-sight environments with a propagation distance of 0.5-30 km, and at velocities up to 100 km/h or higher. These operating environment constraints limit the maximum radio frequency the systems can use as operating at very high frequencies, i.e. approaching microwave frequencies, results in excessive channel path loss, and excessive Doppler spread at high velocity.

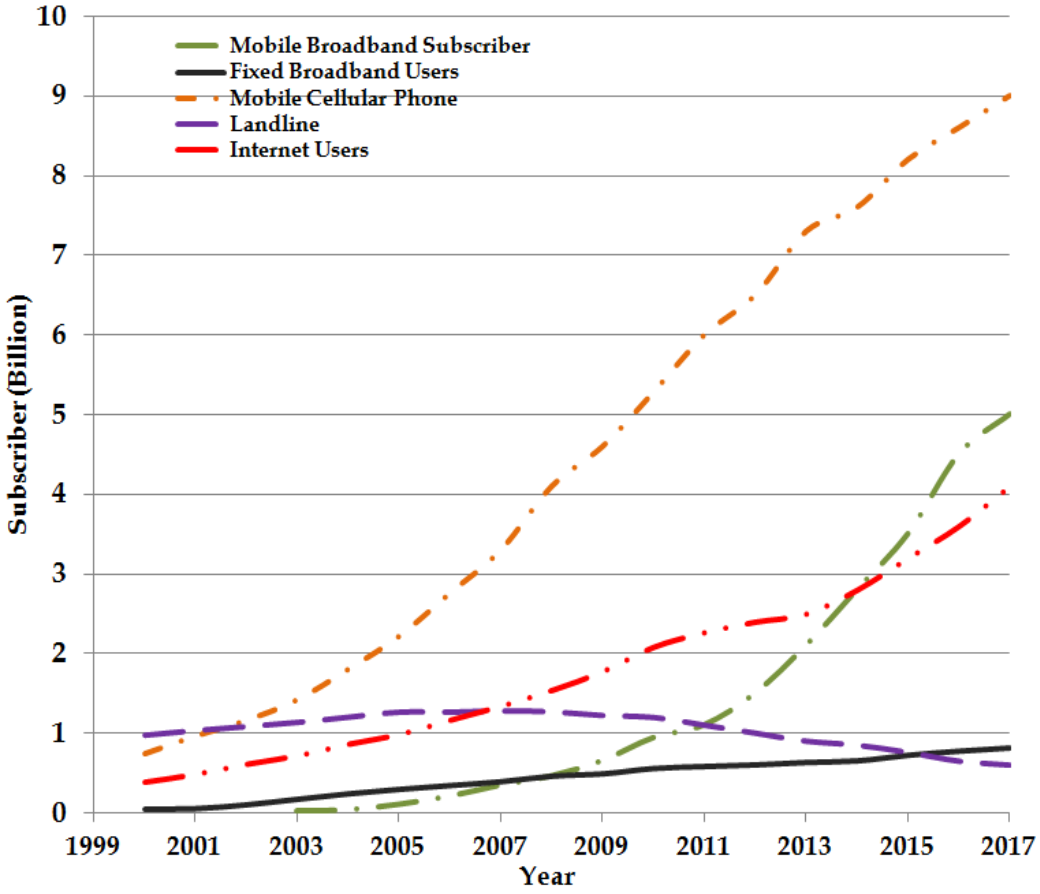

Figure 1-2: Worldwide subscriber growth in the numbers of mobile telephony, internet, and broadband access users [3][5].

This limits the spectrum suitable for mobile applications making the value of the radio spectrum extremely high. As an example, in Europe auctions of 3G licenses for the use of radio spectrum began in 1999. In the United Kingdom, 90 MHz of bandwidth was auctioned off for £22.5 billion (GBP). In Germany, the result was similar, with 100 MHz of bandwidth raising $46 billion (US). This represents a value of around $ 450 million (US) per MHz. The duration of these license agreements is 20 years. Therefore, it is vitally important that the spectral efficiency of the communication system should be maximized, as this one of the main limitations to providing low cost high data rate services [6][7].

1.2. Evolution of Data Traffic and Future Demand

Globally, mobile communication data traffic is expected to increase 45-fold between 2010 and 2016 and reach 10.8 exabytes (1.08×10^7 Terabytes) per month by 2016.

Furthermore, the Compound Annual Growth Rate (CAGR) of mobile data traffic is expected to reach 72 percent over the period 2010 to 2016. Moreover, during 7 years from 2005 to 2012 mobile data traffic will have increased a thousand-fold. In 2010, about 49.8% of mobile data traffic was video traffic [8][9].

By the end of 2011, video traffic over mobile networks reached about 52.8% of the total traffic on mobile networks. It is expected that almost 67% of the world's total mobile traffic will be video by 2016 and that the volume of video traffic on mobile networks will have doubled every year over the period 2010 to 2016 [8][9]. In Figure 1-3, the worldwide growth in data traffic rates per month are compared for mobile terminals and other devices. Figure 1-3 (a) shows the anticipated growth of data traffic by user terminal type for the following terminal types: tablets, machine-to-machine (M2M), home gateways, smartphones, laptops, non-smartphones, and other portable devices. It is predicted that in 2015, 82.4% of all network data traffic, about 5.768 exabytes per month, will be being transported to and from just by two types of portable wireless devices. Specifically, it is predicted that 55.8% and 26.6% of all network data traffic will relate to laptop and smartphone users, respectively. As shown in Figure 1-3 (b), the expectation is that the data traffic rate related to mobile devices will be about 10.8 exabaytes per month by the end of 2016 [9].

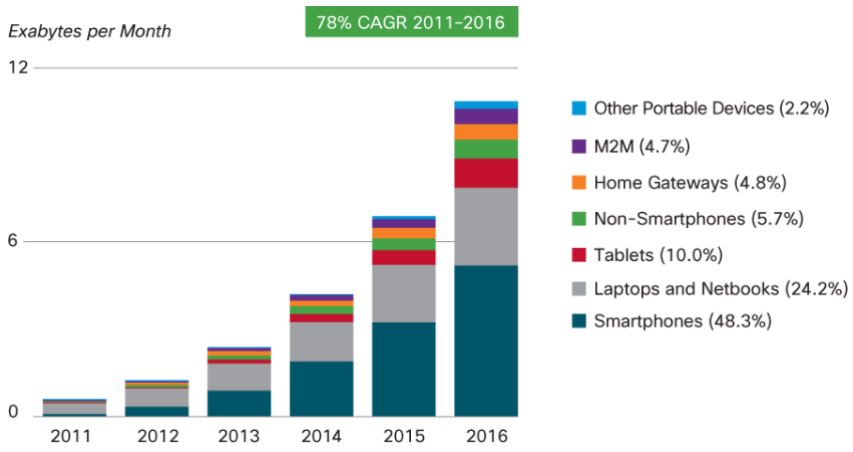

(a)

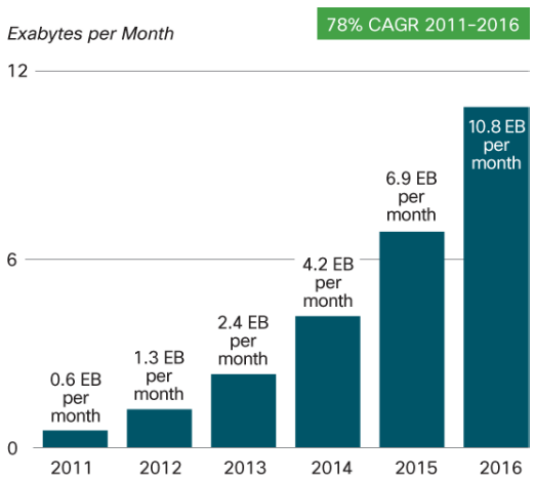

(b)

Figure 1-3: The anticipated growth of data traffic (a): by user terminal type, (b) forecast of mobile data traffic growth by 2016[9].

High-Definition Television (HDTV) can now be provided in many countries throughout the world while Ultra High Definition Television (UHDTV) is now being studied in Japan as the most promising candidate for next-generation television beyond HDTV, and Super-High-Definition Television (SHDTV). UHDTV consists of extremely high-resolution images and multi-channel 3D video and sound to give viewers a stronger sensation of presence. The UHDTV project's commercializing outlook is to become available in domestic homes over the period 2016 to 2020 [10][11].

1.3. Motivation of Super-broadband Access Network Deployment

Globally the evolution of internet video services will be in the three following phases: 1) experiencing a growth of internet video as viewed on the PC, 2) internet delivery of video to the TV, and 3) interactive video communications, which is shown in Figure 1-4. Therefore, there is significant growth in the Internet Protocol (IP) transport of cable and mobile IPTV, and video on-demand services [4] and as forecast, by 2016 about two-thirds of the network traffic will be video streaming [9]. Thus, by considering the future ultra high, super high and high definition resolution of end-user demanded and generated data traffic; each phase will impact on a

different aspect of the end-to-end delivery network such as bandwidth, spectral efficiency, cost, power consumption, architecture, and technology.

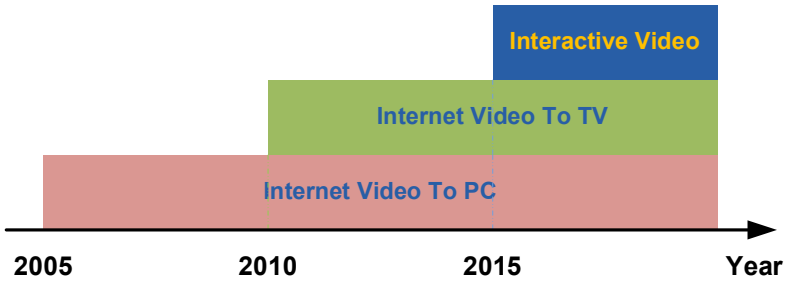

Figure 1-4: Three waves of consumer Internet traffic growth.

Furthermore, in the recent years wireless services have been taking a steadily increasing share of the telecommunications market. Mobile voice services are already considered a necessity by many end-users, and mobile data, video, and TV are now becoming an essential part of some end-users' lives. End users not only benefit from their main virtue, mobility, but are also demanding ever larger bandwidth. Super-broadband access network can deliver beyond Gigabit/s traffic to the end-users premises. Thus, ultra-fast and super-broadband are recognized as becoming increasingly important as demands for bandwidth multiply. Moreover, there is an essential need to increase the capacity of delivery networks for mobile broadband, data access, and video services to retain subscribers as well as keep cost in check. Furthermore, larger wireless capacity per user requires the reduction of the wireless cell size, i.e. establishing pico-cells.

In response to this remarkable development, core and metro networks have experienced a tremendous growth in bandwidth and capacity with the widespread deployment of fibre-optic technology over the past decade [4]. Fibre optic transmission has become one of the most exciting and rapidly changing fields in telecommunication engineering. Fibre optic communication systems have many advantages over more conventional transmission systems. They are less affected by noise, are completely unaffected by Electro-Magnetic Interference (EMI) and Radio Frequency Interference (RFI), do not conduct electricity and therefore, provide electrical isolation, are completely unaffected by lightning and high voltage switching, and carry extremely high data transmission rates over very long distances

with low attenuation [12]. As shown in Figure 1-1, data speeds in metro and long-haul systems are evolving from 10-40 Gbps to 100 Gbps per wavelength channel systems [8]. Wavelength Division Multiplexing (WDM) techniques, such as: Dense WDM (DWDM), and Highly DWDM (HDWDM) offer the potential of Tera-bit per second (Tbps) bandwidth of fibre optic networks with all-optical switching and routing in the future. Therefore, by deploying converged Fibre and Wireless (Fi-Wi) communication technologies, network operators and service providers can meet the challenges of providing low cost high data rate services to wireless users. Only the relatively huge bandwidth of a fibre optic access network can currently support low cost high data rate services for wired and wireless users. This makes the case for Radio over Fibre (RoF) networks as a future proof solution for supporting super-broadband services in a reliable, cost-effective, and environmentally friendly way.

However, investment in the development of next-generation optical-wireless converged access technologies will enable a future network to be deployed that will radically reduce FiWi infrastructure costs by removing local exchanges and potentially much of the metro network [13-15].

1.4. Aims and Contributions

The aim of this thesis is design a Fully-Photonic Digital Radio over Fibre (FP-DRoF) architecture for application of a future-proof super-broadband access network and investigation of its performance to evaluate its physical functionality. Because of all digital transportation of digitized-RF signal over fibre, the proposed FP-DRoF could be integrated with a conventional access, or metropolitan, and or backhaul of digital fibre optic communication network infrastructures. This shares the network implementation cost overhead and investment between several service providers and operators for desired services and applications.

The key components of Digital Radio over Fibre (DRoF) are electronic data converters such as Analogue-to-Digital converter and Digital-to-Analogue Converter (ADC and DAC). The challenge and upper limit of ADCs at higher sampling rate is performance degradation associated to timing jitter and uncertainty of sampling

time. Because of this physical constraint, all photonic data conversion systems are proposed that is deployed in the proposed FP-DRoF architecture.

In this research, all-photonic signal conversion systems such as Photonic ADC (PADC) and Photonic DAC (PDAC) are designed and optimized for a desired 60 GHz sampling frequency and 10 GHz bandwidth under investigation. In the following of PADC and PDAC design and their performance evaluation the FP-DROF system is proposed. Design and performance evaluation of the proposed FP-DRoF system in the simulation environment is performed in Opti-Wave Opti-System and Matlab simulation tools environment. In this model the system functionality and performance is assessed through a shared fibre transportation medium whereas the FP-DRoF and an Analogue Radio over Fibre (ARoF) systems performance is investigated and compared.

The outline of this research work contributions are as follows:

1. Design of the key sub-systems of the FP-DRoF system such as all Photonic Analogue-to-Digital and Digital-to-Analogue Converters, (PADC and PDAC) to process the signals all optically. All optical signal conversion systems are proposed by designing a novel all-photonic pipelined ADC and a new all-photonic binary-weighted DAC. The proposed PADC and PDAC systems' performance and functionalities are investigated.
2. Design of a 3R regeneration system based on time-stretching, electro-optical sampling and optical hard-limiter in order to improve the PADC and the PDAC systems' performance. The proposed 3R regeneration system's functionality and performance are investigated for different length of fibre link and in different conditions of the degraded input signal and transmission channel.
3. Designing and proposing a new FP-DRoF system for future super-broadband access network application. The proposed FP-DRoF system's performance is investigated in the different schemes of wavelength allocation and the channel conditions. The simulation results are compared with an ARoF link to assess the link performance improvement and functionality evaluation of the FP-DRoF against ARoF system.

The rest of this thesis is organised as follows: In chapter 2, the following subjects are discussed: an overview of the ARoF technology, review of optical communication system, link and components impairments, key parameters impacts on the link performance and RoF link design methodology. This discussion facilitates the design of the proposed FP-DRoF system, the generated results analysis and justification.

In Chapter 3, following of a concise introduction on DRoF, discussion on the state-of-the-art of the key components of the conventional DRoF such as ADC and DAC, are presented whereas their physical parameters and specifications are discussed. A future-proof solution is proposed by replacing electronic systems with the corresponding photonic systems. Subsequently, existing photonic ADC's and DAC's architectures are reviewed. In the following of state-of-the art architectures presentation, the proposed pipelined PADC and binary-weighted PDAC are proposed, designed and their performances are investigated.

To improve the proposed FP-DRoF system performance, the design and deployment of a Retiming and Reshaping and Reamplifying (3R) regeneration system are proposed. Therefore, in chapter 4 an introduction theory about data and clock recovery in electronic and optical systems, the building blocks and state-of-the-art of optical 3R regeneration system are studied. A 3R regeneration system is proposed based on time-stretching, electro-optical sampling and optical hard-limiter to retime and reshape the digital optical signals. Subsequently, the performance of the proposed system is investigated in different conditions and compared with the system without 3R regeneration.

Chapter 5 discusses the design of the proposed FP-DRoF system and evaluating its performance in different channel conditions. The FP-DRoF system performance is investigated and compared with an ARoF system. The systems are modelled to transport the digital and analogue traffic at different wavelength over a shared and a dedicated optical communication link in different conditions and wavelength allocation schemes.

Eventually, the research findings of this thesis along with the future work are presented in Chapter 6.

1.5. References

[1] J. Laskar, S. Pinel, D. Dawn, S. Sarkar, B. Perumana, P. Sen ,"The Next Wireless Wave is a Millimeter Wave", IEEE Microwave Journal, vol.90, no. 8, , pp. 22-35, August, 2007.

[2] J. Mcdonough ,"Moving Standards to 100 Gbps and Beyond", IEEE Communication Magazine, vol. 45, no.11, pp. 6-9 , Nov. 2007.

[3] Ericsson Traffic and Market Report on the Pulse of the Networked Socity, June 2012.

[4] Optical Access Seamless Evolution (OASE), Available from http://cordis.europa.eu/fetch?CALLER=PROJ_ICT&ACTION=D&CAT=PROJ&RCN=93075, Feb., 2010.

[5] ITU ,"The World in, ICT Facts and Figs", Available from http://www.itu.int, 2009.

[6] OMEGA ICT Project ,"Gigabit Home Networks", Seven Framework Programme, Available from http://www.ict-omega.eu, 2008-2011.

[7] R. Yuen,; X. N. Fernando,; S. Krishnan ,"Radio Over Multimode Fiber for Wireless Access", IEEE Canadian Conference on Electrical and Computer Engineering, vol.3, pp. 1715-1718, May 2004.

[8] FP7, "A Converged Copper-Optical-Radio OFDMA-Based Access Network with High Capacity and Flexibility", ICT Objective 1.1 The Network of the Future, Jan. 2010.

[9] Cisco Visual Networking Index, "Global Mobile Data Traffic Forecast Update", Sep. 2012.

[10] M. Sugawara, K. Masaoka, M. Emoto, Y. Matsuo, Y. Nojiri, "Research on Human Factors in Ultra-high-definition Television to Determine its Specifications", SMPTE Technical Conference, October 2007.

[11] K. Kudo, “Introduction of High-Definition TV System in NHK News Center”, ABU Technical Committee 2005 Annual Meeting, November 2005, Hanoi.

[12] Y.F. Guo, G.S. Kuo, “A novel QoS-guaranteed power-efficient management scheme for IEEE 802.15.3 HR-WPAN”, 4th Annual IEEE Consumer Communications and Networking Conference (CCNC 2007) pp. 634-638, 2007.

[13] H. C. Ji, H. Kim, Y. C. Chung, “Full-Duplex Radio-Over-Fiber System Using Phase-Modulated Downlink and Intensity-Modulated Uplink”, IEEE Photonics Technology Letters, vol. 21, no. 1, pp 9-11, Jan. 2009.

[14] T. Koonen, “Fiber to the Home/Fiber to the Premises: What, Where, and When? ”, Proceedings of the IEEE , vol. 94, no. 5, , pp. 911-934, May 2006

[15] C. Lim, A. Nirmalathas, M. Bakaul, P. Gamage, K. L. Lee, Y. Yang, D. Novak, R. Waterhouse, “Fiber-Wireless Networks and Subsystem Technologies”, IEEE Journal of Lightwave Technology, vol. 28, no. 4, pp. 390-405, 2010.

Chapter 2

Radio over Fibre Technology and Network

2.1. Introduction

Currently Fibre-to-the-home (FTTH) access technologies provide huge bandwidth to users, but are not flexible enough to allow roaming connections. On the other hand, wireless networks offer mobility to users, but do not possess sufficient bandwidth to meet the demand for multi-channel video services with high definition quality. The seamless integration of wired and wireless services over future-proofed access networks would enable the provision of high bandwidth to both fixed and mobile users in a single low-cost transport platform. This can be accomplished by using hybrid optical and wireless networks, which not only can transmit signals received wirelessly at the Base Station (BS) over fibre, but also simultaneously provide services received over fibre to wireless end users.

An optical communication system can be designed to transport digital or analogue information. The crucial difference between these two scenarios is that on a network comprised of links carrying digital information the potential capacity of the links is far more effectively exploited. In technical terms, in a digital optical link the modulation depth is perfect (100%) but in an analogue link the modulation index is less than the digital modulation depth.

Optical and wireless access network infrastructure is being deployed around the world. When these heterogeneous access networks converge to a highly integrated network via a common optical feeder network, network operators can lower the operating costs of their access networks and meet the capital costs of future network upgrades more easily. In addition, the converged access network facilitates greater sharing of network infrastructure between multiple network operators.

In such a scenario of convergence, the transportation of radio signals over optical fibre links would be a way of simplifying the architecture of remote BSs. By relocating key functions of a conventional BS to a central location, BSs could be simplified into remote antenna units connected to a Central Office (CO) via a high performance optical fibre feeder network.

Wireless networks typically show considerable dynamics in the traffic load on their Radio Access Points (RAPs), due to fluctuations in the numbers of users as a consequence of roaming and variations in the nature of the services users require. The traditional RAPs approach to addressing this issue involves ensuring all the wireless nodes can handle highest demand for bandwidth that can be presented to an individual node which results in the inefficient use of resources. The alternative approach, using dynamic reconfigurable micro/pico or femto wireless cells, increases network complexity. Furthermore, new wireless subscribers signing up with wireless network operators are with an increasingly demanding more capacity for ultra-high data rate transfer at speeds of several Giga-bit-per second, while radio spectrum is limited. This demand for ever more bandwidth places a heavy burden on the operators' available radio spectrum and causes spectral congestion at lower microwave frequencies; Millimetre Wave (mm-Wave) communication systems offer a means to improve these problems [1].

Radio over Fibre (RoF) communication networks; modulate a Radio Frequency (RF) sub-carrier onto an optical carrier for distribution over a fibre network. An Analogue RoF (ARoF) (also known as RoF) link includes an optical source, modulator, optical amplifier & filters, an optical channel and a photodiode as a receiver, electronic amplifiers and filters. ARoF technology is currently receiving a lot of attention due to its ability to provide simple antenna front ends, increased capacity, and multi wireless access coverage.

ARoF links are mainly transmitting microwave and mm-wave signals by applying an intensity modulation technique onto an optical carrier [2]. Fundamentally, two methods exist for transmission of the microwave/mm-wave signals over

conventional optical links with intensity modulation: (1) direct intensity modulation, (2) external modulation.

In direct intensity modulation, an electrical parameter of the light source is modulated by the RF information signal. In practical links, the parameter used is the current of the laser diode serving as the optical transmitter. In Figure 2-1, the simplest and most cost-effective architecture, Intensity-Modulation Direct-Detection (IMDD), is depicted. In this architecture, the detection is performed using a Photo diode (PD). In the direct-modulation process a semiconductor laser directly converts a small-signal modulation of current (around a bias point set by a dc current) into a corresponding small-signal modulation of the intensity of the photons emitted (around the average intensity at the bias point). Thus, a single device serves as the optical source and the RF/optical modulator.

In this system, for the downlink at the central station, a wireless signal is modulated onto an optical carrier that generated by a Laser Diode (LD) and the modulated optical signal is transported over a fibre optic cable. The transported optical signal is detected at the base station using a PD. The recovered wireless signal after performing analogue signal processing is fed to an antenna. For uplink signal transmission from the base station to the central station, the received signals from the antenna are directed to a Low Noise Amplifier (LNA) and the output of the amplifier is modulated onto an optical carrier generated by another LD. The resulting optical signals are sent to the central station for signal processing and detection.

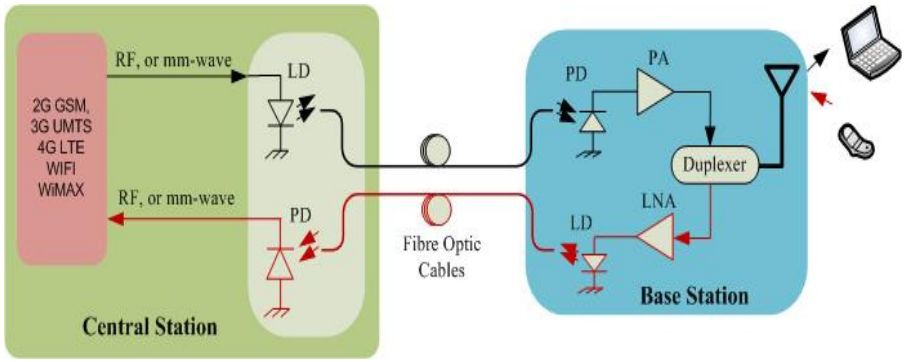

Figure 2-1: An architecture of a full-duplex ARoF link with direct intensity modulation and direct detection (IMDD).

In the external modulation technique, an unmodulated light source is modulated with a RF information signal using an electro-optical intensity, phase, frequency modulator or Electro-Absorption modulator. Figure 2-2 shows ARoF link architecture for indirect intensity modulation that uses an electro-optical modulator for modulating an electrical wireless signal onto a continuous wave laser source.

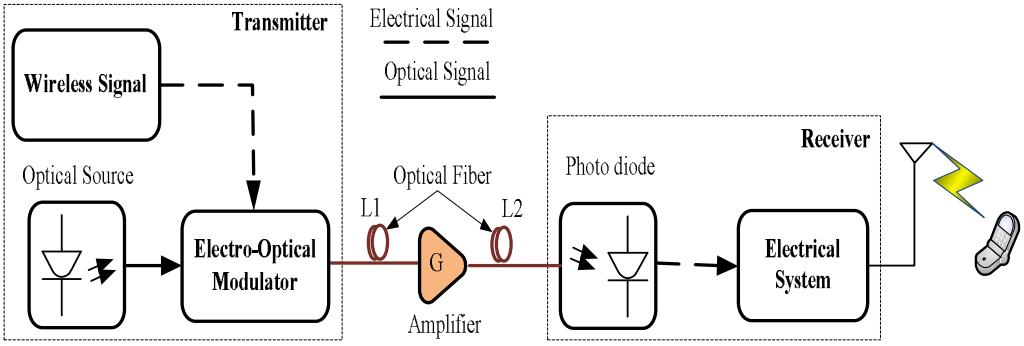

Figure 2-2: Architecture of an ARoF link with indirect intensity modulation (downlink).

An important limitation of IMDD architecture is the modulation bandwidth restriction on the laser for super-broadband access networks and mm-wave band access. Direct intensity modulation lasers operating at up to 50 GHz or even higher have been developed but these diodes are expensive and not cost-effective in the commercial market. Therefore, at frequencies above 10 GHz, external modulation rather than direct modulation is applied. However, because of the high number of BSs in RoF networks, simple and cost-effective components must be utilized. Consequently, in the uplink of a RoF network system, it is convenient to use direct intensity modulation with cheap lasers; this may require down conversion of the uplink RF signal received at the BS. In the downlink either lasers or external modulators can be used.

When the RF signal is directly modulated by an optical source the laser is usually a significant source of noise and distortion in a radio over fibre link; the laser diode normally exhibits nonlinear behaviour. When the laser diode is driven well above its threshold current, its input/output relationship can be modelled by a Volterra series of order 3. It follows that in high data rate links indirect modulation has better performance than direct intensity module. Nevertheless, an ARoF link suffers from

the nonlinearity of both the microwave and optical components that constitute the optical link [2-4].

2.2. Radio over Fibre's Link Architecture

The signal that is transmitted over the optical fibre can either be originally an RF, Intermediate Frequency (IF), or BaseBand (BB) signal. For the IF and BB transmission cases additional hardware for up converting the signal to RF band is required at the BS. At the optical transmitter, the RF/IF/BB signal can be modulated onto the optical carrier using direct or external modulation of the laser light. In an ideal case, the output signal from the optical link will be a copy of the input signal. However, there are some limitations because of non-linearity and frequency response limits in the laser and the modulation device as well as dispersion in the fibre. The transmission of analogue signals puts certain requirements on the linearity and dynamic range of the optical link. These demands are different and more exact than the requirements on digital transmission systems.

Figure 2-3 illustrates typical ARoF links' configurations, which are classified based on the kinds of frequency bands transmitted over the optical fibre link. In the downlink from the Central Station (CS) to the BSs, the information signal from a Public Switched Telephone Network (PSTN), an Internet Service Provider (ISP), a mobile communication operator, an Intelligent Transportation System (ITS) or other source is fed into the optical network at the CS. The signal that is either RF, IF or BB band modulates an optical signal from a LD. As described earlier, if the RF band is low, it's possible to modulate the LD signal with the RF band signal directly. If the RF band is high, such as the mm-wave band, it's better to use an external modulator. The modulated optical signal is transmitted to the BS via optical fibres. At the BS, the RF/IF/BB band signal is recovered by detect the modulated optical signal by using a PD. The recovered signal, which needs to be up converted to RF band if it is an IF or BB signal, is transmitted to the mobile user's device via the antennas of the BS.

In the configuration shown in Figure 2-3 (a), the modulated signal is generated at the CS in an RF band and directly transmitted to the BS by an external modulator, which

is called “RF-over-Fibre”. At each BS, the modulated signal is recovered by detecting the modulated optical signal with a PD and directly transmitted to the user’s wireless devices by an antenna. Signal distribution using RoF has the advantage of a simplified BS design but is susceptible to fibre chromatic dispersion that severely limits the transmission distance [5]. In the configuration shown in Figure 2-3 (b), the modulated signal is generated at the CS in an IF band and transmitted to the BS by an external modulator, which is called “IF-over-Fibre”. At each BS, the modulated signal is recovered by detecting the modulated optical signal with a PD, up converted to an RF band, and transmitted to the user’s wireless device. In this scheme, the effect of fibre chromatic dispersion on the distribution of IF signals is much reduced, although incorporating IF-over-Fibre transport capability in antenna BS implemented for a RoF system requires additional electronic hardware such as a mm-wave frequency LO for frequency up- and down conversion.

In Figure 2-3 (c), the modulated signal is generated at the CS in baseband and transmitted to the BS, which is referred to as “BB-over-Fibre”. At each BS, the modulated signal is recovered by detecting the modulated optical signal with a PD, up converted to an RF band through an IF band or directly, and transmitted to the user’s wireless device. In baseband transmission, the impact of the fibre dispersion effect is negligible, but the BS configuration is the most complex. This is especially important when RoF at mm-wave bands is combined with Dense Wavelength Division Multiplexing (DWDM). This increases the amount of equipment at the BSs because an up converter for the downlink and a down converter for the uplink are required. In RF subcarrier transmission, the BS configuration can be simplified only if a mm-wave optical external modulator and a high-frequency PD, respectively, are applied to the Electric-to-Optic (E/O) and the Optic-to-Electric (O/E) converters.

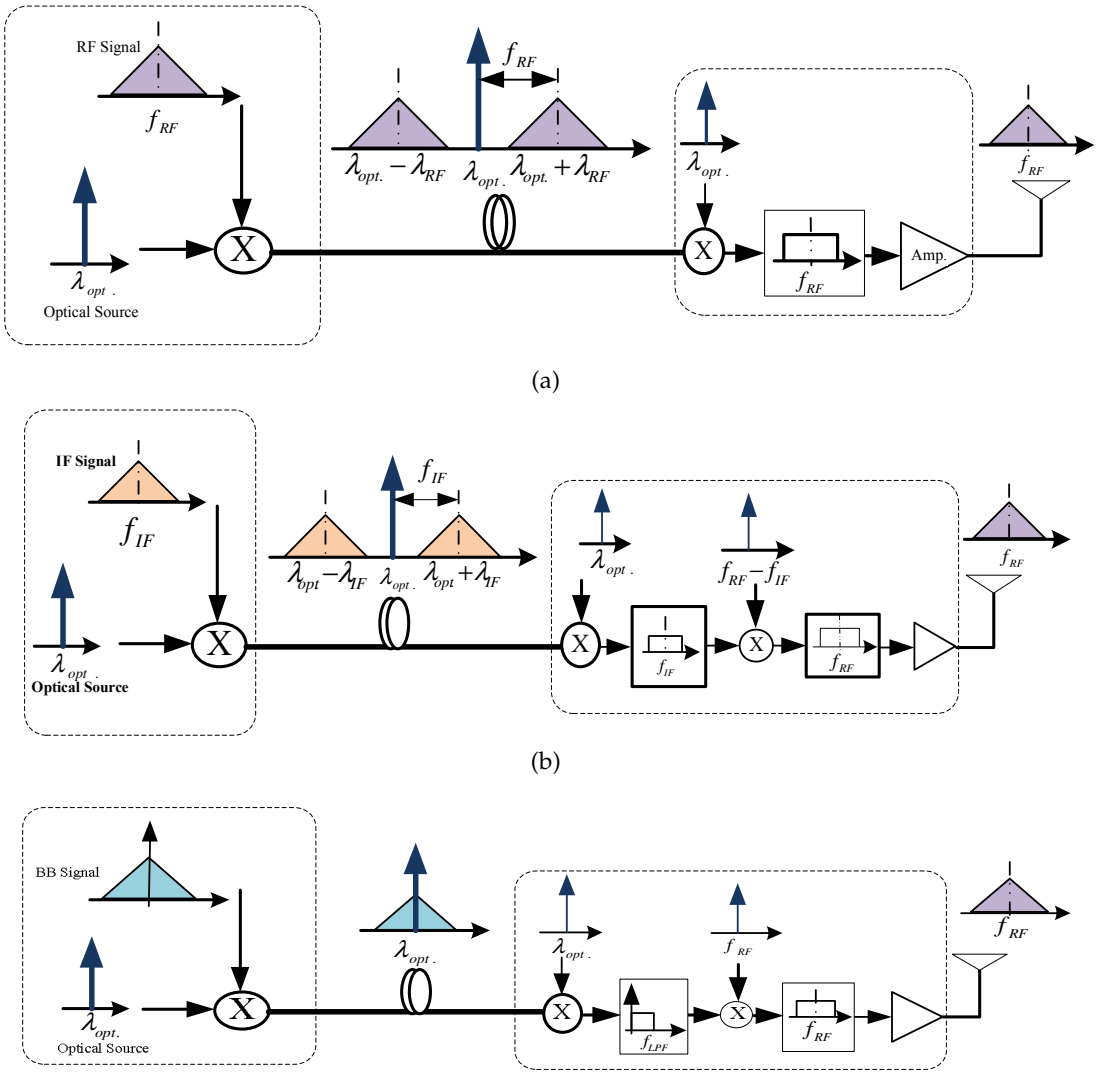

Figure 2-3: Different schemes for signal modulation onto optical carrier and distribution. (a) Radio over Fibre; (b) IF over Fibre; (c) BB over Fibre.

2.3. Radio over Fibre Features

The ARoF technique has been considered a cost-effective and reliable solution for the distribution of future wireless access technologies communications by using optical fibre with vast transmission bandwidth capacity. Moreover, within the optical access network layer, WDM Passive Optical Networks (PONs) allow an extra level of reconfiguration as wavelengths can be accessed either by static or dynamic routing.

An ARoF link is used in remote antenna applications to distribute signals to a microcell or picocell BS. The downlink RF signals are distributed from a CS to many BSs known as a RAP through the fibres. The uplink signals received at RAPs are sent

to the CS for any signal processing. RoF has the following main features: 1) it is transparent to bandwidth or modulation techniques, 2) It accommodates simple and small BSs, 3) Centralized operation is possible, 4) It supports multiple wired and wireless standards simultaneously, 5) It has relatively low power consumption. However, the RoF technique faces challenges for implementation such as: fibre optic network implementation cost, optical communication components nonlinearity, and fibre dispersion. Consequently, in last decade several research projects have sought to develop and discover new solutions to overcome these challenges and broaden the benefits of the RoF concept.

2.4. Network Topologies

There are different topologies for deploying the RoF network from a central exchange station to an end-user's premises such as: 1) point-to-point (P-to-P): where individual fibres run from the central station to end-users, 2) point-to-multi-point (P-to-MP) active star architecture: where a single feeder fibre carries all traffic to a remote active node close to the end-users, and from there individual short branching fibres run to the end-users. In this architecture, the fibre network's implementation cost is less than that of a point-to-point topology but the main disadvantages of this architecture are: a) the bandwidth of the feeder fibre is shared between several end-users and the dedicated bandwidth for each end-user is less than in the point-to-point architecture. b) the requirement for active equipment in a remote node will impose some restrictions on network deployment such as the availability of a reliable and uninterruptable power supply, proper space for installation of active equipment, air conditioning and ventilation, and maintenance costs, 3) point-to-multi-point passive star architecture: in which the active node of the active star topology is replaced by a passive optical power splitter/combiner that feeds the individual short range fibres to end-users. This topology has become a very popular and is known as the PON. In this topology, in addition to a reduction in installation cost, the active equipment is completely replaced by passive equipment avoiding the powering and related maintenance costs [7].

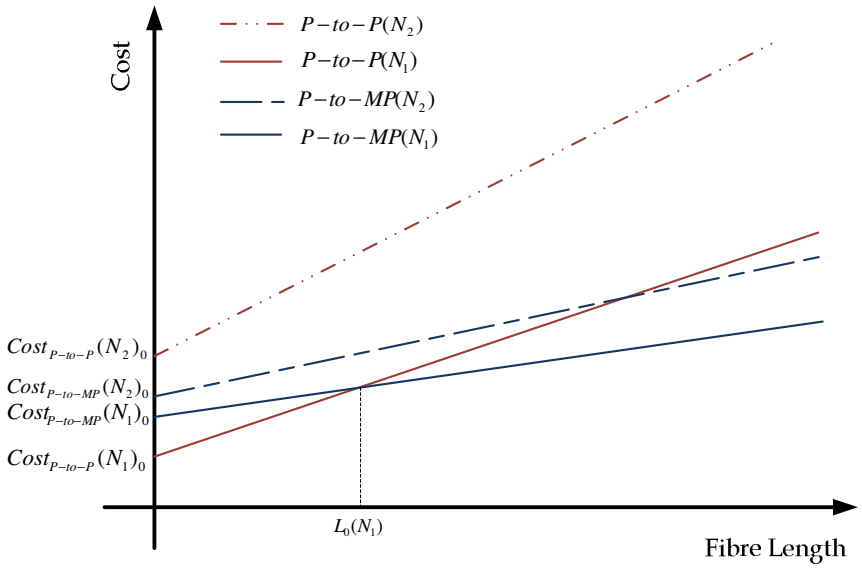

Figure 2-4: The comparison of systems cost of FTTH for different topology networks versus duct length to end-users premises [7].

Besides the technical issues of implementation, the maintenance and operation costs overhead should be accounted for as it plays a key role in choosing a particular architecture. In the P-to-P architecture, for each end-user, two dedicated Optical Line Terminations (OLT) are needed, while, in the P-to-MP scheme, for each end-user one dedicated OLT is required at the end-user side, another shared OLT at the central station is interfaced between several end-users. When the number of customers increases, the system costs of the P-to-P architecture grow faster than those of the P-to-MP architecture, as more fibres and more line terminating modules are needed. Therefore, sharing the implemented infrastructures between several operators, service providers, technologies, and end users is essential to reduce the cost of network infrastructure. Figure 2-4 illustrates that the initial cost of a P-to-P topology ($Cost_{P\text{-}to\text{-}P}(N_1)$) for N_1 users will be lower than initial cost of a P-to-MP topology ($Cost_{P\text{-}to\text{-}MP}(N_1)$) for relatively short duct lengths. However, as duct lengths increase and reaches, at point L_0 in Figure 2-4, were the $Cost_{P\text{-}to\text{-}P}(N_1)$ graph crosses the $Cost_{P\text{-}to\text{-}MP}(N_1)$ graph and is greater than it for fibre lengths longer than L_0. Furthermore, the initial cost of a P-to-MP topology for a large enough number, N_2, of users, where $N_2 > N_1$, is less than the initial cost of a P-to-P topology for N_2 users.

In the P-to-P and P-to-MP active star architectures, each fibre link only carries a data stream between two electro-optic converters, and the traffic streams of the end-users

are multiplexed electrically at these terminals. Therefore, there is no risk of collision of optical data streams; the traffic multiplexing is done optically in a PON topology by the integration of the data streams at the passive optical power combiner. To avoid collisions between individual data streams it is necessary to implement a well-designed multiplexing technique. A model of WDM PON network is shown in Figure 2-5.

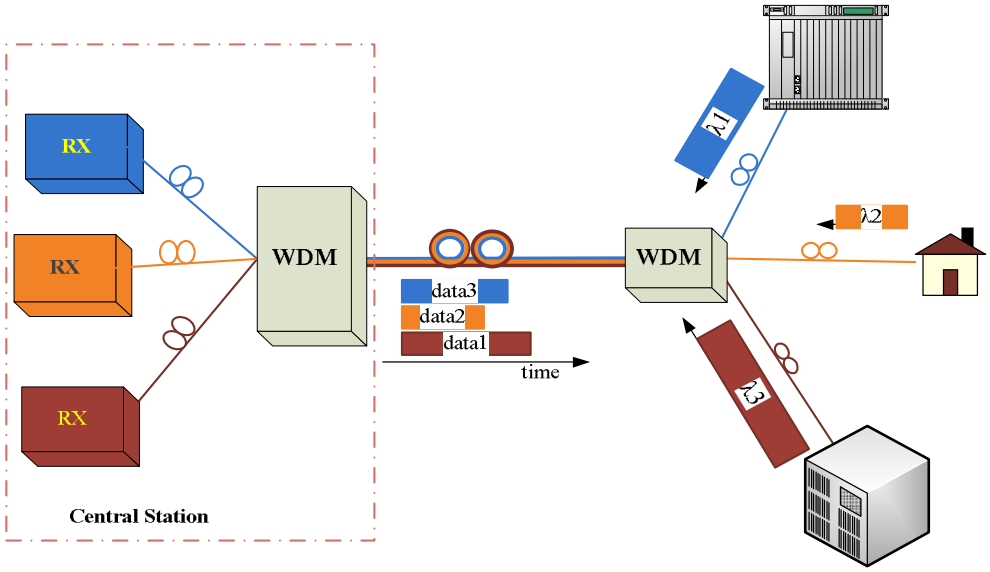

Figure 2-5: A model of a point-to-multi-point passive optical network topology.

Several multiplexing techniques are used in PON networks, such as Time Division Multiple Access (TDMA), SubCarrier Multiple Access (SCMA), Wavelength Division Multiple Access (WDMA), and Optical Code Division Multiple Access (OCDMA). Except for the wavelength division multiplexing technique, these multiplexing techniques are available in wireless or wired telecommunication systems. As shown in Figure 2-6, in a WDM PON, each Optical Network Unit (ONU) uses a different wavelength channel to send its packets to an OLT in a central office. The wavelength channels can be routed from the OLT to the appropriate ONUs and vice versa by a wavelength demultiplexing/multiplexing device located at the PON splitting point. This wavelength multiplexing technique ensures independent communication channels and the network could transport different signal formats; even if the channels use different multiplexing techniques no time synchronization between the channels is needed.

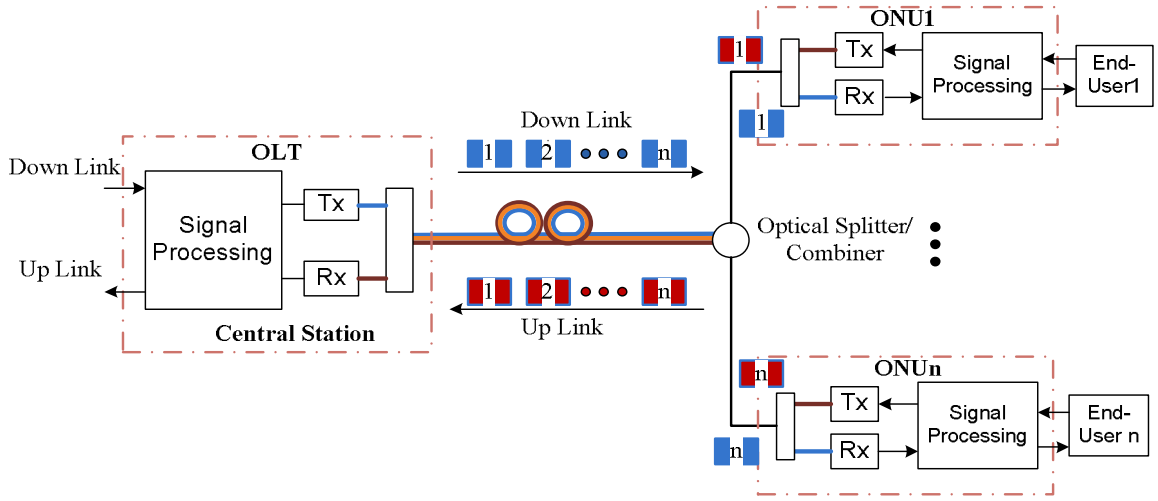

Figure 2-6: WDM over a passive optical network.

2.5. WDM in the RoF System

The application of WDM in RoF networks has many advantages including simplification of the network topology by allocating different wavelengths to individual BSs, enabling easier network and service upgrades and providing simpler network management. Thus, WDM in combination with optical mm-wave transport has been widely studied [6][8].

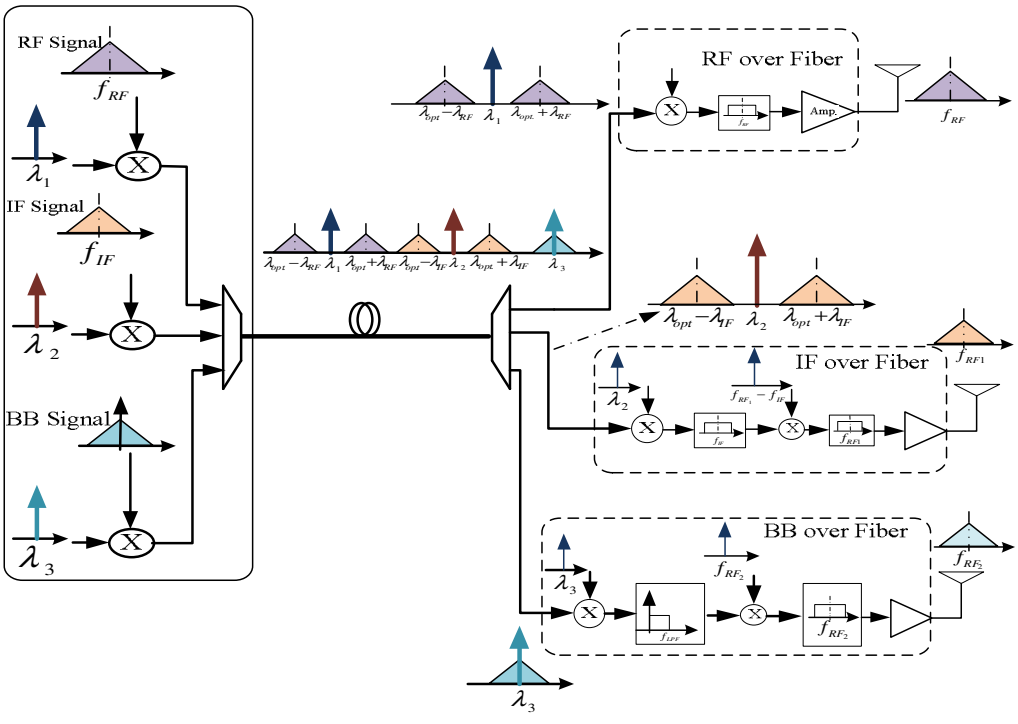

Figure 2-7: Schematic illustration of a WDM scheme application in RoF network.

A schematic arrangement is illustrated in Figure 2-7, where for simplicity only downlink transmission is depicted. Optical mm-wave signals from multiple sources are multiplexed and the generated signal is optically amplified, transported over a single fibre, and demultiplexed to address each BS. A challenging issue is that the optical spectral width of a single optical mm-wave source may approach or exceed WDM channel spacing. There have been several reports on DWDM applied to RoF networks [6][8][9]. By utilizing the large number of available wavelengths in the DWDM technique, the lack of free transmission channels for further BS deployment in mm-wave bands RoF networks will be overcome. Another issue is related to the number of wavelengths required per BS. It is desirable to use one wavelength to support full-duplex operation. In [10], a wavelength reuse technique has been proposed which is based on recovering the optical carrier used in downstream signal transmission and reusing the same wavelength for upstream signal transmission.

By creating multiple wavelengths in a common fibre infrastructure, the capabilities of this infrastructure can be extended into an additional dimension. This wavelength dimension can implement independent communication planes between nodes. For example, interconnections in this plane can be asynchronous, have different quality-of-service requirements, and can transport signals with widely differing characteristics. By using the WDM technique, the access network can: 1) separate services; 2) separate service providers; 3) enable traffic routing; 4) provide higher capacity; 5) improve scalability. For assignment of wavelengths to channels the system may follow different scenarios such as: a) static allocation; b) semi-static allocation; c) dynamic allocation [11].

The static wavelength multiplexing scheme sets a virtual P-to-P topology up between two nodes of the network. However, the rapid growth in access network traffic requires flexible and adaptive planning of the wavelength allocation to each different channel or wired and wireless service to avoid congestion resulting from variable data rates demanded or to guarantee data traffic transportation or services to/from the end-users. By using adaptive wavelength allocation, deliverable services will be more cost-effective on the same network and the vast potential bandwidth of

fibre optical networks will be more fully exploited. By assigning the wavelength dynamically at the ONU, with flexible wavelength routing, the access network capabilities can be considerably enhanced. This configuration allows the setting up of a new wavelength channel before breaking down the old one. Alternatively, wavelength tuneable transmitters and receivers may be used, which can in principle, address any wavelength in a certain range. The network management and control system determines to which downstream and to which upstream wavelength channel each ONU transceiver is switched. By issuing commands from a central station, the network operator actually controls the virtual topology of the network, and thus is able to allocate the networks resources in response to the traffic at the various ONU sites. By changing the wavelength selection at the ONUs, the network operator can adjust the system's capacity allocation in order to meet the local traffic demands at the ONU sites.

In this scenario, as soon as the traffic to be sent upstream by an ONU grows and no longer fits within its wavelength channel, the network management system can demand the ONU be allocated another wavelength channel in which adequate free capacity is available. Obviously, this dynamic wavelength reallocation process reduces the system's blocking probability, i.e. it allows the system to handle more traffic without blocking and thus it can raise the profits of the operator from a given group of communication resources at the central station.

2.6. Physical Impairments

In this section physical impairments of lightwave communication technology are concisely discussed. Some of these impairments are related to the inherent properties of components and there is no way for them to be mitigated under general conditions and some of them depend on the link design conditions that commonly occur.

2.6.1. Attenuation in Fibre Optics

Power loss is an important parameter during the transmission of a signal; attenuation is the measure of the loss between the input and the output. In an optical

fibre, it is a contribution of 1) material absorption losses, 2) waveguide imperfections, 3) excess bending of fibre, and 4) Rayleigh scattering. The output transmitted power P_{out} at the length L of fibre is expressed by:

$$P_{out} = P_{in} e^{-\alpha L} \tag{2-1}$$

Where P_{in} represents the launched power into the fibre and α is the attenuation constant that represents the contribution of fibre induced losses from all sources. The attenuation or loss in decibels is given by:

$$\alpha_{dB} = -\frac{10}{L}\log(P_{out}/P_{in}) = 4.343\alpha \quad (dB/km) \tag{2-2}$$

2.6.1.1. Material Absorption

Material absorption can be divided into two categories: Intrinsic absorption losses correspond to absorption by fused silica (the material used to make fibres) whereas extrinsic absorption is related to those losses caused by impurities within silica.

A) Intrinsic Absorption

Any material absorbs light at certain wavelengths corresponding to the electronic and vibrational resonances associated with specific molecules. For silica molecules, electronic resonances occur in the ultraviolet region (wavelength < 0.4 um), whereas vibrational resonances occur in the infrared region (wavelength > 7 um). Because of the amorphous nature of fused silica, these resonances are in the form of absorption bands whose tails extend into the visible region. Figure 2-8, shows that intrinsic material absorption for silica in the wavelength range 0.8~1.6 um is below 0.1 dB/km. In fact, it is less than 0.03 dB/km in the 1.3 to 1.6 um wavelength range which is commonly used for lightwave systems. Optical fibre has two low-attenuation regions. Centered at approximately 1300 nm is a range of 200 nm in which attenuation is less than 0.5 dB/km. The total bandwidth in this region is about 25 THz, and centered at 1550 nm is a region of similar size with attenuation as low as 0.2 dB/km. Assuming that these two regions potential bandwidth can be utilized concurrently provides a theoretical upper bound of about 50 THz of transmission

channels bandwidth. By using these large low-attenuation areas for data transmission, the signal loss for a set of one or more wavelengths can be made very small, thus reducing the number of amplifiers and repeaters actually needed. In single channel long-distance experiments, optical signals have been sent over hundreds of kilometers without amplification. The extremely low attenuation or transmission loss of optical fibres is one of the most important factors in bringing their wide acceptance as a medium of transmission.

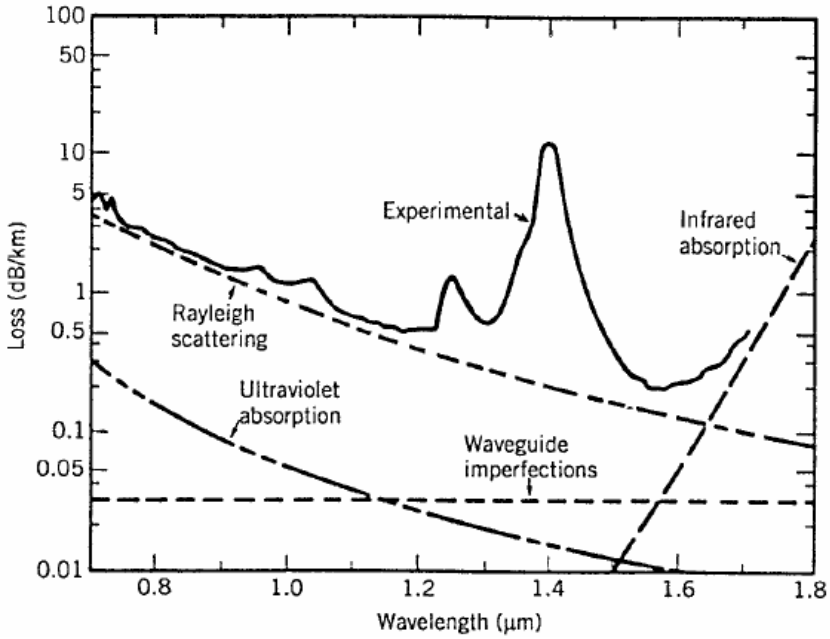

Figure 2-8: Measured loss spectrum of a silica fibre, the dashed curve shows the contribution resulting from Rayleigh scattering [20].

B) Extrinsic Absorption

Extrinsic absorption results from the presence of impurities. Transition-metal impurities in Fe, Cu, Co, Ni, Mn, and Cr absorb strongly in the wavelength range 0.6~1.6um. Their amount should be reduced to below 1 part per billion to obtain a loss levels below 1 dB/km. Such high-purity silica can be obtained using modern techniques. The main source of extrinsic absorption in state-of-the-art silica fibres is the presence of water vapor. A vibrational resonance of the OH ion occurs near 73 um, while its harmonic and combination tones with silica produce absorption at the 1.39 um, 1.24 um and 0.95 um wavelengths. As shown in Figure 2-8, there are three

spectral peaks occurring near these wavelengths which are due to the presence of residual water vapor in silica.

Shown in Figure 2-9, is the attenuation in a new kind of glass fibre known as dry fibre. In dry fibre the OH ion concentration is reduced to such low levels that the 1.39 um peak almost disappears; this property is used to enable the transmission of multiple wavelength signals over the entire 1.30 um to 1.65 um wavelength range.

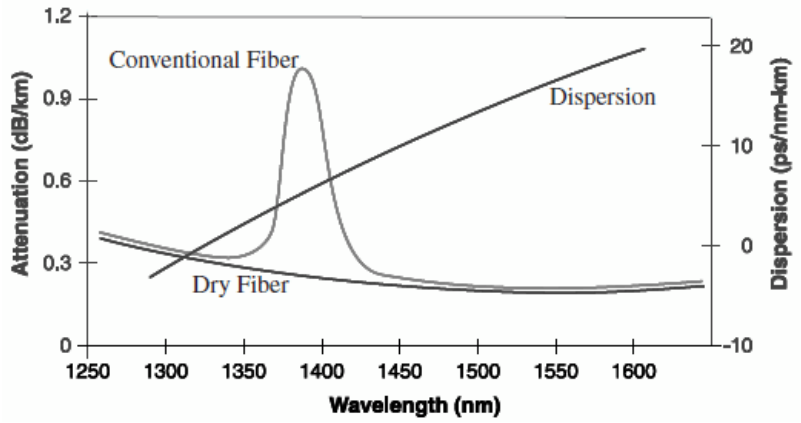

Figure 2-9: A comparison of Attenuation and Dispersion in Dry and Conventional Optical Fibres [20].

2.6.1.2. Fibre Effective Length

The fibre length L refers to the physical length of the fibre. Whereas the effective length of the fibre L_{eff} refers to the maximum length of fibre over which the fibre can be considered lossless. The effective length is defined as:

$$L_{eff} = \frac{1-\exp(-\alpha L)}{\alpha} \tag{2-3}$$

$L_{eff} = L$ when $\alpha = 0\,\text{dB/km}$. As α increases the difference between L_{eff} and L increases exponentially. α limits L_{eff}, the effective length is bounded by $L_{eff} < 1/\alpha$.

2.6.1.3 Waveguide Imperfections

An ideal single mode fibre with a perfect cylindrical geometry guides the optical mode without energy leakage into the cladding layer. In reality, imperfections at the core-cladding interface, such as random core-radius variations, can lead to additional losses which contribute to the total fibre loss.

2.6.3. Dispersion

Dispersion is the widening of pulse duration as a pulse travels through a fibre. As a pulse widens, it can broaden enough to interfere with neighbouring pulses (bits) on the fibre, leading to intersymbol interference, which limits the bit spacing and the maximum transmission rate on a fibre-optic communication system. There are several kinds of dispersion in optical communication systems, such as: chromatic, intermodal, and polarization dispersion.

2.6.3.1. Chromatic or Group Velocity Dispersion

When a lightwave interacts with the boundary electrons of a dielectric material the medium's response in general depends on the optical frequency ω of the wave. This property, referred to as chromatic dispersion, represents the frequency dependence of refractive index $n(\omega)$. In a dispersive medium, the index of refraction is a function of wavelength. Therefore, if the transmitted signal consists of more than one wavelength, certain wavelengths will propagate faster than other wavelengths. Fibre dispersion plays a critical role in the propagation of short optical pulses because of the different spectral components associated with a pulse travelling at different speeds given by $c/n(\omega)$. Therefore, after propagating through a channel, the spectral components have a much broader temporal distribution. If they broaden too much and the pulses are sent on very close intervals the data may not be retrievable. Since no laser can create a signal consisting of an exact single wavelength, chromatic dispersion will occur in most fibre optic communication systems. At 1300 nm, chromatic dispersion in a conventional single-mode fibre is nearly zero. Luckily, this is also a low-attenuation window (although the attenuation loss is higher than at 1550 nm). Through advanced techniques such as dispersion shifting, fibres with zero dispersion at a wavelength between 1300-1700 nm can be manufactured.

2.6.3.2. Phase velocity

Phase velocity describes the velocity of a constant phase value that propagates in the direction of the power flow of an optical field, (the Poynting vector). We assume a polarized wave propagating along an axis z is given by:

$$E(t,z) = E_0 e^{j(\omega t - \beta z)} \tag{2-4}$$

Where $\omega = 2\pi\upsilon$ and $\beta = 2\pi n/\lambda$ are angular velocity and wave propagation constant along the z axis, respectively.

If we assume that the gain and phase of the wave do not change as it moves along the z axis, $\omega t - \beta z = K$ where K is a constant, and $z = vt$. Thus, the phase velocity is denoted by:

$$v_p = \omega/\beta \tag{2-5}$$

The ratio of the speed of light to the phase velocity is the refractive index $n = c/v_p$. Furthermore, $k_2 < \beta < k_1$ means that β is bounded by the propagation constant with core, k_2, and the cladding of the fibre, k_1, where $k_i = 2\pi n_i / \lambda_0$.

2.6.3.3. Group Velocity

Consider an Amplitude Modulated (AM) analogue signal $E_{AM}(t,z)$ at the entrance of the fibre $(z = 0)$, which is given by:

$$E_{AM}(t,z)\big|_{z=0} = E_0.(1 + m.\cos\omega_i t).\cos\omega_c t \tag{2-6}$$

Where ω_i and ω_c are the angular frequencies of the information signal and the carrier and m is the modulation depth, respectively. Using Euler's formula, equation (2-6) can be rewritten by:

$$E_{AM}(t,z)\big|_{z=0} = E_0.\mathrm{Re}\left\{e^{j\omega_c t} + \frac{m}{2}.e^{j(\omega_c-\omega_i)t} + \frac{m}{2}.e^{j(\omega_c+\omega_i)t}\right\} \tag{2-7}$$

Consequently, it can be implied that in the signal input to the fibre there are three different frequency components. Each component travels with a specific phase velocity. In general, to find the output field the value of the mode propagation constant β for each frequency, ω, should be known. By expanding β in a Taylor series:

$$\beta(\omega) = n(\omega).\frac{\omega}{c} = \beta_c + \frac{\partial\beta}{\partial\omega}\Big|_{\omega=\omega_c}.(\omega-\omega_c) + \frac{1}{2}\frac{\partial^2\beta}{\partial\omega^2}\Big|_{\omega=\omega_c}.(\omega-\omega_c)^2 + \frac{1}{6}\frac{\partial^3\beta}{\partial\omega^3}\Big|_{\omega=\omega_c}.(\omega-\omega_c)^3 + \ldots \quad (2\text{-}8)$$

The second term does not distort the envelope in spite of the third and fourth terms, which are denoted first and second order dispersion coefficients, respectively. Neglecting second and third order derivatives, the propagation constant can be given by:

$$\beta(\omega) = \beta_c + \frac{\partial\beta}{\partial\omega}\Big|_{\omega=\omega_c}.(\omega-\omega_c) \quad (2\text{-}9)$$

Therefore, the propagation constants for three components of wave are: $\beta(\omega)\Big|_{\omega=\omega_c} = \beta_c$; $\beta(\omega)\Big|_{\omega=\omega_c+\omega_i} = \beta_c + \Delta\beta; \beta(\omega)\Big|_{\omega=\omega_c-\omega_i} = \beta_c - \Delta\beta$, where $\Delta\beta \triangleq \frac{\partial\beta}{\partial\omega}\Big|_{\omega=\omega_c}.\omega_i$. Thus, by using equation (2-7), the signal propagating through fibre along axis z can be given by:

$$E_{AM}(t,z) = E_0.[1 + m\cos(\omega_i t - \Delta\beta z)]\cos(\omega_c t - \beta_c z) \quad (2\text{-}10)$$

The accumulated phase shift on the carrier and envelop signal phases are $\beta_c z$ and $\Delta\beta z$, respectively. Based on the definition of group velocity, the field envelope's phase should be maintained constant at group velocity. Therefore, the group velocity v_g is given by:

$$v_g = \partial\omega / \partial\beta \quad (2\text{-}11)$$

Several frequencies are required to describe a pulse. Different spectral components of a pulse travel at slightly different group velocities. This is indicative of Group Velocity Dispersion (GVD) and it is also referred to as "chromatic" dispersion. Therefore, wavelength dependent effects limit the maximum bit rate that can be transmitted over fibre. For a SMF of length L a spectral component of frequency ω reaches the end of the fibre after a time delay of $T = L/v_g$ and $v_g = c/n_g$, where n_g is group refractive index of the medium. A significant consequence of GVD is pulse broadening because of different arrival delays of spectral components of a launched pulse at the fibre output.

$$\partial T \big/ \partial \omega = L \frac{\partial^2 \beta}{\partial \omega^2} \tag{2-12}$$

$$\beta_2 \triangleq \frac{\partial^2 \beta}{\partial \omega^2} \tag{2-13}$$

The parameter β_2 is often referred to as the GVD parameter and determines by how much the pulse will be broadened as a result of propagation through fibre.

$$\partial \omega \big/ \partial \lambda = -\frac{2\pi c}{\lambda^2} \tag{2-14}$$

$$\partial T \big/ \partial \lambda = D.L \tag{2-15}$$

$$D \triangleq \frac{\partial}{\partial \lambda}\left(\frac{1}{v_g}\right) = -\frac{2\pi c}{\lambda^2}.\beta_2 \tag{2-16}$$

Where D is the dispersion parameter of the fibre with units $ps/(km.nm)$. A basic condition which emphasizes the impact of dispersion on communications $B.\Delta T < 1$ where ΔT is a pulse's broadening time through a fibre link and B is the bit rate through the link. Using equation (2-15), the condition can be rewritten to describe a restriction on the transmitted data rate (B) and the link length (L).

$$BL|D|\Delta\lambda < 1 \tag{2-17}$$

For instance according to equation (2-17), for 1 km of fibre length, the maximum bit rate B of a system with a $1.3\mu m$ laser source, with $\Delta\lambda$ about $2-4nm$, and $D \cong 1(ps/nm.km)$ is less than $100\,Gb/s$.

The two main contributions to chromatic dispersion D in a fibre are: (a) material dispersion, (b) waveguide dispersion. Materials dispersion results from the dependence of the refractive index of silica on the optical frequency while waveguide dispersion is caused by the changes in the propagation path of a mode due to the different incidence and reflection conditions of different wavelengths.

$$D = \frac{-2\pi}{\lambda^2}\left(2\frac{\partial \bar{n}}{\partial \omega} + \omega \frac{\partial^2 \bar{n}}{\partial \omega^2}\right) \tag{2-18}$$

In general, the dispersion parameter D can be written as the sum of two terms, where $\bar{n}$ is a mode index

$$D = D_m + D_w \tag{2-19}$$

Where D_m and D_ω are the material and waveguide dispersions, respectively.

2.6.3.4. Material Dispersion

The dependence of the refractive index on the angular frequency of the lightwave is given by the Sellmeier equation:

$$n^2(\omega) = 1 + \sum_{j=1}^{M} \frac{B_j \omega^2{}_j}{\omega^2{}_j - \omega^2} \tag{2-20}$$

Where ω_j is the material resonance frequency and B_j is the strength of the j th resonance [21]. In equation (2-20), the generic refractive index value n can represent core and cladding properties individually. The sum of equation (2-20) extends over all material resonance frequencies. The group refractive index can be obtained using the Sellmeier equation because:

$$n_g = n + \omega . \frac{\partial n}{\partial \omega} \tag{2-21}$$

and the material dispersion is related to the slope of n_g :

$$D_m = -\frac{2\pi}{\lambda^2} . \frac{\partial n_g}{\partial \omega} = \frac{1}{c} . \frac{\partial n_g}{\partial \lambda} \tag{2-22}$$

Therefore, the material dispersion range for different domains of wavelength can be given by:

$$D_m = \begin{cases} > 0 & \lambda > \lambda_{ZD} \\ 0 & \lambda_{ZD} = 1.276 \mu m \\ < 0 & \lambda < \lambda_{ZD} \end{cases} \tag{2-23}$$

Where λ_{ZD} is the zero dispersion wavelength.

2.6.3.5. Waveguide Dispersion

Waveguide dispersion is caused because the propagation of different wavelengths depends on waveguide characteristics such as the indices of reflection and shape of the fibre core and cladding. The contribution of waveguide dispersion can be given by:

$$D_W = -\frac{2\pi}{\lambda^2}\left[\frac{n^2{}_{2g}}{n_2\omega}.\frac{V\partial^2(V.b)}{\partial V^2}+\frac{\partial n_{2g}}{\partial\omega}.\frac{\partial(V.b)}{\partial V}\right] \quad (2\text{-}24)$$

where n_{2g} is the group index of the cladding material of the fibre and V and b are:

$$V = -K_0 a(n_1{}^2 - n_2{}^2)^{1/2} \quad (2\text{-}25)$$

$$b = \frac{\beta/K_0 - n_2}{n_1 - n_2} = \frac{\overline{n} - n_2}{n_1 - n_2} \quad (2\text{-}26)$$

Where $K_0 = 2\pi/\lambda$, and the parameter V determines the number of modes supported by the fibre. In this expression, it is assumed that $\Delta = (n^2{}_1 - n^2{}_2)/2n^2{}_1$ does not change with spectral frequency. Furthermore, both $\partial(V.b)/\partial V$ and $V\partial^2(V.b)/\partial V^2$ are positive. Consequently, D_W is negative for $0 < \lambda < 1.6\mu m$. The Waveguide dispersion coefficient D_W depends on V, which is a function of the core radius a and the refractive index n. The main effect of the waveguide dispersion contribution is to shift λ_{ZD} slightly toward a longer wavelength; $\lambda_{ZD} = 1.3\mu m$ for standard fibre. Therefore, the zero dispersion wavelength of the fibre can be shifted by accounting for the waveguide dispersion which can be designed for a specific zero dispersion wavelength.

2.6.3.6. Intermodal Dispersion

This is caused when multiple modes of the same signal propagate at different velocities along the fibre. Perhaps an easy way to visualize dispersion is to consider pulse propagation in a MMF. Light launched into a MMF can effectively travel through several optical paths. Therefore, there is no intermodal dispersion in a single-mode fibre.

The power in a narrow pulse signal will be distributed into many possible modes. Modal dispersion is a function of the path length difference. The path length difference between the lowest and highest order modes can be given by:

$$\Delta L = \frac{L}{\cos\theta} - L \tag{2-27}$$

Where L is the path length and θ is the diffracted angle of incident light into the core. The corresponding time delay between modes becomes:

$$\Delta\tau = \frac{\Delta L}{(c/n)} \tag{2-28}$$

2.6.3.7. Polarization Mode Dispersion

Variations from perfect cylindrical symmetry result in birefringence. This causes different mode indices for orthogonal polarized field components of the fundamental fibre mode. If both polarization states of the fundamental mode are excited at the input, they will disperse as a function of propagation distance due to their different group velocities. This is the source of Polarization Mode Dispersion (PMD). The magnitude of pulse broadening resulting from PMD can be estimated from the time delay ΔT between the two polarization components after propagation over a length L of fibre [15].

$$\Delta T = \left|\frac{L}{v_{gx}} - \frac{L}{v_{gy}}\right| = L\left|\beta_{1x} - \beta_{1y}\right| = L\Delta\beta_1 \tag{2-29}$$

$$\beta_1 \triangleq \frac{\partial\beta}{\partial\omega} \tag{2-30}$$

Where x and y refer to the orthogonal polarization states and $\Delta\beta_1$ is related to the fibre birefringence. The relation $\Delta T/L$ represents the PMD in a similar way to the intermodal dispersion. For polarization preserving fibre $\Delta T/L \cong 1\ (ns/km)$ when both polarization components are excited at launch but it can be reduced to zero when launched along one axis. PMD is characterized by the Root-Mean Square (RMS) value of ΔT denoted by $\sigma_T \cong D_p\sqrt{L}$, where D_p is PMD parameter the value of which is in the range $0.1-1\ ps/km$ [21].

2.6.3.8. Dispersion Power Penalty

As explained previously, dispersion in an optical pulse creates pulse broadening such that the pulse spreads into the time slots of the other pulses in the time domain. This not only causes Intersymbol Interference (ISI) but it also introduces a power penalty, which can cause degradation of the systems Signal to Noise Ratio (SNR). The power penalty is given by [15][18-20]:

$$P_{Disp.} = 5\log_{10}(1+\frac{DL\sigma_{\lambda}^{2}}{\sigma_{0}}) \tag{2-31}$$

Where, σ_{λ} is the rms spectral width of the input pulse in unit (nm), and σ_{0} is the optical pulse width at the transmitter end (sec.). Further, the following equation expresses the maximum dispersion tolerable length of fibre *L* for a data rate with bandwidth *B*:

$$B^{2}L < 16\frac{\lambda^{2}D}{2\pi c} \Rightarrow L_{Max} < \frac{16\lambda^{2}D}{2\pi cB^{2}} \tag{2-32}$$

It is obvious that if the occupied bandwidth is increased the transmission range will be decreased proportional to the square of bandwidth *B*.

2.6.4. Walk-Off Length

Walk off refers to the temporal separation of two signals with different carrier frequencies during propagation. Because of group velocity mismatch between the signals, the temporal separation increases during propagation. In other words, the pulses "walk-off" from each-other. The walk-off length L_{W} can be defined:

$$L_{W} = \frac{T_{1}}{|d|} \tag{2-33}$$

Where T_{1} is the fundamental pulse half-width at 1/e of the peak power and d is the group velocity mismatch parameter defined as:

$$d = \frac{v_{g2} - v_{g1}}{v_{g2}.v_{g1}} \tag{2-34}$$

Where v_{g2} and v_{g1} are the co-propagated and fundamental signals group velocities, respectively.

2.6.5. Frequency chirp

The intensity modulation onto an optical carrier at the transmitter end causes phase modulation onto the optical carrier because of the refractive index change. Such optical pulses with a time dependent phase shift are called chirped pulses. Therefore, the spectrum is broadened due to this chirp.

2.6.6. Noise

There are many sources of noise in a RoF link which can be listed as noise from the laser diode, noise from amplifiers, shot noise, and noise from matching circuits and components. Laser noise arises from random fluctuation of the intensity and phase of the signal. The Relative Intensity Noise (RIN) is the ratio of mean square of power fluctuation per unit bandwidth $<\Delta P>^2$ to the square of the signal power average $<P>^2$.

$$RIN_{(dB/Hz)} = 10\log(\frac{<\Delta P^2>}{<P>^2}) \tag{2-35}$$

Where the units are (dB/Hz) and <> indicates ensemble averaging. Furthermore, the phase noise of the laser source can be converted to intensity noise throughout the fibre link by GVD [17][22]. Therefore, the *RIN* can be given by

$$RIN(\omega, z) = \frac{4\Delta\omega}{\Delta\omega^2 + \omega^2} \tag{2-36}$$

The photo diode contributes shot and flicker noises [23]. Furthermore, at higher optical power the laser interacts with fibre and optical components, producing noise from several different scattering and interference effects [24][25].

Sources of noise that impact of on SNR such as shot noise, thermal noise, amplifier noise that are explained briefly in the following subsections.

Shot Noise: The shot noise limited SNR in a given electrical bandwidth B_e can be given by:

$$SNR_{Shot} = \frac{< i >}{2eB_e} \tag{2-37}$$

Where $< i >$ is the average photo diode current and e is the electron charge.

Thermal Noise: With respect to thermal noise, the corresponding SNR is given by

$$SNR_{Thermal} = \frac{< i >^2 R_{eq}}{4KTB_e} \propto \frac{< i >^2}{4KTB_e^2 C} \tag{2-38}$$

Where K is the Boltzman constant, T is the temperature, R_{eq} and C are the equivalent input resistance and total capacitance of the photo diode.

Amplifier Noise: In an optical link ASE noise is a concern. The signal ASE beat noise limited SNR can be expressed as:

$$SNR_{ASE} = \frac{(m^2/2)(R_{PD}P_s)^2}{2(R_{PD}P_S)(R_{PD}\rho_{ASE})B_e} = \frac{(m^2/2).P_s}{2\rho_{ASE}.B_e} \tag{2-39}$$

Where P_s is the optical signal power, ρ_{ASE} is the ASE power spectral density and R_{PD} is the responsivity of the PD. In addition, m is the modulation index defined as $m = \frac{\pi V_{RF}}{V_\pi}$, where V_{RF} and V_π are the RF voltage amplitude and the half-wave voltage, respectively. Assuming a single optical amplifier is used, the previous equation can be rewritten as:

$$SNR_{ASE} = \frac{(m^2/2)P_{s,in}.G}{2[2n_{sp}h\nu(G-1)]B_e} \approx \frac{(m^2/2).P_{s,in}}{4n_{sp}.h\nu B_e} \tag{2-40}$$

Where h is Plank's constant, ν the optical carrier frequency, G the amplifier gain, and n_{sp} is the population inversion parameter with a value close to 2 for a typical amplifier [18].

2.6.7. Scattering

There are different types of scattering impairment in optical fibres communications systems such as Rayleight Scattering, Brillouin Scattering, and Raman Scattering. These impairments significantly impact on communication system performance and links signal transmission and distribution distance.

2.6.7.1. Rayleigh scattering

Rayleigh scattering is a loss mechanism arising from local microscopic fluctuation in density. Silica molecules are randomly moving in the molten state and freeze in place during fibre fabrication process. Density fluctuation leads to random fluctuations of the refractive index on a scale smaller than the optical wavelength. Light scattering in such a medium is known as Rayleigh scattering. Scattering depends not on the specific type of material but on the size of the particles relative to the wavelength of light. The closer the wavelength is to the particle size, the greater the scattering. In fact, the amount of scattering increases rapidly as the wavelength decreases. The intrinsic loss level is estimated and given by

$$\alpha_R = \frac{C_R}{\lambda^4} \tag{2-41}$$

Where, the constant C_R is in the range 0.7-0.9 dB/(km-μm^4) depending on constituents of the fibre core. As α_R is in the range $0.12 - 0.15$ dB/(km) near 1.55 μm, losses in silica fibres are dominated by Rayleigh scattering [26].

2.6.7.2. Brillouin and Raman Scattering

Brillouin scatering and Raman scattering arise from the interaction of light with acoustic and quantum vibration waves that are always present in any material and are nonlinear phenomena. From a strictly classical point of view, the compression of the medium will change the index of refraction and therefore lead to some reflection or scattering at any point where the index changes (Brillouin scattering). From a quantum point of view, Raman proposed that the process can be considered as one of interaction of light photons with acoustic or vibrational quanta (phonons) (Raman scattering).

In Brillion scattering, acoustic waves modulate the refractive index (photo-elastic effect); thus an optical signal from a low power laser traversing the medium is scattered with a different frequency (which depends on the angle of observation; in the backward direction the frequency shift is larger and of the order of 10 GHz in silica). In general, the optical field also induces strains (via electrostriction) that

reinforce the acoustic waves, but this is a small effect at low laser intensity launched optical power. However, at high laser intensity, this leads to a Stimulated Brillouin Scattering (SBS) regime. SBS is manifested as a strong reflection of light in the medium (back-scattering). In typical telecom fibres, the SBS threshold is about 1 mW, which is a limitation for fibre optic communications system. Furthermore, SBS is a great concern in photonic devices which rely on nonlinear optical effects, such as parametric amplifiers and wavelength converters. Moreover, SBS is usually avoided by broadening the laser spectrum above the width of the Brillouin line, which in silica fibres is typically 20-40 MHz. However, for optical wavelength conversion, this solution is inconvenient, since it also broadens the spectrum of the converted signal [27].

2.6.8. Nonlinearity

A linear medium is characterized by a linear relation between the polarization density P and the electric field E.

$$P = \varepsilon_0 \chi E \tag{2-42}$$

Where ε_0 is the permittivity of free space and χ is the electric susceptibility of the linear medium.

The refraction index n of a medium can be given by:

$$n^2 = 1 + \chi \tag{2-43}$$

But, in nonlinear medium the relation between P and E is nonlinear and can be expressed by contribution of the linear and nonlinear terms

$$P = \varepsilon_0 \chi^{(1)} E + P_{NL} \tag{2-44}$$

$$P_{NL} = \varepsilon_0 (\chi^{(2)} EE + \chi^{(3)} EEE + \ldots) \tag{2-45}$$

Where $\chi^{(2)}$ and $\chi^{(3)}$ are the second and third order susceptibility of the nonlinear medium. However, in fibre optic the second order nonlinearity is absent [16][21][28][29]. The nonlinear phenomena happen due to the dependency of the

physical properties of medium on the incident light intensity. Nonlinear effects in fibre may potentially have a significant impact on the performance of WDM optical communications systems. Nonlinearities in fibre may lead to attenuation, distortion, and cross-channel interference. In a WDM system, these effects place constraints on the spacing between adjacent wavelength channels, limit the maximum power on any channel, and may also limit the maximum bit rate. The details of the optical nonlinearities are very complex and beyond the scope of this chapter. It should be emphasized that they are the major limiting factors in the available number of channels in a WDM system.

2.6.8.1. Kerr Impact

The Kerr impact is a nonlinear optical effect occurring when intense light propagates in any medium and a nonlinear polarization is generated because of third order nonlinearity, $\chi^{(3)}$. The nonlinear change of susceptibility of the propagation medium of the light can be expressed by:

$$\Delta\chi = 6\chi^{(3)}\frac{n}{\varepsilon_0}\sqrt{\frac{\mu_0}{\varepsilon_0}}I \tag{2-46}$$

Where n is the medium refractive index, I the optical intensity of incident light, μ_0 is the permeability of free space. It can be modelled as a variation in the medium refractive index. The variation of the refractive index can be expressed as:

$$N_{NL}(I) = n_{NL}I \tag{2-47}$$

Where the optical Kerr coefficient is

$$n_{NL} = \frac{3}{n^2\varepsilon_0}\sqrt{\frac{\mu_0}{\varepsilon_0}}\chi^{(3)} \tag{2-48}$$

Therefore, the medium refractive index is given by:

$$n(I) = n + N_{NL}(I) \tag{2-49}$$

Where n is the intensity independent linear refractive index and $N_{NL}(I)$ is the variation in the refractive index due to intensity dependent third order nonlinear susceptibility of the nonlinear medium [16].

2.6.8.2. Self Phase Modulation

Self-Phase Modulation (SPM) is a nonlinear optical effect of light-matter interaction, which is an important phenomenon in optical systems that use short and intense pulses of light, such as lasers and optical fibre communication systems. When an ultra short pulse of light is travelling in a medium, it will induce a varying refractive index in a medium due to the optical Kerr-effect. This variation in refractive index will cause a phase shift in the optical pulses, leading to a change of the pulse's frequency spectrum. The intensity of a Gaussian shape ultra short pulse at time t, with constant phase is given by:

$$I(t) = I_0 \exp(-(t/\tau)^{2m}) \tag{2-50}$$

Where I_0 is the intensity peak, τ the half width at 1/e intensity of pulse duration, and m is the order of the Gaussian pulse that is illustrated in Figure 2-10.

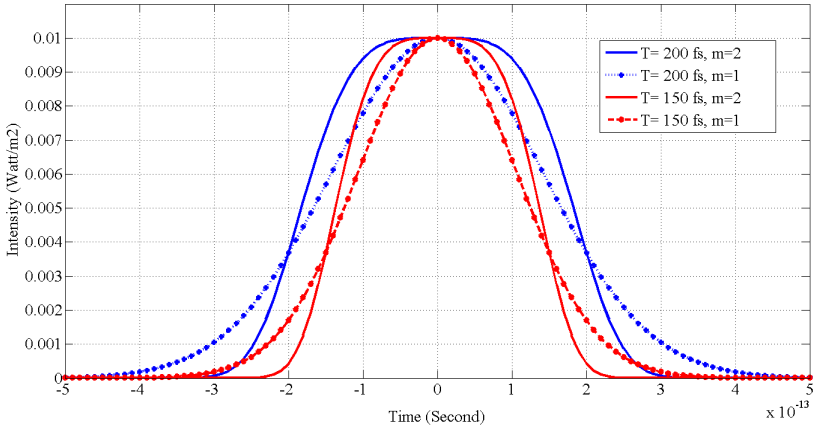

Figure 2-10: Different order and duration of Gaussian pulse versus time.

Based on equations (2-49) and (2-50), the time varying refractive index is given by:

$$\frac{dn(I)}{dt} = \frac{dN_{NL}(I)}{dt} \tag{2-51}$$

Substituting for $N_{NL}(I)$ from equation (2-47) into (2-51) gives:

$$\frac{dn(I)}{dt} = n_{NL}\frac{dI(t)}{dt} \tag{2-52}$$

And substituting for $I(t)$ from equation (2-50) into equation (2-52), the refractive index variation with respect to time can be given by:

$$\frac{dn(I)}{dt} = n_{NL}.I_0\frac{-2mt^{2m-1}}{\tau^{2m}}\exp-(\frac{t}{\tau})^{2m} \tag{2-53}$$

This variation in refractive index causes instantaneous phase shift of the pulse:

$$\varphi(t) = \omega_0 t - kx = \omega_0 t - \frac{2\pi}{\lambda_0}.n(I)L \tag{2-54}$$

Where ω_0 and λ_0 are the optical pulse's frequency and wavelength in free space, and L is the wave travel length in the medium. Therefore, the nonlinear phase shift denoted by $\phi_{SPM}(t)$ is represented by:

$$\phi_{SPM}(t) = \bar{\gamma}P_{in}(t)L_{eff} \tag{2-55}$$

Where $P_{in}(t)$ is the optical input power, $\bar{\gamma}$ is the nonlinear coefficient that is given by:

$$\bar{\gamma} = \frac{2\pi n_{NL}}{\lambda_0 A_{eff}} \tag{2-56}$$

Where A_{eff} is the effective area of the cross section of the core [30][31]. Figure 2-11 shows the refractive index change versus time when different Gaussian pulses travel though out a nonlinear medium.

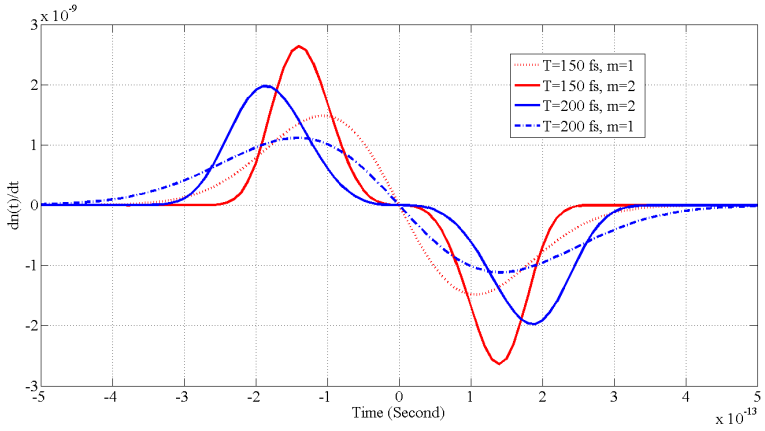

Figure 2-11: Refractive index variation for different pulse orders and widths.

As the nonlinear phase shift is time variable, so it causes a frequency chirp that is spreading the signal spectrum in frequency domain. There is a restriction on maximum tolerable phase shift in an optical communication system. Therefore, this phenomenon limits the maximum input power level.

2.6.8.3. Cross Phase Modulation

Cross Phase Modulation (XPM) is another nonlinear phase change of an electromagnetic wave. It is due to the interaction of a wave with another wave in a nonlinear medium. The refractive index nonlinearity seen by fundamental wave E_f because of the impact of another copropagaiting wave E_c in the medium can be expressed by a polarization third order nonlinearity relation with the electrical field. If we assume fundamental and co-propagating waves of angular frequency ω_f and ω_c and the total electric field can be given by [32]:

$$E(t) = E(\omega_f)\exp(-j\omega_f t) + E(\omega_c)\exp(-j\omega_c t) \tag{2-57}$$

By substituting equation (2-57) in equation (2-45), the polarization density at frequency ω_f can be expressed by:

$$P_{NL}(\omega_f) = \chi_{eff}^{(3)}[\left|E(\omega_f)\right|^2 + 2\left|E(\omega_c)\right|^2]E(\omega_f) \tag{2-58}$$

Where $\chi_{eff}^{(3)} = \frac{3}{4}\varepsilon_0\chi^{(3)}$ [22]. Assuming that the refractive index of the medium is same for the two waves, equation (2-58) can be rewritten as:

$$P_{NL}(\omega_f) = 2n\varepsilon_0 N_{NL}E(\omega_f) \tag{2-59}$$

Therefore

$$N_{NL} = n_{NL}(I_f + 2I_c) \tag{2-60}$$

Where $I_f = \frac{n}{2}\sqrt{\frac{\varepsilon_0}{\mu_0}}\left|E(\omega_f)\right|^2$ and $I_c = \frac{n}{2}\sqrt{\frac{\varepsilon_0}{\mu_0}}\left|E(\omega_c)\right|^2$ are the intensities of the waves. This nonlinear refractive index change causes a phase shift in the fundamental wave

$\varphi_{NL}(t)$ during the incident waves' propagation throughout the medium with length L that can be given by:

$$\varphi_{NL}(t) = \bar{\gamma} L_{eff} (P_f + 2P_c) \tag{2-61}$$

Thus, an optical beam modifies not only its own phase but also other copropagating beams phase. The sensitivity arises from XPM induced phase shift $\phi_{XPM}(t)$.

$$\phi_{XPM}(t) = 2\bar{\gamma} L_{eff} |E_c(t)|^2 \tag{2-62}$$

The extent of XPM induced spectral broadening is governed by the instantaneous change in fundamental signal frequency Δf_f

$$\Delta f_f(t) = -\frac{1}{2\pi} . \frac{\partial \phi_{XPM}(t)}{\partial t} = -\frac{\bar{\gamma} L_{eff}}{\pi} . \frac{\partial P_c(t)}{\partial t} \tag{2-63}$$

XPM is severely harmful and is twice as powerful as SPM. The induced phase shift is due to the "Walk Over" effect. Whereby in optical communication, two pulses at different bit rates or with different group velocities walk across each other. The total phase shift depends on the net power of all the channels. Maximum phase shift is produced when two 1 bits walk across each other due to the high power in both the bits. (as opposed to the lower power levels when both bits are not at logical 1). Mathematically, the total nonlinear phase shift is

$$\phi_{NL}(t)\Big|_f = \bar{\gamma} L_{eff} \left[P_f(t) + 2\sum_{k=1}^{W} P_k(t) \right] \tag{2-64}$$

Where W is the total number of channels, and $P_k(t)$ is the power of the kth channel.

2.6.8.4. Four Wave Mixing

Four Wave Mixing (FWM) is a third order nonlinearity in optical links that can be compared to the intermodulation distortion in standard electrical systems. FWM is a nonlinear phenomenon in which three optical signals with frequencies f_i, f_j and f_k were $k \neq i, j$, interact through the third-order electric susceptibility of the optical fibre to generate a fourth wave with channel frequencies denoted by:

$$f_{ijk} = f_i + f_j - f_k \tag{2-65}$$

Thus, three co-propagating waves generate nine new optical channels. The number of FWM channels produced can be given by:

$$N = \frac{m^2}{2}(m-1) \tag{2-66}$$

Where N is the number of produced FWM channels and m is the number of interacting optical signals.

2.7. Radio over Fibre Link Design

The key parameters to consider when designing a RoF link are loss, bandwidth, noise Figure, and dynamic range. The modulation devices and photo diodes have the greatest impact on all four parameters. The fibre length impacts on the loss and noise Figure. Furthermore, the fibre length impacts indirectly on the bandwidth via its dispersion while fibre effects on dynamic range are negligible. Network planners need to optimize the various electrical and optical parameters to ensure smooth operations of network. When the transported data bit rate is not too high and the transmission distance is not too long, it is often not important to consider these parameters. However, as the bit rate and transmission range increase, the link physical parameters play a key role if suitable performance is to be maintained. In this section an optical links design methodology to provide an optimum system is provided by considering different physical impairments and the restrictions in an optical link. In the following subsections the physical effects on the link design and the design methodology are explained.

2.7.1. Physical Parameters

There are some key parameters that must be defined and calculated prior to the design and implementation of the RoF link. These parameters are the link gain, bandwidth, noise, dynamic range, and distortion.

An important parameter to consider in the design of a link is the power budget and gain management. To maintain proper performance, a designer considers the needed power penalty to have an acceptable signal level at the receiver. The loss of a RoF link is a function of four variables, transmitter efficiency, link loss, receiver efficiency,

and link impedance. The link impedance is governed by the output impedance ($Z_{out,Rx}$) and the input impedance ($Z_{in,Tx}$), where $Z_{out,Rx}$ is the load impedance at the receiver output and $Z_{in,Tx}$ is the input impedance of transmitter such as a laser diode or an external modulator. In the absence of any amplifier on the link, the sample direct-modulated direct detection RoF link's insertion loss, $\alpha_{Link-DM}$ can be given by:

$$\alpha_{Link-DM} = \frac{P_{Rx-out}}{P_{Tx-in}} = \alpha_m(\eta.R_d.\alpha.\alpha_s.\alpha_c.\alpha_D)^2.G_{Amp,Tx}.G_{Amp,Rx}.\left(\frac{Z_{out,Rx}}{Z_{in,Tx}}\right) \quad (2\text{-}67)$$

Where P_{Rx-out} and P_{Tx-in} are receiver output and transmitter input RF electrical power levels respectively, α_m is the matching circuit loss, η is the laser external differential efficiency for one facet with units of (W/A), R_d is the photo-detector responsivity with units of (A/W), α is the fibre loss, α_s is the fusion, splice and connectors losses, α_c is the laser-fibre coupling loss, α_D is the fibre-detector coupling loss, and $G_{Amp,Tx}$ and $G_{Amp,Rx}$ are the gains of the link RF input and output amplifiers, respectively [12].

The optical power is proportional to the electrical current while the electrical power is proportional to the square of the electrical current. Therefore, the optical loss terms all squared in this equation due to the square law detector which converts the incident optical signal into an electrical current. The insertion loss of the external modulation $\alpha_{Link-EM}$ link is given by:

$$\alpha_{Link-EM} = \frac{P_{Rx-out}}{P_{Tx-in}} = \left(\frac{1}{2V_\pi}.P_o.\alpha_{\mathrm{mod}}.\alpha_L.\gamma_0\right)^2.G_{Amp,Tx}.G_{Amp,Rx}.\left(1-|\Gamma|^2 Z_{out,Rx}.Z_{in,Tx}\right) \quad (2\text{-}68)$$

Where Γ is the reflection coefficient, V_π the voltage for perfect modulation, P_o is the optical power out of the laser, α_{mod} the modulator optical insertion loss, α_L the optical losses in the link including connectors, fibre losses and splicing, and γ_0 is the detector responsivity [12].

To consider 0-dB loss the insertion loss and the optical amplifier gain are same. Therefore, links gain can be given by:

$$G_{Link} = \alpha_{Link} \tag{2-69}$$

The accumulated attenuation should be calculated properly, because, if the attenuation was greater than the input launched power P_{in}, the signal could not be detected at the receiver end. Furthermore, to establish and maintain a successful connection, the received power at the receiver end must be above the receiver sensitivity. Moreover, if the power level is higher than sensitivity level, a successful transmission is not guaranteed because the maximum power level not only must be within the receiver dynamic range but also must satisfy the critical power level to prevent the nonlinearity degradations and impacts on the fundamental signals by SPM, XPM, FWM, Stimulated Raman Scattering (SRS), SBS, etc. throughout the link. There are some other impairment such as GVD and PMD that seriously impact on the link performance at high data rates and for long distance transmission. The dispersion impact causes the signal to broaden in the time domain which reduces the signal average power in the time domain. Therefore, the power penalty of compensating the dispersion impact must be considered, while there is a restriction on increasing the power level because of nonlinearity impairments. Consequently, the transmission length is limited by considering these parameters. The restriction for maximum launched power and the link inherent attenuation limits the maximum length of transmission according to the following fundamental equation

$$P_{TxMax}(dB) = \left(\alpha_{Link} + G_{link} + P_{RxMin}\right)(dB) \tag{2-70}$$

Where P_{TxMax} and P_{RxMin} are the maximum launched power into the link, and minimum received power required to satisfy the receiver sensitivity, respectively. Therefore, placing optical amplifier into the link segments is essential to relay the signal over longer transmission ranges and for better noise figures.

However, an optical amplifier not only enhances the fundamental signal power but also adds ASE noise power to the signal as it amplifies other sources' noise. Consequently, keeping in check the Optical Signal-to-Noise Ratio (OSNR) is always necessary. The most important Figure of Merit (FoM) for providing reliable performance in worst case conditions is the Bit Error Rate (BER) of the transmission

link. According to International Telecommunication Union (ITU) standards, the minimum BER requirement for an optical communication link is a BER<10^{-12} .

2.7.2. Figure of Merits

To design a system, it is essential to comply with the BER requirement of the network. The Q-factor provides a qualitative description of the receiver performance because it is a function of the signal to noise ratio. The Q-factor suggests the minimum SNR required to obtain a specific BER for a given signal. A higher the value of Q-factor means a better BER. Increasing the input power has a significant impact on the Q factor because of nonlinearity impairments. Mathematically, the Q factor of an optical signal is given by:

$$Q = \frac{I_1 - I_0}{\sigma_1 - \sigma_0} \tag{2-71}$$

where , I_1 is the value of the 1-bit current, I_0 is the value of the 0-bit current, σ_1 is the standard deviation of the 1-bit current of the Gaussian distribution and σ_0 is the standard deviation of the 0-bit current of the Gaussian distribution. The Optical Signal to Noise Ratio (OSNR) is the most important parameter that is associated with an optical signal. It is a measurable quantity for a given signal and network. The Q-factor can be calculated based on OSNR using the following equation:

$$Q_{dB} = 20\log(\sqrt{OSNR}.\sqrt{\frac{B_o}{B_c}}) = OSNR_{dB} + 10\log(\frac{B_o}{B_c}) \tag{2-72}$$

Where, B_o is the optical bandwidth of the receiver (photo detector) and B_c is the electrical bandwidth of the receiver filter. If B_o was less than B_c, $Q_{dB} < OSNR_{dB}$. Typically, when designing a high bit rate system, the Q-factor is 2 dB less than the OSNR. The Q-factor relationship with the BER is given by:

$$BER = \frac{1}{2} erfc(\frac{Q}{2}) \tag{2-73}$$

As the BER of the optical link must be very low, of order of magnitude of10^{-12}, BER measurement in steady state requires very long periods of time to evaluate the

system performance which is normally quite difficult and sometimes not possible. This is the reason that the Q-factor is used to determine the BER.

The linearity of a RF system is characterized by its Spurious Free Dynamic Range (SFDR) which is defined as the dynamic range that is the ratio of signal power in a wavelength band to noise power in a wavelength band. For SFDR measurement, two RF signals are generated with two independent CW RF signal generators, with a very small frequency difference. Another important parameters for assessing link performance is the Carrier to Noise Ratio (CNR) of an analog radio over fibre link [15].

$$CNR = \frac{(m.R.P)^2 / 2}{\sigma_s^2 + \sigma_{th}^2 + \sigma_{RIN}^2} \tag{2-74}$$

where m is the modulation depth, R is the responsivity of the photo diode, P is the average optical power on the photodiode, σ_s, σ_{th}, and σ_{RIN} are standard deviations of the photodiode noise current associated with shot, thermal, and RIN noise. Standard expressions for σ_s, σ_{th}, and σ_{RIN} are [14]:

$$\sigma_s^2 = 2q(RP + I_d)\Delta f \tag{2-75}$$

$$\sigma_{th}^2 = 4K_b TF_n \Delta f / R_L \tag{2-76}$$

$$\sigma_{RIN}^2 = (RIN)(RP)^2 \Delta f \tag{2-77}$$

Where q is the charge on the electron, I_d is the detector dark current, Δf is the system bandwidth, K_b is Boltzman's constant, T is the temperature, F_n is the noise figure of an amplifier following of the photodiode, R_L is the equivalent load resistance of the photodiode, and RIN is the effective intensity noise of the optical source.

2.7.3. Design Criteria and Conclusion

In an optical communication network, the main loss of a link is not attenuation due to transmission, but is associated with the various subsystems along the link. A

typical link consists of multiple nodes, each equipped with a variety of components. The loss due to each component is significant. Consequently, each component added increases the power penalty for system design. Table A-1 of Appendix A, shows the insertion loss due to typical elements. Furthermore, the losses due to impairments in transmission must be taken into the account by considering correspondent penalty in dB. Consequently, Table A-2 of Appendix A presents the power margin requirement to provide acceptable performance.

To design a RoF system properly it is important to calculate the OSNR and design the system based on both OSNR and dispersion limitations. However, OSNR compensation requires 3R regeneration that is complicated for multi-channel WDM systems. A viable OSNR-based design is essentially one were the OSNR at the final stage meet the requirements in terms of BER.

Accounting for the accumulative chromatic, modal, and polarization mode dispersion throughout the link is an important issue. An optical transmission system could not function because of high ISI and pulse spreading caused by dispersion. For high data rates and long range transmission dispersion effects will be significant and must be compensated for accordingly. Depending on the type of dispersion, there is a corresponding solution to mitigate or compensate the dispersion effects. Two main parameters that play key roles here are the data rate and the length of link. Therefore, deployment of a suitable method in the form of a Dispersion Compensation Unit (DCU) and the optimum length for compensate the dispersion is essential to maintain the quality of services.

2.8. References

[1] H. C. Ji, H. Kim, Y. C. Chung, "Full-Duplex Radio-Over-Fibre System Using Phase-Modulated Downlink and Intensity-Modulated Uplink" , IEEE Photonics Technology Letters, Vol. 21, No.1, , pp 9-11, Jan. 2009.

[2] H. Al-Raweshidy, S. Komaki, "Radio over Fibre Technology for Mobile Communication Networks" , Artech House, 685 Canton Street, MA 02062 , pp. 136-138, 2002.

[3] C. H. Cox, , "Analog Optical Links", Cambridge University Press, , Cambridge UK, 2004.

[4] G. L. Li., P. K. L. Yu, "Optical Intensity Modulators for Digital and Analog Applications" , Journal of Lightwave Technology. Vol. 21, , pp. 2010-2030, 2003.

[5] U Gliese, S. Norskow, T. N. Nielsen, "Chromatic Dispersion in Fibre-Optic Microwave and Millimeter-Wave Links", IEEE Transaction of Microwave Theory Technology, Vol. 44, No. 10, pp. 1716.1724, Oct. 1996.

[6] R. A. Grifin, P. M. Lane, J. J. O'Reilly, "Radio-Over-Fibre Distribution Using an Optical Millimeter-Wave/DWDM Overlay", Proceeding of OFC/IOOC 99, Vol.2, pp. 70-72, Feb. 1999.

[7] T. Koonen, , "Fiber to the Home/Fiber to the Premises: What, Where, and When?" Proceedings of the IEEE , Vol. 94, No. 5, pp. 911-934, May 2006.

[8] H. Toda, T. Yamashita, T. Kuri, K. Kitayama, "Demultiplexing Using an Arrayed-Waveguide Grating for Frequency-Interleaved DWDM Millimeter-Wave Radio-on-Fibre Systems", Journal of Lightwave Technology, Vol. 21, No. 8, pp. 1735-1741, Aug. 2003.

[9] R. A. Grifin, "DWDM Aspects of Radio-over-Fibre", Proceeding of LEOS 2000 Annual Meeting, Vol. 1, pp. 76-77, Nov. 2000.

[10] A. Nirmalathas, D. Novak, C. Lim, R. B. Waterhouse, "Wavelength Reuse in the WDM Optical Interface of a Millimeter-Wave Fibre-Wireless Antenna Base Station", IEEE Transaction of Microwave Theory Technology, Vol.49, No.10, pp. 2006-201, Oct. 2001.

[11] P. J. Urban, B. Huiszoon, R. Roy, M. M. de Laat, F. M. Huijskens, E. J. Klein, G. D. Khoe, A. M. J. Koonen, H. D. Waardt, "High-Bit-Rate Dynamically Reconfigurable WDM–TDM Access Network", Journal of Optical Commuincation Network, Vol. 1, No. 2, pp. 143-159, July 2009.

[12] W.E. Stephens and T. R. Joseph," System Characteristics of Dirct Modulated and Externally Modulated RF Fiber-Optic Links", IEEE Journal of Lightwave Technology, vol. 5, no. 3, March 1987.

[13] R. F. Kalman, J. C. Fan, and L. G. Kazovsky, " Dynamic Range of Coherent Analog Fiber-Optic Links", IEEE Journal of Lightwave Technology, vol. 12, no. 7, July 1994.

[14] G. P. Agrawal, Fiber-optic communication systems, 3rd ed. New York: John Wiley & Sons, Inc., 2010.

[15] Orazio Svelto, "Principles of Lasers", 5th Edition, Springer, 2010.

[16] B.E. A Saleh and M. C. Teich, "Fundamental of Photonics", Wiley - Interscience, Second Edition, 2007.

[17] John M. Senior, " Optical fiber Communication", Pearson Prentice Hall, Third Edition, 2009.

[18] Agilent Technologies, "Lightwave Technology: Passive Component", Revision 1.1, Dec. 2000.

[19] Ashwin Gumaste, Tony Antony, "DWDM Network Designs and Engineering Solutions", Cisco Press, 2002.

[20] T. Li (ed.), Optical Fibre Communications: Fibre Fabrication, Vol. 1 (Academic Press, San Diego, 1985.

[21] Govind P. Agrawal , "Nonlinear Fiber Optics", Academic Press, Third Edition, 2001.

[22] W. K. Marshall, B. Crosignani, and A. Yariv, " Laser Phase noise to intensity noise conversion by lowest-order group-velocity dispersion in optical fibre: exact theory", Optics Letters, vol. 25, no. 3, pp. 165-167, Feb. 2000.

[23] E. Rubilo, E. Salik, Y. Nan, and L. Maleki, " Flicker noise in high speed p-i-n photodiodes," IEEE Transaction of Microwave Theory Technology, Vol. 54, no. 2, pt. 2, pp. 816-820, Feb. 2006.

[24] R. M. Shelby, M. D. Levenson, and P.W. Bayer, " Guided acoustic wave Brilliouin Scattering," Rev. B, vol. 31, no. 8, pp. 5244-5252, Apr. 1985.

[25] W. Shieh and L. Maleki, "Phase Noise of Optical Interference in Photonic RF Systems", IEEE Photonic Technology Letter, vol. 10, no. 11, pp. 1617-1619, Nov. 1998.

[26] Richard B Miles, Walter R Lempert and Joseph N Forkey, "Laser Rayleigh scattering", Institute of Physics Publishing, Journal of Measurement Science and Technology, pp. 33-55, 2001.

[27] Andrey Kobyakov, Michael Sauer, and Dipak Chowdhury, "Stimulated Brillouin scattering in optical fibers",Optical Socity of America, Advances in Optics and Photonics 2, pp. 1–59, 2010.

[28] Nicolaas Bloembergen "Nonlinear Optics", World Scientific, 4th Edition, 2010.

[29] Y. R. Shen, "The Principle of Nonlinear Optics", Wiley - Interscience, 2003.

[30] R. H. Stolen and C. Lin, "Self-phase-modulation in silica optical fibers", Physical Review A, vol. 17, no. 4, pp. 1448-1453, 1978.

[31] Bostjan Batagelj, "Need of Knowing Fiber Non-linear Coefficient in Optical Networks", The International Conferences WSEAS 2002

[32] Frits Zernike and John E. Midwinter , "Applied Nonlinear Optics", Wiley-Inrerscience, 1974.

Chapter 3

Digital Radio over Fibre Technology

3.1. Introduction

In an analogue system the bandwidth and dynamic range are limited by devices performance, parasitic components and transmission medium impacts on signal amplitude, phase, and etc. All analogue systems exhibit some degree of nonlinear behaviour that limits their dynamic range. In such case, the magnitude of the output does not follow the input which results in the distortion of the signal. As an example, due to nonlinearity and out-of-band signal can interfere with the signal of interest and result in loss of information. The nonlinear behaviour is memory-less or dynamic with memory (frequency dependent) [1]. Memory-less nonlinearity is frequency independent, resulting direct mapping between the instantaneous magnitudes of the input signal to the corresponding output magnitudes. On the other hand, in the presence of memory effects, nonlinear distortion of the signal depends on the input signal behaviour over a period of time instead of a single time instant. An ARoF link can also add significant frequency-dependent nonlinear distortion. In such a link, the analogue RF signal modulates the optical field, generating RF signal side bands and their harmonics in the optical field. In the presence of dispersion, these harmonics and sidebands components undergo different phase shifts at different frequencies and therefore, frequency dependent nonlinearity distortion at the photodiode output is unavoidable [2].

Digital systems are flexible, more reliable and robust against additive noises of devices and channel, achieve better dynamic range than analogue systems and more conveniently interface with other systems. Following of the previous chapter regarding to the ARoF systems, in this chapter, an introduction about Digital Radio

over Fibre (DRoF) system is discussed and the state-of-the Analogue-to-Digital and Digital-to-Analogue Converters (ADC and DAC, respectively) is presented [3]. ADCs and DACs are the interfaces between the analogue and the digital world of signal processing and data handling and are the key components of the existing digital systems. The rest of this chapter organized as follows: in Section 3.2 the brief review of DRoF is explained. Section 3.3 provides a description about technical specification of the DRoF components. Section 3.4 discusses all-photonic signal conversion and Section 3.5 explains the pipelined PADC architecture and discusses the related analysis. The proposed 2-Bit pipelined architecture and its discussion are presented in Section 2.6. Section 3.7 gives the generic model of the proposed pipelined PADC architecture. The DAC is discussed in Section 3.8 and the proposed 2-Bit binary weighted PDAC architecture is described in Section 3.9. In Section 3.10 discussion about 8-Bit binary weighted PDAC is presented and finally conclusion is given in Section 3.11 following by references in Section 3.11.

3.2. Digital RoF Architecture

In a Digital RoF (DRoF) system, an electrical RF signal is digitized by using an Electronic ADC (EADC) [4]. Then, the generated digital data is modulated with a continuous coherent optical carrier wave either using a direct modulation technique or by using an external electro-optical modulator as shown in Figure 3-1 [5][6]. The modulated optical carrier is transmitted through the fibre. At the base station, after detecting the optical signal using a photo diode, the detected digital data is converted back to the analogue domain using an Electronic DAC (EDAC). Finally, the analogue electrical signal is fed to an antenna.

The Digital RoF (DRoF) link can maintain the dynamic range more independent of optical fibre link distance than ARoF and can employ the present infrastructure for transporting the digitized radio traffic [7][8]. However, current EADC systems experience problems such as jitter in the sampling clock [9][10], the settling time of the sample and hold circuit, the speed of the comparator, mismatches in the transistor thresholds and passive component values. The limitations imposed by all of these factors become more severe at higher frequencies. Wideband ADC's

sampling pulse clock timing jitter is a critical problem encountered in broadband communication and radar systems [11][12].

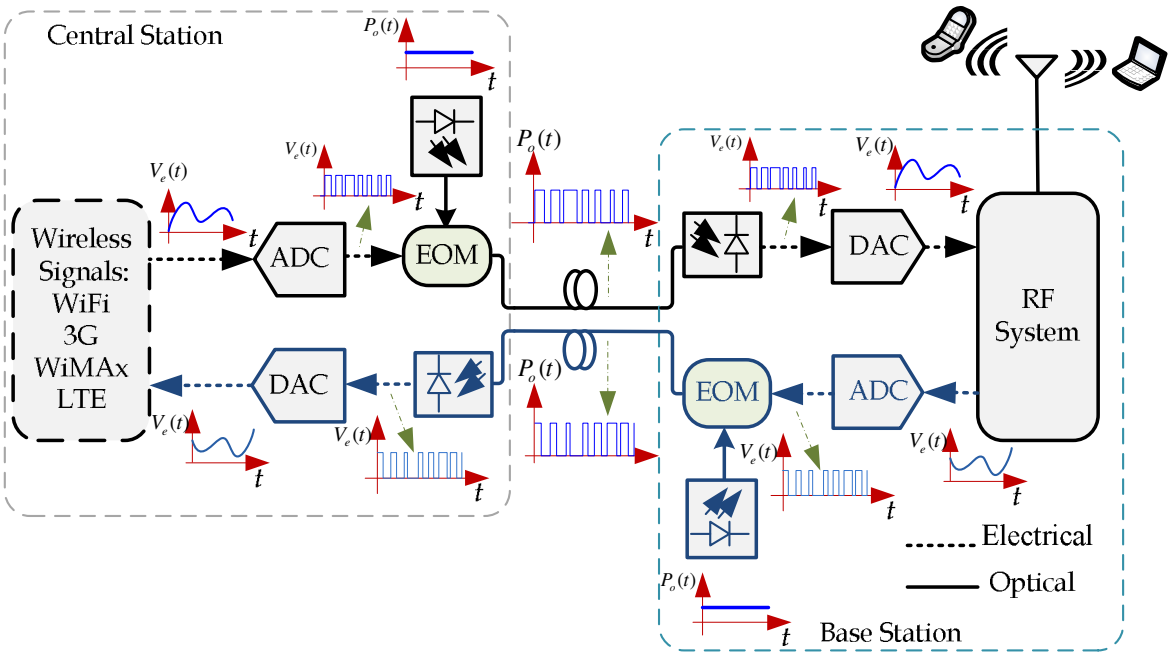

Figure 3-1: Conventional DRoF architecture using EADC.

For the future beyond Gigabit/s mobile and wireless end-user traffic rates due to the limitations electronic technology for implementing ultra high-speed, high performance EADC and resolution of exciting EADC, the deployment of conventional DRoF link is not simply achievable [5-8].

Moreover, if a conventional DRoF link could be achieved for Gigabit/s traffic rates the generated digital traffic creates a new challenge, namely, for this architecture to use more electro-optical modulators and photo diodes to implement the wavelength division multiplexing (WDM) technique to diminish the chromatic dispersion caused by the restrictions on the modulation bandwidth for super broadband access by RoF network.

3.3. Digital Radio over Fibre Components

In addition to an ARoF links key components such as EOM and laser source, Photo diodes, and some other passive and active components, a DRoF link has two key

components ADC and DAC that are highly impact on the DRoF link performance. Therefore, in the following subsections, we discuss them technically in more details.

3.3.1 Analogue-to-Digital Converter

Analogue-to-Digital converter continually samples a time-varying waveform, regularly at fixed-time intervals, and generates a sequence of digital numbers to approximate the analogue sampled values. The input to the ADC is a time varying analogue signal $S_{in}(t)$ and the output is a series of digital numbers S_{ji}. In fact, a discrete sample $S(t_i)$ of the input signal's value at discrete time t_i is transformed to a digital output, as illustrated in Figure 3-2. There are 2^N possible quantization levels S_j, where N is the number of bits of precision. Each of the levels S_j can be expressed as a unique binary number in the form $S_j = (\overline{A_{(N-1)}A_{(N-2)}...A_2A_0})$; where A_k is a binary digit ("0" or "1"), $A_{(N-1)}$ and A_0 are the Most Significant Bit (MSB) and the Least Significant Bit (LSB), respectively.

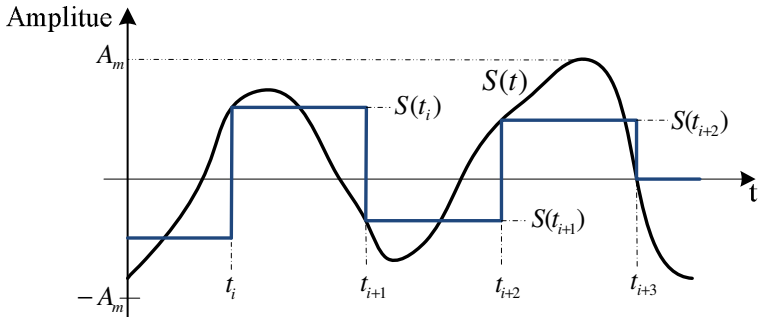

Figure 3-2: Sampling of a time-varying signal.

A sample-and-hold circuit maintains the values of the sampled signal constant during sufficient length of time for a coder for correct quantization. A conventional block diagram of an ADC is given in Figure 3-3.

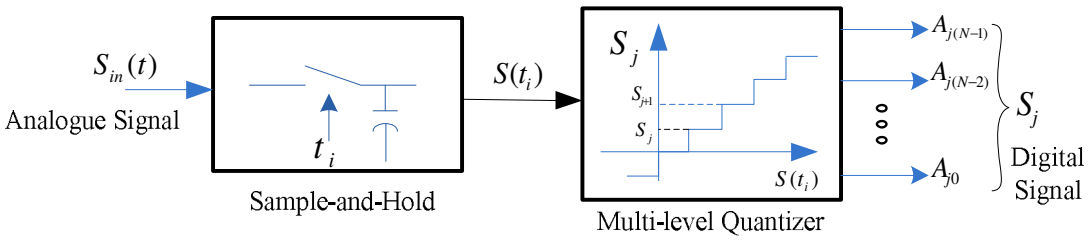

Figure 3-3: Analogue-to-digital conversion process.

In an N-bit ADC, equation (3-1) can be governed between the analogue input and digital output.

$$S_{in}(t) = \overline{S_j}.G_{ref} + errors = \sum_{k=0}^{N-1} A_{jk}.2^k G_{ref} + errors \quad (3\text{-}1)$$

Where $\overline{S_j}$ is the decimal equivalent value of the digital binary signal, S_j and G_{ref} is the reference value of quantization conversion. The sampling interval is $\Delta t = t_{i+1} - t_i$ and the quantization level spacing $q_s = S_{j+1} - S_j$ or the step size of consecutive levels of quantization which is the LSB of the binary representation of that value given by:

$$q_s = \frac{V_{FS}}{2^N - 1} \quad (3\text{-}2)$$

However, the second term in equation (3-1) is the conversion error that is constructed with different intrinsic impairments and conversion impacts on the ADCs' performance, such as: thermal noise, sampling clock's timing uncertainly, sample-and-hold's charge leakage and drift, comparators ambiguity and thermal drift, and quantization error.

Consequently, the rest of this section discusses the source of errors in ADCs. However, an important source of error in any ADC is quantization error because of the finite number of discrete values, whereas the analogue signal varies continuously. The quantization process introduces an irreversible error in an ADC, even the sampling time uncertainty and the all added noise impacts are dismissed.

The quantization error depends on the quantization bit numbers and is on the order of one LSB in amplitude. It is quite small compared to full-amplitude signals, nevertheless in weaker input signals, the quantization error becomes significant. The sampled input value $S(t_i)$ is then rounded to the nearest level

$$S_j(n) = S(t_i)\Big|_{t_i=n} + e(n) \quad (3\text{-}3)$$

Transfer function of an ideal N-bit ADC is shown in Figure 3-4. In this case, the maximum error is quantization error. For an input signal, which is large compared to

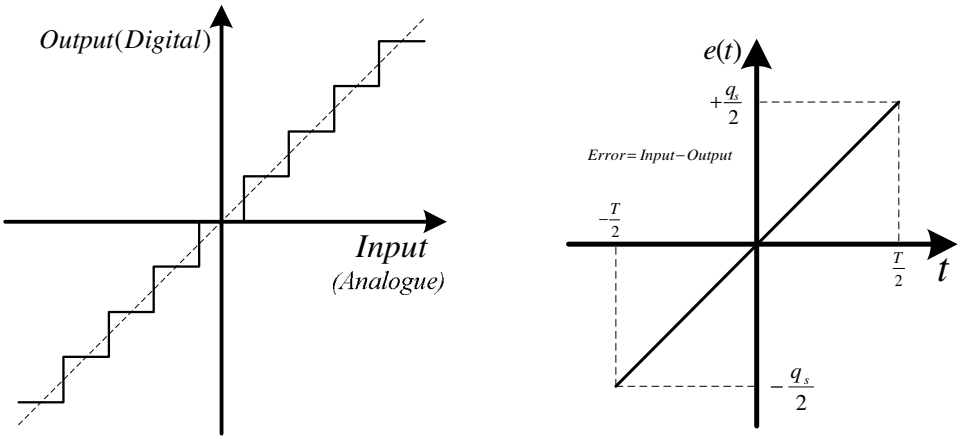

(a) (b)

Figure 3-4: (a): The transfer Function of N-bit ADC and (b): Quantization Error Function.

an LSB step, the error term $e(n)$, is a random quantity in the interval $(-\frac{q_s}{2}, \frac{q_s}{2})$ with equal probability, then the noise power (variance) σ_e^2 , can be expressed by:

$$\sigma_e^2 = E[e^2(t)] = \frac{1}{T}\int_0^T \left[q_s(\frac{t}{T} - \frac{1}{2}) \right]^2 .dt = \frac{q_s^2}{12} \tag{3-4}$$

Where E(.) denotes statistical expectation, and σ_e^2 is steady-state quantization noise power. Figure 3-5 shows the noise spectral density in the Nyquist frequency range. Since, the noise power is spread over the entire frequency range equally; the level of noise power spectral density can be given by:

$$N(f) = \frac{q_s^2}{12 f_s} \tag{3-5}$$

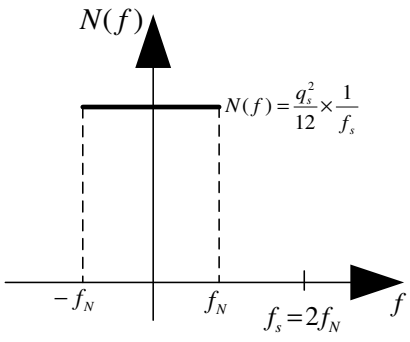

Figure 3-5: Noise spectrum of Nyquist samplers.

3.3.1.1 Analogue-to-Digital Converters Characteristics

An ADC performs two functions on a time varying signals: 1) sample and hold it for a specified time and 2) quantize the held signal into a number of levels. Both timing and amplitude errors reduce the performance of ADCs. The most important time errors are random jitter and broadening of the sample time. Random noise (thermal, shot noise) and nonlinearities are the major source of the amplitude error. However, despite the variety in ADC's, their performance can be summarized by a relatively small number of parameters, 1) stated resolution (number of bits per sample) N, 2) Signal to Noise Ratio (SNR), 3) Spurious-Free Dynamic Range (SFDR) and 4) power dissipation.

The SNR and SFDR are the most important parameters of dynamic performance for high-speed applications. The SNR and SFDR provide a more accurate measure of ADC performance than the stated number of bits. All error sources decrease the effective resolution from the N to the Effective Number of Bit (ENOB) while without noise the ENOB increases to N. When the only source of noise is quantization error, the signal-to-noise ratio (SNR_Q) can be related to the number of bits N through [3].

$$SNR_Q(dB) = 20\log(V_{FS,rms} / Quantization\ Noise_{rms}) \tag{3-6}$$

where the $V_{FS,rms}$ is rms value of full-scale voltage and equals to $V_{FS}/\sqrt{8}$ for a sine wave. By substituting $V_{FS,rms}$ and quantization noise rms in equation (3-6), The SNR_Q over Nyquist bandwidth (DC to $f_s/2$) can be given by:

$$SNR_Q(dB) = 20\log_{10}(\frac{V_{FS,rms}}{\sigma_e}) = 6.02.ENOB_{SNR_Q} + 1.76(dB) \tag{3-7}$$

$$ENOB_{SNR_Q} = [SNR_Q(dB) - 1.76(dB)]/6.02 \tag{3-8}$$

Furthermore, the measurement over limited bandwidth BW (where $BW<f_s/2$) increases the SNR.

$$SNR_Q(dB) = 20\log_{10}(\frac{V_{FS,rms}}{\sigma_e}) = 6.02.ENOB_{SNR_Q} + 1.76(dB) + 10\log_{10}(\frac{f_s}{2.BW}) \tag{3-9}$$

The increasing amount of the SNR is process gain:

$$Process\ Gain = 10\log_{10}\left(\frac{f_s}{2.BW}\right) \tag{3-10}$$

Furthermore, using the Fast Fourier Transform (FFT) to analysis the ADC performance, FFT acts like a limited bandwidth spectrum analyser with bandwidth f_s/M, where M is the number of points in FFT. Therefore, the theoretical noise floor of FFT is $10\log_{10}\left(\frac{M}{2}\right)$ dB below the quantization noise floor due to process gain of FFT [13]. For arbitrary sources of noise and nonlinear distortion characterized by the Signal-to-Noise and Distortion Ratio (SNDR) or (SINAD) is given by [13]:

$$SINAD = \frac{S}{n_0 + THD} \tag{3-11}$$

Where S and n_0 are the signal and noise power, respectively and THD is the total harmonic distortion of first 6 harmonics that is expressed by:

$$THD\ (dB) = 20\log_{10}\sqrt{\left[10^{-V_2/20}\right]^2 + \left[10^{-V_3/20}\right]^2 + \ldots + \left[10^{-V_6/20}\right]^2} \tag{3-12}$$

Figure 3-6 illustrates the location of distortion products within the first Nyquist zone for an input signal with frequency f_a and sampling rate f_s. The harmonic frequency is given by:

$$F_n = \left|\pm Kf_s \pm nF_a\right| \tag{3-13}$$

Where n is the order of harmonic and K=0, 1, 2, 3,

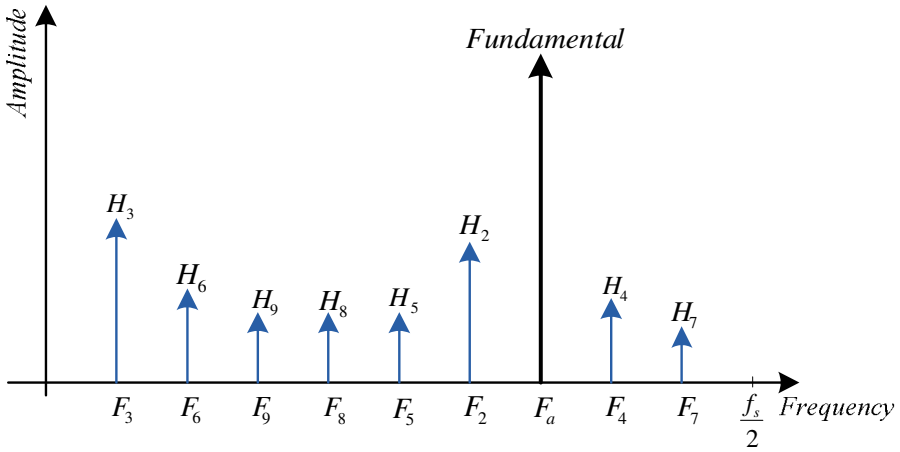

Figure 3-6: The location of distortion products for a sample input signal at frequency f_a with sampling rate f_s.

Thus, SINAD in dB is given by:

$$SINAD\,(dB) = 20\log_{10}\sqrt{\left[10^{-SNR/20}\right]^2 + \left[10^{-THD/20}\right]^2} \tag{3-14}$$

Therefore, ENOB can be represented by:

$$ENOB_{SNDR} = [SINAD\,(dB) - 1.76(dB)]/6.02 \tag{3-15}$$

Moreover, another parameter to measure the nonlinearity of the ADCs is SFDR which is defined as the ratio of the rms signal amplitude to the rms value of peak spurious signal over the bandwidth of interest as shown in Figure 3-7, [3][14] and spur is typically a harmonic of the original signal. The ENOB is given by:

$$ENOB = SFDR(dBc)/6.02 \tag{3-16}$$

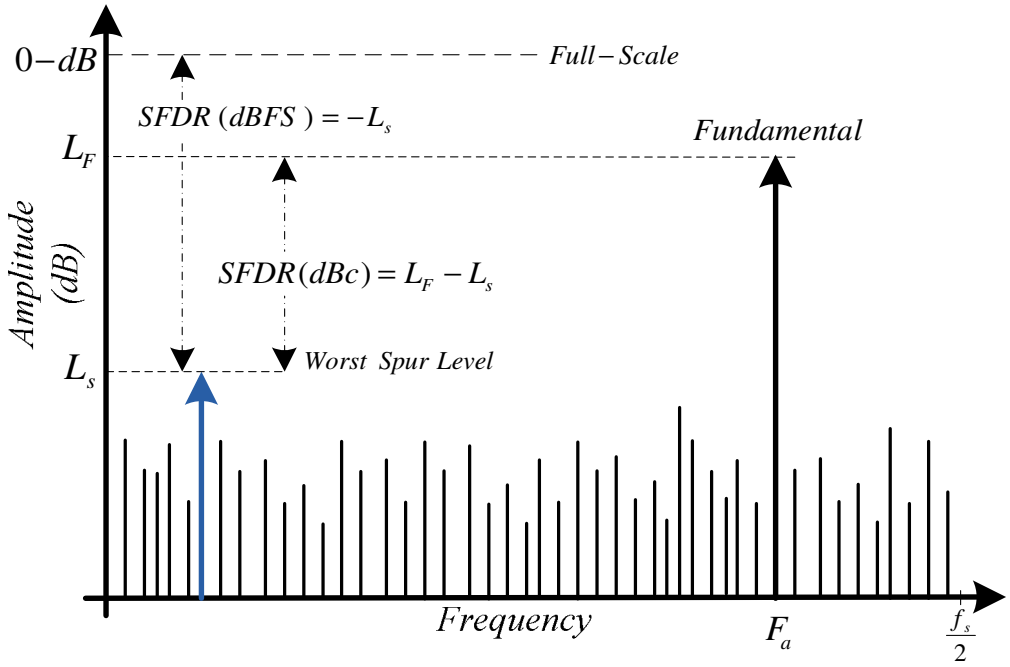

Figure 3-7: Spurious Free Dynamic Range (SFDR).

In section 2.6.6 of chapter 2, discussions about the contribution of shot, thermal, and ASE noise sources on SNR are presented. Thermal noise, quantization noise, and aperture jitter noise have significant impact on electronic ADCs' performance [15]. The contributions from all the error mechanisms can be presented by noise spectrum which includes the noises of quantization, circuit, and aperture uncertainty and comparator ambiguity [3]. Furthermore, when an analogue signal is sampled prior to

quantization, an aperture jitter noise is produced by the jitter in the sampling clock that must be considered as additional noise. This is called aperture uncertainty error which is the main problem to achieve a high resolution in a high speed ADC [3]. If we assume that the sampling pulse with sampling time uncertainty δ is used to sample a sine wave signal $x(t) \triangleq A \sin(2\pi f_{RF} t)$, where A is the signal amplitude and f_{RF} is the maximum input RF signal frequency. Therefore, the induced error $e_j(t)$ because of sampling timing jitter is given by:

$$e_j(t) = x(t) - x(t+\delta) \approx 2\pi f_{RF} \delta \cos(2\pi f_{RF} t) \tag{3-17}$$

If the sampling uncertainty is an uncorrelated Gaussian random process with standard deviation σ_j resulting SNR is related to the root-mean-square (rms) jitter σ_j [3]. To model the distortion by aperture jitter as another noise source, [16] is given an expression of signal-to-aperture-jitter noise ratio (SANR) versus sampling rate which is expressed by:

$$SANR = -20\log_{10}(2\pi f_{RF} \sigma_j) \ dB \tag{3-18}$$

Where the analogue bandwidth of ADC is the frequency at the FFT determined spectral output magnitude is reduced by 3 dB. Furthermore, the input signal's frequency and the ADC's resolution determines the maximal aperture jitter τ_a is given by:

$$\tau_a = \frac{1}{2^N . \pi f_S} \tag{3-19}$$

Where $f_s = 2 f_{RF}$ is the sampling frequency [3]. Therefore, when timing jitter is the only source of ADC performance degradation, there is a simple relation between the upper-bound of ENOB and the sampling rate f_s times the rms jitter σ_j which has been derived by [3][13][15]:

$$ENOB_{Jitter} = Log_2[1/(\pi f_s \sigma_j)] \tag{3-20}$$

Figure 3-8 gives the upper limit of ENOB and relates SANR versus sampling rate against rms timing jitter. As it shows, by decreasing the timing jitter achievable ENOB at specific SANR could be maintain at higher sampling rate.

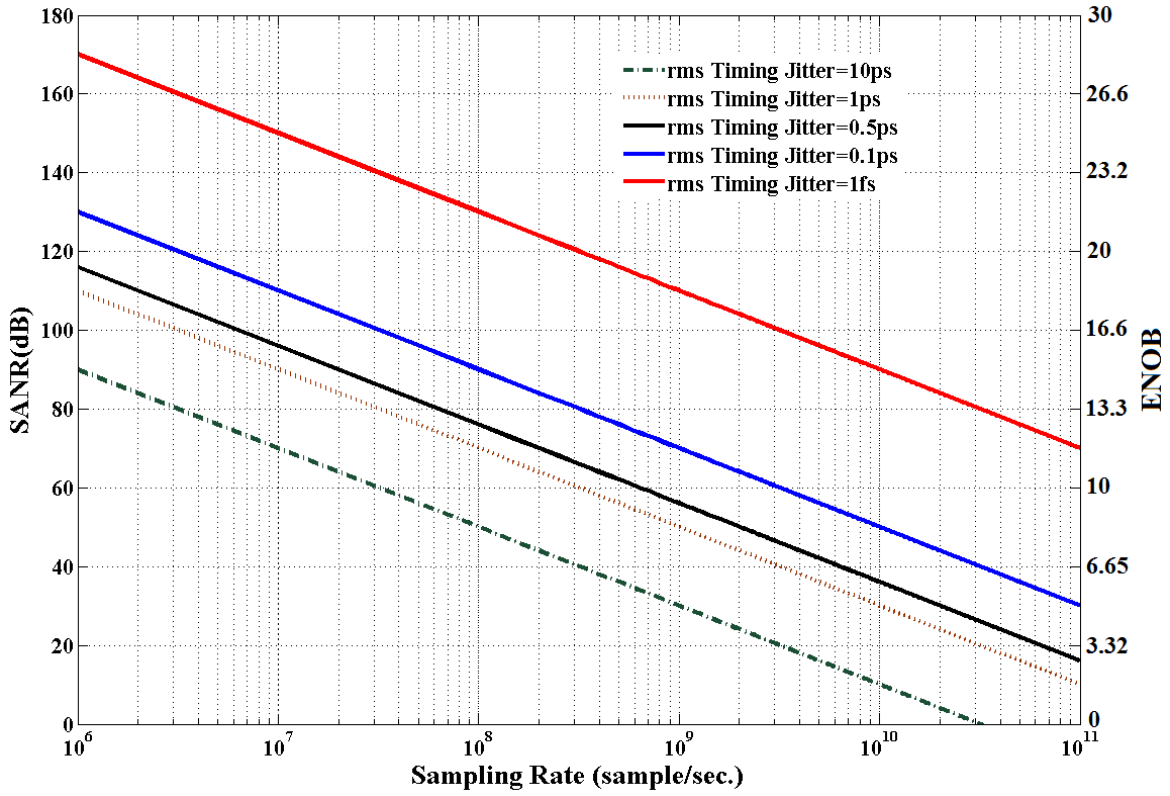

Figure 3-8: Theoretical SANR and upper bound of the ENOB due to timing jitter versus sampling rate.

Another index to assess the converter performance is two-tone intermodulation distortion (IMD) which is measured by applying two spectrally pure sine waves to the ADC at frequencies f_1 and f_2, usually relatively close together. The amplitude of each tone is set slightly more than 6 dB below full scale so that the ADC does not clip when the two tones add in phase. The locations of the second and third-order products are shown in Figure 3-10. The second-order products fall at the frequencies that can be removed by digital filters. However, the third-order products $2f_2$-f_1 and $2f_1$-f_2 are close to the original signals and more difficult to filter. This intermodulation distortion can significantly reduce the dynamic range of an ADC.

Differential nonlinearity (DNL) is a measure of the uniformity of the quantization step size over operating range of ADC. In this performance characteristic each step size in the quantization process is compared to the ideal step size with the difference

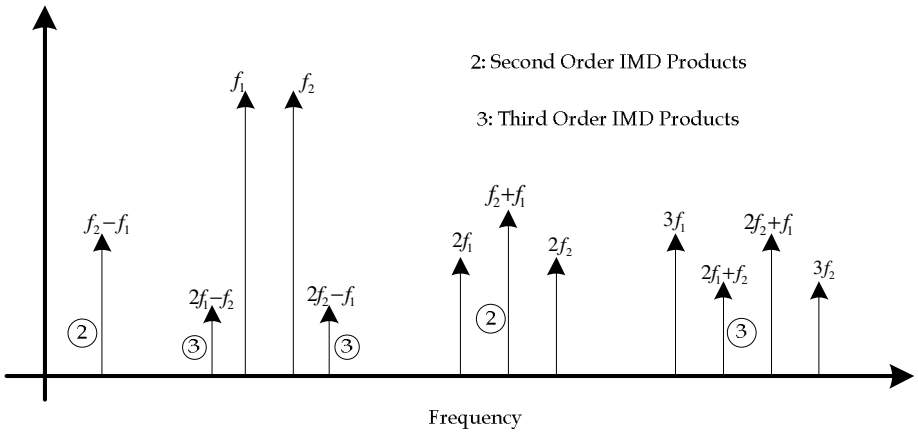

Figure 3-9: Two-tone intermodulation distortion.

in magnitude reported as the nonlinearity error. Integral Nonlinearity (INL) is defined as the deviation of the code midpoint values from the ideal. The differential error is a measure of the error in step size at a specific location within the ADC transfer function. INL is the summation of these individual errors over entire ADC transfer function [13]. The relation between DNL and INL is given by:

$$INL_n = \sum_{i-0}^{n} DNL_i \tag{3-21}$$

However, in the analysis of ADCs, two figure of Merit P and F are widely used which are defined by:

$$P = 2^{ENOB}.f_s \tag{3-22}$$

$$F = \frac{2^{ENOB}.f_s}{P_{diss}} \tag{3-23}$$

Where P_{diss} is the ADC power dissipation [17]. However, to investigate the ADC performance [3] focused on the ADC ENOB resolution versus the sampling rate, where the ENOB resolution is based on either SFDR or SNR which is referred to SNDR [3][17] concentrates more on the SNR than the SFDR due to the inclusion of noise and error in an ADC.

3.3.1.2. ADCs Architectures

Generally, there are seven architectures for the ADCs: 1) Pipelined, 2) Successive Approximation Register (SAR), 3) Sigma-Delta, 4) Flash, 5) Half Flash, 6) Folding,

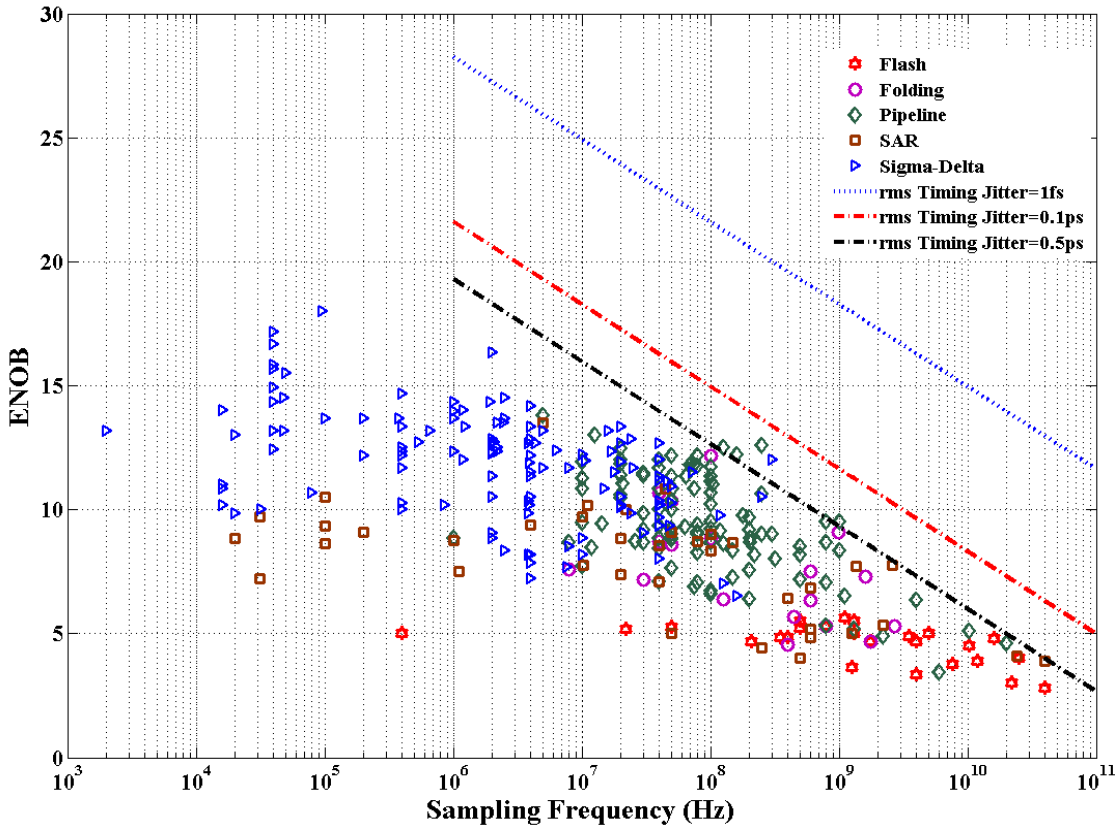

Figure 3-10: The ADC's comparison and the timing jitter limitation impacts on the performance.

7) Undiscloused [15][17]. Resolution, sampling rate, bandwidth, power consumption, noise, area, clock latency, scalability, complexity, technology, etc. determine the most feasible topologies for that particular system. As an example, Figure 3-10 gives a classification of reported ADCs based on speed, resolution, and the physical noises limitation and impacts on the performance.

Pipelined architecture is based on distributing the quantization over several stages, where each stage samples the input and performs low-level quantization. In this way, each stage can process different samples simultaneously, achieving a high throughput with pipelining. This architecture is useful when the latency requirements are relaxed, other architectures offers the potential for savings in power dissipation and area. The pipelined architecture has best overall performance, and it is suitable choice for high performance requirement such as digital wireless transceiver [18].

In SAR ADCs architecture, the successive-approximation ADC can be seen as the implementation of a binary search algorithm. In a single stage, the input is sampled

and then a state-machine controls a DAC output, deciding the bits from MSB to LSB one by one. As the search algorithm is iterative, only one comparator is needed and the comparator output sequentially updates the successive approximation register (SAR). The input signal is sampled at the beginning of the conversion and after k clock cycles the conversion is complete and a new sample is taken. Therefore, the sample rate is lower than the internal clock frequency, which is the drawback of the SAR ADC architecture. They have wide range of sampling rates, but they are not the fastest devices. However, in terms of speed, resolution, cost, and power dissipation it is popular ADC.

Sigma-Delta ADCs have the highest resolution with relatively low sampling rates from Ksample/s to Megasample/s whereas flash ADCs are the fastest single-standing ADC topology, whose operation relies on the parallel decision of a number of comparators. On the other hand, a Flash ADC needs 2^N-1 comparators for an N-bit conversion. For instance, a 3-bit Flash ADC needs only 7 comparators whereas an 8-bit one consists of 255 comparators. This exponential increase in the number of comparators puts an upper limit on resolution and increase high power dissipation, and the input capacitance. The flash ADC architecture has the highest sampling rates up to Gsample/s due to it parallel architecture but because of nonlinearity its resolution is limited no more than 8 bits. However, it is suitable when low resolutions or low latency is required.

In folding ADCs, when medium resolutions are required and the latency is still important, using a flash ADC could lead to high power dissipation and large area. This can be improved by moving away from the fully parallel comparator array. Folding is a technique where the decision is divided into parts with two flash sub-ADCs, each quantizing the coarse and fine bits of the full resolution, respectively. In this way, an $n+m$ bit resolution can be achieved with an n-bit and m-bit ADC, which is significantly reducing the number of comparators for medium resolutions. In order to quantize the fine bits, the fine sub-ADC needs to be preceded by an analogue folding circuit. However, the folding circuit also introduces a delay and in order not to limit the bandwidth, the coarse and fine sub-ADCs should sample the

signal at the same time instant. Compared to the full flash architectures, the folding architecture is more efficient but cannot achieve the highest conversion rates of the flash ADCs. In order to realize very high sample-rates, especially at medium resolution, a single ADC is not adequate and time-interleaving of ADCs is required. Another motivation to use time-interleaved ADCs is that it allows power efficient architectures such as SAR and Pipelined ADCs to be used to realize low-to medium resolutions at sample rates that still within the reach of flash ADCs. In the time-interleaved configuration, each sub-ADC samples the input in a sequential manner.

3.4. All-Photonic Signal Conversion

The graphs that are illustrated in Figure 3-8 and Figure 3-10 identify future technical challenges of EADCs as reducing aperture uncertainty to below 0.1ps, increasing sampling frequencies beyond 10 GHz, which is providing about 6 ENOB. A Photonic ADC (PADC) is a device that uses photonic technology to digitize an analogue RF electronic signal. PADCs help to improve these problems using mode-locked laser pulses with about one femtosecond timing jitter. They are promising candidates for realizing 100-Gsample/s ADCs with above 11 ENOB which is shown in Figure 3-8. It allows designers to push the resolution bandwidth by many orders of magnitude beyond what electronic sampling systems can achieve currently. In this section, we present the state-of-the-art of photonic signal conversion. Then, we present our proposed PADC and PDAC architectures and investigate their performance.

3.4.1. Photonic Analogue-to-Digital Conversions

Based on the sampling and quantization techniques and components technology, PADCs can be classified into the following groups: 1) Photonic assisted ADC, 2) Photonic sampled and electronically quantized ADCs, 3) Electronically sampled and photonic quantization ADC, 4) Photonic sampled and quantization ADC. Each type of ADC has its specific advantages and disadvantages. In the following subsection, the technical specifications of each group are discussed.

3.4.1.1 Photonic Assisted ADC

In this architecture, the RF signal modulated onto an optical carrier and photonics assists an electronic ADC. In this technique, an ultra-stable mode locked laser source switches electronic track and hold circuit. The advantages of these systems are: 1) reduced aperture time, 2) high clock isolation, 3) low clock jitter, 4) optical clock distribution. Photonic assisted ADC classified into the following subgroups: 1) Optical clocked tracked-and hold circuits, 2) optical replication pre-processor for electronic ADC, 3) Optical time stretch pre-processor for electronic ADC. 4) spatial-spectral holographic pre-processor for electronic ADC.

A) Optically locked track-and-hold circuits

In this scheme, because of the faster rise time and the lower pulse-to-pulse jitter, optical short pulses are used to make fast optoelectronic switching for electronic sampling [19-22]. The optical pulses from a Mode-Locked Laser (MLL) source distributed to multiple point of the ADC using optical fibre [23-26]. However, there is the signal precossing speed restriction of the electronic technology [27-33]. The maximum 4 ENOB is reported at 100 Gs/s in [32][33] and the ENOB was 4 at 40 Gs/s in [31].

B) Optically replication pre-processor for electronic ADC

There are two classes of ADCs which used fibre optic replicating loops to generate multiple sample of an RF signal. In the first scheme, generating multiple copies of the same RF signal allows a low rate ADC to quantize the sampled pulses [34][35]. In the second scheme, the number of samples within the pulse can be increased by small shifting of the sampling time over a sampled RF signal [36][37]. The main drawback of these systems is deploying an electronic ADC, which at higher sampling rate its performance decreases [38][39].

C) Optical time stretch pre-processor for EADC

In this technique a super continuum optical source is used which its spectrum is broadened using a dispersive medium like optical fibre, subsequently it is

modulated with an RF signal. Then, the modulated signal is stretched using a second time stretching fibre L2. The output of the stretched pulse is demultiplexed and after detection is quantized by EADCs which is shown in Figure 3-11. The main challenges of this architecture is the matching and calibration of channels, the quantization accuracy used EADC, the calibration and matching between them to multiplex the data, high frequency noise and distortion in dispersive medium, dispersive penalty, interferences between upper and lower sidebands in the second dispersive medium [40][41]. One of the main problems of optical time stretch is frequency dependent nonlinearity [42][43].

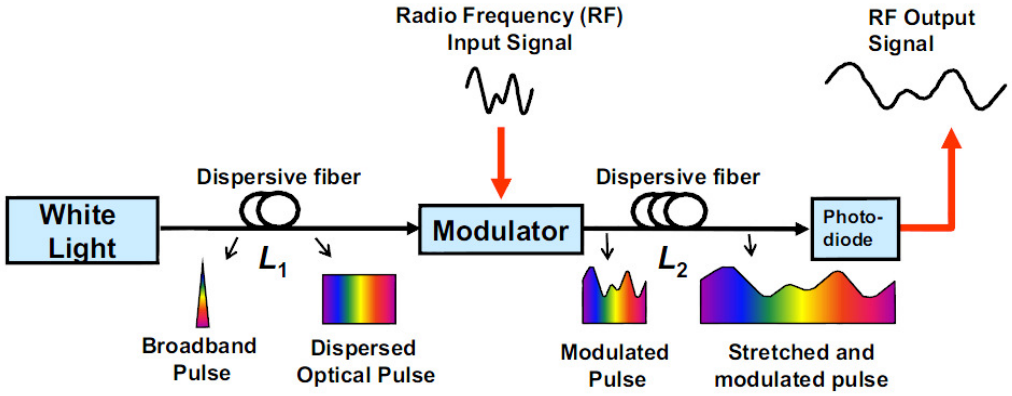

Figure 3-11: Time stretching photonic assisted ADC [40].

D) Spatial-Spectral Holographic (SSH) pre-processor for electronic ADC

In the first step of this scheme, an interested RF signal is mixed with another reference RF signal. The second step is to write spectral hologram of the Fourier transforms of the mixed RF signal in a rare-earth-doped crystal at a temperature around 4K. The third step is to read the hologram out with a slowly chirped optical source, effectively compressing the frequency content of the RF signal or stretching it in time. In this technique, rather than stretching a photo diode converts the optical signal to an electrical and low rate ADC is digitizing signal in time domain. The SSH-ADC stretches a signal in frequency domain [44][45] in comparison to time stretching architecture [40-43]. As shown in Figure 3-12, in the waveform capture process, the Signal of Interest (SoI) and reference waveform is converted into optical domain and illuminate the SSH material to produce a spectral hologram.

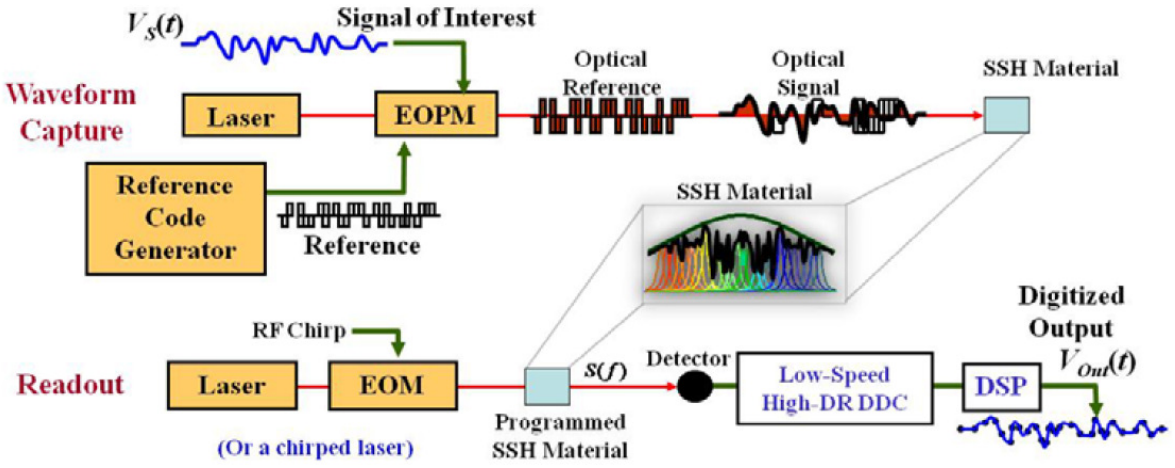

Figure 3-12: The SSH PADC architecture [46].

Then, in the readout process, a chirped optical wave form reads the absorption profile, which is detected and digitized with high fidelity, low speed ADCs, and post processed to yield the digitized version of the SoI [44-46].

3.4.1.2. Photonic sampled and electronically quantized ADCs

In this technique, a MLL is used to sample an electronic RF signal. There are three main architectures in this group: 1) Optical sampling and quantization by using a single high rate EADC, 2) Optical sampling with wavelength demultiplexing and using a bank of lower rate EADCs, 3) Optical sampling with time demultiplexing with deployment of lower rate EADCs. The key components of this system are a MLL, an EOM, a detector and an EADC for quantization as shown in Figure 3-13. This system contains a analogue optical link and thus its performance is characterized by the link SNR, SFDR, modulator bandwidth and modulation index, photo diode saturation current and bandwidth [47][48][53]. Photonic sampled ADCs have several other issues besides jitter and pulse width. This architecture, like analogue optical links, requires linear modulator response. One way to obtain linear modulator response is to use a low modulation index but this often increases the optical power requirements. Another solution is digitizing both outputs of the MZM and invert the nonlinear transfer function of the modulator with post processing [49-52]. Another key function is the linearity of photo diode and requirement of high speed ADC for quantization of sampled values. The EADC must work at the same rate of MLL pulse rate. Two major source of error in photonic sampled ADC are -

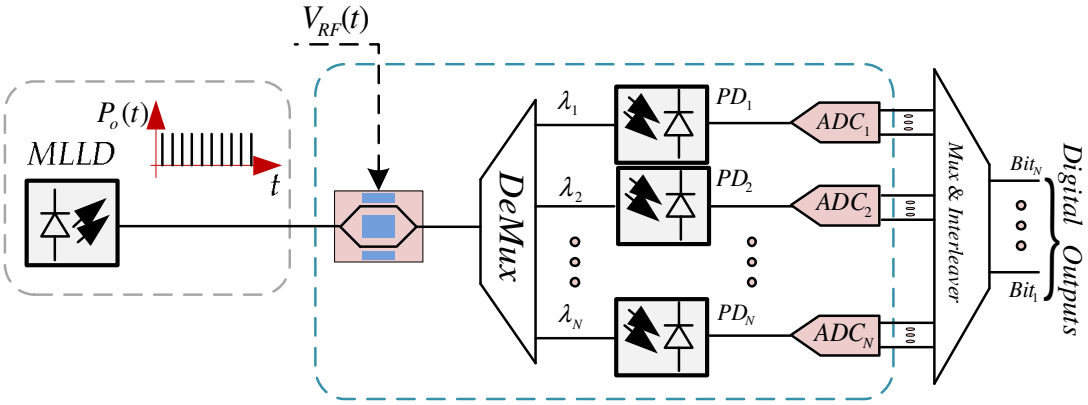

Figure 3-13: The architecture of the ADC with optical sampling, wavelength multiplexing and electronic quantization.

pulse-to-pulse amplitude fluctuation and timing jitter. A path-matching, cross talk, and calibration are important issues.

3.4.1.3 Electronically Sampled and Photonic Quantization ADC

In this architecture, RF modulated on a CW optical carrier and photonic process aids or replaces electronic quantizer. However, an electronic sample and hold circuit produces a stair case voltage waveform that is used to vary the wavelength of a semiconductor laser [54-61]. Then the generated optical signal split into N channels and N filters of variable length that produces a digital output called a "Gray code", as shown in Figure 3-14.

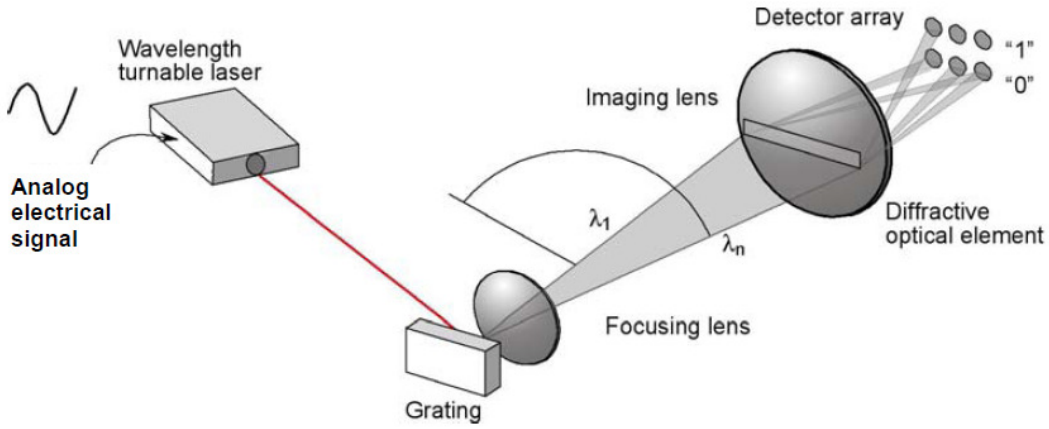

Figure 3-14: An architecture of ADC with electronically sampled and optically quantization [61].

3.4.1.4. Photonic Sampled and Quantization ADCs.

In this architecture both sampling and quantization are performed in optical domain. These PADCs can be classified into the following classes: 1) Intensity

modulation and conversion to Gray code, 2) Intensity modulation and optical comparator, 3) Voltage controlled optical beam diffraction/deflection, 4) Optical delta-sigma modulators. The first two schemes are mainly focused on photonic sampling and intensity quantization. The intensity quantization of sampled signal can be performed using different physical phenomena and components: semiconductor saturable absorbers, n_2 nonlinearity, Cross Phase Modulation (XPM), and Self-Phase Modulation (SPM) and etc.

A) Intensity Modulation and Conversion to Gray Code

Figure 3-15 illustrates a well-known architecture for PADC, this scheme is proposed by Taylor in which an array of parallel Mach-Zehnder Modulators (MZMs) are used [62]. The idea of this architecture is proposed based on four modulators with different length of electrical electrode that are binary weighted and generate digital bit at the output of each channel [62][64]. In this scheme, with an appropriate bias voltage, the light intensity at the output of the modulator is a function of a driven voltage. Consequently, after detection of the optical intensity and using an electronic comparators cluster at the threshold intensity, $I_{th,}$ the output Gray code is generated [62-66].

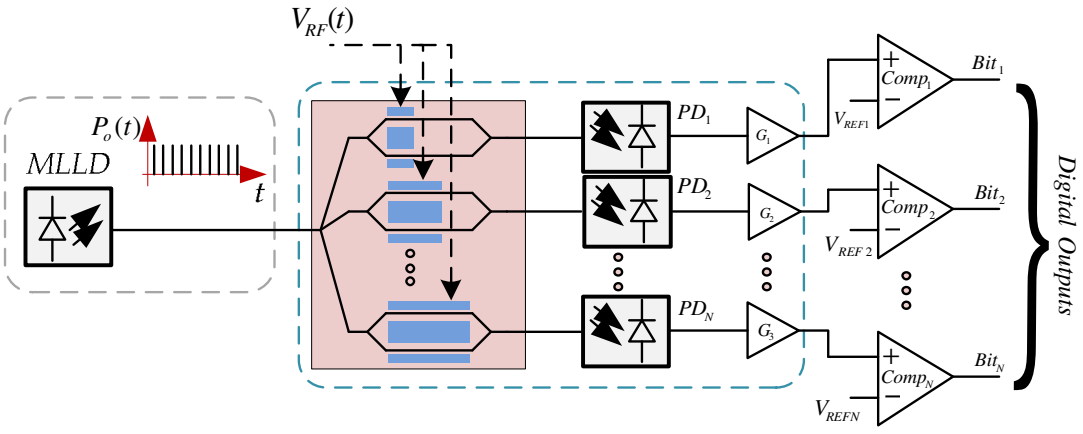

Figure 3-15: Taylors' photonic ADC architecture with multi-interferometric.

However, the main challenges of this system are, its output is not digital and it is completely analogue device [69] and it is more photonic assisted ADC. Each extra bit resolution requires another factor of 2 in the length of modulator, which is limited by modulator insertion loss and drive voltage. The maximum number of bits obtained

with this method has always been less than 4 bits, whereas the nonlinear optical switched based on the Sagnac interferometer is required to achieve the Gray code [67][68][129].

The major limitation related to Taylor's scheme is that the half-wave voltages (V_π) of the MZM at the LSB should be very low, which is difficult to realize. To avoid it, employing cascaded MZMs with identical V_π was proposed [70] or phase modulators [71] instead of binary weighted electrodes length MZMs array [62][75], whereas the synchronization between signal applied to modulator is a limitation [72]. Furthermore [73] is developed an architecture using MZMs with identical half-wave voltages which is shown in Figure 3-16. The quantization and digital coding are achieved by properly biasing MZMs, with each MZM being connected to a comparator with the threshold setting at half of maximum voltage. A binary code representing the input analogue signal is generated and the bit resolution is $N = Log_2(2n)$, where n is the number of the MZMs. However, in this scheme there are $\left(2^n - 2n\right)$ invalid words that need post processing to be replaced by the nearest valid code [80][81][90].

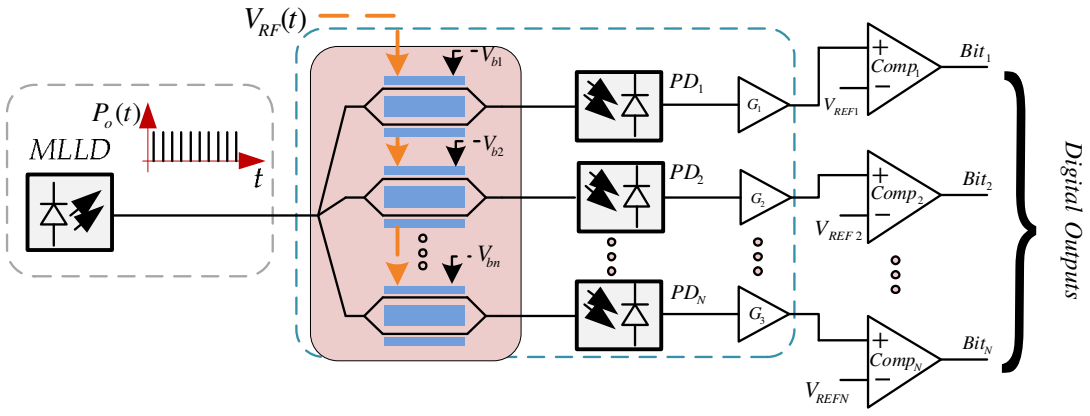

Figure 3-16: An n-channel ADC using n MZMs with identical V_π [73].

To increase the bit resolution without increasing the number of the MZMs, multiple comparators are used while each having a different threshold levels. However, this scheme needs the MZMs with different V_π. Therefore, Figure 3-17 gives another architecture with reported 4-bit resolution which is using an array of the MZMs with

identical V_π and multiple comparators for each channel [74]. In this scheme, the MZMs are biased at different bias voltages. However, this scheme still needs several MZMs, PDs for higher resolution bits and combination of logic and calibration between the channels.

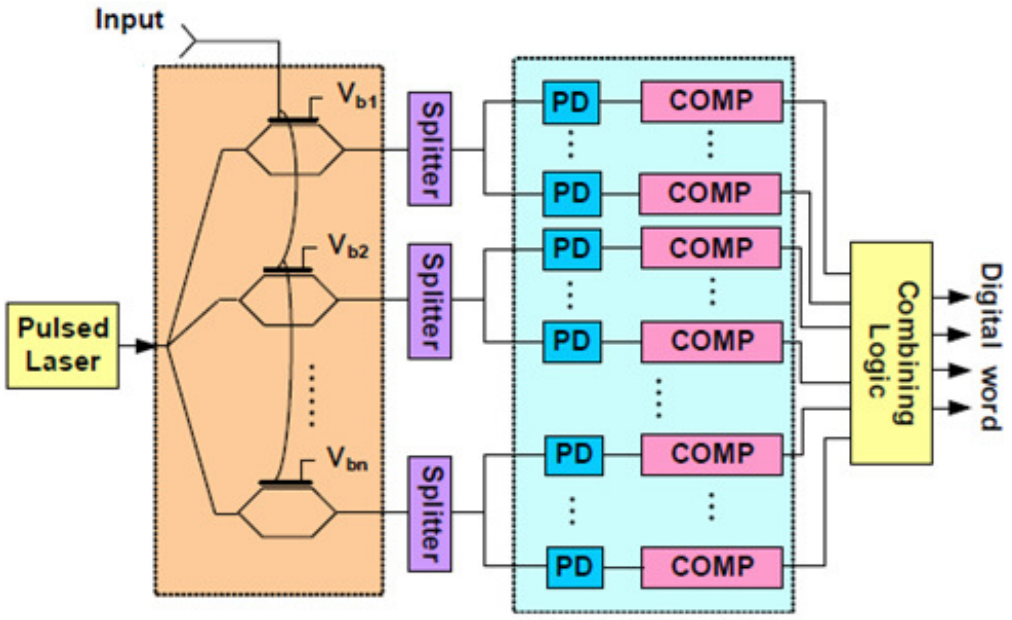

Figure 3-17: An n-channel ADC using MZMs with identical V_π [74].

In [76] a PADC's architecture based on time and wavelength interleaving is reported, which is shown in Figure 3-18. A MLL's pulse with repetition period T is demultiplexed into N trains with different wavelength, where N is the number of channel. The pulse trains pass through the optical delay lines, which introduce incremental delays of T/N between them. The trains are then recombined with a multiplexer to produce a pulse train with repetition period T/N, where pulse wavelengths repeat periodically every N pulses. The RF signal is sampled using the optical pulse train and an EOM. The modulated pulse train is split into N channels using a wavelength demultiplexer. The sampled pulses in all channels are converted to the electrical domain with PDs, while amplified and digitized with electronic ADCs. These ADCs are synchronized with the MLL pulse and take one sample per pulse, exactly at the pulse peak. During post-processing, the samples captured in different channels are compensated for distortions and interleaved to obtain the final digital representation of the RF signal. This scheme with N channels not only

increases the sample rate by N, but also reduces the required analogue bandwidth of PDs and electronic ADCs. This scheme can deliver 7.0 ENOB using discrete components to implement at 41 GHz sampling rate with timing jitter accuracy about 15 fs which is 4-5 times better than the state-of-the-art electronic ADCs. However, the integrated implementation of this scheme provided 3.5 ENOB to digitize a 10 GHz RF signal.

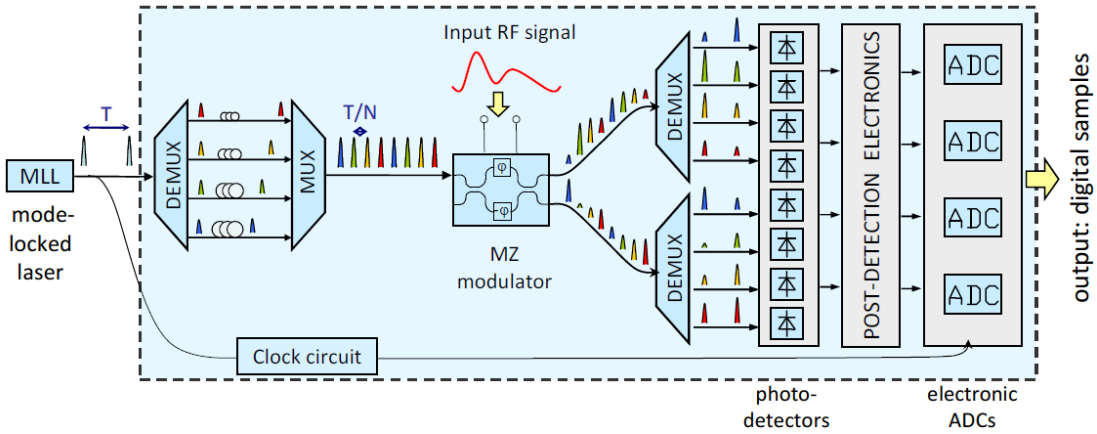

Figure 3-18: Time and wavelength mapping and interleaving PADC [76].

B) Intensity Modulation-Optical Comparator

The attraction of direct quantization is simplicity and potentially lower insertion loss but the disadvantage is that 2^N comparators are needed for N bits. A signal may be digitized to N bits with 2^N comparators set at 2^N levels. There are many optical processes and devices that can be as a comparator but the sharp transitions, the response time is very important. The main problems of these techniques are low ENOB and sampling rate.

C) Voltage Controlled Optical Beam Diffraction/Deflection

In this scheme, an input voltage is used to deflect the optical beam to 2N position then producing the Gray code to quantize the optical signal [77][78], which is shown in Figure 3-19. The beam deflector could be mechanical, acoustical or electro-optical [11]. The challenge of acousto-optic modulator is the low time response [79]. In [80], free space interferometer scheme is used. A Phase Modulator (PM) incorporated in one arm of the interferometer whereas the RF input voltage changes the phase of optical source. Then, the diffracted pattern that is generated at the output of

interferometer emitted to an array of photo diodes at the specific locations. Thus, electronic comparators linearly decode this phase change to a digital data. The advantages of this technique are the PM linearity against Intensity modulator (IM) and deployment of one phase modulator in comparison with optical sampling and intensity modulation scheme. However, the quantization still is not purely based on optical technique.

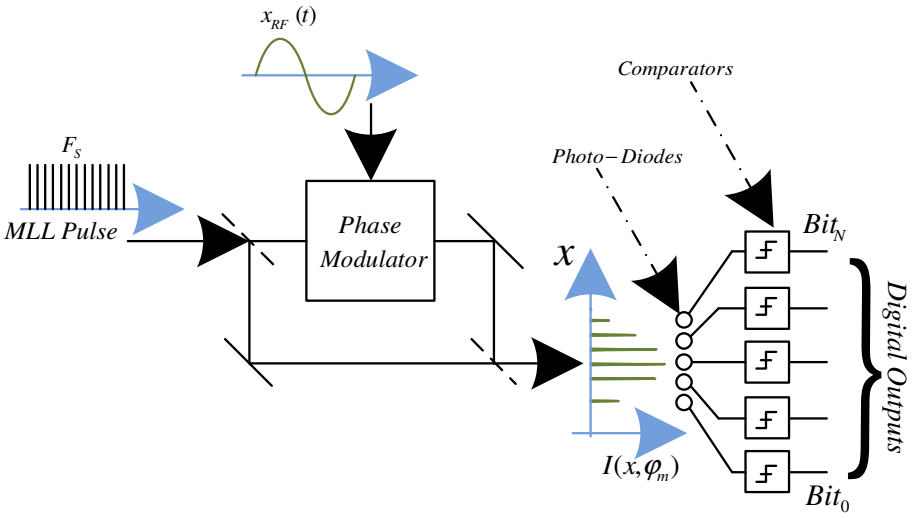

Figure 3-19: ADC based on voltage controlled beam diffraction and deflection [80][81].

In [82], the circular-code architecture is presented which is shown in Figure 3-20 (a). The operation principle is based on the polarization-differential interference. The difference between the two schemes is that a single arm Mach–Zehnder interferometer with polarization-differential interference and multiple phase-shifted outputs is designed. The key issue in both interferometric ADC approaches is to realize the desired phase shift between the transmission characteristics of each two adjacent channels in order to achieve optical quantization. It is realized through free-space adjustment and fibre stretching in [82].

The analogue signal is sampled by optical pulses using phase-modulator while two orthogonal polarizations of the pulse are used into the two x and y arms of the interferometer by a Polarization Controller (PC). The phase difference between the two polarizations is linearly changed with the input analogue voltage. The pulses are separated into N channels by a 1 to N splitter and added a Constant Phase-Shift

Step (CPSS) between the two polarizations from each channel to the next by a Tuneable Optical Phase Shifter (TOPS) array.

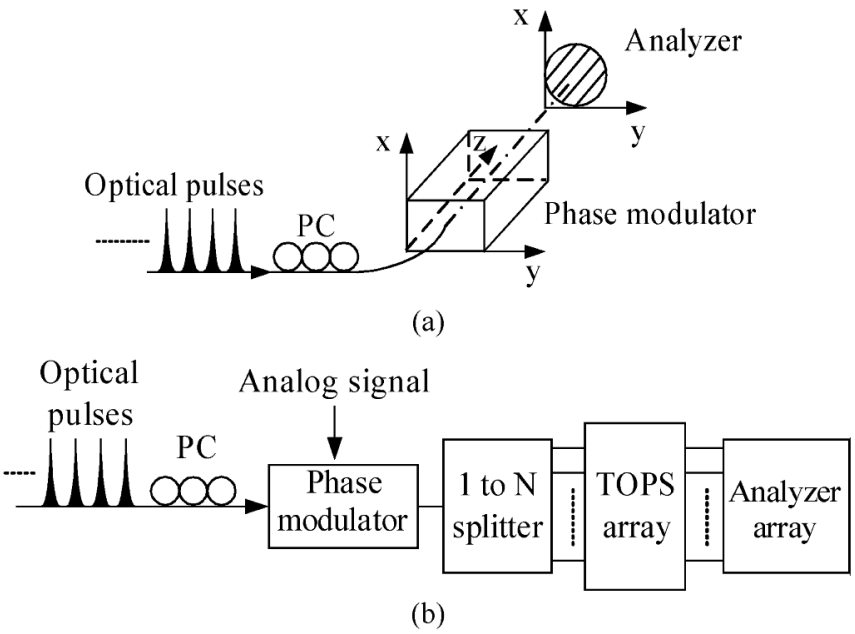

Figure 3-20: The architecture of interferometric photonic ADC, (a): Free space adjustment, (b): Fibre stretching [82].

Two polarizations are then made to interfere through an in-line analyzer whose transmission axis is 45° to the x and y axes that is shown in Figure 3-20 (b). The transmission intensity of the mth channel is given by:

$$I_m = I_o Sin^2(\frac{\pi}{2}.\frac{V}{V_\pi} + m\Delta\varphi) \quad (3\text{-}24)$$

Where I_o is the light intensity, V_π the half-wave voltage of the phase modulator, and $\varphi = \frac{T}{2N}$ the CPSS, and T is the period of transmission characteristic. The transmission characteristics of channels with CPSS are used to aid the quantization process. An ENOB of 4.1 bits for 2.2 GHz input signal based on software sampling has been reported. The main limitations of this scheme are the speed and bandwidth of phase modulator, detectors and interfacing electrical logic devices.

In [83], a PADC by utilizing intrinsic multi-wavelength phase shift in lithium niobate Phase Modulator (PM) is reported, as shown in Figure 3-21. In this scheme, a synchronized MLL pulse train with different wavelengths and same polarization which are multiplexed together can be used as a sampling pulse into a $LiNbO_3$ PM

to sample an electrical analogue signal. A polarizing beam splitter as in-line analyzer follows the PM, whereas the transmission axis of the analyzer is parallel to the polarization state of the input pulse train. Therefore, the maximal polarization interference will happen through it. The phase difference induced by the electro-optic effect of the PM linearly changes with the analogue applied voltage and due to the dispersion effect in $LiNbO_3$. In the quantization process, the phase shift between the transmission characteristics of each two adjacent channels should be $\frac{\pi}{N}$ (or $2n\pi+\frac{\pi}{N}$), where N is the number of channels. When V_{pp} of the analogue signal is $2V_{\pi}$, $2N$ quantized levels can be realized. The reported ENOB is 4.3 bits for sampled CW 2.5-GHz input RF signal for implemented 5-bit ADC with 16-channel but sampling rate is not reported.

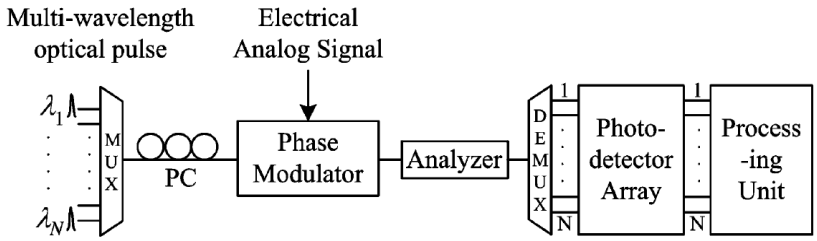

Figure 3-21: PADC based on multi-wavelength phase shift in lithium niobate phase modulator [83].

Figure 3-22 shows the proposed architecture in [84], which is using time and wavelength interleaved optical sampling pulse train at 40 Gigasample/s sampling rate of 2.5 GHz CW electrical signal with 3.45 bits achieved ENOB. The difference of this scheme with [77-81][82][83] is in the technique of desired phase shift, utilizing electronically controlled fibre squeezer which is easier to be realized and controlled.

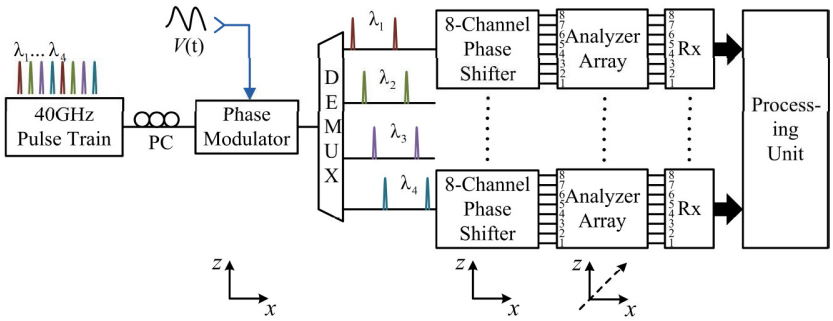

Figure 3-22: The architecture of time and wavelength interleaved interferometric photonic ADC [84].

In [85], a method of phase shifting between adjacent quantization channels is achieved using an unbalanced MZM and specific filter array. As shown in Figure 3-23, this scenario needs only one EOM and two wavelengths regardless of the resolution. The 8-bit reported number of bits at the sampling rate up to 40 GS/s can be realized theoretically.

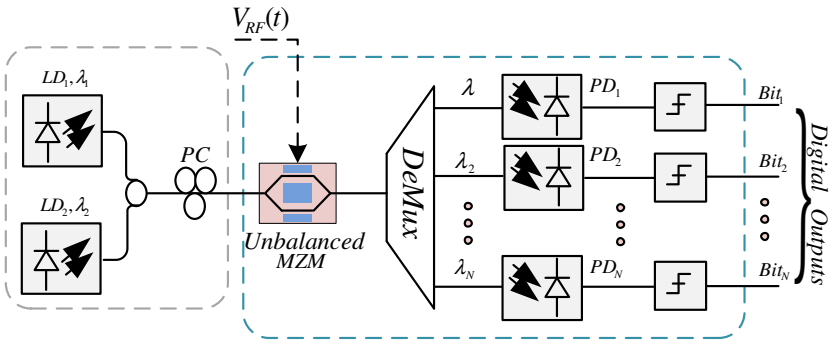

Figure 3-23: The architecture of phase shifted photonic ADC [85].

The method in [86] is based on the polarization modulator, polarization controllers and polarisers as shown in Figure 3-24. The system is free of bias-drift that commonly exists in previous intensity modulating methods. This scheme, there are 2N distinct quantization levels (N is the number of channels in the system) and therefore a theoretical resolution of $\log_2(2N)$.

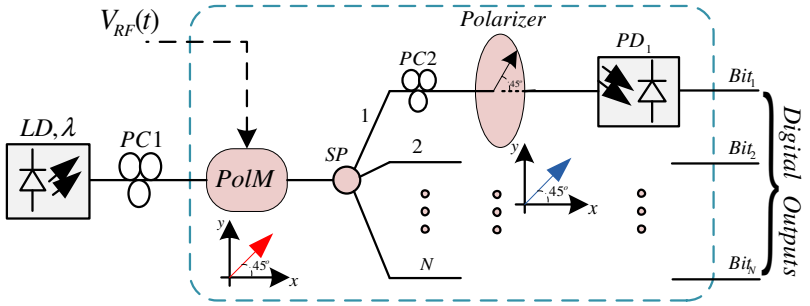

Figure 3-24: Photonic ADC architecture based on polarization modulation and polarizer [86].

Figure 3-25 illustrates a PADC which is reported with differential encoding by employing a phase modulator and Delay-Line Interferometers (DLIs) [87]. In this scheme, a MLL pulse train is used to sample an analogue signal $V_s(t)$ using an electro-optical PM. The sampled pulse train is split into N channels via a coupler which is fed to an individual DLI. The DLIs in all channels have an identical delay τ but different phase shift, which can be realized by placing an electrically controllable

phase shifter in one arm of each DLI. The delay τ should be set to the corresponding bit time of the sampling rate. The signal passed on through the DLI is then detected by a PD and sent to a comparator. A bit of 1 or 0 is obtained at the output of the comparator according to the electrical level of the detected pulse. This architecture is similar to [83][84].

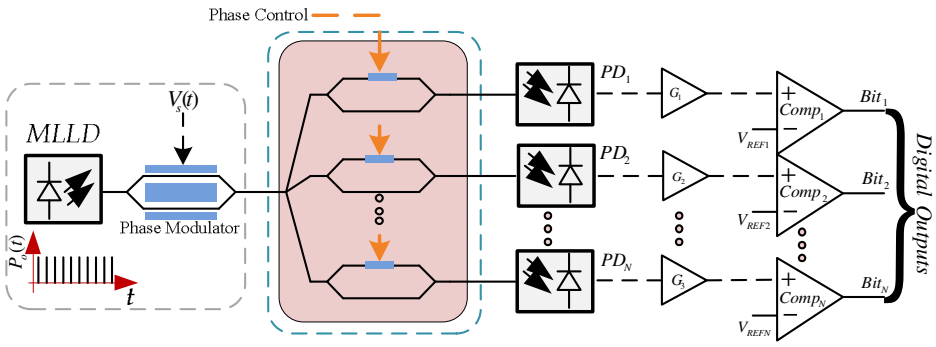

Figure 3-25: PADC architecture with differential encoding employing a phase modulator and delay-line interferometers (DLIs) [87].

The given photonic ADC scheme in [88] is based on phase-shifted optical quantization (PSOQ) [42][82-87], and 5-bit resolution has been realized with 8 phase shift quantization channels and an extra MZM which is shown in Figure 3-26. In this architecture, first the sampling pulses are fed to a polarizer to make the two orthogonal polarizations of the sampling pulse aligned with the x or y axis of the phase modulator (PM).

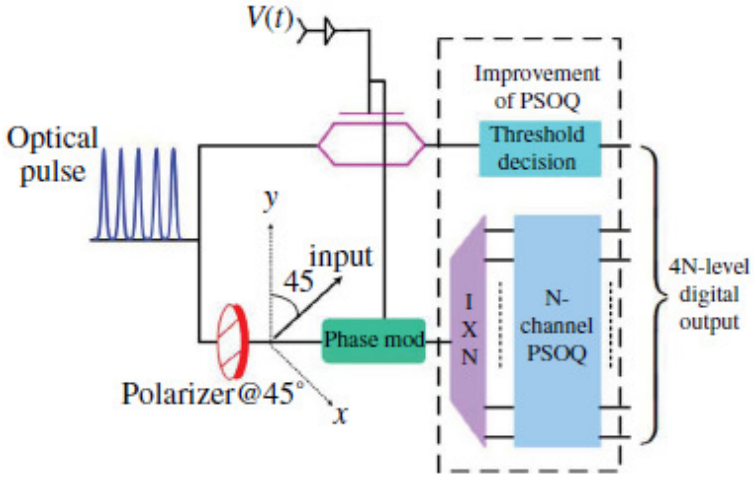

Figure 3-26: Improved phase shifted optical quantization [88].

Then, they pass into the PM, and the phase differences between two orthogonal polarizations of the pulses change linearly with the amplitude of the input signal

voltage. The $4V\pi$ full-scale analogue RF signal sampled by optical pulses using the PM and the MZM, where $V\pi$ is half-wave voltage of the PM. The output of the PM is fed to an N-channel PSOQ, each channel of which induces an extra phase shift of $(i-1)\pi/N$ between two polarizations, where i is the number of the channel. Furthermore, a MZM with half-wave voltage $2V\pi$ deploys an independent quantization channel whereas the electrical recovered signal digitized by an electrical comparator. The combination of N channel and MZM (N+1 channels) could realize $4N$ quantization levels, while $2N$ channels are needed in pure PSOQ [82-87]. Therefore, $N-1$ channels could be reduced, which simplifies the system configuration.

In the given architecture in Figure 3-27, a cascaded PM system for high-speed photonic ADCs is reported [89][90]. It is utilizing distributed phase modulation to quantize the signals in the optical domain; thus, the output is in a form similar to a nonreturn-to-zero (NRZ) optical data pattern based on the architecture in [62].

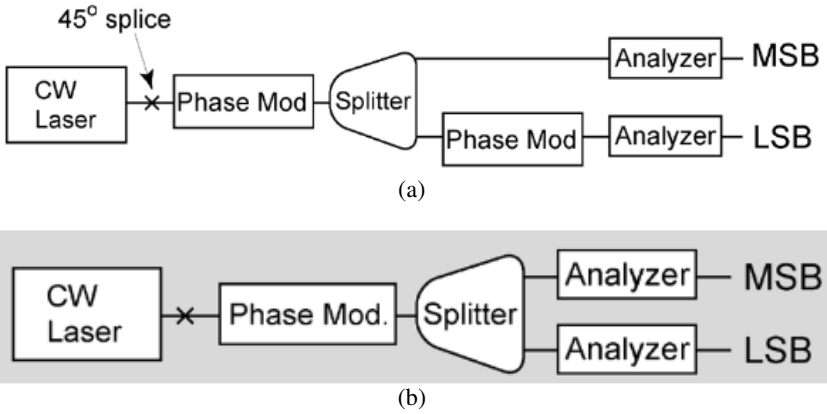

Figure 3-27: Architecture of a 2-bit pipelined PADC based on distributed phase modulation, (a): standard binary system, (b): Gray code binary system [89][90].

This cascaded photonic signal processing departs from the previous similar photonic ADC architecture by dramatically reducing the electronic ADC hardware complexity, analogue signal channel timing and synchronization.

As shown in Figure 3-28, the Spatially Distributed Successive Approximation Register (SDSAR) ADC scheme in [91] is a developed architecture of [89][90] in an integration with the scheme in [62] that encoding input analogue voltage into the phase.

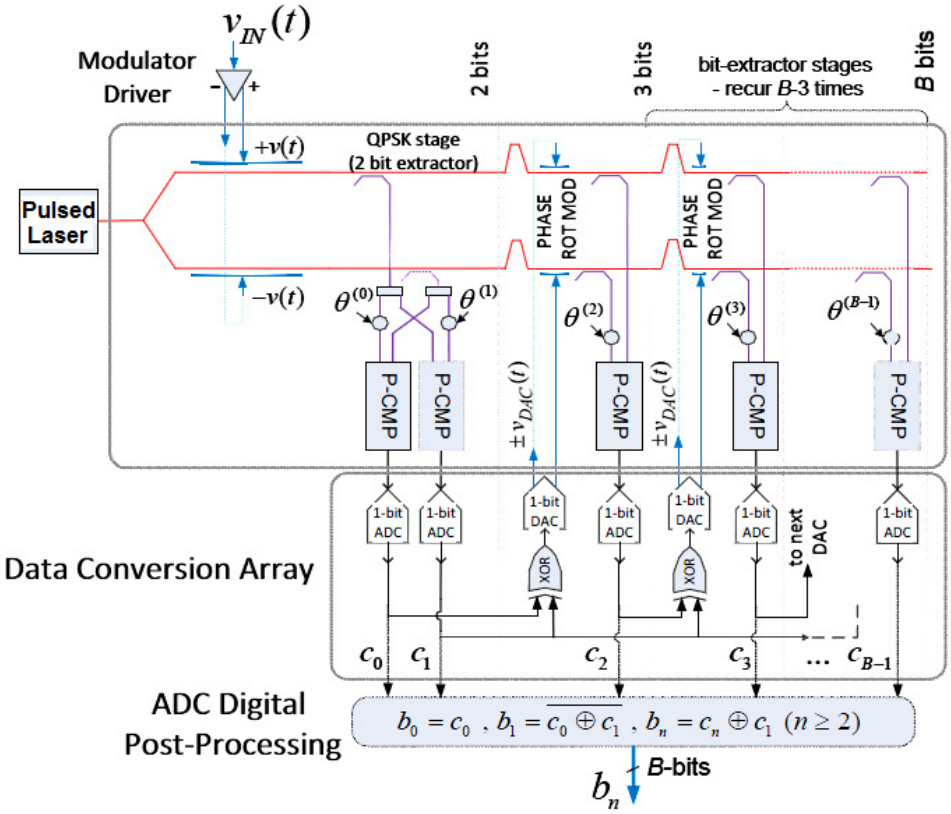

Figure 3-28: The architecture of the SDSAR PADC [91].

Two basic optical building blocks of this PADC are: 1-bit optical phase comparator (1-bit ADC) based on interferometric comparison of phases with balanced photo-detection configuration, and the optical 1-bit DAC, namely electro-optic modulation with a bipolar electrical pulse. Phase comparators (P-CMP) are biased by quasi-static phase controls.

In this architecture an optical pulse train is fed into the dual PMs driven by input analogue voltage, cascaded interferometric 'bit extractor' measurement stages converge onto the sampled signal phase by successively subtracting a binary sequence of the phase values from the accumulated phases of the optically sampled pulses along the optical transmission line. The subtracted phase values, as generated by 1-bit DAC voltages, are determined by the phase measurements of the prior stages. The 1-bit ADC outputs, c_n, are processed by simple combinational logic in order to generate the B bits codeword b_n of the ADC. Therefore, photonic and electronic matching delays are required to synchronize the successive stages in this feed-forward approach.

D) Optical Sigma-Delta Modulators

The optical sigma-delta modulator ADC is based on an electronic ∑-Δ modulator and is known as oversampling ADC. In this ADC, increasing the sampling rate by factor 2, causes the improvement of the ENOB by factor ½, Figure 3-29 shows a 1st order ∑-Δ modulator [13].

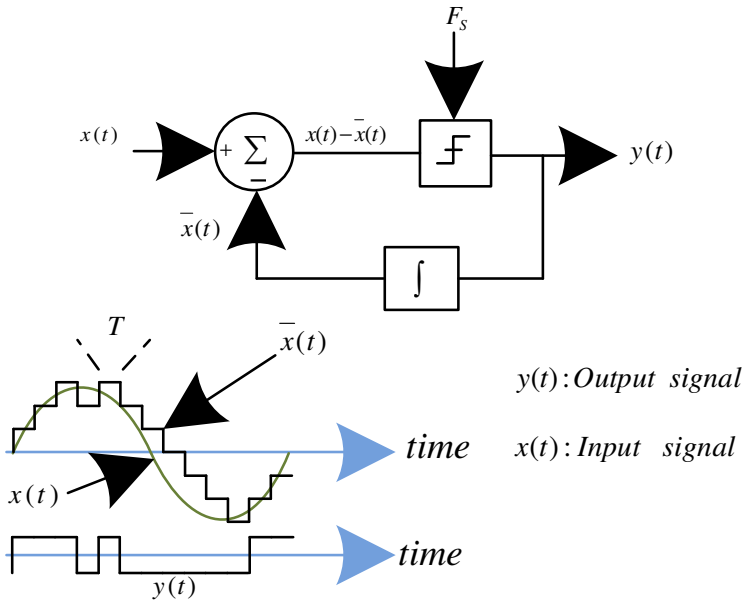

Figure 3-29: 1st-order sigma-delta modulator architecture.

In the presented architecture in [92][93], mode locked laser pulses are used to over sample a RF signal using dual drive MZM. These MZMs perform amplitude and direction accumulation with the combination with a detector, a comparator, and an optical circulator. Figure 3-30 shows an optical 16-bit Sigma-Delta Modulator ADC with 264 Msample/s sampling rate.

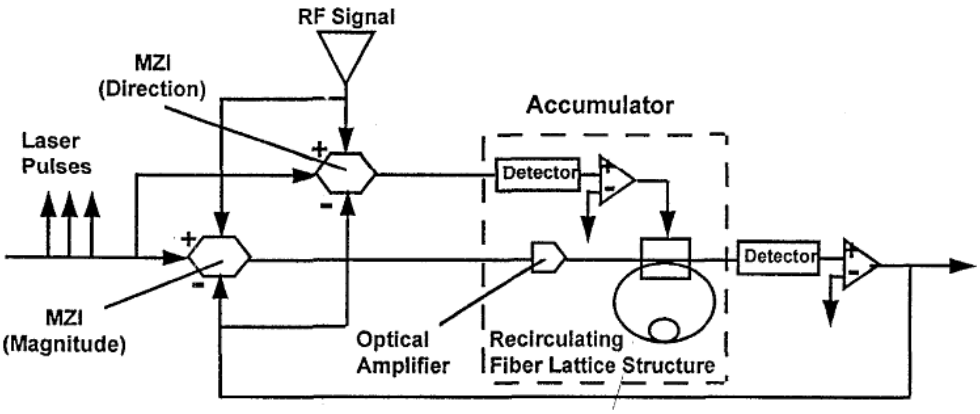

Figure 3-30: 1st-order integrated optical sigma-delta modulator [92][93].

The challenges of the optical ∑-Δ modulators are the lack of fully optical components such as adder, integrator, DAC [94][95] and the maximum low sampling rate because of the delay of the loop and it needs very fast comparator.

3.5. Pipelined Photonic Analogue-to-Digital Converter

Wideband analogue to digital conversion is a critical problem encountered in broadband communication and radar systems. The pipelined is a popular architecture for modern applications of ADCs due to its high sustained sampling rate, low power consumption and linear scaling of complexity. The term "pipelined" refers to the stage-by-stage processing of an analogue input signal. In the diagram depicted in Figure 3-31, the analogue input signal enters the ADC.

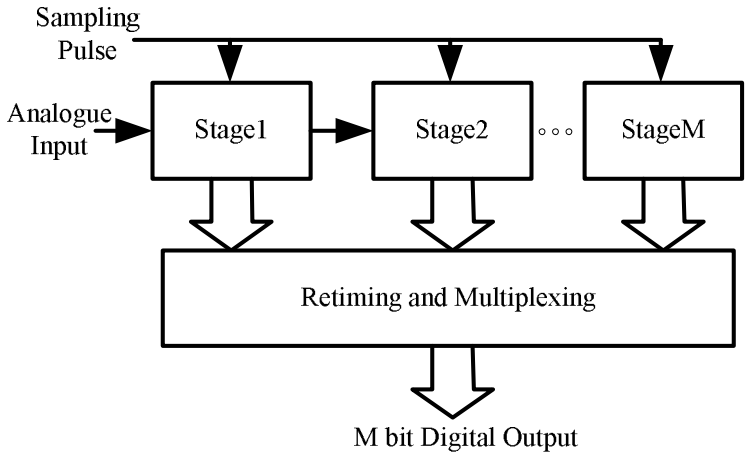

Figure 3-31: A basic block diagram of a pipelined ADC.

Each subsequent pipelined stage of the ADC resolves a certain n number of bits to be contributed to the final conversion output. Simultaneously, after each stage has finished the quantiziation process of its input sample to n bits, it outputs converted to an analogue residue signal that serves as the input to the next stage. Furthermore, each stage's digital decision is then passed to a digital block that properly retimes the output bits for processing the final digital decision.

The pipelined ADC's stages block is shown in Figure 3-32. The input signal is sampled in each stage. Subsequently, an n-bit flash ADC quantizes the analogue signal and produces a digital decision of n bits. The digital decision is then fed through an n-bit flash DAC to be re-converted into an analogue signal.

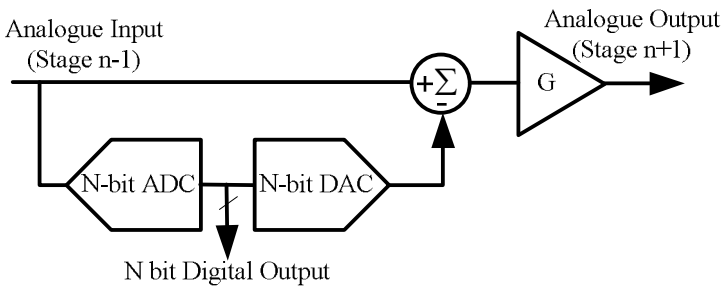

Figure 3-32: Pipelined ADC stage n's block diagram.

The summation node presented in the above diagram takes the input signal and subtracts the DAC output signal from it. This difference signal is then fed through a gain stage with gain G to produce the residue voltage (full-scale range), the output voltage of this stage [96][97]. This means that all the stages can be implemented identically and there is a linear relationship between required hardware and resolution.

Pipelined architecture offers good trade-off between conversion rate, resolution and power consumption. It consists of several cascade stages and timing circuits. The concurrent operation of all pipelined stages makes this architecture suitable to achieve very high conversion rates. The overall speed is determined by the speed of single stage [98]. Based on the above discussion, Photonic ADC (PADC) groups and classes can be summarized into the chart in Figure 3-33.

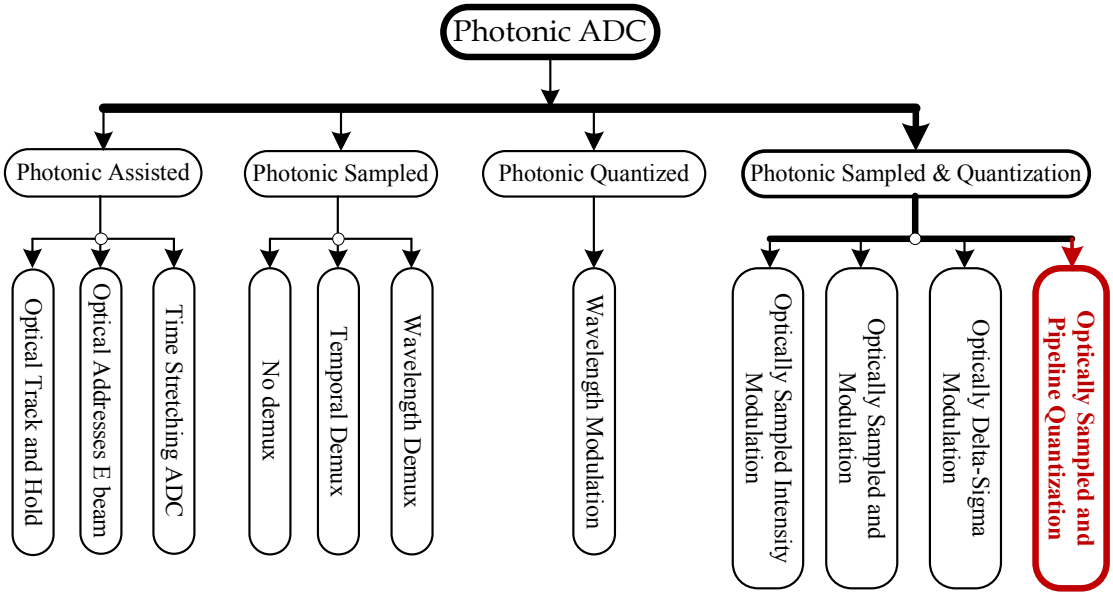

Figure 3-33: The photonic ADC classification.

3.5.1. Proposed Pipelined Photonic ADC

In this section the concept of the proposed pipelined ADC is presented. To discuss and analysis the system in detail a simple 2-bit ADC is proposed and modelled which is illustrated in Figure 3-34. In this figure, a sample RF information signal $x_{RF}(t)$ has been sampled by sampling pulse train $S[n]$. The sampled signal $X_{RF}[n]$ is connected to the input of a 1-bit ADC and a positive input of a subtractor. The 1-bit ADC quantizes the sampled symbol which generates the most significant bit (MSB) B_2 at the output. Therefore, based on pipelined architecture, the MSB output signal is converted back to the analogue form using a 1-bit DAC that its input is connected to the output of 1-bit ADC. The generated signal at the output of 1-bit DAC $X'_{RF}[n]$ is subtracted from the input sampled signal $X_{RF}[n]$. Therefore, the result $X''_{RF}[n]$ signal is given by:

$$X''_{RF}[n] = X_R F[n] - X'_{RF}[n] \tag{3-25}$$

The output signal of subtractor $X''_{RF}[n]$ is fed to the second 1-bit ADC to be quantized as the least significant bit (LSB) B_1.

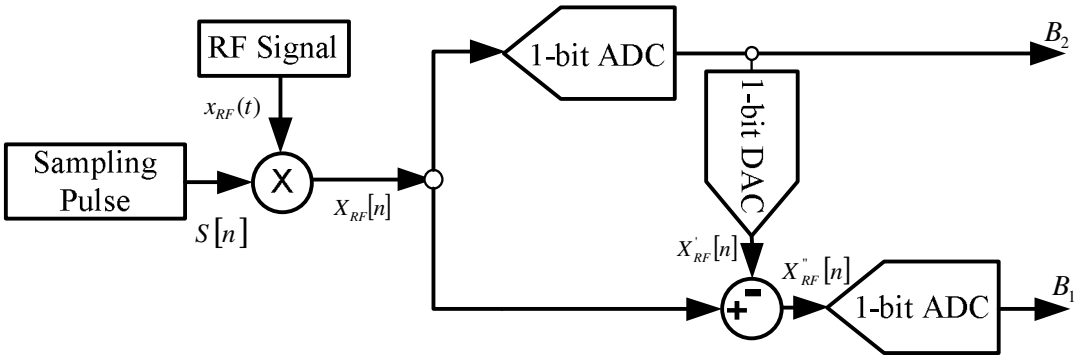

Figure 3-34: The proposed architecture of 2-bit PADC.

The waveforms of different points of the simulated model of Figure 3-34 are shown in Figure 3-35.

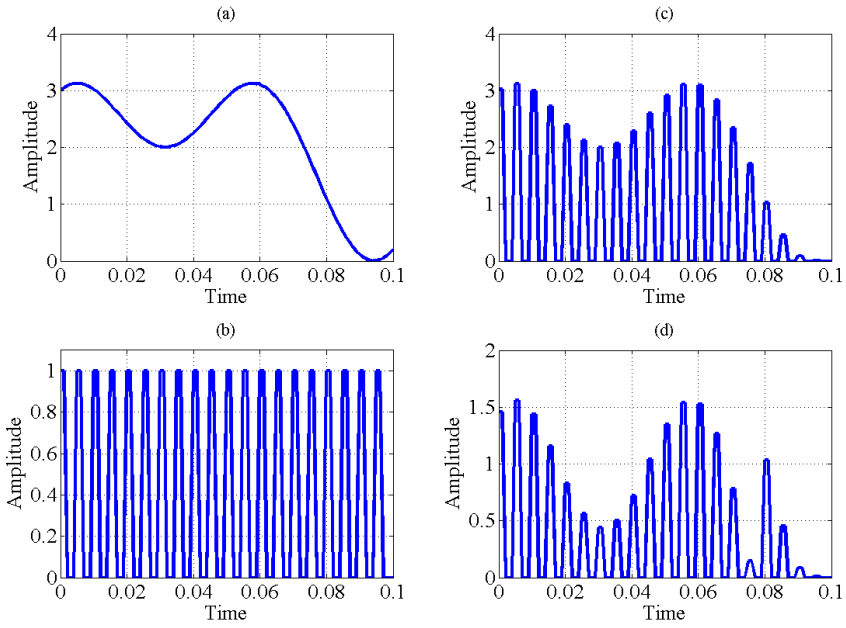

Figure 3-35: The waveform of different points of ADC: (a) The input signal $x_{RF}(t)$. (b) The sampling signal $S[n]$. (c) Sampled signal $X_{RF}[n]$. (d) The difference signal of the output the subtractor $X''_{RF}[n]$.

The waveform Figure 3-35 (a) represents $x_{RF}(t)$ as a sample input signal to the ADC and Figure 3-35 (b) shows the sampling pulse waveform. The sampled signal $X_{RF}[n]$ is shown in Figure 3-35 (c). Figure 3-35 (d) represents the output signal of the subtractor, $X''_{RF}[n]$.

Figure 3-36 shows the output waveforms of the quantized outputs of the ADC. Figure 3-36 (a) and Figure 3-36 (b) show the MSB, B_2 and LSB, B_1 of the proposed ADC, respectively.

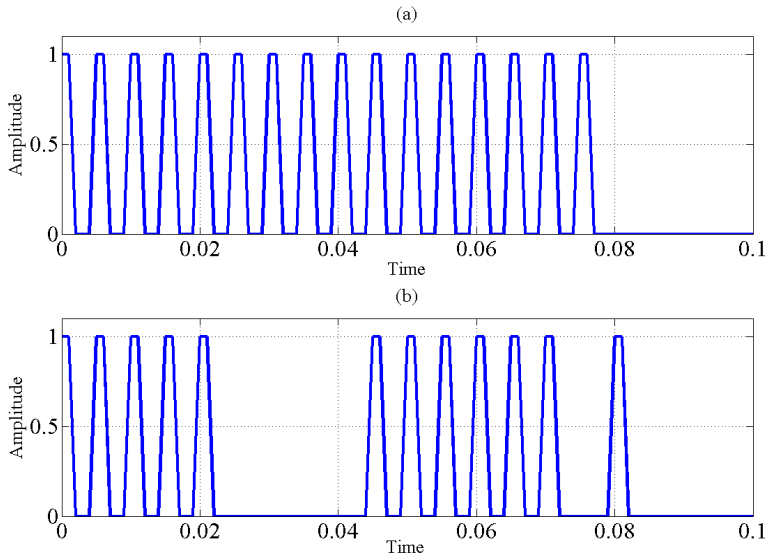

Figure 3-36: The waveform of the 2-Bit ADC output: (a): B2 the MSB, (b): B1 the LSB.

To demonstrate the ADC function, the two output bits of ADC is fed to a sample modelled flash DAC. The DAC converts back the digital data to the corresponding analogue sampled data.

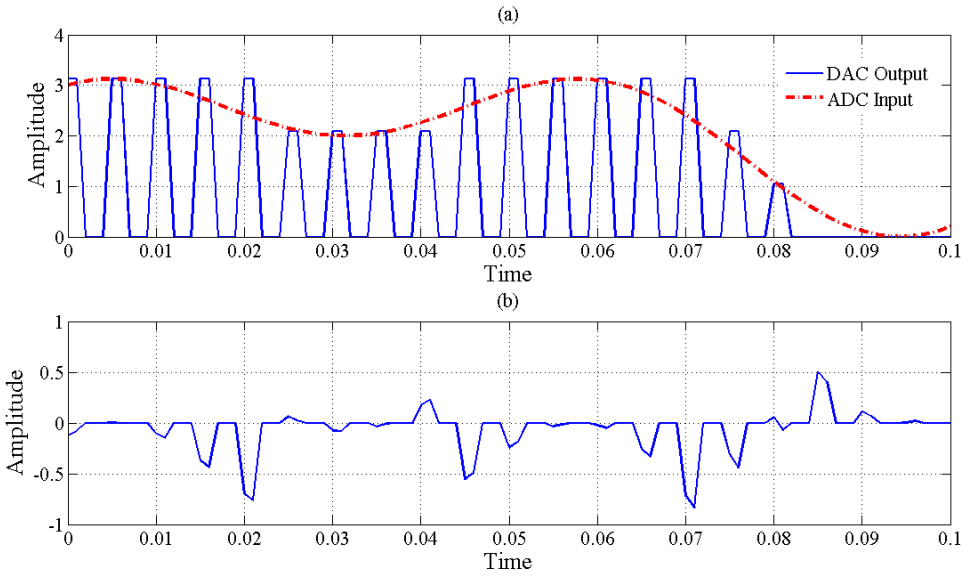

Figure 3-37: The waveforms to evaluate the ADC: (a) The ADC input $x_{RF}(t)$ and output waveform of a 2-bit flash DAC; (b) The ADC and DAC conversion error as the difference of the ADC input $x_{RF}(t)$ and the output of DAC.

The DAC output is shown in Figure 3-37 (a). The regenerated sampled output of the DAC is very close to the sampled signal $X_{RF}[n]$ that is shown in Figure 3-35 (d). A comparison of the DAC output signal with input $x_{RF}(t)$ signal is shown in Figure 3-37 (a). Moreover, in this model, there is not any additional noise; and total ADC and DAC conversion peak-to-peak error is about 1.34 of the normalized unit amplitude that is illustrated in Figure 3-37 (b).

3.5.2. Architecture Analysis

The design of fully photonic ADC is the final aim of this section. Therefore, the proposed architecture in Figure 3-34 is mathematically modelled that is shown in Figure 3-38 to analysis the model in details to defining a prospected fully-photonic system. For some simplification, in this model, the optical sampling pulse $S(t)$ is assumed as an impulse train and the input RF signal is considered as sine wave $x(t)$. Therefore, the sampled optical signal power can be given by:

$$x[n]=\sum_{n=0}^{\infty}x(t).\delta(t-nT_0)=\sum_{n=0}^{\infty}x(nT_0).\delta(t-nT_0) \tag{3-26}$$

According to the proposed architecture that is shown in Figure 3-34, the sampled signal $X_{RF}[n]$ is connected to the input of the 1-bit ADC and the subtractor. The corresponding model of this connection is an optical splitter that the output power ratio of optical splitter is depending on the number of output and the splitting ratio. In this model, there are two outputs and the splitting ratio is 50/50.

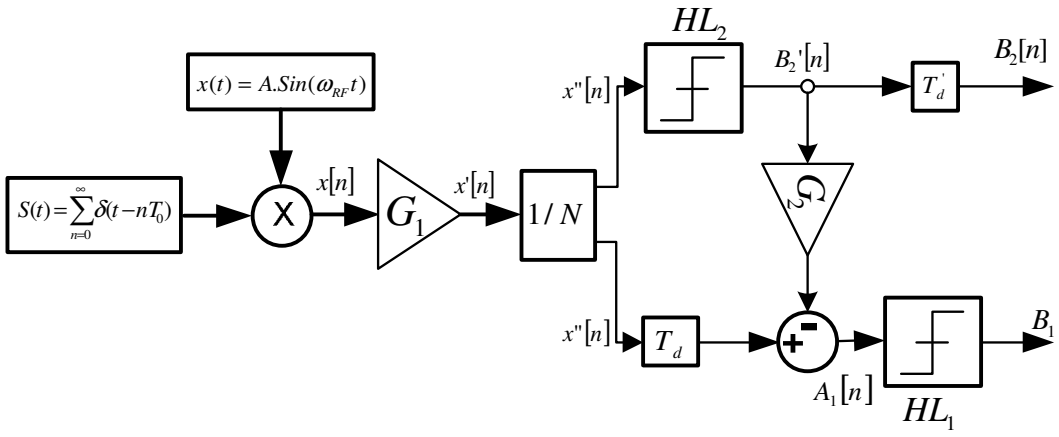

Figure 3-38: The mathematical model of 2-bit PADC architecture.

Thus, the output power of splitter is reduced by 50% in each output port in addition of the insertion loss of the splitter. To compensate the power loss and to save the number of amplifier, the input sampled signal before feeding to the splitter must be amplified using an amplifier, G_1. Therefore, the signal $x'[n]$ can be given by:

$$x'[n]=G_1.x[n] \tag{3-27}$$

Where G_1 can be represent based on:

$$G_1(dB)=\alpha_{splitter}(dB)+N(dB) \tag{3-28}$$

Where $\alpha_{splitter}(dB)$ is the splitter insertion loss, and N is the number of splitter output that equals to the number of quantization bit of ADC. In the illustrated model of Figure 3-38, $N=2$. The 1-bit ADC in the Figure 3-34 can be modelled as a hard limiter with a defined threshold level. This threshold level is related to the value of the

quantization bit. The threshold levels are defined based on the input signal full scale FS and the modulation depth at the sampling multiplier which is given by:

$$B_2^{'}[n]=\begin{cases}1 & if \ \ |x''[n]| \geq A_{Th2} \\ 0 & otherwise\end{cases} \tag{3-29}$$

Where A_{Th2} is the threshold level of HL_2 to distinguish the level '1' from '0', in which this case it is equal to $\frac{FS}{2^{N-1}}$. The output of the subtractor $A_1[n]$ can be expressed by:

$$A_1[n]=x''[n-T_d]-G_2B_2^{'}[n] \tag{3-30}$$

Where G_2 is the amplifier gain equal to a $\frac{FS}{2^{N-1}}$ to convert back the MSB, B_2 to its equivalent analogue value. Furthermore, T_d is an equivalent delay of the split signal propagation time from the input of the hard limiter, HL_2 through the amplifier, G_2 to the input of the subtractor. The output of the subtractor $A_1[n]$ is connected to the second hard limiter, HL_1. The second quantized bit, B_1 as the LSB of the converter can be given by:

$$B_1[n]=\begin{cases}1 & if \ \ x''[n] \geq A_{Th1} \\ 0 & otherwise\end{cases} \tag{3-31}$$

Where the threshold level, A_{Th1} is equal to $\frac{FS}{2^N}$.

3.5.3. Photonic System Modelling

In this section a modelling of the proposed system is discussed which is shown in Figure 3-57 based on the photonic components and devices. There are four following key physical functions such as a sampling pulse generation, an electro-optical modulator, an optical hard-limiter as a 1-bit ADC, and a 1-bit optical DAC that are functionally explained in Figure 3-38. In the previous sections, to demonstrate the proposed system overall functionality, the system description, sample waveform and

its mathematical analysis are explained in ideal conditions. Therefore, in this section more details are provided and analysis of system is discussed.

3.5.3.1. Optical Sampling Pulse

Optical pulse generation is a key physical function to generate very low jitter and reliable sampling pulse train. The most common component to generate optical pulse is a mode-locked laser. In this section, firstly a brief theoretical discussion about Mode Locked Laser Diode (MLLD) is presented; secondly the system level modelling of the MLLD by including the timing jitter and amplitude noises is described. Finally, the simulation and analysis results of the MLLD modelling are provided. A laser source operates in a large number of longitudinal modes that are falling within the gain bandwidth. The frequency spacing of the modes is given by:

$$\Delta\omega = \frac{c}{2L_c} \tag{3-32}$$

Where c is the light speed and L_c is the cavity length. Therefore, the total optical field of $2n+1$ modes can be expressed by:

$$E(t) = \sum_{q=-n}^{n} E_q \exp[i(\omega_q t + \varphi_q)] \tag{3-33}$$

Where E_q, ω_q and φ_q are the amplitude, frequency and the phase of the mode q [99-101].

A) Mode-Locked Laser Concept

A mode-locked laser is a multi-mode laser source, if its two consecutive modes have a fixed phase relationship. It means, the phase difference of the consecutive modes can be expressed by:

$$\varphi_q - \varphi_{q-1} = \varphi \tag{3-34}$$

When the modes phases are "locked" (φ is constant), the inference between the modes is constructive and otherwise is destructive. Thus, the short duration pulses

appear at the output of the laser cavity. However, the mode locking term originates from a description in the frequency domain. A short pulse is formed in the laser resonator when a fixed phase relationship is achieved between its longitudinal modes of the laser output. In Figure 3-39, a synthesis of a periodic pulse by superposition of sinusoidal oscillations with equally spaced frequencies, corresponding to different axial resonator modes in a mode-locked laser is simulated.

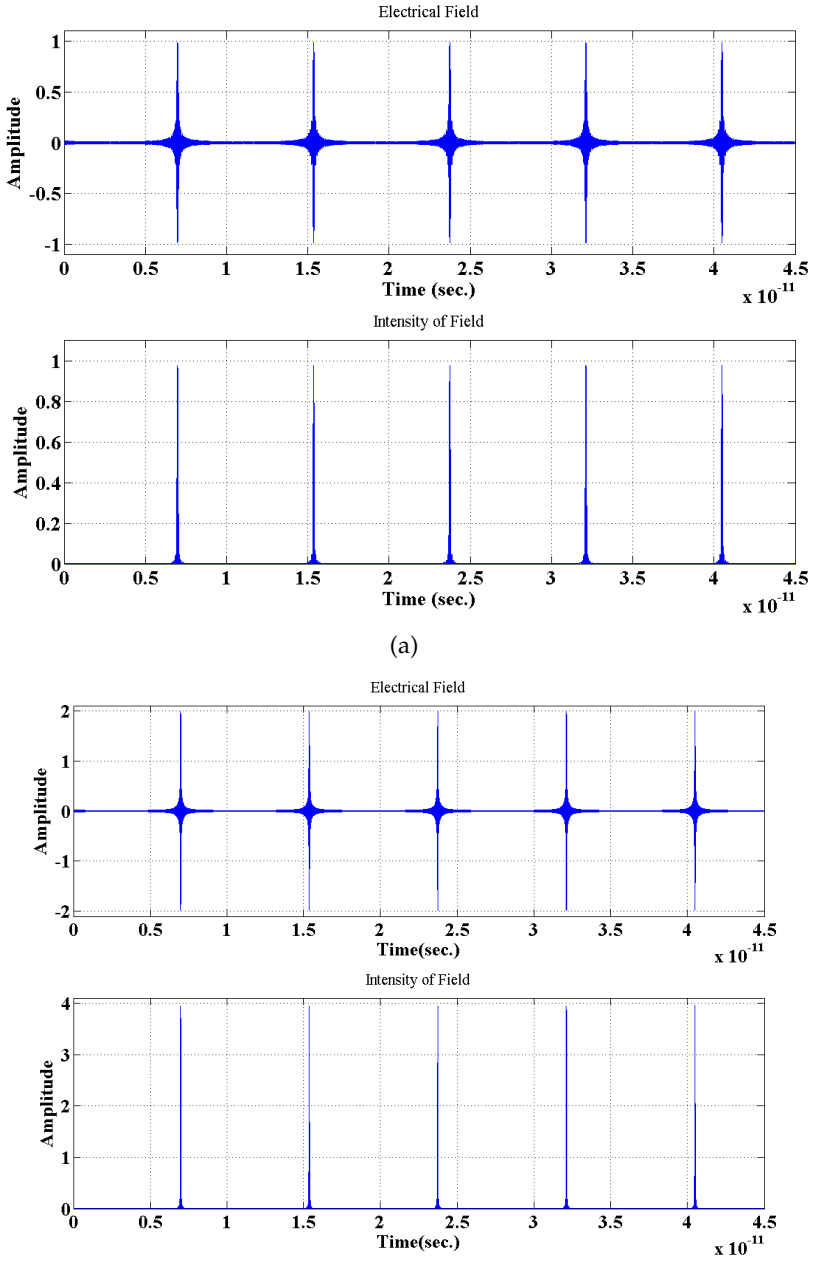

Figure 3-39: The mode-locking concept to generate short pulses (a): optical pulse electrical field and optical pulse intensity, number of interfered modes=100 (b): optical pulse electrical field and optical pulse intensity, number of interfered modes=200.

In this model, a laser cavity with $L_c = 200\mu m$ is modelled with including 100 and 200 interfered longitudinal modes and bandwidth $\Delta\lambda = 88.07nm$ around wavelength $1495.5nm$. It is clear that the pulse duration decreases when the number of modes is increased.

B) Mode Locking Techniques

There are two fundamental schemes to lock the modes that are classified into active and passive mode locking methods. Each mode locking methods can be performed in different ways that each of them has its specific advantages and disadvantages. In this subsection, these two main mode locking techniques are discussed concisely; more details of mode-locking techniques can be studied in [99-101].

B-1) Active mode locked Laser

Active mode Locked lasers involve the periodic modulation of the resonator losses or the round-trip phase change achieved. There are three main types of active mode locking: 1) Amplitude Modulation (AM) mode locking, 2) Frequency Modulation (FM) mode locking, 3) Synchronous pumping. In the first two methods, the mode locking is performed by using an electro-optical modulator that is integrated with the laser cavity [100]. In the third method, the mode locking is performed by periodic modulation of the laser cavity gain at the repetition rate equal to the fundamental cavity frequency [99]. If the modulation is synchronized with the resonator round trips, this can lead to the generation of ultra-short pulses usually with picosecond pulse durations. In most but not all cases, the pulse duration achieved is governed by a balance of pulse shortening through the modulator and pulse broadening via effects such as the limited gain bandwidth.

Figure 3-40 shows a sample structure of an active mode locked laser that includes four key parts: 1) gain medium, 2) full reflection mirror 3) partially reflection mirror 4) modulator; the first three parts are same as general lasers and the fourth part inserted to the medium close to the full reflection medium.

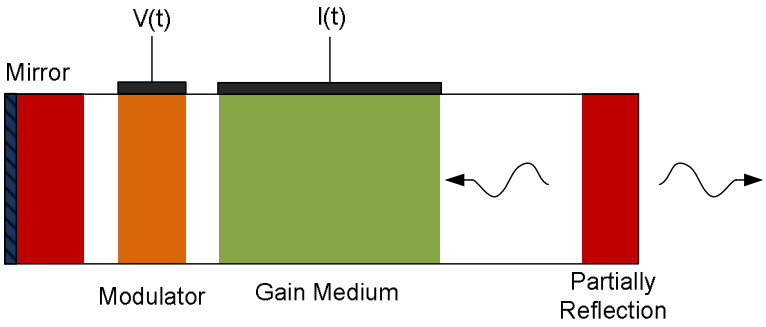

Figure 3-40: Schematic diagram of actively mode-locked laser.

B-2) Passive Mode-Locked Laser

The passive mode-locking is an all-optical nonlinear technique capable of producing optical pulses, without any active component inside the cavity. Passive mode-locked laser generates much shorter (about femtosecond) pulses by using saturable absorbers. A saturable absorber allows the high intensity waves to pass and absorbs the low intensity waves. Therefore it is driven by short pulses, which can modulate the resonator losses. The shorter pulses modulate the cavity medium loss faster which is provided shorter recovery time. Thus, a saturable absorber works much faster than an electronic modulator [101]. Furthermore, the pulse duration can be even well below the recovery time of the absorber. In some cases, reliable self-starting mode-locking is not achieved. In Figure 3-41 the similar structure of an active mode locked laser except the replacement of active electro-optical modulator with a passive optical absorber.

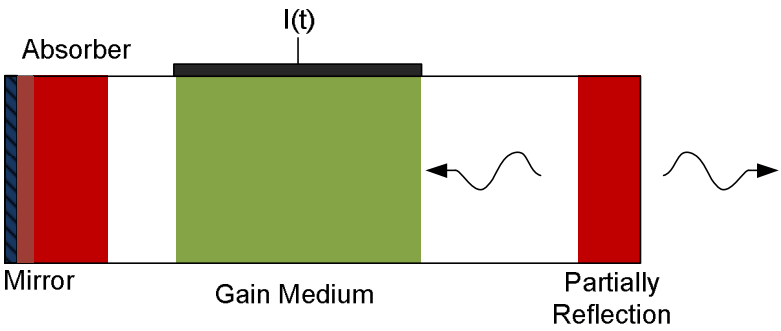

Figure 3-41: A passive mode-locked laser.

In some mode-locked lasers active and passive mode locking are applied simultaneously. Such hybrid mode-locked laser combines some key advantages, such fine controlled pulse repetition rate and fairly short pulses [99].

C) Mathematical Analysis

It is helpful to consider a simple model of mode locking in which all oscillating modes have equal amplitude, E_0 which is given by:

$$E(t) = E_0 \sum_{q=-n}^{n} \exp[i(\omega_q t + \varphi_q)] \tag{3-35}$$

Therefore, ω_q and φ_q can be writhen as:

$$\begin{cases} \omega_q = \omega_0 + q.\Delta\omega \\ \varphi_q = \varphi_0 + q.\phi \end{cases} \tag{3-36}$$

Where ω_0 is the angular frequency of a central mode, $\Delta\omega$ is the angular frequency spacing between modes, and φ_0 is the phase of the central mode and we assume is zero. Thus, the equation (3-33) can be rewritten as:

$$E(t) = E_0 e^{i\omega_0 t} \sum_{q=-n}^{n} e^{i(q\Delta\omega t + \varphi_q)} \tag{3-37}$$

Then, it can be expressed as:

$$E(t) = A(t) e^{i\omega_0 t} \tag{3-38}$$

Where

$$A(t) = E_0 \sum_{q=-n}^{n} e^{-iq(\Delta\omega t + \varphi)} \tag{3-39}$$

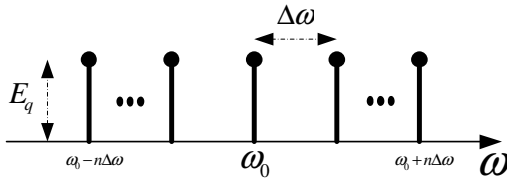

Figure 3-42: An approximation of uniform distribution of the modelled mode-locked laser impulse train's spectrum.

The spectrum of pulse train of the modelled mode locked laser is shown in Figure 3-42. In this model, an amplitude modulated wave oscillating at the central mode frequency ω_0 . If we assume $\Delta\omega t' \triangleq \Delta\omega t + \varphi$ and therefore, $A(t)$ can be given by [99]:

$$A(t') = \frac{\sin[(2n+1)\Delta\omega t'/2]}{\sin(\Delta\omega t'/2)} \tag{3-40}$$

Furthermore, the intensity of the wave field is related to the square of the field amplitude which is given by:

$$I(t) = \frac{1}{2} c\varepsilon_0 E^2(t) \tag{3-41}$$

Where ε_0 is the vacuum space permittivity, and c is the light speed in vacuum. Thus, the field intensity $I(t)$ is proportional to $|A(t)|^2$. Therefore, the $|A(t')|^2$ can be represented by:

$$I(t') \propto |A(t')|^2 = \frac{\sin^2[(2n+1)\Delta\omega t'/2]}{\sin^2(\Delta\omega t'/2)} \tag{3-42}$$

This function describes a periodic pulse trains which are equally spaced in time axis with very weak side lobe peaks around the main lobe as shown in Figure 3-43.

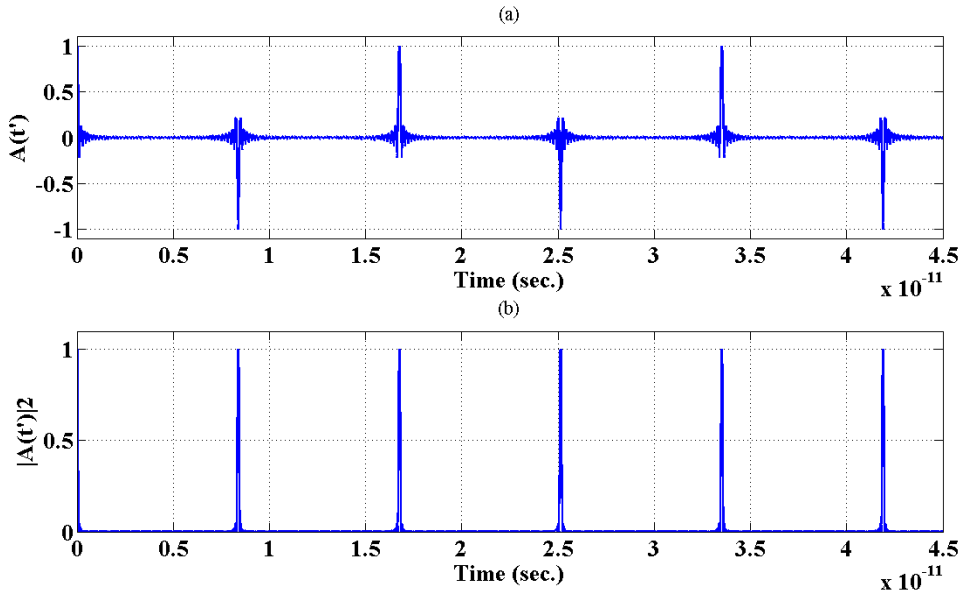

Figure 3-43: The waveform of mathematically constant amplitude approximated mode-locked Laser fields amplitude $A(t')$ and intensity $I(t')$ for 100 of interfered modes (a): the electrical field of optical pulses, (b): the intensity of optical pulses.

In addition to the simulation results in Figure 3-39, mathematical analysis proves that by increasing the number of modes the pulse duration decreases while its amplitude

increases. However, $\tau = \frac{2\pi}{\Delta\omega}$ expresses the period of the repetition of the pulses; therefore, the pulse Full Width at Half Maximum (FWHM), $\Delta\tau_{FWHM}$ can be given by:

$$\Delta\tau_{FWHM} = \frac{2\pi}{(2n+1)\Delta\omega} = 1/\Delta\upsilon, \tag{3-43}$$

Where $\Delta\upsilon'$ represents total oscillation bandwidth.

To calculate the intensity of the laser pulse, it is assumed that the oscillating modes have nonuniform amplitude distribution. This is a valid approximation for real ultra-short mode-locked laser pulses, where there are large numbers of closely spaced oscillating modes and their amplitude distribution usually has a Gaussian-like profile. The wave form of the field amplitude and intensity of mode-locked laser for 100 interfered locked modes and cavity length of $L_c = 10\mu m$ is shown in Figure 3-44. In this model, the cavity length is significantly short to show the magnitude fluctuation in shorter time duration of simulation.

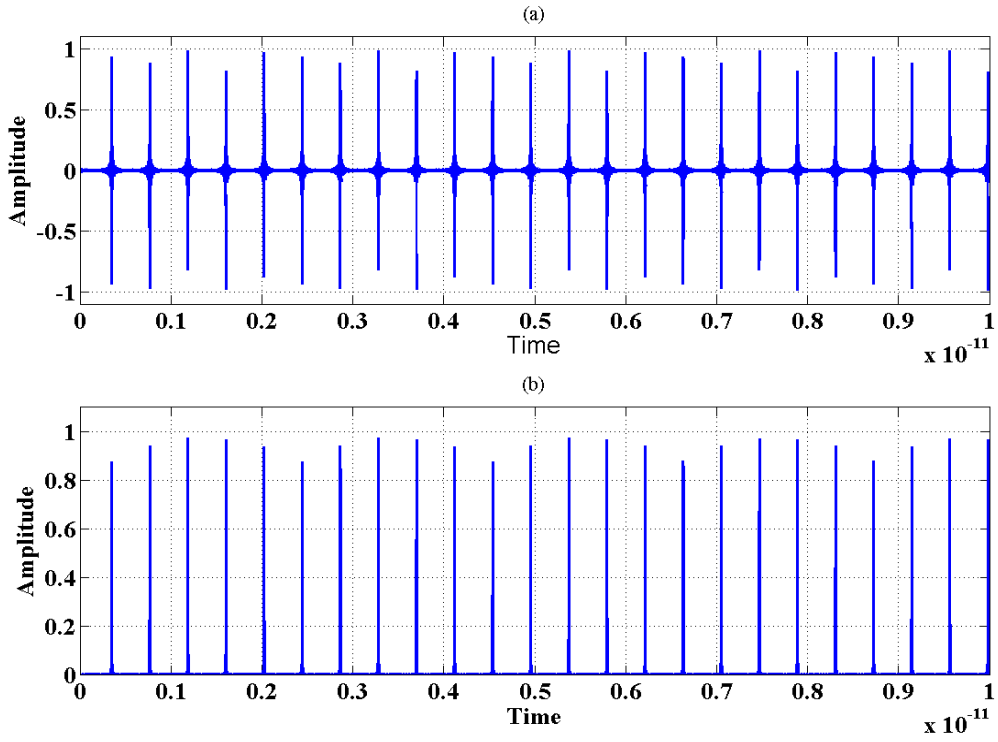

Figure 3-44: The waveform of Mode-Locked Laser field's amplitude $A(t')$ and intensity $I(t')$ of 100 of interfered modes (a): the electrical field of optical pulses, (b): the intensity of optical pulses.

Therefore, the field modes amplitude can be expressed by:

$$E_q^2 = E_0^2 \exp[-\left(\frac{2q\Delta\omega}{\Delta\omega_L}\right)^2 Ln2] \tag{3-44}$$

Where $\Delta\omega_L$ is the FWHM of the spectral bandwidth.

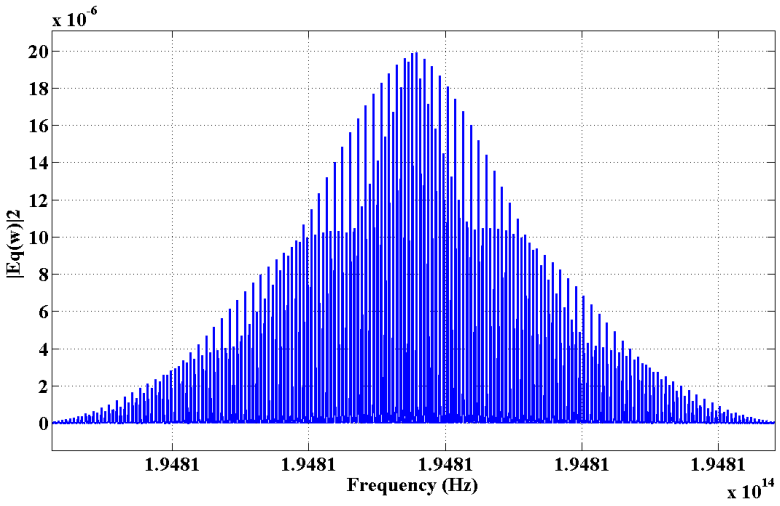

(a)

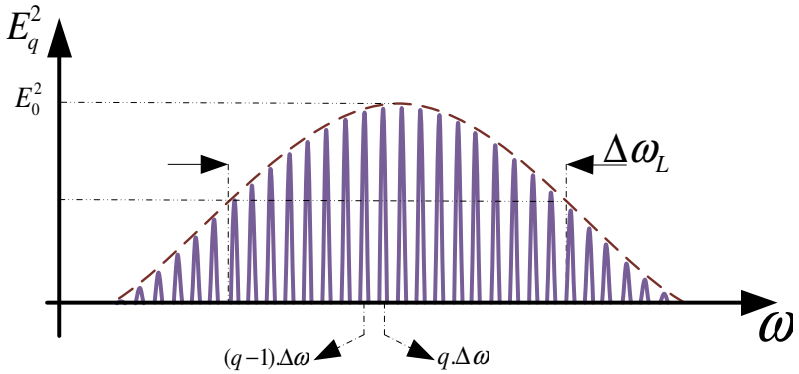

(b)

Figure 3-45: Mode locked laser output modes spectrum amplitude: (a) simulated for 100 interfered modes around, (b): Gaussian distribution approximation.

The mode-locked-laser output modes amplitude for the Gaussian approximation is shown in Figure 3-45 for a 100 interfered longitudinal modes into a laser cavity with $L_c = 200\mu m$ bandwidth $\Delta\lambda = 88.07nm$ around central wavelength $1495.5nm$. The simulation result demonstrates that the modes spectrum distribution function is Gaussian. In this case, the expression of $A(t')$ can be written by $A(t') = \sum_{q=-\infty}^{+\infty} E_q e^{iq\Delta\omega t'}$.

Then it can be approximated as an integral expression by:

$$A(t) = \int E_q e^{iq\Delta\omega t} dq \tag{3-45}$$

This integral is an Inverse Fourier Transform. Thus, in the time domain the amplitude of a multi-mode output is given by the transform of the amplitude distribution of modes in the frequency domain. Therefore, the mode-locked oscillating modes spectrum with a Gaussian distribution of amplitude will result in Gaussian pulse in time domain which is given by:

$$\left|A(t)\right|^2 = \exp[-Ln2(\frac{2t}{\Delta\tau})^2] \tag{3-46}$$

Furthermore, the duration of the FWHM of the pulse is given by:

$$\Delta\tau_{FWHM} = \frac{2Ln2}{\pi\Delta\omega_L} = \frac{0.441}{\Delta\omega_L} \tag{3-47}$$

D) Mode Locked Laser Modelling

Based on the analysis in section 3.5.3.1 (C), the mode locked laser (MLL) pulses can be approximated as Gaussian periodic pulses with FWHM about $\Delta\tau_{FWHM}$ and repetition rate τ that is shown in Figure 3-46. Figure 3-46 (a), shows the modelled pulse with side lobs around the main lobe. However, because of the significant differece between the intensity amplitudes of the pulse main lob and first side lobs, the side lobes intensity effects could be neglected. Therefore, the modelled laser pulses can be considered as Gaussian pulse train that is depicted in Figure 3-44 (b). Therefore, to model the MLL in the proposed ADC, an AM-mode locked laser is modelled that the modulator is inserted in the cavity to modulate the cavity loss. The loss modulation causes amplitude modulation of the electrical field of the mode $E_q(t)$, which is given by:

$$E_q(t) = E_0[1 - (\frac{m}{2})(1 - \cos(\omega_m t)]\cos(\omega_q t + \varphi_q) \tag{3-48}$$

Where ω_m is the modulated signal frequency, m is the modulation index and the mode locking condition can be satisfied, if $\omega_m = \Delta\omega$ [99].

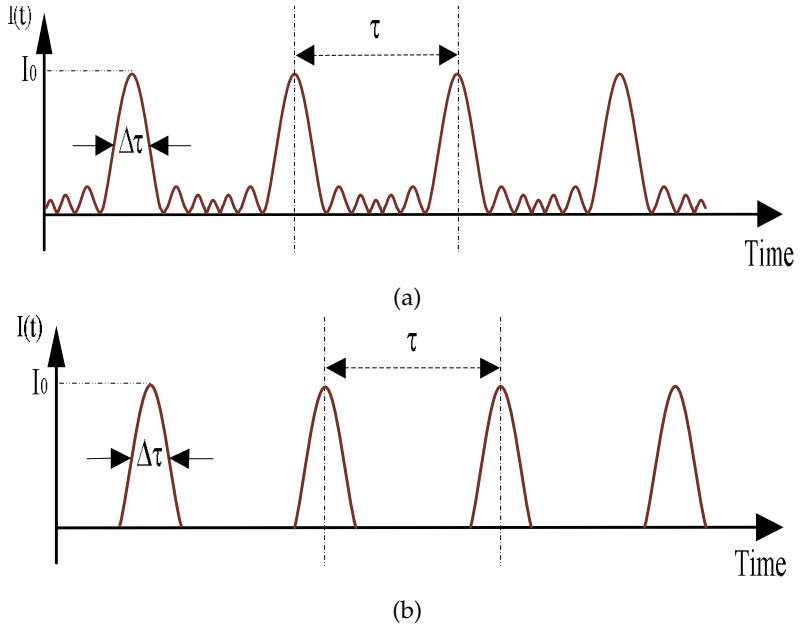

Figure 3-46: MLL output Gaussian pulse train with equal amplitude approximation (a) with including the side lobs around the main lob, (b) with excluding the side lobes.

However, for simulating the MLL, some other physical impairment such as phase and amplitude noises must be included to evaluate the system's performance in the conditions very close to those MLL pulses. The particular noises of mode locked lasers are: 1) timing jitter, 2) optical phase noise and 3) carrier envelop offset noise. These types of noises mainly originated from the effects of mechanical vibration, thermal effects in the laser cavity, and the quantum fluctuations [102]. Therefore, various mechanisms for mode locking can exhibit various kinds of instabilities. For instance, a laser generates multiple pulses with unstable spacing, pulses with unstable energy. As all those noises are coupled according to the physical mechanism and they lead noise correlation [102][103]. Therefore, the electrical field can be assumed with included the amplitude and phase noises. Thus, based on that assumption equation (3-48) can be rewritten:

$$E_q(t) = (E_0^{'} + S_n)\cos(\omega_q^{'} t + \varphi_q^{'} + \phi_n) \tag{3-49}$$

Where $E_0^{'}, \omega_q^{'}$, and $\varphi_q^{'}$ are the MLL modes amplitude, frequency and phase, respectively, and S_n and ϕ_n are the included noises on the modes amplitude and phase, respectively. In Figure 3-47, a model is proposed to simulate an active MLL system.

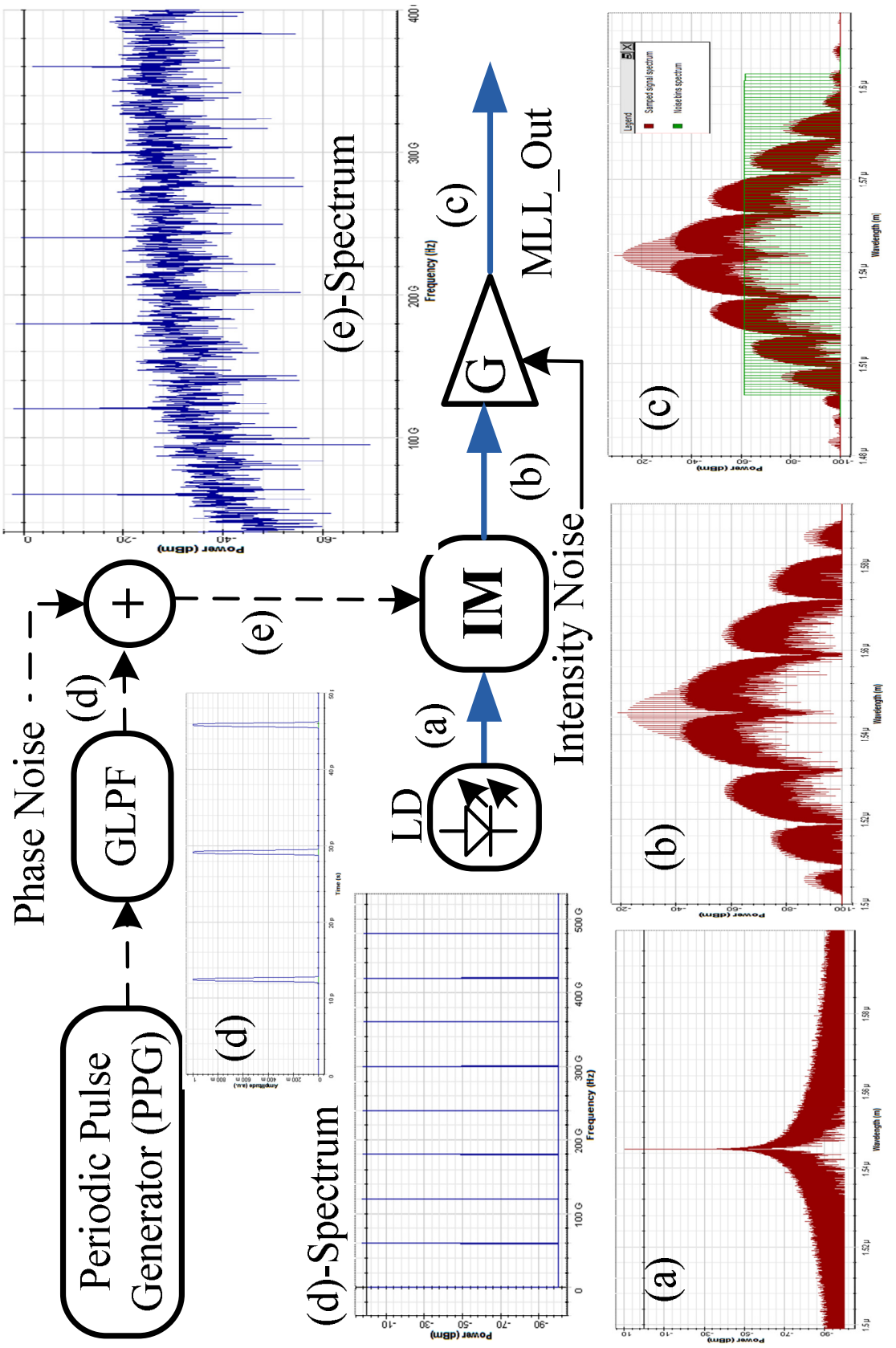

Figure 3-47: The simulated model of the active mode locked laser to include timing jitter and optical phase and amplitude noises.

In this model, a Periodic Pulse Generator (PPG) generates a sequence to model periodic short Return to Zero (RZ) pulses. The periodic pulses are passed through a Gaussian LPF (GLPF) with 3-dB bandwidth equal to the digital signal bandwidth of the RZ pulses for Gaussian shaping purpose of them. The pulse waveform and its power spectrum are given by Figure 3-47 (d). Then, the output of the GLPF is fed to an adder's input, whereas the Gaussian random phase noise is added to it. By representing timing jitter in terms of phase perturbation, the phase error (advance or retard) can be denoted with the function $\varphi_j(t)$, so the Gaussian pulse stream $S_j(t)$ affected by timing jitter that can be given by:

$$S_j(t) = P_G[2\pi f_d t + \varphi_j(t)] \tag{3-50}$$

Where P_G is a sequence of periodic Gaussian pulses and f_d is the data rate frequency. Since the $\varphi_j(t)$ is in radians, dividing $\Delta\varphi$ (peak or rms) by 2π expresses jitter in terms of either the Unit Interval (UI), or bit period

$$J(UI) = \frac{\Delta\varphi}{2\pi} \tag{3-51}$$

Furthermore, dividing the jitter in unit intervals by the frequency of the pulse or multiplying by the bit period yields the jitter in units of time [104]

$$J(t) = \frac{\Delta\varphi}{2\pi f_d} \tag{3-52}$$

This added phase noise causes random and deterministic timing jitter on the zero crossing of the random data sequence [9][10][128]. Figure 4-37 (e) gives the power spectrum of the signal with added rms jitter 0.06 bit period and total random and deterministic jitter about 0.258 of bit period for sequence rate about 60 Gbps. The SNR of the fundamental 60 GHz signal is reduced from 100 dB to 39 dB. Therefore, the NF of this block prior to feeding to an intensity modulator is about 61 dB. The phase distorted Gaussian pulses are modulated onto an optical continuous wave (CW) carrier using an intensity modulator (IM). The optical CW carrier is generated by a laser diode (LD) with 10 MHz linewidth, 1554 nm wavelength, 10 dBm power

and Optical Signal to Noise Ratio (OSNR) about 110 dB in Figure 3-47 (a). Furthermore, the OSNR at the output of IM is about 94.7 dB in Figure 3-47 (b). The Figure 3-48 gives the amplitude and phase of electrical field of the optical signal in time domain.

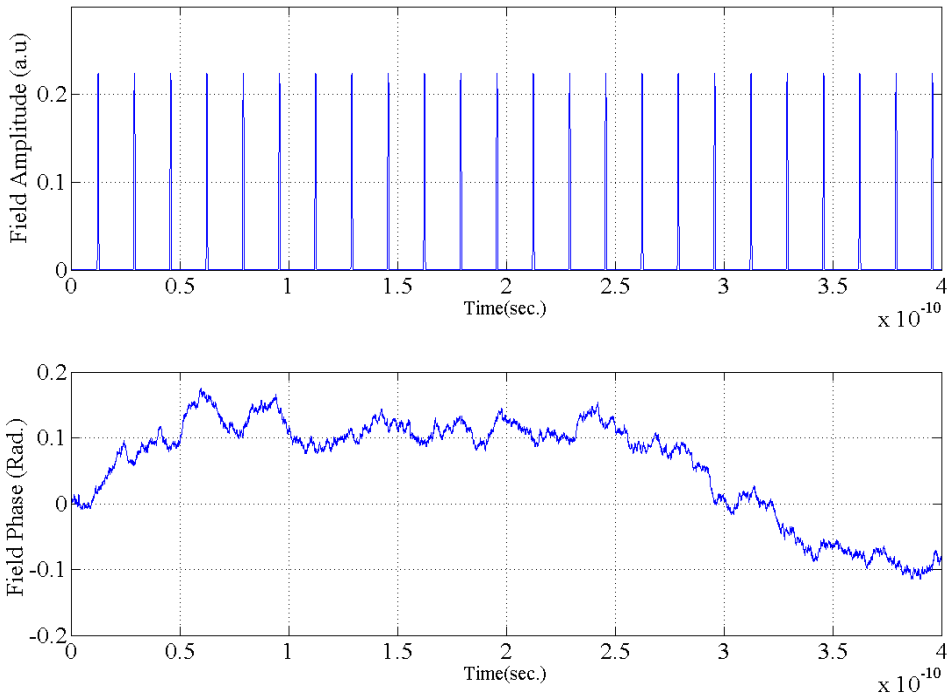

Figure 3-48: The modelled optical signal field amplitude and phase at point (b).

To add the amplitude noise to the modulated signal, the IM output is amplified by an optical amplifier with gain G that its gain is 10 dB, and Noise Figure (NF) about 4 dB. The OSNR at the output of amplifier is about 18.7 dB which its power spectrum is shown in Figure 4-37 (c). In this Figure, the noise floor is about -60 dBm which is illustrated by green line.

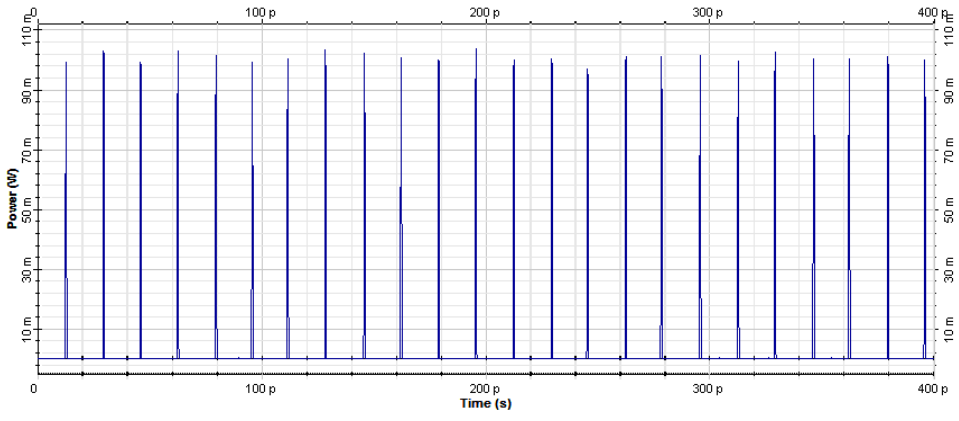

Figure 3-49: The signal power at the output of mode-locked laser with added phase and amplitude noise.

Figure 3-49 gives the output signal power of the modelled mode locked laser where its average power is about 100 mW. Figure 3-50 shows the eye diagram of the signal at the output of modelled MLL with rms timing jitter about 0.011 of the bit period and total random and deterministic jitter about 0.027 of the bit period for sequence rate about 60 Gbps with about 67.7% of the eye opening height.

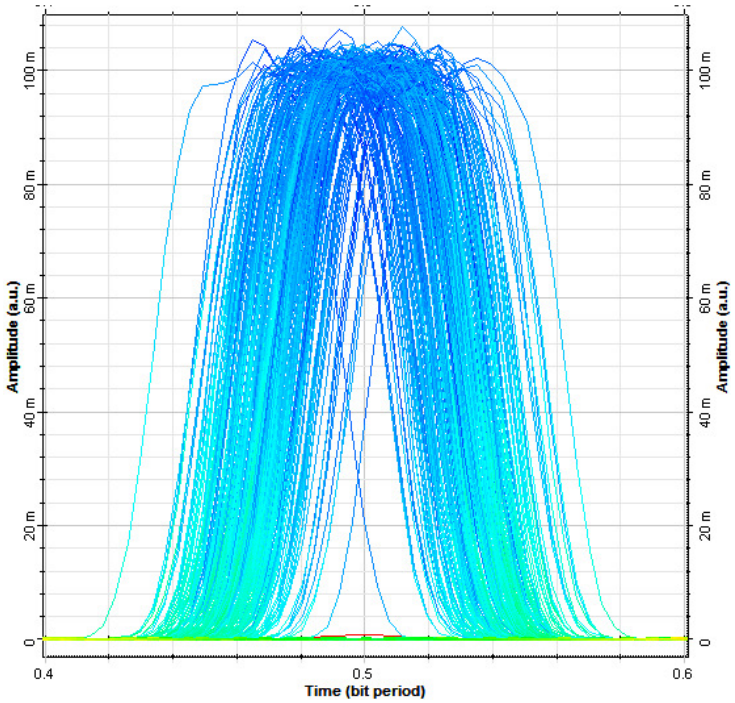

Figure 3-50: An eye diagram of the modelled MLL's output signal with rms timing jitter about 0.011 (UI) for 60 Gbps sequence rate.

3.5.3.2. Electro-Optical Modulator

An electro-optical modulator (EOM) is a key component of the PADC. In the proposed system, a MZM has been used as a modulator and a sampling component, which its transfer function is given by:

$$E_{out}(t) = E_{in}\cos(\frac{V(t)\pi}{2V_{\pi}}) \tag{3-53}$$

Where $E_{out}(t)$ is the modulated electrical field at the output of the MZM and E_{in} is the amplitude of electrical field of the input optical carrier that is generated by the modelled MLL diode which is launched to the MZM input. Where $V(t)$ is the voltage of an applied RF signal and V_{π} is a half-phase voltage [105][106]. Based on equation

(3-35), it is assumed in that the optical field at the input of the MZM which is launched by laser diode can be represented by:

$$E_{in}(t) = E_0 \sum_{q=-n}^{n} \exp[i(\omega_0 + q\Delta\omega)t] \tag{3-54}$$

Where E_0 and ω_0 denote the amplitude and angular frequency of the electrical field of the optical carrier, respectively. Furthermore, it is assumed a sample single tone RF carrier can be given by:

$$x_{RF}(t) = A_c.\cos(\omega_c t + \varphi_c) \tag{3-55}$$

Both A_c and φ_c, the amplitude and the phase values of the RF carrier are constant, Substituting equation (3-55) in (3-53), the optical field at the output of the MZM can be expressed by:

$$E_{out}(t) = E_0\{\sum_{q=-n}^{n} e^{i(\omega_0+q\Delta\omega)t}.Cos(U.\cos(\omega_c t + \varphi_c))\} \tag{3-56}$$

Where U is the modulation index equals to $\frac{A_c\pi}{2V_\pi}$. By using the Bessel function [6], to expand the element inside of the braces, the output electrical field can be rewritten as:

$$E_{out}(t) = E_0 \sum_{q=-n}^{n} e^{i(\omega_0+q\Delta\omega)t}.[J_0(U) + 2(\sum_{k=1}^{\infty}(-1)^k J_{2k}(U).Cos(2k\omega_c t + 2k\varphi_c))] \tag{3-57}$$

Where $J_k(U)$ denotes the Bessel function and for any integer k

$$J_k(U) = \frac{1}{\pi}\int_0^{\pi} Cos(U.\sin\theta - k\theta)d\theta \tag{3-58}$$

Therefore, the sampled output signal of the MZM in the proposed PADC at $t = m.\tau$ can be given by:

$$E_{out}(t) = E_0 J_0(U)\sum_{q=-n}^{n} e^{i(\omega_0+q\Delta\omega)t} + 2E_0\sum_{q=-n}^{n} e^{i(\omega_0+q\Delta\omega)t}\sum_{k=1}^{\infty}(-1)^k J_{2k}(U).Cos(2k\omega_c t + 2k\varphi_c) \tag{3-59}$$

By defining the second term of equation (3-59), $E_{Mod}(t)$ can be expressed by:

$$E_{Mod}(t) \triangleq E_0 \sum_{q=-n}^{n} \sum_{k=1}^{\infty} (-1)^k e^{i(\omega_0 + q\Delta\omega)t} J_{2k}(U).Cos(2k\omega_c t + 2k\varphi_c) \quad (3\text{-}60)$$

As $\omega_q = \omega_0 + q\Delta\omega$ and if we define $\omega_k \triangleq 2k\omega_c$ and $\varphi_k \triangleq 2k\varphi_c$, then by expanding the terms in equation (3-60), the $E_{Mod}(t)$ can be given by:

$$E_{Mod}(t) = \frac{E_0}{2} \sum_{q=-n}^{n} \sum_{k=1}^{\infty} \{(-1)^k J_{2k}(U).[e^{i(\omega_q + \omega_k)t + \varphi_k} + e^{i(\omega_q - \omega_k)t - \varphi_k}] \quad (3\text{-}61)$$

Therefore, the output electrical field is given by:

$$E_{out}(t) = E_0 J_0(U) \sum_{q=-n}^{n} e^{i\omega_q t} + 2E_{Mod}(t) \quad (3\text{-}62)$$

The first term of equation (3-62) is the MLL optical carrier and the second term discuses the sidebands of the sampled RF signal. As represented in this equation, the nonlinearity of the MZM modulator produces infinite terms of signal spurious band. Consequently, the field, $E_{out}(t)$ of the sampled signal at the output of the MZM at $t = m\tau$ can be given by:

$$E_{out}(t)\big|_{t=m\tau} = E_0 e^{i\omega_m t}[J_0(U) + \sum_{k=1}^{\infty} (-1)^k J_{2k}(U).(e^{(i\omega_k t + \varphi_k)} + e^{-(i\omega_k t + \varphi_k)})] \quad (3\text{-}63)$$

It shows the electrical field of the sampled signals at the output of the MZM includes some harmonic signals which are induced by nonlinearity of the MZM. The amplitude of the electrical filed is related to the Bessel function coefficient. This harmonics causes some fluctuation on the fundamental signal amplitude which is occurred as spur signals in the spectrum of the signal.

3.5.3.3. Optical Hard-Limiter

In this section a proposed Optical Hard Limiter (OHL) with integrated wavelength conversion (WC) is discussed. The sampled signal by a MZM that is represented by equation (3-63) is fed to a splitter which is split symmetrically which is shown in Figure 3-38. The OHL receive the split optically sampled signal from the splitter's output.

In General optical limiters are nonlinear devices which have linear transfer function at low intensities and strongly attenuate the beam at high intensities to mitigate the impact of high intensities light beam based on different optical physical properties [107-115]. The OHL function in this work is completely different with the general purposed optical limiter. Here, an optical limiter behaves like an optical comparator and switches simultaneously. Therefore, if the input signal power is higher than a defined threshold level the signal with specific power will be transmitted at the output. But, if the input signal is less than the threshold level it will be attenuated at the output significantly. The proposed architecture is deisgned based on an optical limiter using Self-Phase Modulation (SPM) [116-118] which is shown in Figure 3-51.

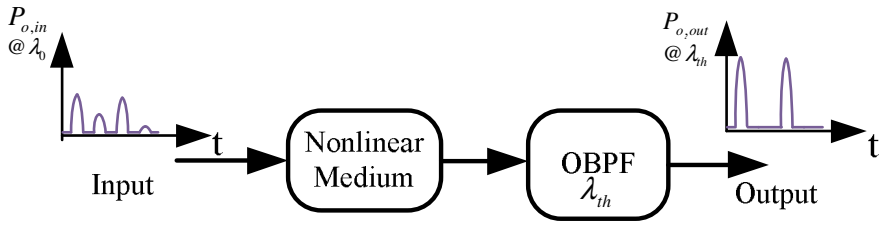

Figure 3-51: an optical limiter based on SPM.

In this architecture, an input pulse is fed to a nonlinear medium with specific power. Thus, because of the SPM, the spectrum of the signal has been broadening proportional to the intensity of the input pulse. In this model, a nonlinear medium can be a Highly NonLinear Fibre (HNLF) [119-121] or a Semiconductor Optical Amplifier (SOA) [122] and the signal can be preamplified by an EDFA to provide enough power to meet the SPM phenomenon criteria. Because of the longer carrier recovery time limitation of the SOA, it is not suitable for very high data rate[118][119]. The quasi-instantaneous response time of Kerr nonlinearities in optical fibres makes the scheme directly applicable to high bit-rate operation. Therefore, the HNLF could be more suitable for the proposed architecture [118].

The proposed integrated optical limiter with wavelength converter (WC) is given in Figure 3-52. As shown in this figure, the input signal is fed to an EDFA with gain G_1 to amplify the input pulses at the specific level which is satisfy the requirement to compare input power level with the P_{th}. The amplified pulses are launched into the

HNLF1. Recalling SPM from chapter 2, in this medium SPM phenomenon is broaden the signal spectrum proportional to the input pulse intensity. The input optical pulse frequency at the leading edge of pulse shifts to lower frequency and the frequency at the trailing edge shifts to higher frequency, the amount of frequency change $\Delta\omega$ caused by SPM is given by:

$$\Delta\omega = -\frac{\Delta\varphi}{\Delta t} = -\bar{\gamma}\left|E_{out}(t)\right|^2_{Max} L_{eff} \frac{\Delta(\left|E_{out}(t)\right|^2)}{\Delta t} \tag{3-64}$$

Where $E_{out}(t)$ is the wave filed at the MZM output, $\left|E_{out}(t)\right|^2_{Max}$ the pulses peak power at the splitter output which is preamplified by an optical amplifier to compensate the splitter insertion losses, L_{eff} is the effective length of propagation medium and $\bar{\gamma}$ is the fibre nonlinearity. Therefore, $\lambda_{th} \triangleq \lambda_0 \pm \Delta\lambda_{th}$ is the wavelength which is broadened spectrum of the corresponding to the specific threshold power level P_{th}. Thus, considering the central wavelength of the Optical Bandpass Filter (OBPF) at the offset spectral broadening $\lambda_{th} = \lambda_2$, the output power of the optical limiter, $P_{L,o}(t)\big|_{t=m\tau}$ can be given by:

$$P_{L,o}(t) = \begin{cases} P_h & P_{sp}(t) \geq P_{th} \\ P_l & otherwise \end{cases} \tag{3-65}$$

Where $P_{sp}(t)$, P_h and P_l represent splitter output power, the limiter output high and low constant power levels, respectively, while $P_h >> P_l$ and $P_l \approx 0$.

In the given design of the Figure 3-52, the output of $P_{L,o}$ of the OHL is represented at wavelength λ_2 that can be met the requirement of the proposed FP-DRoF link for WDM network in chapter 5, to transmit each quantized bit of the PADC with an individual wavelength throughout the fibre link. However, a 1-bit DAC is designed to perform a mathematical subtraction operation of the pipelined scheme in the second stage to quantize the LSB as given in Figure 3-56, whereas the wavelength conversion is an essential issue. In the proposed system, WC based on SPM is integrated with optical signal comparator and limiter. In the Figure 3-52 of the WC

system, the output signal of the comparator and the limiter block at wavelength λ_2 is amplified using the EDFA with gain G_2 and the amplified power is launched into the HNLF2 followed by the OBPF filter at wavelength λ_0. Therefore, the signal wavelength is converted from λ_2 to λ_0 which is given at the output $P_{WC,o}$ of the OHL.

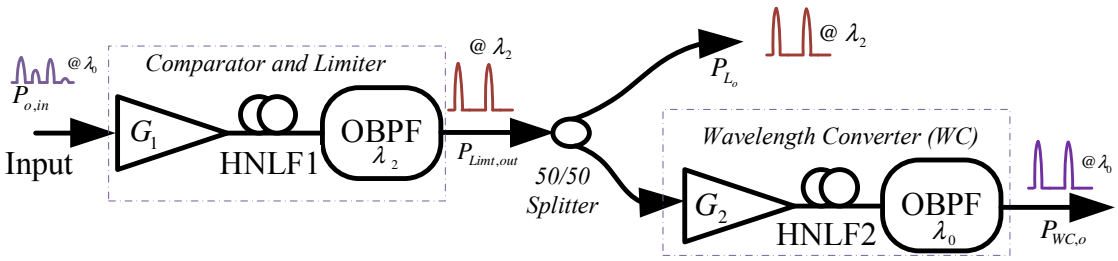

Figure 3-52: The proposed OHL with an integrated optical limiter and wavelength converter.

The parameters of simulated model of the OHL are given as follows: the input pulse wavelength is 1545nm, G_1 is the gain of the EDFA for a 5m fibre length, the fibre core radius is 2.2 µm, Er doping radius 2.2 µm, Er metastable lifetime 10 ms, numerical aperture 0.24, Er. Ion density is 10e+24, loss at 1550nm about 0.1 dB/m, loss at 980nm about 0.5 dB/m, forward pump power 100mW, forward pump wavelength 980nm, backward pump wavelength 980nm, noise dynamic 3dB, and HNLF1 parameters are fibre length 0.8km, attenuation 1.8471 dB/km, dispersion -0.1ps/nm.km, effective area 11.5 µm^2, n_2 about 35.46e-21 m^2/w, OBPF wavelength $\lambda_2 = 1560\ nm$, bandwidth about 1nm-3nm. Based on equation (3-64), there are three choices to set the threshold power level of the limiter such as changing the EDFA gain, HNLF parameters, and OBPF wavelength and bandwidth. Based on the relationship between the broadened pulse spectrum and the detuned OBPF position, three possible regimes for the transfer function can be identified [118] as 1) non-monotonous, 2) locally flat region, 3) purely monotonous.

The transfer function of the modelled optical limiter is given in Figure 3-53. As shown, the transfer function slope changes with increasing the OBPF bandwidth from 1nm to 3nm. However, the output power decreases when the input power is increased beyond the limited level.

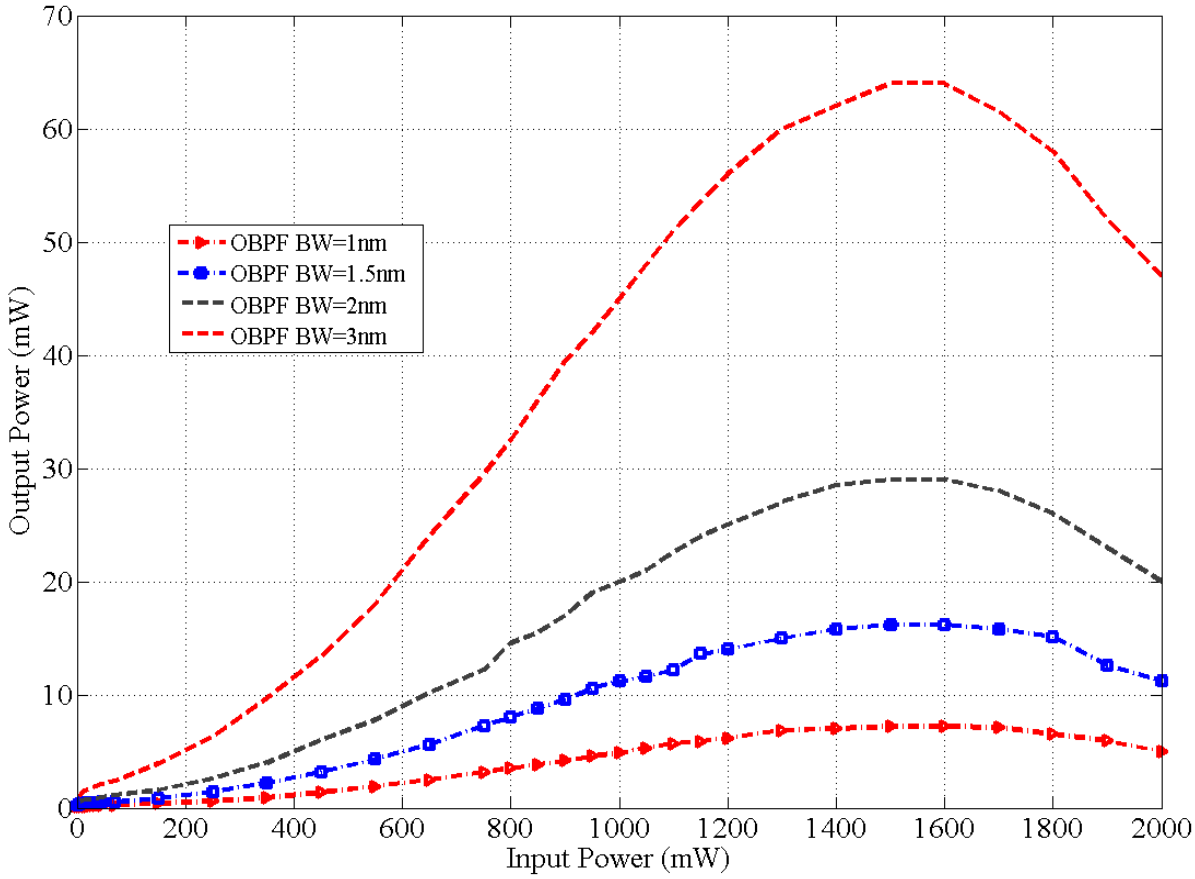

Figure 3-53: The non-monotonous transfer function of the optical limiter.

The maximum phase shift of SPM ϕ_{Max} can be given by:

$$\phi_{Max} = \bar{\gamma}\left|E_{out}(t)\right|^2_{Max} L_{eff} \tag{3-66}$$

Around the "critical point" that the SPM induced phase changes about π radians the self-phase modulated pulse power starts to oscillate versus frequency [100]. Thus, the output of OBPF1 significantly changes beyond the π radians which is induced by input signal intensity. Figure 3-54 gives the output of HNLF1 spectrum changes versus the wavelength. The spectrum is broadening proportionally by increasing the input signal power. However, for an excess input power more than the "critical point" power, the power spectrum significantly fluctuates versus wavelength which is directly impact on the offset filter (OBPF1) output. The impact of this phenomenon is shown in transfer function of optical limiter in Figure 3-53.

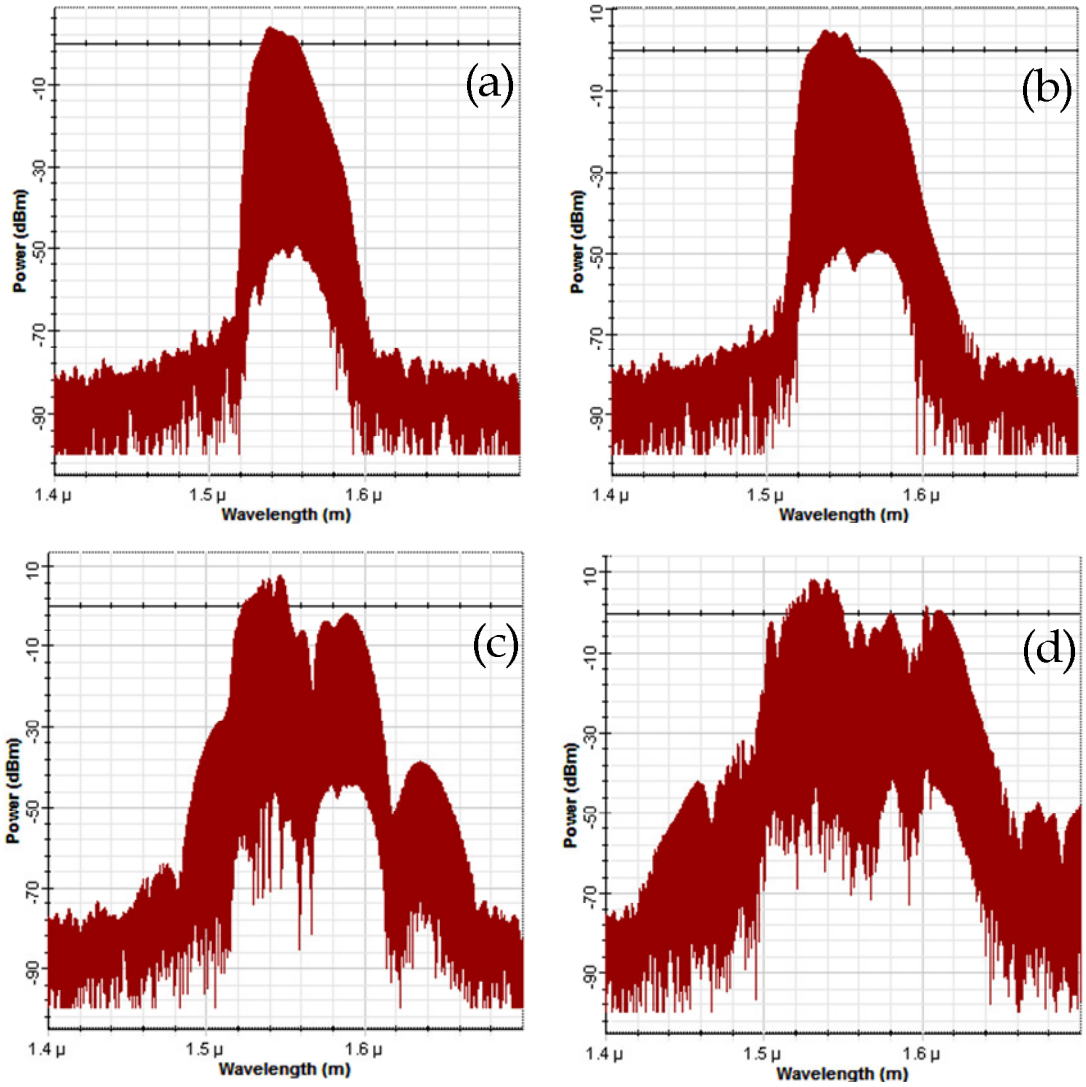

Figure 3-54: The output spectrum of the HNLF1 versus changing the input power into the optical limiter system, (a) input power 1 W, (b) input power 2 W, (c) input power 3 W, (d) input power 5 W.

By changing the system parameters, the transfer function could be optimized to the type (2) like a locally flatted transfer function. Thus, by changing the HNLF1 nonlinear index n_2 to 0.100462e-18 m^2/w and EDFA fibre length, the P_{th} and the transfer function slope changes as it is shown in Figure 3-55. It is clear that the transfer function based on this designed criteria represents the preferred operational regime. However, to assess the optical limiter performance, the impact of different gain of the EDFA by changing the lengths of the amplifier fibre is investigated. This transfer function represents a suitable optical limiter that can be used as an optical quantizer in the proposed PADC architecture.

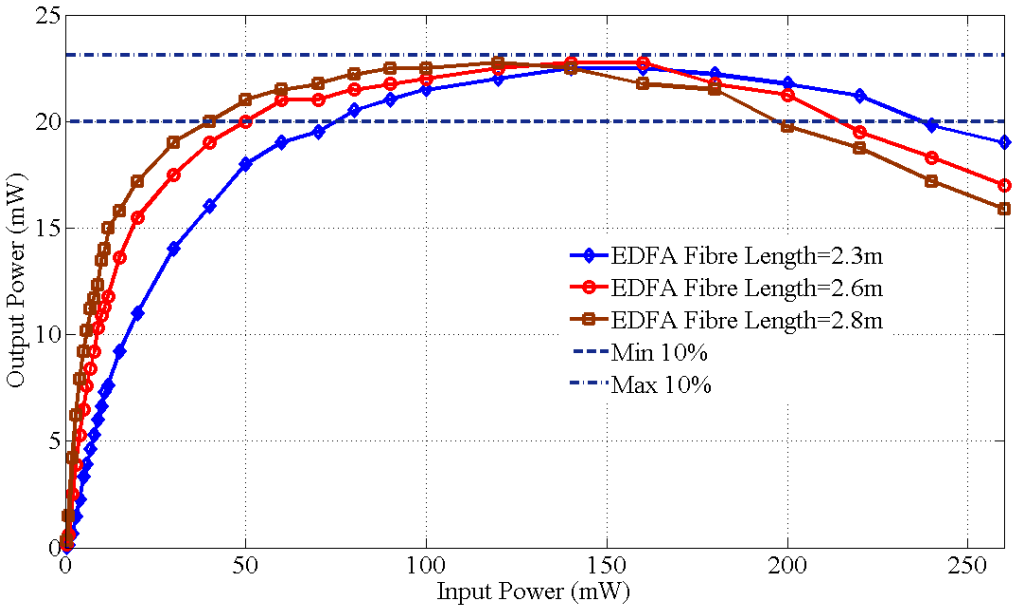

Figure 3-55: The locally-flat transfer function of the optical limiter.

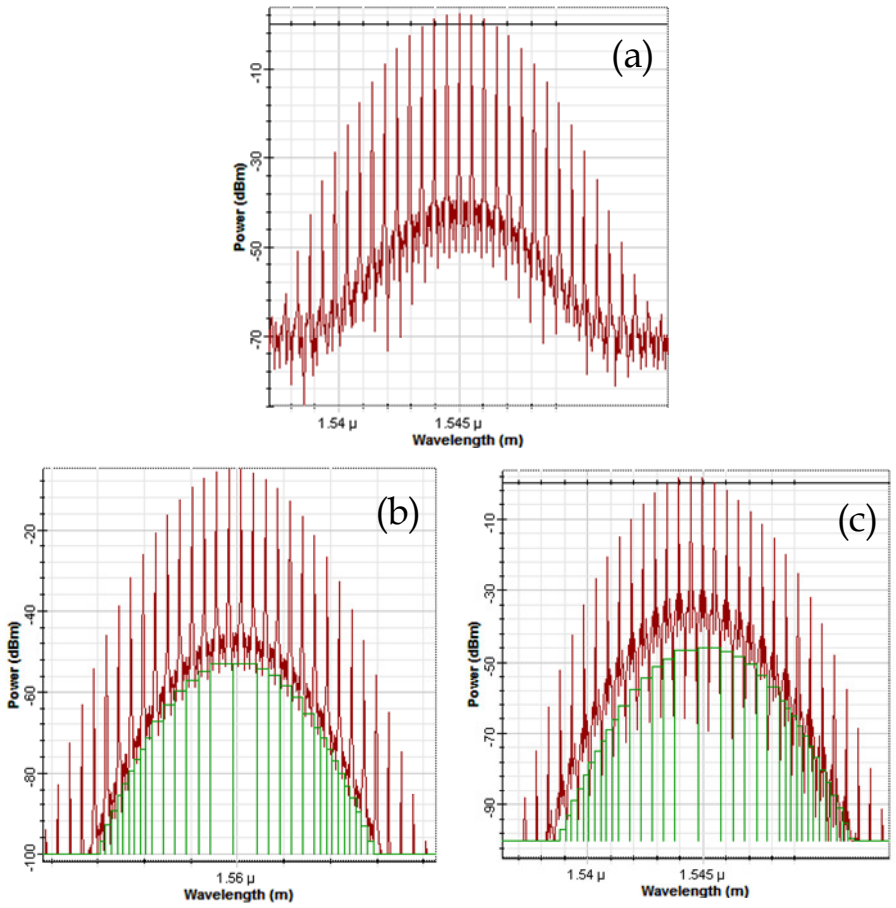

Figure 3-56: The signals spectrum of OHL (a): a sample MLL pulse with 65 GHz repetition rate at $\lambda_0 = 1545\ nm$, (b) the output spectrum of optical comparator and limiter $P_{L,o}$ at $\lambda_2 = 1560\ nm$ (c) the output spectrum of wavelength converter at $\lambda_0 = 1545\ nm$.

Figure 3-56 gives the signal spectrum of the OHL. However, for wavelength conversion, the second stage of the OHL performs like as the first stage of the optical comparator and limiter. Depending on the first stage parameters (wavelength), by changing G_2 the gain of the EDFA, the fibre length and the nonlinearity factor of the HNLF2 of the second stage, the pulse wavelength can be converted into a specific wavelength $\lambda_0 = 1545nm$. The fibre length of the EDFA with gain G2 in the simulated model is 5 m, the central wavelength of $OBPF_2$ is $\lambda_0 = 1545\ nm$ and the optimized bandwidth is about 3nm.

3.6. 2-Bit PADC System Simulation and Discussion

The fully photonic model of 2-bit PADC system is shown in Figure 3-57. In this model, the optical pulse is generated based on the simulated model of MLLD which is fed to a dual drive MZM with splitting ratio 1.3, bias voltage1 -2.8 V and bias voltage2 -1.1 V. This EOM samples the input electrical RF signal and modulated it onto the optical carrier. The sampled optical signal at the output of MZM is amplified using an optical amplifier with 6 dB gain and NF is 4 dB. The amplified sample sequence is split into two parts SP1 and SP2. The amplifier is used to compensate the power division proportion rate of the splitter and its insertion loss by pre-amplifying the samples at the output of the MZM.

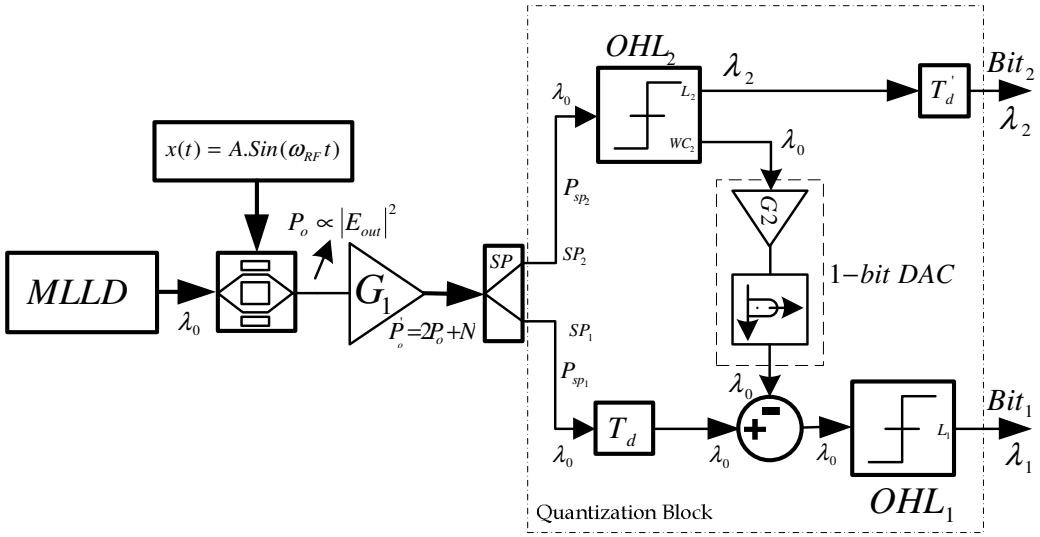

Figure 3-57: The all-optical model of the 2-bit PADC.

The outputs power of splitter which are symmetrically split can be given by:

$$P_{SP2}(t)\Big|_{t=m\tau} = P_{SP1}(t)\Big|_{t=m\tau} = \frac{P_o^{'}(t)\Big|_{t=m\tau}}{2} \tag{3-67}$$

Where $E_{SP}^2(t)\Big|_{t=m\tau} \propto P_{SP}(t)\Big|_{t=m\tau}$ and E is the electrical field of the optical wave. The splitter output signals are fed to an all-optical pipelined quantization block. The quantization block has the following sub-blocks: OHLs, a 1-Bit DAC and an optical subtractor. The OHL architecture is discussed in previous section. The two splitter outputs correspond to the number of quantization bits.

The SP2 power, P_{SP_2} is fed to the input of OHL2 to perform the quantization of the PADC most significant bit, Bit2. The OHL2 threshold level has been setup based on the half-magnitude of the full-scale amplitude of electrical field at the output of the splitter which is a proportion of the input electrical signal amplitude. Therefore, comparing the input signal power $P_{SP2}(t)$ with the threshold level $P_{th-Bit2}$ the electrical field amplitude $\left|E_{Bit2}^2(t)\right|$ of the digital output and recalling from equation (3-65), the electrical field of the MSB can be expressed by:

$$\left|E_{Bit2}^2(t)\right|_{t=m\tau} = \begin{cases} \left|E_h^2\right| & P_{SP2}(t) \geq P_{th-Bit2} \\ \left|E_l^2\right| & otherwise \end{cases} \tag{3-68}$$

Where $\left|E_{Bit2}^2(t)\right| \propto P_{Bit2}(t)$, if the input signal power $P_{SP2}(t)$ was greater than $P_{th-Bit2}$. Then the corresponding output bit $P_{Bit2}(t)$ is 'one= P_h', otherwise it is equal 'zero= P_l'.

The OHL2 has two digital outputs L_2 and WC_2. The output WC_2 wavelength is identical with the input wavelength λ_0 to be used for quantization process and L_2 with wavelength λ_2 is for WDM application to transport the digital data through the fibre link. However, the output with identical wavelength λ_0 is passing through a 1-bit DAC. The 1-bit DAC is a key component of the proposed PADC. The proposed scheme of 1-Bit DAC is shown in figure 3-58. This architecture is included an optical amplifier and a Gaussian filter. The combination of these two components performs the 1-Bit DAC task. In this model, the amplifier gain G is setup based on the

quantization threshold of predecessor quantized bit, Bit2. The gain G_2 of the amplifier is about the ratio of P_h and P_{th_Bit2} and the G_2 (dB) is given by:

$$G_2(dB) = P_h(dB) - P_{th\_Bit2}(dB) \tag{3-69}$$

The bandwidth of OBPF is 16 nm at 1545 nm, the 1-Bit DAC is a tuneable block that depends on the sampling rate of the PADC and its parameters such as amplifier gain and OBPF bandwidth that have been setup properly. Therefore, for each sampling frequency there is an optimised set point that the PADC has the best achievable performance.

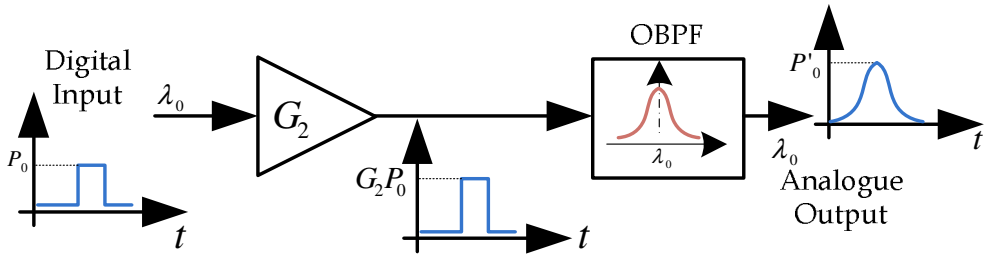

Figure 3-58: The model of 1-Bit DAC which is used in the 2-bit PADC architecture.

To quantize the LSB of the PADC Bit_1, the output power of 1-bit DAC is subtracted from $P_{SP1}(t)$. To compensate the propagation delay of the quantization process of Bit_2, a delay T_d is inserted into the path of the optical subtractor. The output of the subtractor is fed into the OHL1 to quantize the Bit_1. The output L_1 represents the Bit_1 at the wavelength λ_1. The outputs of the OHL1 and the OHL2 which are representing Bit1 and Bit2 of the PADC respectively are using WDM to transport through the fibre link in the proposed FP-DRoF that will be discussed in the Chapter 5.

Figure 3-59 shows the output spectrum of the 2-Bit PADC of the simulation results. Figure 3-59 (a) represents the FFT of a 5 GHz single tone which is sampled at 60 GHz and is illustrated within the first Nyquist zone. As given in this Figure, the fundamental signal amplitude is -5.7 dB and the strongest spur signal amplitude is about -17 dB, whereas the process gain is removed. Thus, the SFDR is 11.3 dBc and the result ENOB is 1.88.

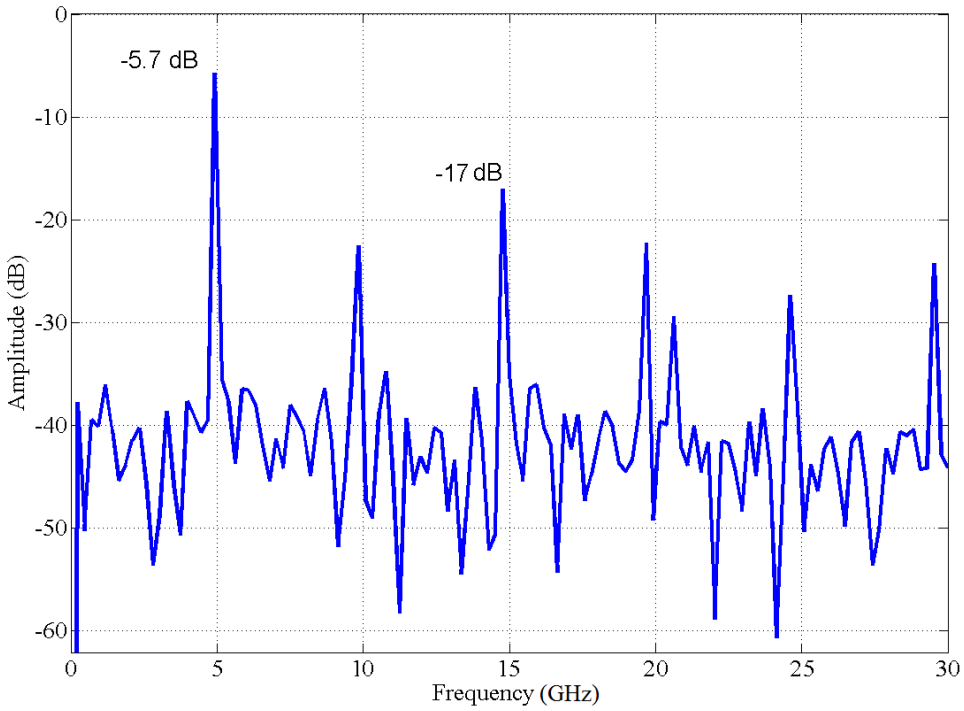

(a)

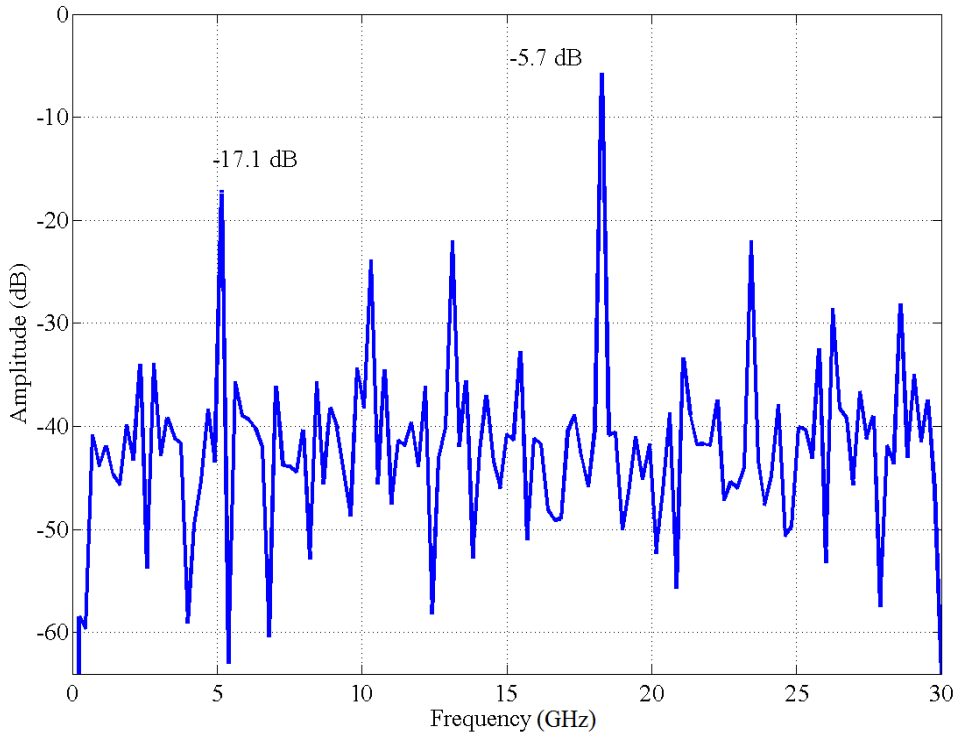

(b)

Figure 3-59: The FFT of 2-bit PADC output of the sampling (a): single tone 5 GHz signal (b): single tone 18 GHz signal at 60 GS/s with 131072 point FFT.

Furthermore, to assess the 2-Bit PADC performance at other input frequency, the FFT of a single tone signal at 18 GHz is sampled signal at 60 GHz sampling frequency is

given in Figure 3-59 (b). In this figure, the fundamental signal amplitude is about -5.7 dB and the biggest spur signal amplitude is -17.1 dB and the SFDR is 11.4 dBc. Therefore, the 2-bit PADC's ENOB is about 1.89.

Moreover, to evaluate the optimised sampling frequency range of the proposed 2-Bit PADC, the ENOB of the 2-Bit PADC is assessed versus an input RF frequency against different sampling frequency. The design target was optimising the PADC for 60 GHz sampling frequency. It will be performed by tuning the bandwidth of the OBPF at the 1-Bit DAC block and its amplifier gain, G_2. Therefore, Figure 3-60 gives the ENOB variation versus a single tone input RF signal at different sampling frequency. This figure demonstrates that the PADC performance is improved around a 60 GHz sampling frequency which is a target sampling frequency in this design.

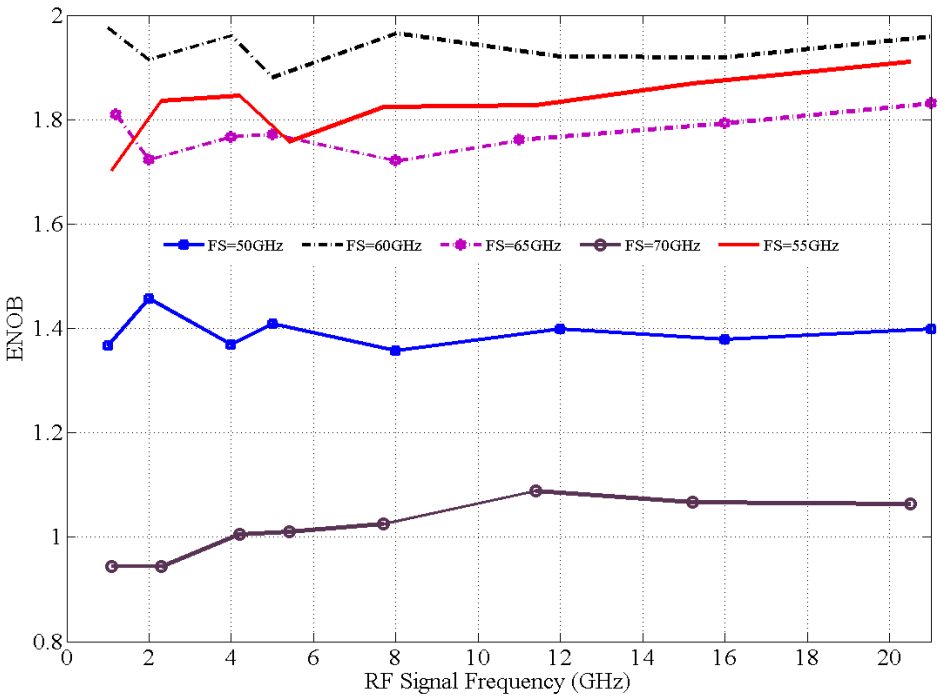

Figure 3-60: ENOB versus input signal frequency for different sampling frequency. As shown, the optimized sampling frequency can provide better performance of the PADC.

To evaluate the PADC performance in another view, Figure 3-61 shows the ENOB versus sampling rate against different input signal frequency. As shown in this figure the PADC ENOB performance variation within a 21 GHz bandwidth is approximately about 10%. The performance significantly depends on the sampling frequency and 10 GHz bandwidth range around of the sampling frequency at 60

GHz is the optimum sampling frequency of the 2-Bit PADC for the present setup of the tuned parameters such as OBPF bandwidth and amplifier gain. As it is illustrated in the Figure 3-61, the proposed PADC performance loss has been less than 10% in terms of ENOB within the sampling frequencies which start around 55 GHz with about 10 GHz bandwidth and stop at frequency 65 GHz. To shift the sampling frequency to other range upon the specific demanded application, the OBPF must be retune and this work can be performed by deploying a tuneable OBPF which is controlled by a circuit with corresponding set point of sampling frequency.

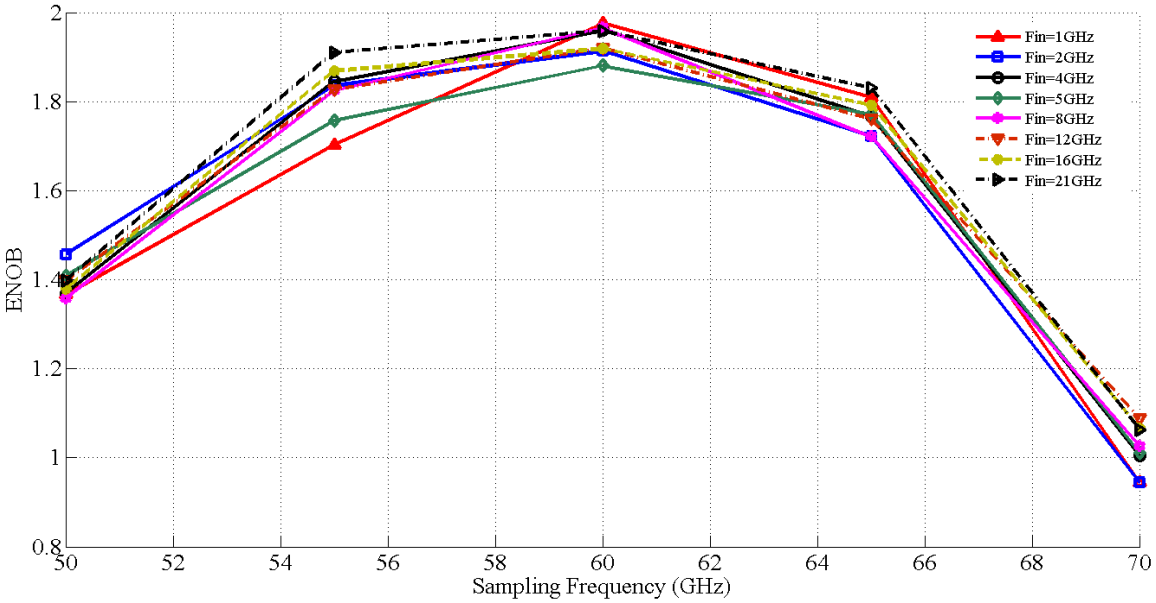

Figure 3-61: ENOB versus sampling frequency at different input signal frequency.

3.7. Generic Architecture of PADC

To design an n-Bit PADC, the proposed architecture is extended. Therefore, architecture of the proposed pipelined photonic sampling and quantization ADC for n-Bit quantization is illustrated in Figure 3-62. This generic architecture is an identical model of the 2-bit PADC whereas is used a MZM as an electro-optical modulator, which is sampled an input RF signal by using a MLLD's pulse train. However, despite of the 2-bit PADC, the optical power of sampled pulses is split into n levels using a symmetrical optical splitter, where n denotes the number of quantization bits. Then, the split signals are fed to a photonic signal processing block for quantization and wavelength conversion operations.

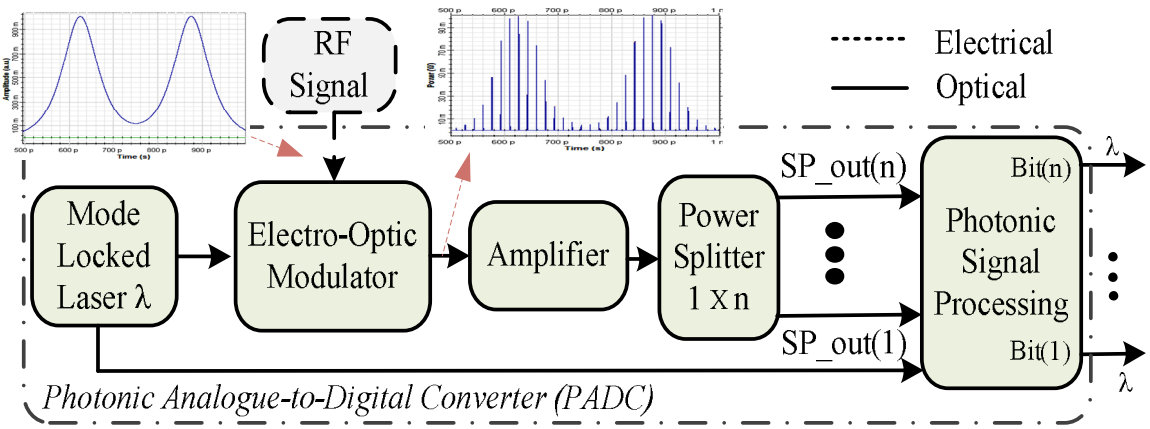

Figure 3-62: Proposed photonic analogue-to-digital converter's architecture.

The quantization procedure is performed by the process of Figure 3-63 in which A and A' are constant parameters. At the first stage of this process, the stage number is equal to '1' (S=1). In this process entire stages are equal to number of quantization bits, i.e., for each output bit there is a corresponding quantization stage.

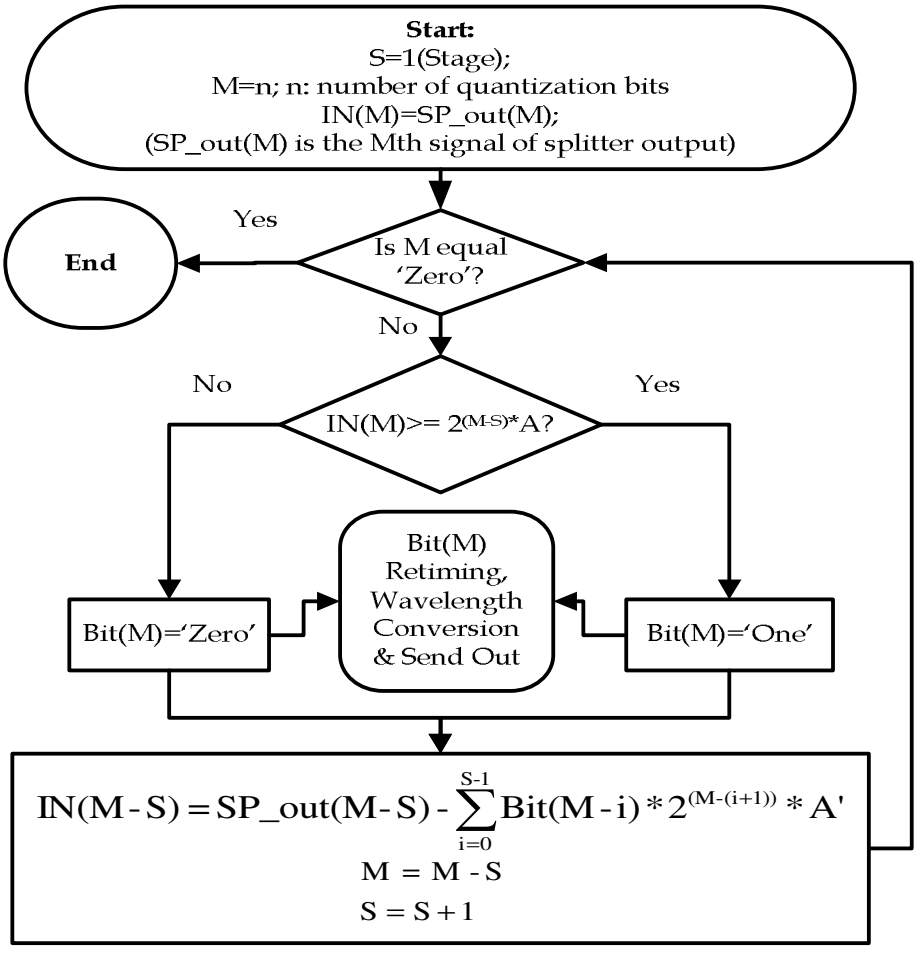

Figure 3-63: The generic flowchart of signal quantization of the PADC.

For quantization of the most significant bit (MSB) the received signal from output number 'n' of the symmetrical splitter SP_out(M) that is defined by the generic number 'M' which is equal to 'n' in this stage. This output optical signal is compared with a reference quantization level equal to '2(M-S) *A'. If the signal power square is greater than or equal to '2(M- S) *A', the output quantization bit is '1'. Otherwise, it is '0'. In this scheme, for performing the pipelined architecture, the quantized bits are converted back into analog domain. Therefore, in stage number '(M-S)', the converted back analog signals from stages 'n' to '(M-S+1)' of the process, are subtracted from the input of the split output signal SP_out(M-S). Then, the given signal is compared with '2(M-S) *A'. The quantization process is repeated in parallel 'n' times for quantizing each sampled optical signal into 'n' bits.

The block diagram of the generic signal quantization system is shown in Figure 3-64. In this system, the Data Recovery (DR) block is used to synchronize all functions with MLLD sampling pulses. DR block is shown in Figure 3-65 and will be discussed in detail in Chapter 4.

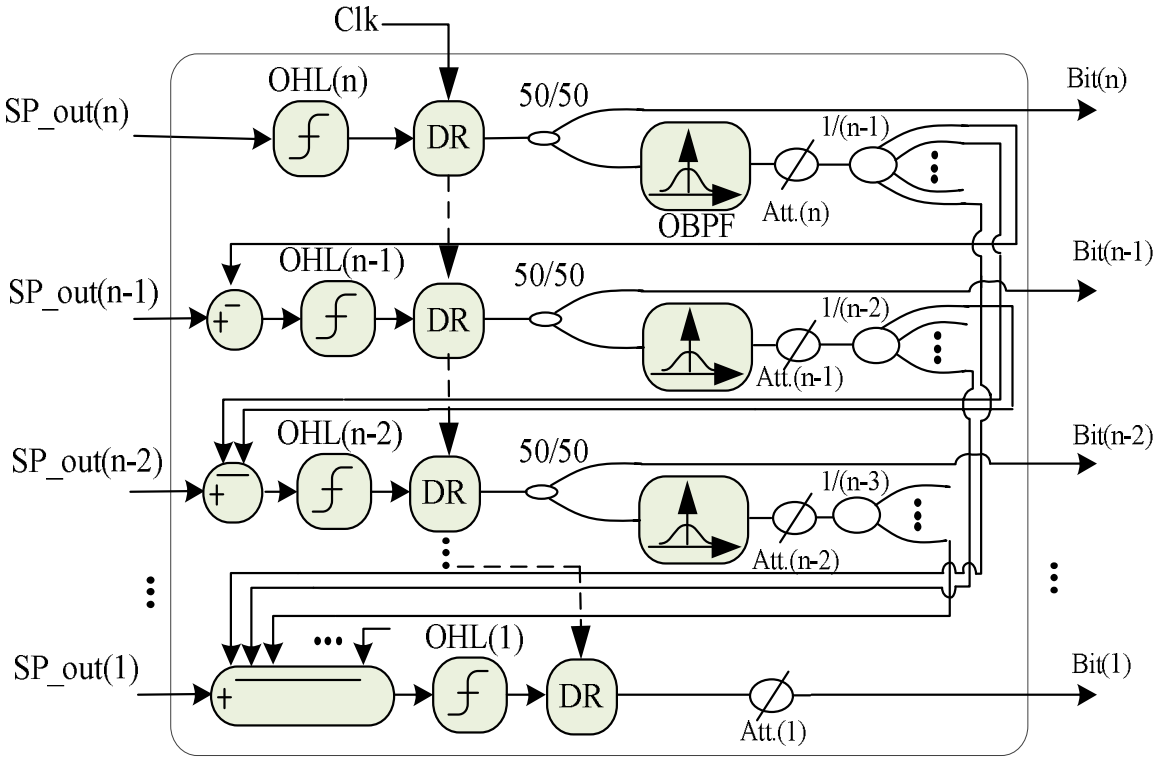

Figure 3-64: Generic n-bit quantization system.

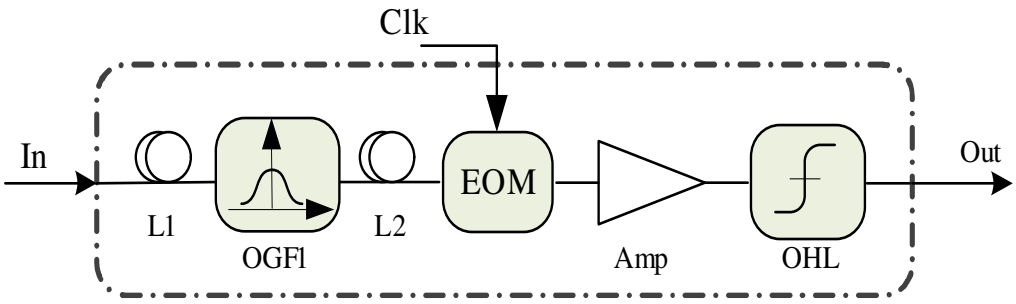

Figure 3-65: Optical data retiming and reshaping.

3.7.1. Analysis and Discussion of 8-Bit PADC

Based on this model and optimized parameters of the 2-Bit PADC at 60 GHz sampling frequency, an eight-bit ADC is designed. Therefore, the digitized optical signal's power have been split into 8 channels and fed to the photonic signal quantization block. The performance of the 8-Bit PADC is evaluated at 60 GHz sampling frequency for single tone RF inputs at different frequencies. As shown in Figure 3-66 (a), the amplitude of the single tone RF input at 1 GHz is about -9.7 dB and the maximum spur signal magnitude is about -34.2 dB. Therefore, the SFDR is 24.4 dBc. According to this SFDR, the ENOB of the 8-bit PADC is 4.06. Furthermore, for a 15 GHz single tone RF input which is illustrated in Figure 3-66 (b), the fundamental signal amplitude is -9.88 dB and the strongest spur signal magnitude is about -34.58 dB which gives the SFDR about 24.7 dBc and the ENOB about 4.1.

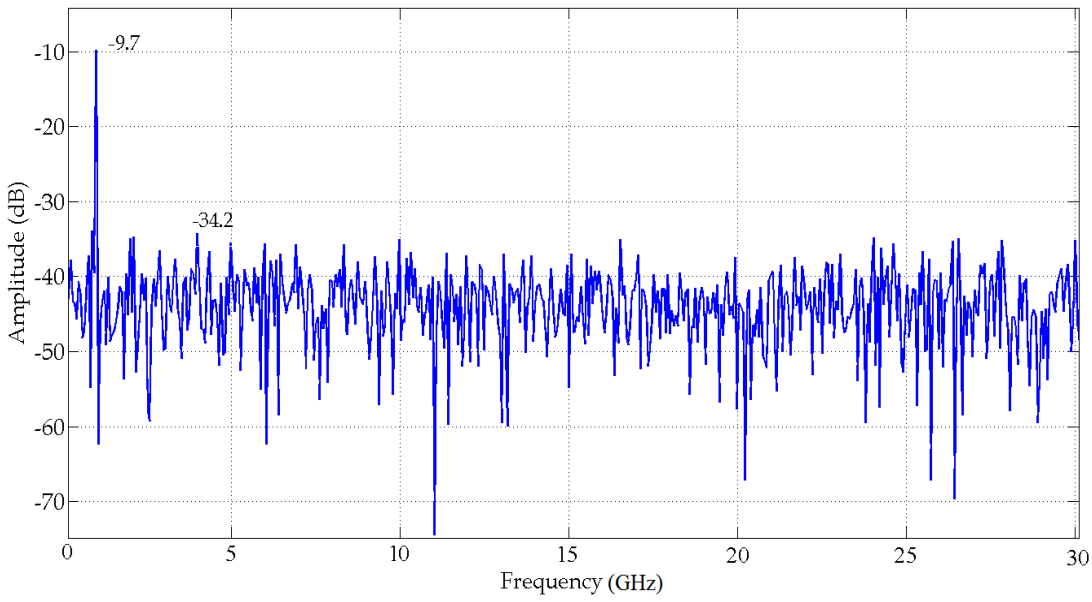

(a)

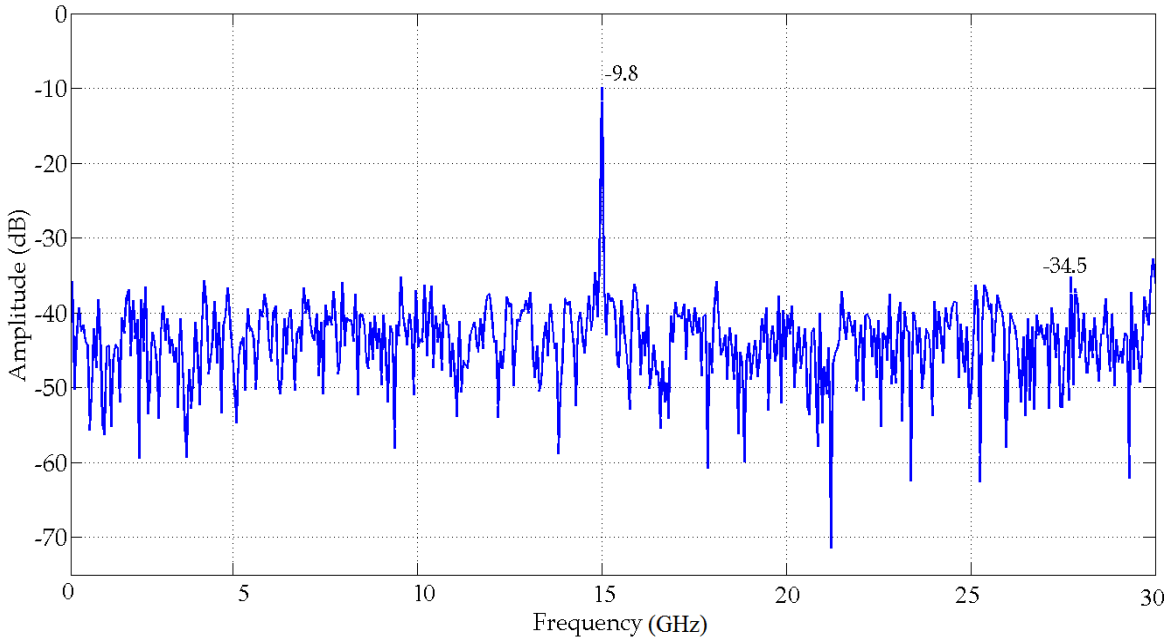

(b)

Figure 3-66: 8-Bit ADC output FFT of single tone at 60 GS/s sampling frequency with 131072 point FFT at: (a) 1 GHz and (b) 15 GHz.

Furthermore, the impact of two tone inter-modulation distortion on the proposed 8-bit PADC performance is assessed. It is investigated by considering two individual single tone RF signals with very small frequency difference. Figure 3-67, shows the FFT amplitude of the output of PADC.

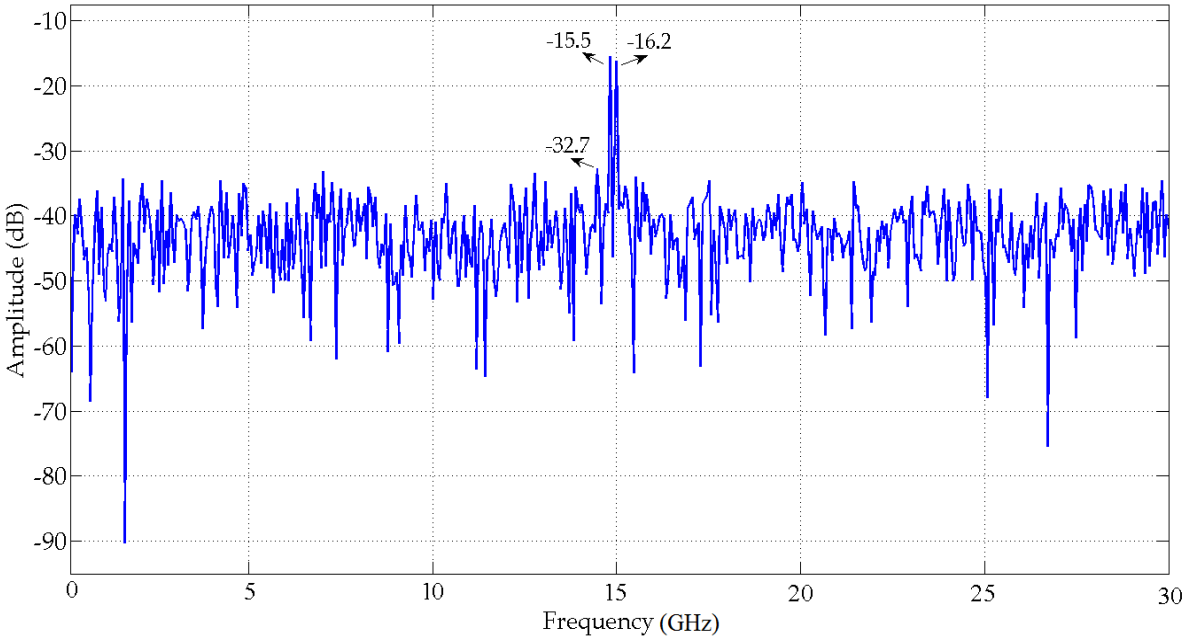

Figure (3-67): Two tone inter-modulation at 14.8 GHz and 15 GHz at 60 GHz sampling frequency for 8-bit PADC.

In this assessment, two single tones at frequency 15 GHz and 14.8 GHz are sampled at 60 GHz and the FFT amplitude gives the magnitude of the fundamental signals and the harmonics distortion. The signal amplitude at 14.8 GHz is about -15.5 dB and -16.2 at 15 GHz, whereas the distortion spurs signal amplitude is about -32.7 dB.

To demonstrate the physical functionality of the 8-bit PADC, a sample waveform is generated which is illustrated in Figure 3-68. Figure 3-68 (a) shows a sample RF signal with a 5 GHz frequency which is sampled with a MLL's pulses with 60 GHz pulses repetition rate. The MLL pulses train is given in Figure 3-68 (b) and the sampled signal in illustrated in Figure 3-68 (c).

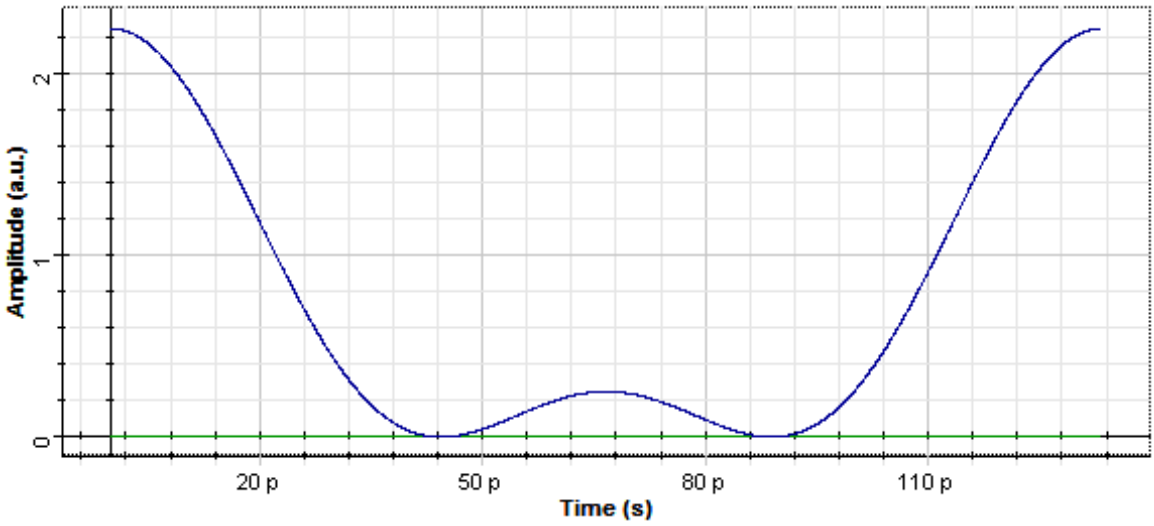

(a)

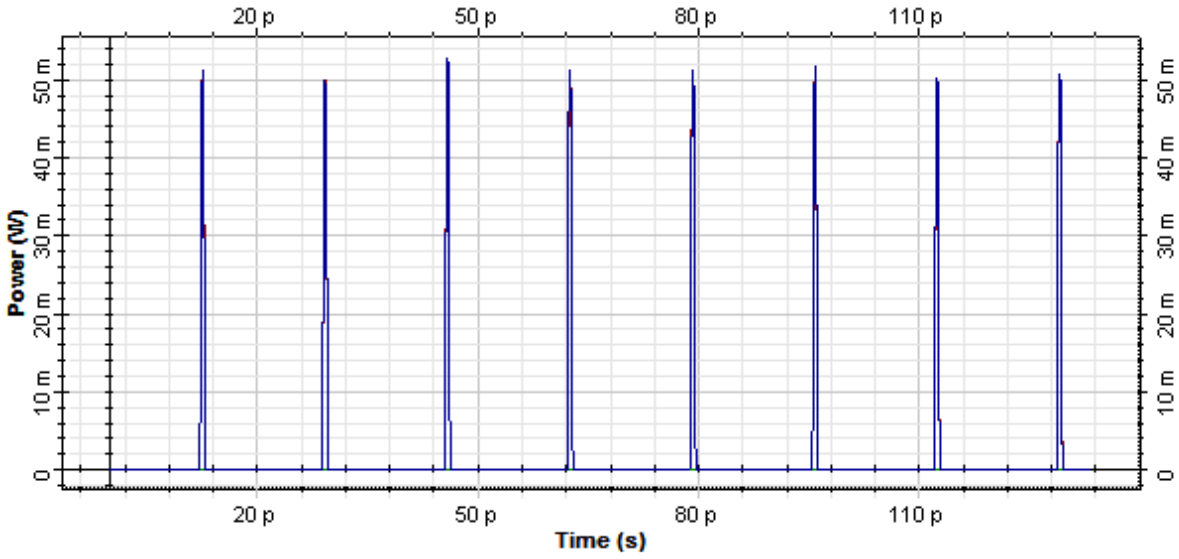

(b)

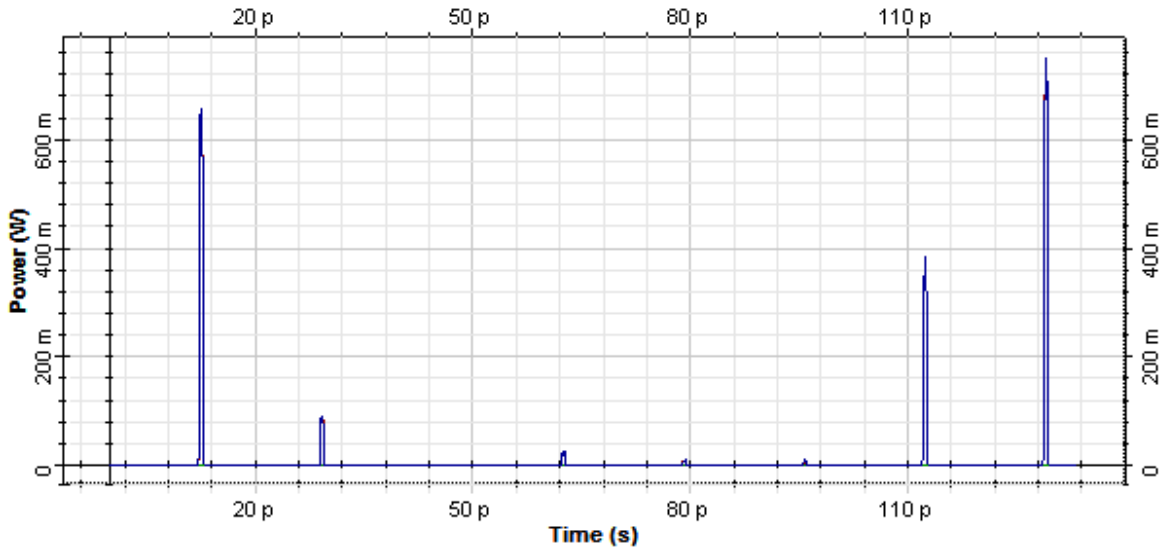

(c)

Figure 3-68: PADC's waveforms: (a) Analogue Input Signal, (b) MLLD Pulse Train, (c) Sampled Signal at MZM Output.

Furthermore, the quantized output bits of the PADC is shown in Figure 3-69 (a)-(h), that were respectively corresponded to Bit_8 to Bit_1 of the PADC. As shown in this figure, each sample of the optical signal in Figure 3-68 (c) is quantized into 8 bits which are corresponded to the time of sampling of the original signal. Therefore, corresponding to the 8 sampling times that are shown in Figure 3-68 (b), the following digitized data is generated at the output of the PADC, the first to eighth sample are quantized to "11111111", "01011111", "00000111", "00111111", "00011111", "00011111", "10111111" and "11111111", respectively.

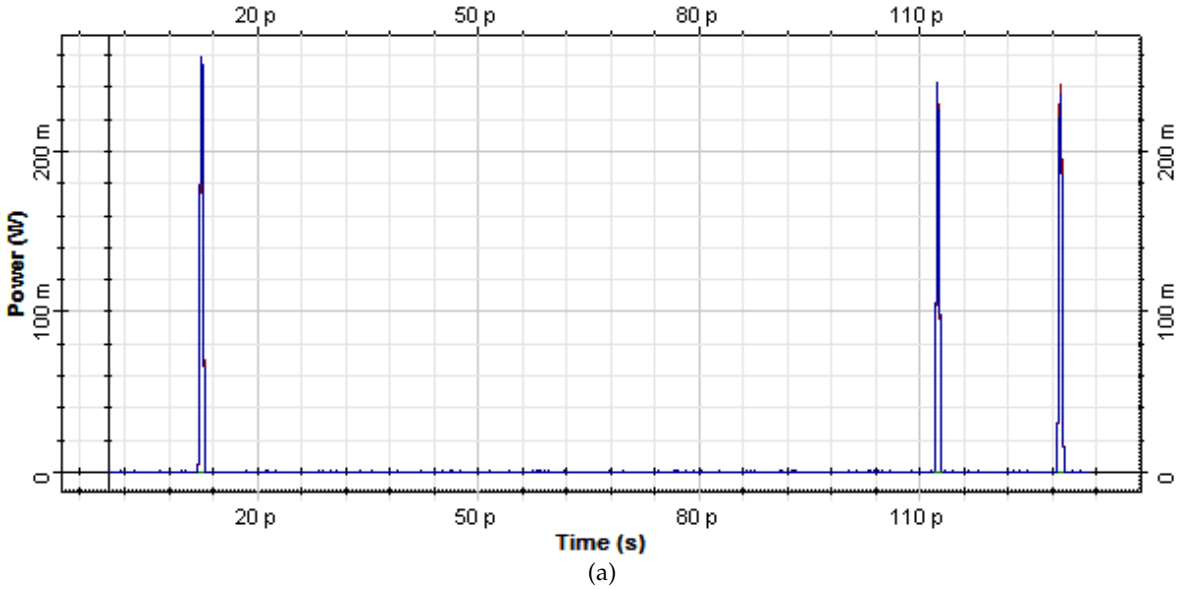

(a)

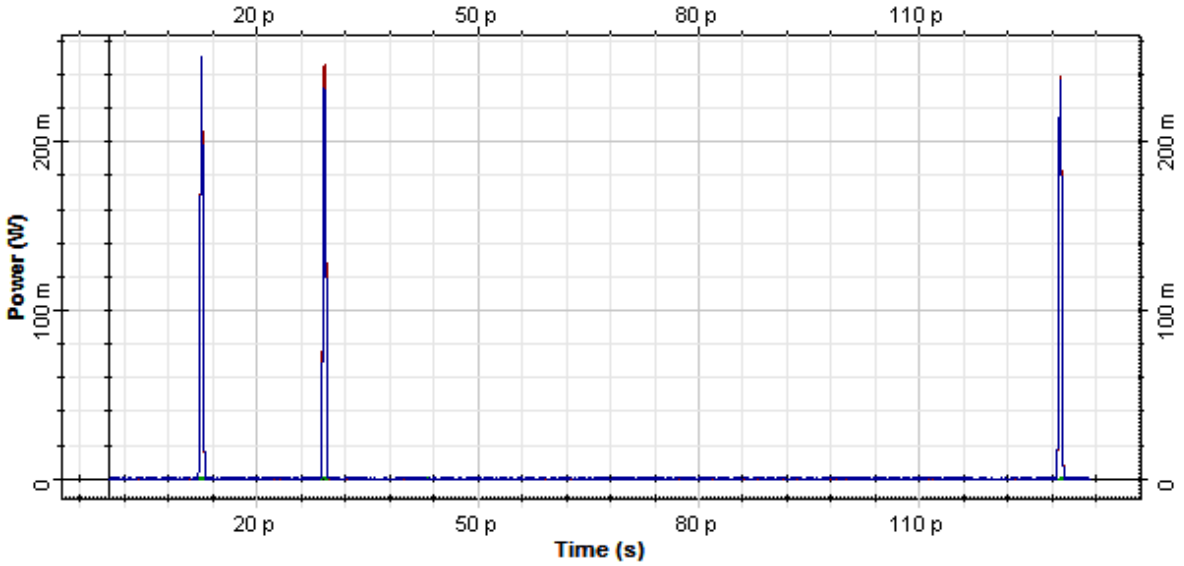
20 p
50 p
80 p
110 p
Power (W)
200 m
100 m
0
Time (s)

(b)

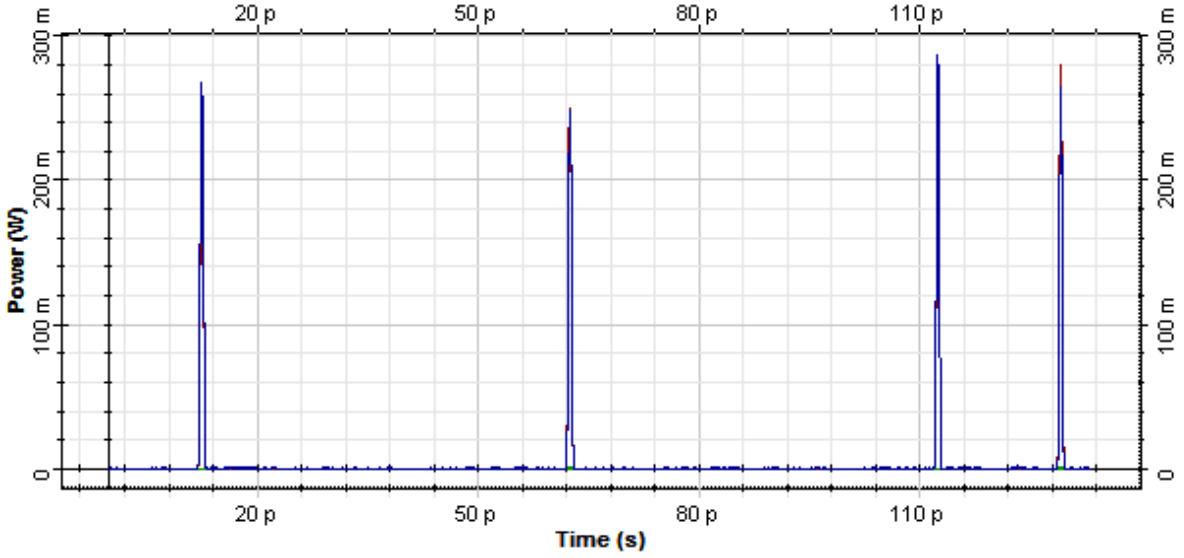
20 p
50 p
80 p
110 p
Power (W)
300 m
200 m
100 m
0
Time (s)

(c)

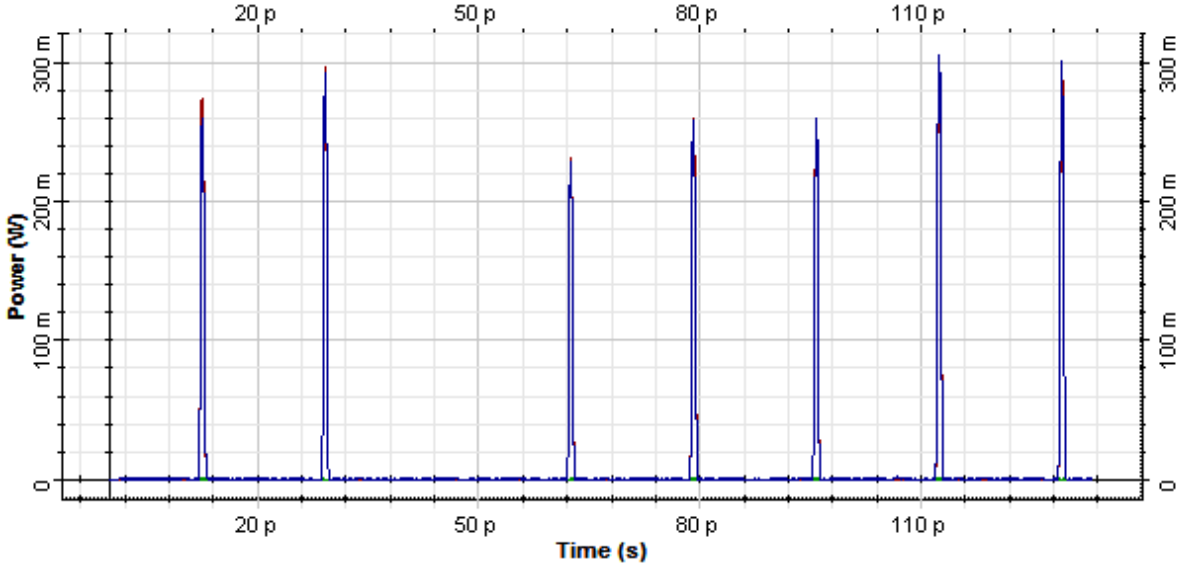
20 p
50 p
80 p
110 p
Power (W)
300 m
200 m
100 m
0
Time (s)

(d)

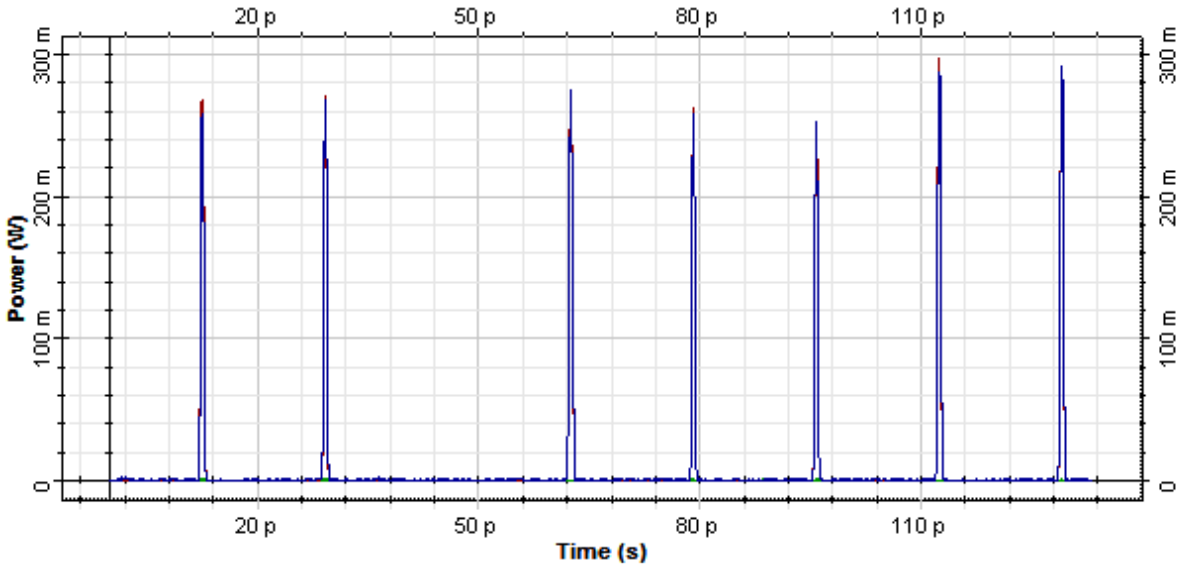
20 p
50 p
80 p
110 p
300 m
200 m
100 m
0
Power (W)
Time (s)

(e)

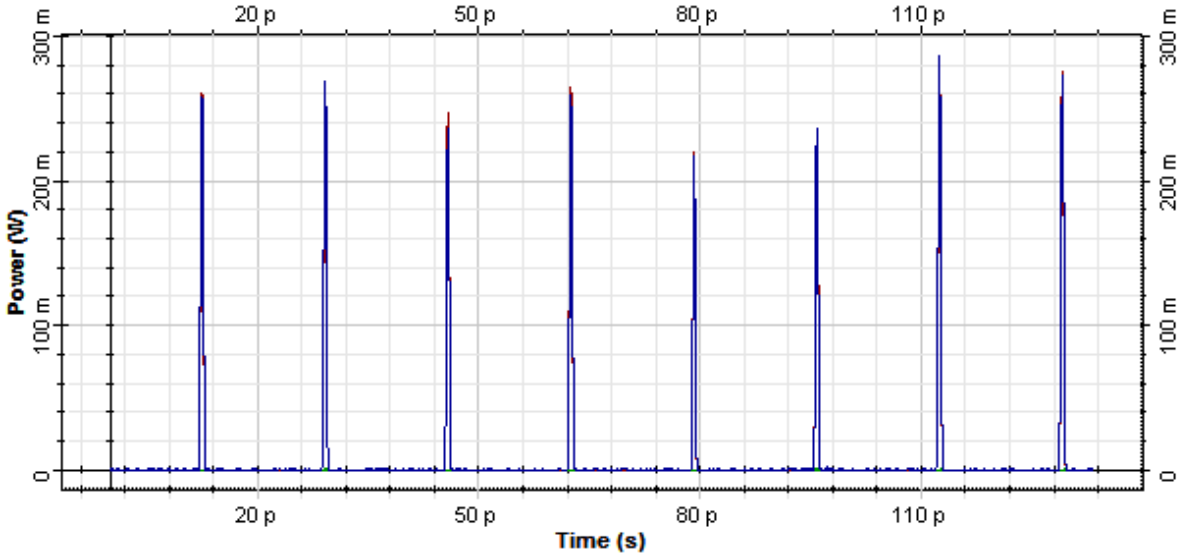
20 p
50 p
80 p
110 p
300 m
200 m
100 m
0
Power (W)
Time (s)

(f)

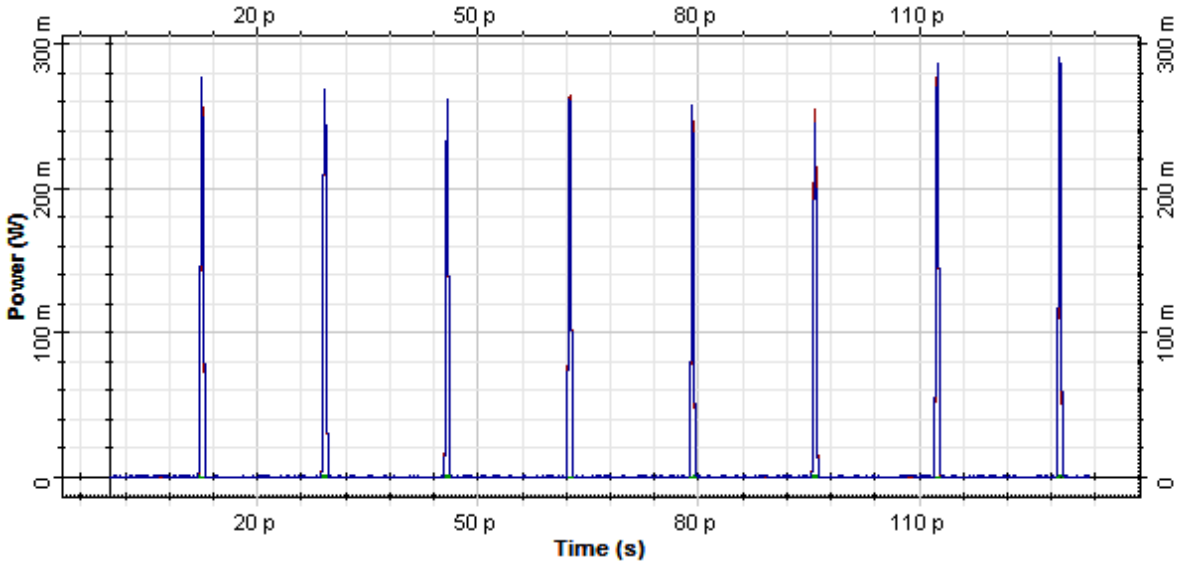
20 p
50 p
80 p
110 p
300 m
200 m
100 m
0
Power (W)
Time (s)

(g)

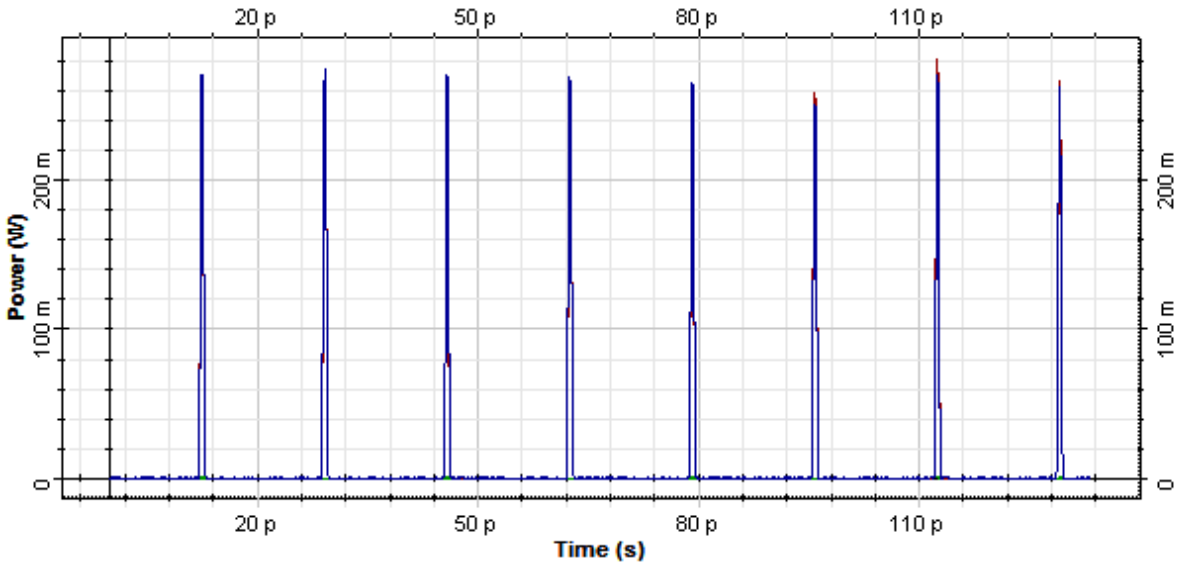

(h)

Figure 3-69: The Generated Digital Data of Sampling a Sample 5 GHz RF Signal with 60 Gigasample/s: (a)-(h) Bit8-Bit1 of PADC's output, respectively.

The amplitude fluctuation of the digital output is related to the performance of the flatness of the OHL's transfer function for high value.

Table 3-1 illustrates the comparison between different reported architectures with our proposed work. In comparison to all of the reported architectures, the proposed architecture is fully optical in both signal sampling and quantization. Furthermore, the output of the proposed architecture is binary with no need to post processing in electronic domain. Some of the reported works have reported sampling frequency, whereas the others reported the analogue input signal frequency. However, 21 GHz bandwidth of the proposed architecture PADC is assessed for a 10 GHz bandwidth of the sampling frequency channel around 60 GHz sampling frequency.

Table 3-1: A comparison of PADCs.

Ref.	ENOB	Sampling Frequency (Gs/s)	Input Frequency (GHz)	Architecture
[31]	4	40	-	Photonic Assisted
[12]	7	40	-	OSEQ
[33]	4	100	-	Photonic Assisted
[46]	10.2	25	-	Photonic Assisted
[68]	<4	-	-	Intensity Modulation

				Electronic Quantization (IMEQ)
[69]	4	-	-	IMEQ
[74]	7	41	-	Phase Modulation Electronic Quantization (PMEQ)
[76]	3.5	-	10	PMEQ
[82]	4.1	-	2.2	PSEQ
[83]	4.3	-	2.5	PSEQ
[84]	3.45	40	2.5	PMEQ
[85]	8	40	-	PSEQ
Our Work	**4.1**	**60**	**21**	**All-Photonic Pipelined**

3.8. Digital to Analogue Converter

In an N-bit digital-to-analogue converter (DAC), parallel input digital signals are converted into an analogue value S_{out} that is given by:

$$S_{out} = \sum_{j=0}^{N-1} B_j .2^j .G_{ref} \tag{3-70}$$

Where, G_{ref} is a reference value and B_j are the binary values of the order j of the digital value of the input signal. Therefore, B_0 and B_{N-1} are the LSB and the MSB, respectively. A functional block diagram of a DAC is shown in Figure 3-70.

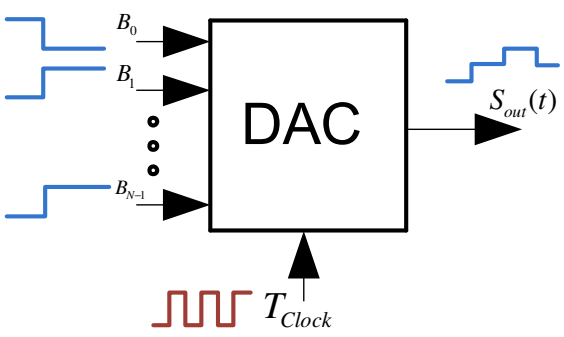

Figure 3-70: General block diagram of DAC.

In this assumption, the minimum change of analogue output S_{out} is equal to a step size or the LSB's value that is equal to reference value G_{ref}. Furthermore, the reference value can be related to the MSB's value. In this assumption, the equation (3-70) can be rewritten by:

$$S_{out} = \sum_{j=0}^{N-1} B_j .2^{-j} .G_{ref} \tag{3-71}$$

Therefore, the minimum change of analogue output or step size q_s can be given by:

$$q_s = G_{ref} .2^{-N+1} \tag{3-72}$$

3.8.1. EDAC Architectures

There are different types of electronic DAC such as: 1) Pulse Width Modulator (PWM) DAC is the simplest type of DAC. In this architecture, stable current or voltage is switched into a low pass analogue filter with a duration determined by the digital input code, 2) Delta-Sigma DAC, this oversampling technique allows using a lower resolution DAC internally. Most of the very high resolution DACs (greater than 16 bits) is of this type due to its high linearity and low cost, 3) The Binary Weighted DAC, which contains one resistor or current source for each bit of the DAC connected to a summing point. These precise voltages or currents sum to the correct output value. This is one of the fastest conversion methods but high precision required for each individual voltage or current. Such high-precision resistors and current sources are expensive, so this type of converter is usually limited to 8-bit resolution or less, 4) The R2R Ladder DAC, which is a binary weighted DAC that creates each value with a repeating structure of 2 resistor values, R and R times two. This improves DAC precision due to the ease of producing many equal matched values of resistors or current sources, but lowers conversion speed due to parasitic capacitance, 5) The Segmented DAC, which contains an equal resistor or current source segment for each possible value of DAC output. However, limitation of this architecture is requirement of high number of segments in the order of 2^N, where N is the number of resolution bits. This is perhaps the fastest and highest precision DAC architecture but at the expense of high cost, 6) Hybrid DACs, which use a

combination of the above techniques in a single converter. However, the system is designed based on the trade-off between difficulty, cost, speed and precision in one device.

3.8.2. Photonic DACs Architecture

Despite of the different types of electronic DAC, several schemes of photonic DACs are reported in recent research reports but the main focus of these reports are based on conversion of digital electrical data into analogue optical signal. A 2-bit PDAC architecture at 1 Gs/s is reported based on weighting and summing of high-speed mode-locked laser pulses [123]. A high speed 4-bit PADC is demonstrated in [124] based on a 4-channel integrated optical phase modulators for 12.5 Gs/s sampling rate. In [125], a PDAC architecture the weighted multi-wavelength pulses are delayed and summed in time domain through dispersion, and each weighted pulse with specific wavelength corresponds to a bit of input digital data. This architecture is evaluated for a 3-bit PDAC with a sample rate of 2.5 GS/s. In [126], a PDAC (DAC) based on a multi-electrode MZI is presented. A 4-bit bipolar PDAC architecture based on the Optical Differential Quadrature Phase Shift Keying (ODQPSK) modulation coupled with differential detection is reported in [127] at 2.5 GS/s sampling rate.

However, all of the existing refrenced methods are optically-assisted PDAC that convert digital electrical signal into modulated optical analogue signal. But, in the proposed binary-weighted architecture of thePDAC, the digital optical signal is converted to an analogue optical signal.

3.9. A 2-Bit Binary Weighted PDAC

Architecture of the proposed 2-Bit BW-PDAC system is given in Figure 3-71. In this scheme, the two optical digital input signals P_{Bit_2} and P_{Bit_1} which represent the MSB and LSB bits power with identical magnitude. The LSB power, P_{Bit_1} is attenuated 6 dB and added to the power of MSB, P_{Bit_2} after passing through a delay block, which imposes a delay of T_d seconds which matchesthe propagation delay of the

attenuator block. The, two input pulses is added in-phase using a directional coupler as an optical adder. This architecture is based on the binary weighted summation of the corresponding electrical field of the MSB and the LSB. A 6 dB attenuator is inserted in the path of LSB because of the half amplitude contribution of the LSB in the binary weighted DAC algorithm which is given by:

$$P'_{Bit_1}(t)\big|_{dB} = P_{Bit1}(t)\big|_{dB} - 6(dB) \tag{3-73}$$

If we assume the electrical field at the input of the attenuator is $E_{Bit1}(t)$ which is expressed by:

$$E_{Bit1}(t) = A(t)e^{-j\omega_0 t} \tag{3-74}$$

The electrical field at the output of the attenuator $E'_{Bit1}(t)$ is given by:

$$E'_{Bit1}(t) = A'(t)e^{-j(\omega_0 t + T'_d)} \tag{3-75}$$

Where

$$|A'(t)|^2 = \left|A(t)/2\right|^2 \tag{3-76}$$

and $T'_d \approx T_d$ is the insertion delay of attenuator which is negligible in comparison to input pulse width.

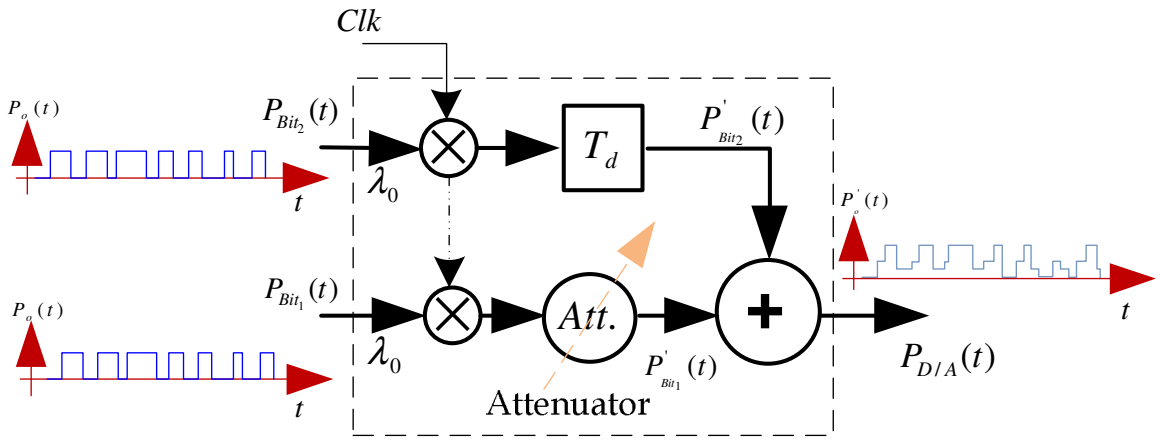

Figure 3-71: Architecture of the 2-Bit BW-PDAC.

Therefore, the output function of the 2-Bit BW-PDAC as an electrical field of the summation signal at the output of optical adder is given by:

$$\left|E_{D/A}(t)\right|^2 = \left|E_{Bit1}^{'}(t) + E_{Bit2}^{'}(t)\right|^2 \tag{3-77}$$

Where $E_{D/A}(t)$ and $E_{Bit2}^{'}(t)$ are signal electrical field at the output of BW-PDAC and the MSB signal after passing through the delay block T_d respectively.

3.9.1. Analysis and Discussion

Transfer function of the 2-Bit BW-PDAC is shown in Figure 3-72 at 60 GS/s sampling frequency. The transfer function shows that the proposed 2-Bit BW-PDAC has a suitable linear transfer function in comparison with the ideal full-scale transfer function.

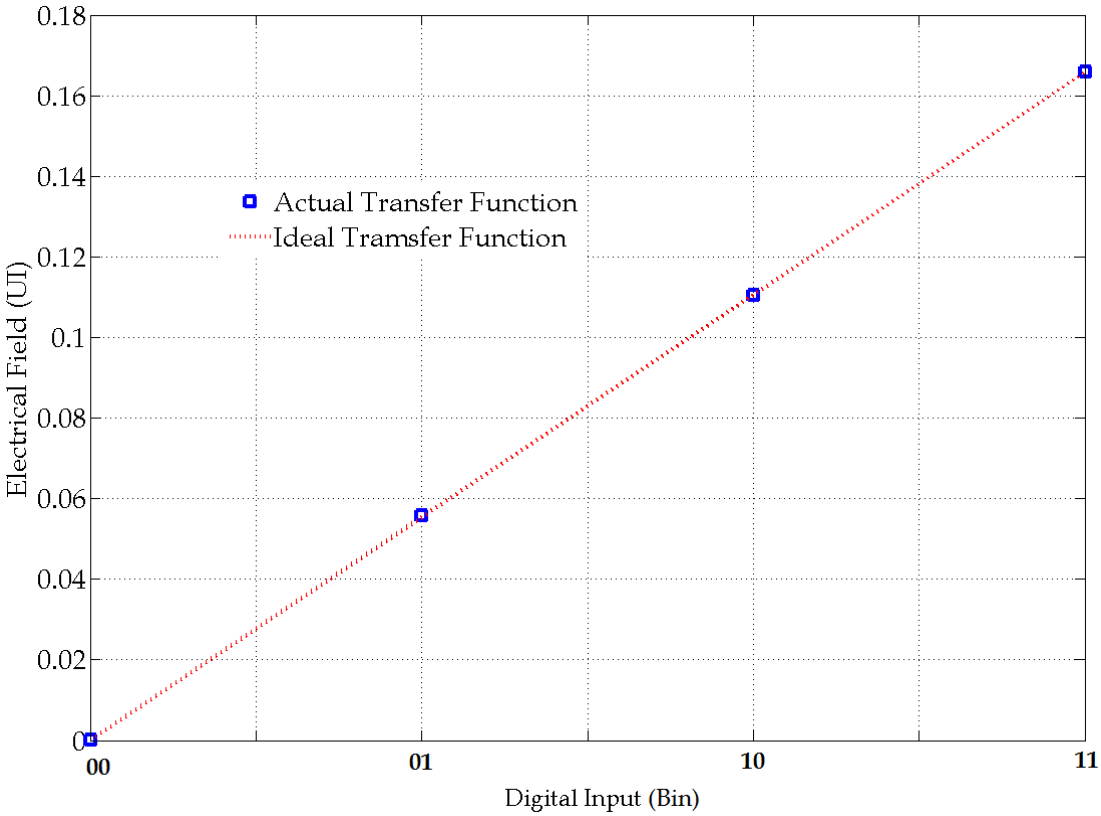

Figure 3-72: Transfer function of the 2-Bit BW-PDAC.

Furthermore, the INL and DNL of the proposed 2-Bit BW-PDAC are investigated to assess it nonlinearity. As shown in Figure 3-73, the INL for a digital input, "01" is

about 0.0072*LSB and for a digital input, "10" is about -0.0018*LSB respectively. The DNL for a digital input, "01" is about 0.0072*LSB, for an input "10" is -0.0091*LSB and for an input "11" is 0.0018*LSB. This, illustrates that the proposed 2-Bit BW-PDAC has appropriate linearity versus digital input signal changes.

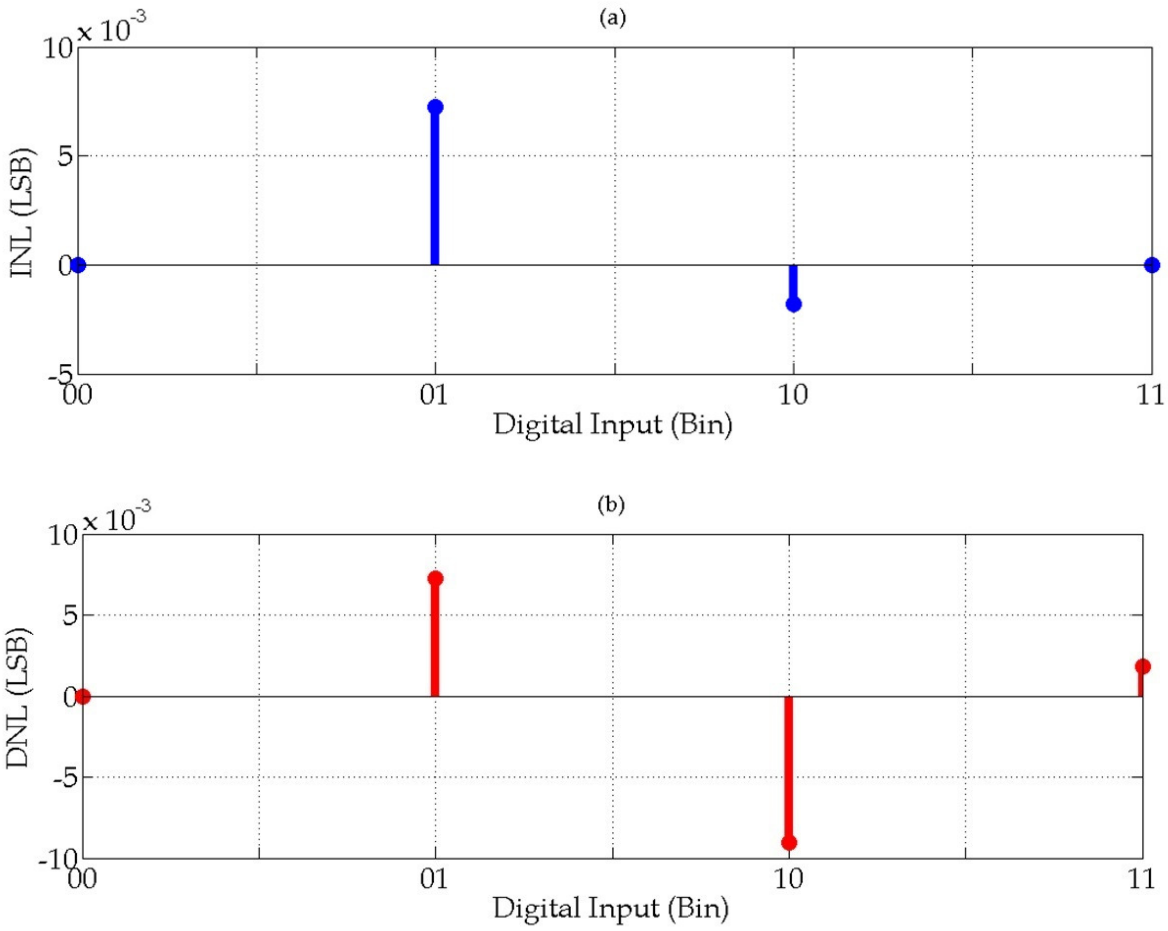

Figure 3-73: The 2-Bit BW-PDAC's nonlinearity assessment, (a): INL, and (b): DNL.

The output spectrum of the 2-bit BW-PDAC is given in Figure 3-74. In the Figure 3-74(a), the fundamental signal amplitude at 586 MHz is -2.66 dB and the strongest spur signal magnitude at the third harmonic is -13.325 dB, therefore, the SFDR is 10.665 dBc. In Figure 3-74 (b), the fundamental signal amplitude is -2.33 dB at 12 GHz and the strongest spur signal at the second harmonic is -12.49 dB at 24 GHz. Therefore, the SFDR is 10.16 dBc. This demonstrates that the proposed 2-Bit BW-PDAC performance in terms of ENOB is about 1.68.

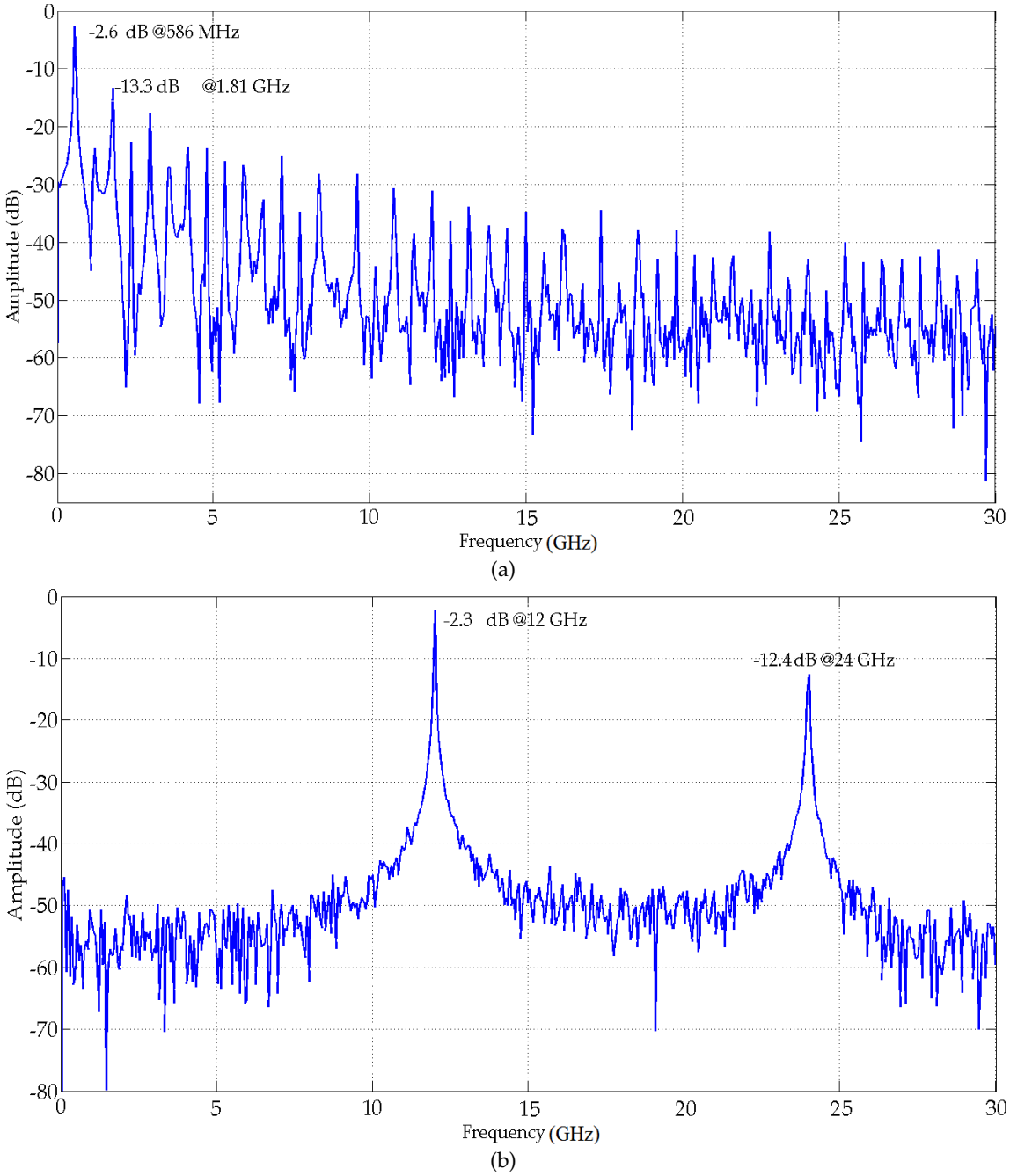

Figure 3-74: Output spectrum at the output of 2-Bit BW-PDAC at Nyquist zone at 60 GHz sampling rate: (a) Input fundamental frequency at 586 MHz (b) Input fundamental frequency at 12 GHz.

3.10. An 8-Bit Binary Weighted PDAC

Based on the 2-Bit BW-PDAC architecture, an 8-Bit BW-PDAC design is proposed in Figure 3-75. As shown in this scheme, the binary weighting schemed is classified into upper and lower nibbles. For upper nibble, optical amplifiers are used, andtheir gains are scaled down based on their binary order similarly to the fundamental 2-Bit

BW-PDAC block but it is deployed for 4 bits. For example, $G_{B(n-1)} = G_{B(n)}/4$, where $G_{B(n)}$ is the gain of amplifier Bit_n. This prevents deployment of very high attenuations at lower value bits. Meanwhile, the procedure is repeated for lower nibble by replacing the binary weighted gain amplifiers with corresponding attenuators. In the simulated model, the gains of the amplifiers were 24 dB, 18 dB, 12 dB, 6 dB for G_{B8}, G_{B7}, G_{B6}, and G_{B5} respectively, and the attenuation for the attenuator was 0 dB, 6 dB and 12 dB, 18 dB, for Att_{B4}, Att_{B3}, Att_{B2}, and Att_{B1}, respectively. To mitigate the ASE noise of the amplifiers, a 16 nm Gaussian Optical Bandpass Filter (OBPF) is used following each amplifier. The optimised bandwidth of the OBPF is chosen based on the sampling frequency of the PDAC which is 60 GHz in this simulated model.

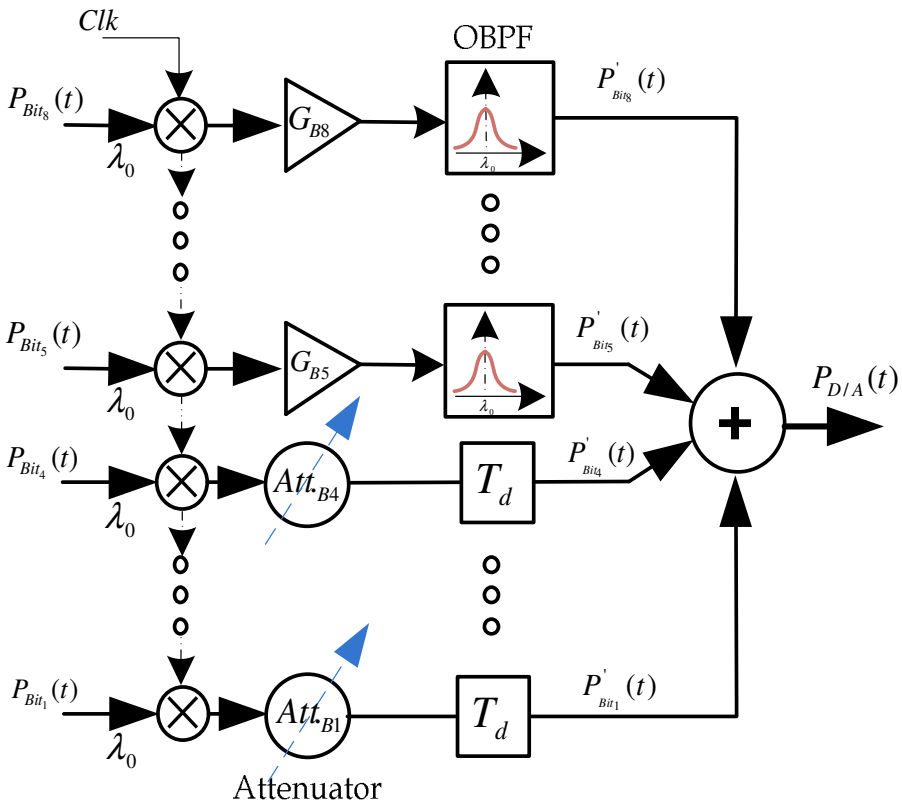

Figure 3-75: The architecture of 8-Bit BW-PDAC.

3.10.1. Analysis and Discussion

Figure 3-76 gives the transfer function and the assessment of the nonlinearity of the proposed 8-Bit BW-PDAC. As shown in the Figure 3-76 (a), the proposed PDAC has

a suitable linear transfer function. Figure 3-76 (b) shows the maximum and the minimum of the INL are about 10.84*LSB and -7.64*LSB, respectively. Furthermore, Figure 3-76 (c) illustrates the DNL of the PDAC which has a maximum difference nonlinearity 15.04*LSB and the minimum difference nonlinearity of about -10.69*LSB.

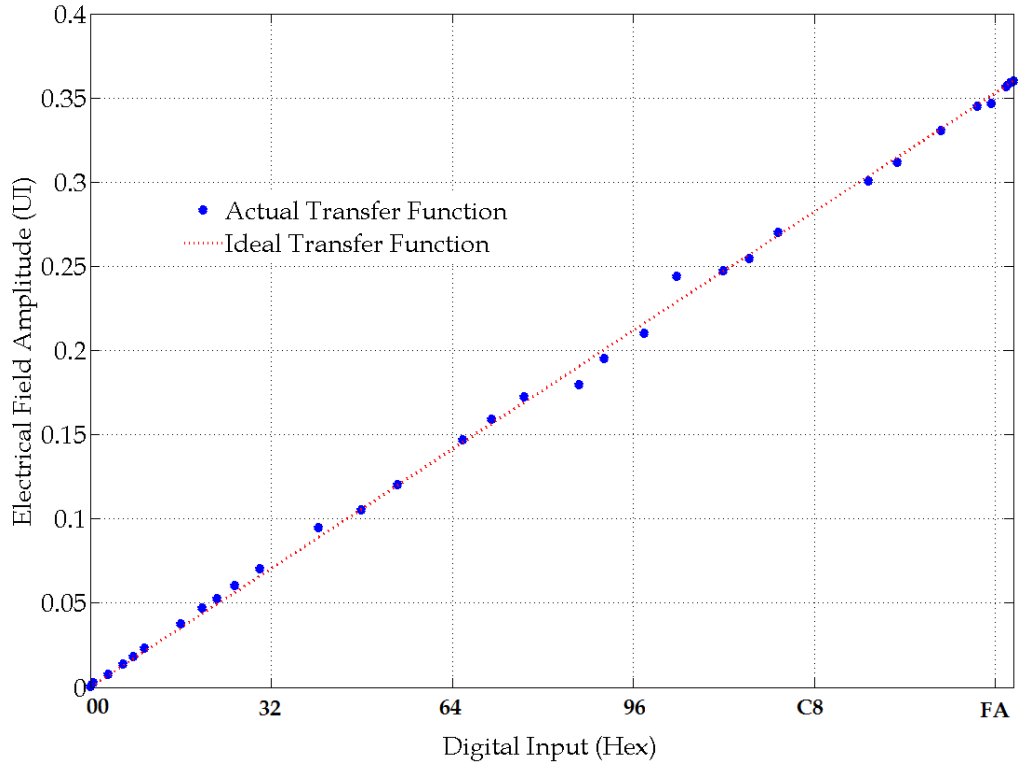

(a)

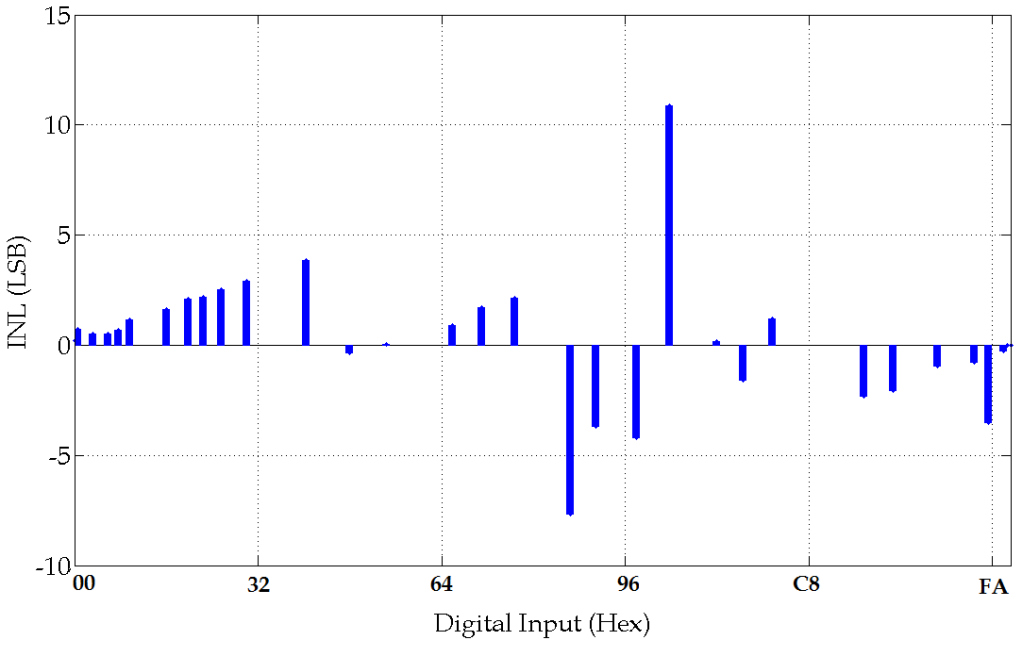

(b)

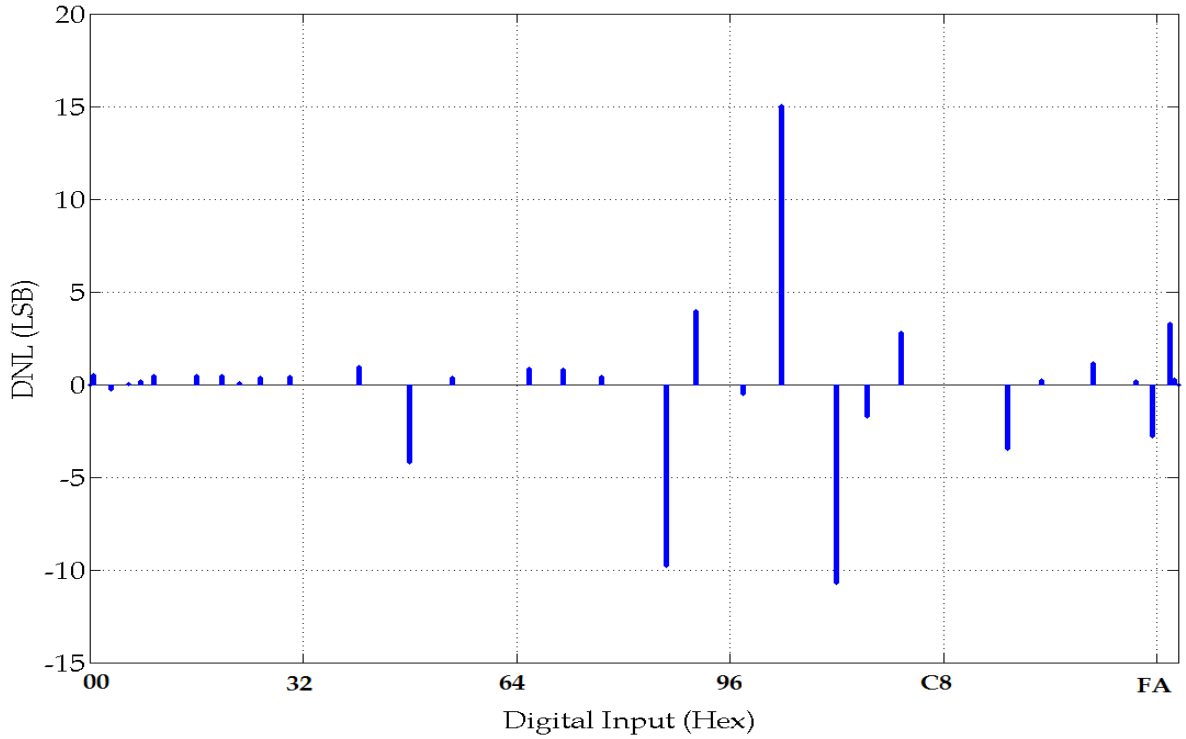

(c)

Figure 3-76: Transfer function of 8-bit BW-PDAC architecture.

Figure 3-77 shows the 8-Bit PADC and BW-PDAC back-to-back test spectrum at the output of BW-PDAC. Figure 3-77(a) shows the output spectrum at the output of the PADC for a single tone RF input at 15 GHz.

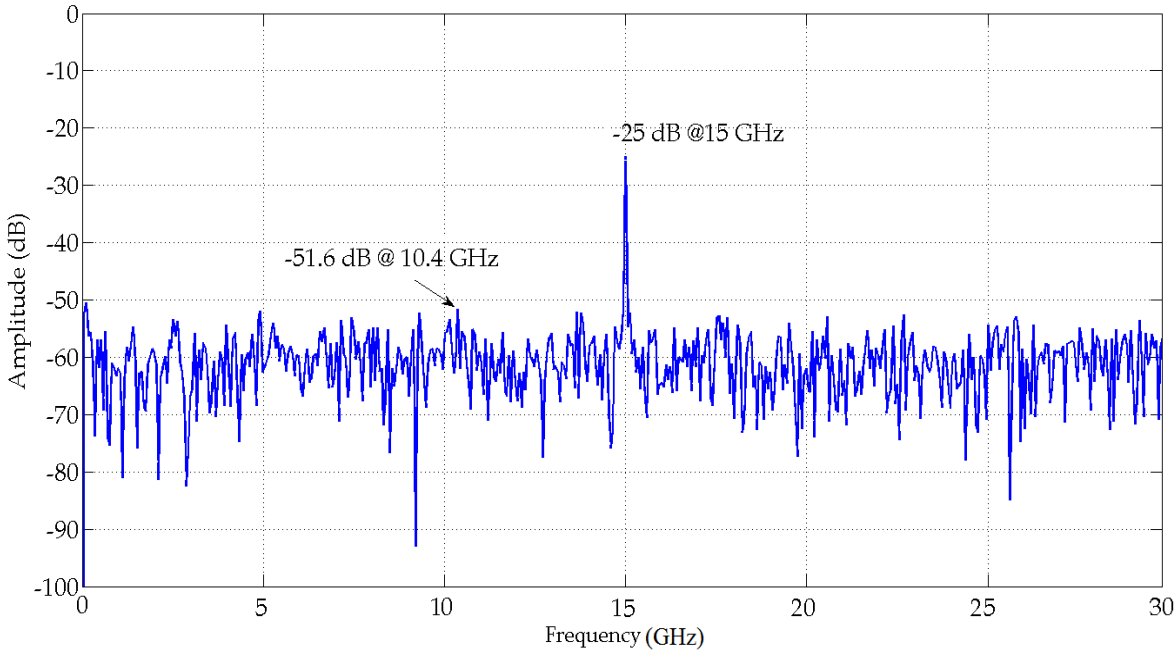

(a)

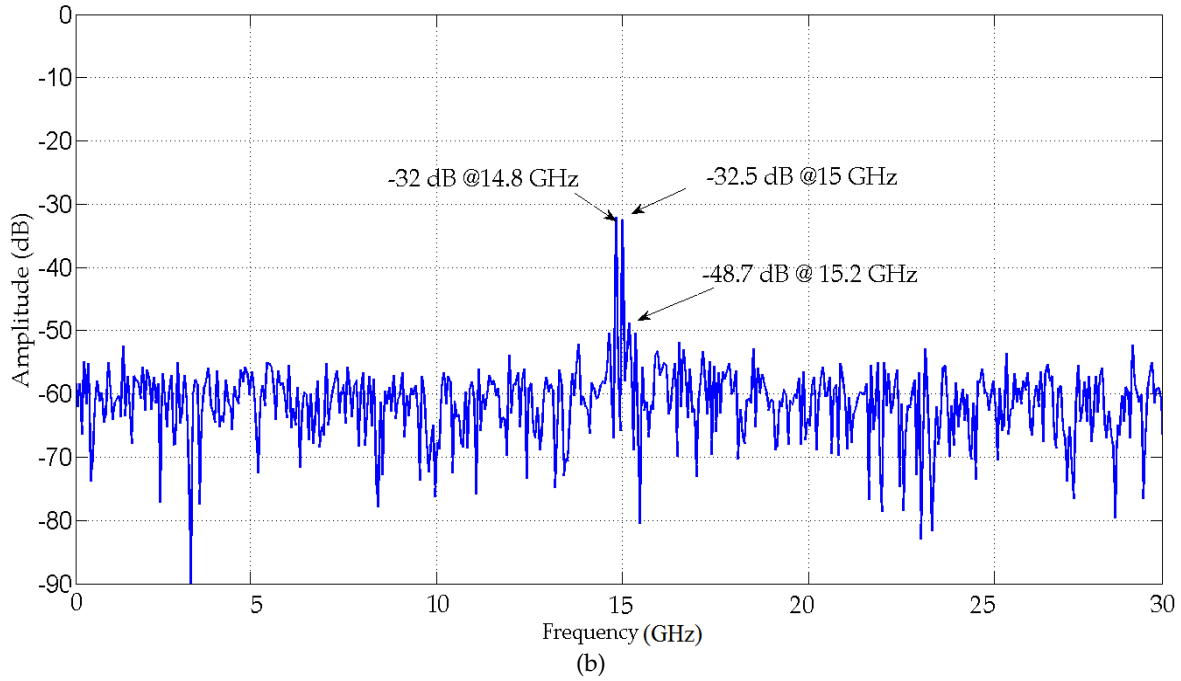

Figure 3-77: FFT Spectrum at the output of 8-Bit PADC and BW-PDAC back-to-back test at Nyquist zone at 60 GHz sampling rate of an input single-tone frequency at 15 GHz.

The FFT amplitude of the fundamental signal is -24.9 dB and the amplitude of the strongest spur signal is -51.6 dB. Therefore, the SFDR is about 26.6 dBc. Furthermore, Figure 3-77 (b) gives an evaluation of the system functionality in response to two-tone input at frequencies 15 GHz and 14.8 GHz. The output spectrum shows that the fundamental signals amplitudes at frequencies 14.8 and 15 GHz are -32dB and -32.4 dB respectively and the strongest inter-modulation distortion amplitude is -48.7 dB. Table 3-2 gives a comparison of the proposed 8-Bit BW-PDAC with other reported references.

Table 3-2: A comparison of PDACs.

Ref.	ENOB	Sampling Freq.	Architecture	Digital Input Signal
[127]	3.65	2.5 GS/s	4-Bit Optical DQPSK	Electrical
[123]	-	1 GS/s	2-Bit Weighted Summing	Electrical
[125]	-	2.5 GS/s	3-Bit Serial Weighted Multiwavelength	Electrical
[124]	3.8	12.5 GS/s	4-Bit InP	Electrical
Our Work	4.42	60 GS/s	8-Bit Binary Weighted	Optical

To demonstrate the DAC functionality in time domain, the generated digital data of the 8-bit PADC which is illustrated in Figure 3-69 are fed to the input of the proposed 8-Bit BW-PDAC. The converted back discrete sampled and correspond filter out analogue signal are shown in Figure 3-78.

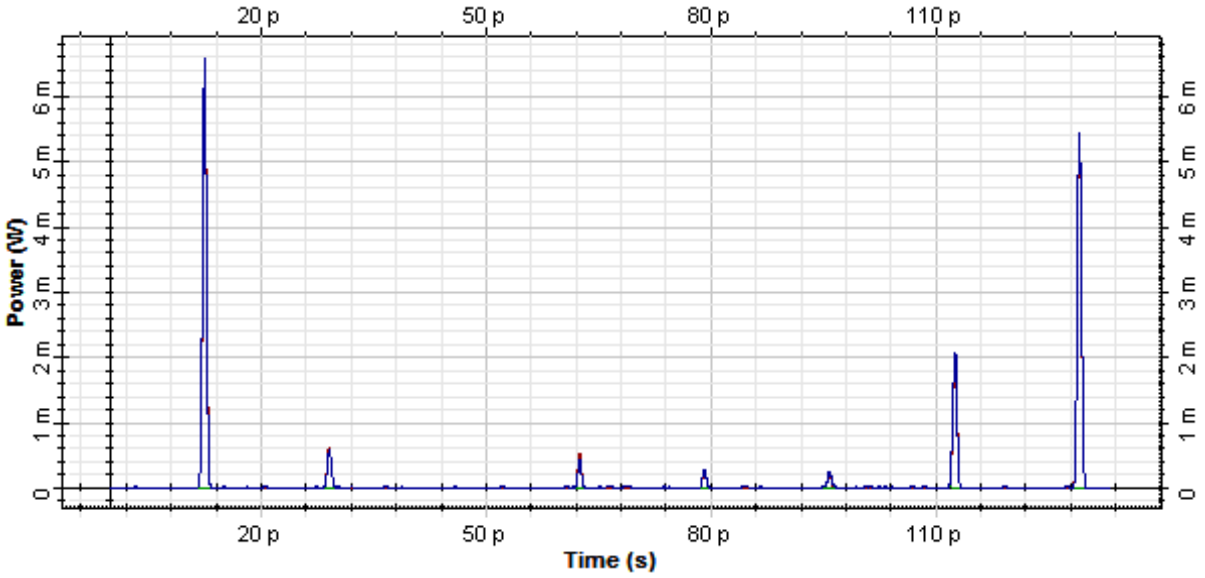

(a)

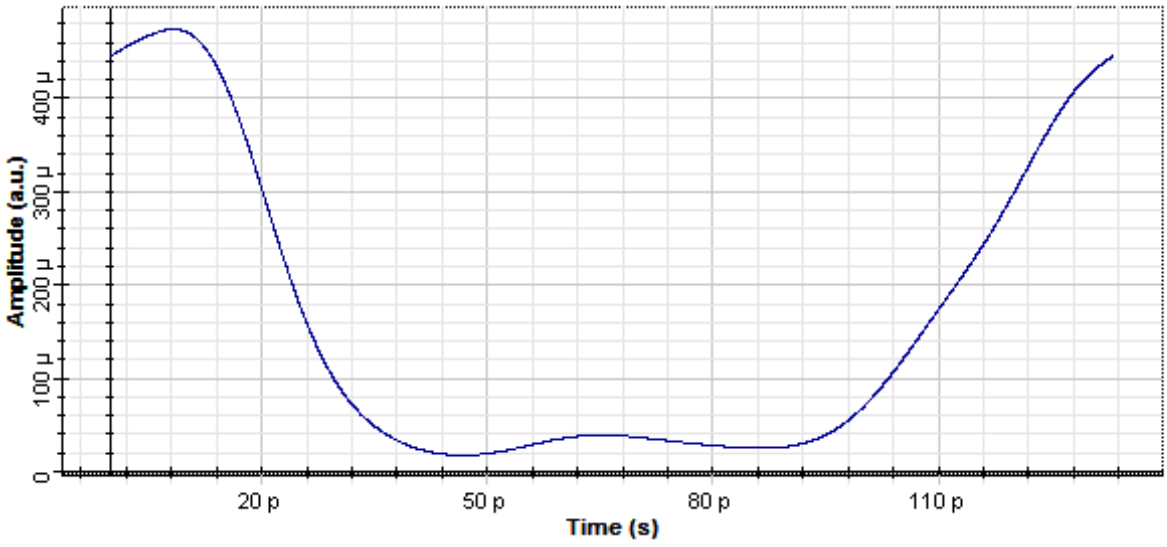

(b)

Figure 3-78: The converted back digital data to analogue waveforms by using PDAC: (a) The converted analogue discrete sample, (b) The analogue continuous signal at the output of a Gaussian low pass filter with 15 GHz bandwidth.

A back-to-back deployment of the proposed 8-bit PADC and the PDAC system is shown in Figure 3-79. In this demonstration setup, the MLLD pulses with a standard deviation about 0.017 of the bit period is modelled random and deterministic jitter which is simulated to sample a 3 GHz RF signal at 15 GHz sampling frequency and

the digital 8 bits sampled data are converted back into the analogue domain using the 8-Bit BW-PDAC. The simulated waveforms which are illustrated on this figure show the system functionality in time domain.

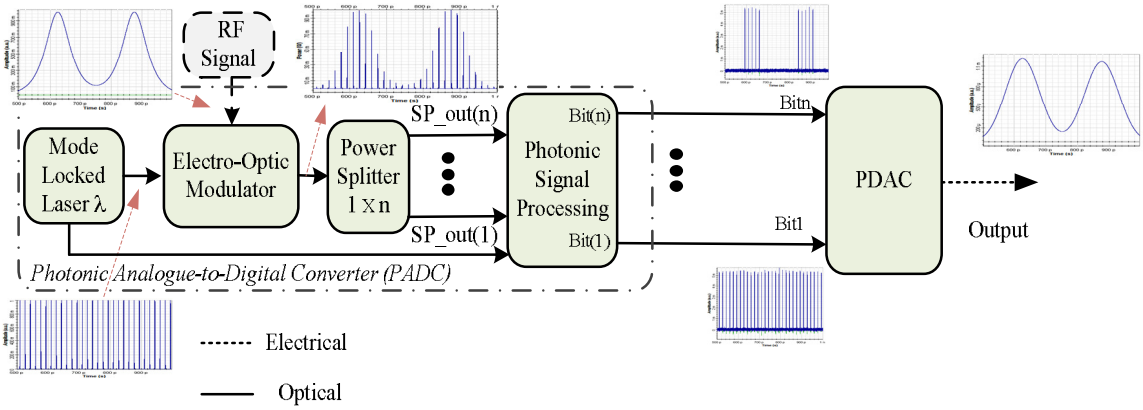

Figure 3-79: The back-to-back PADC and PDAC functionality evaluation in time domain for an input 3 GHz RF signal which is sampled at 15 Gsample/s.

3.11. Conclusion

In this chapter the two key components of the proposed FP-DRoF system are designed and their performance and physical functionality are investigated and evaluated using Optiwave-Optisystem and Matlab simulation tools. Theses two key components of the proposed FP-DRoF, the PADC and the PDAC are designed fully photonically and their performance and functionality are investigated at 60 GHz of sampling frequency.

The system simulation results show that the proposed pipelined PADC has 10 GHz bandwidth around 60 GHz of sampling frequency. Furthermore, by changing the bandwidth of the OBPF, switching to another band of sampling frequency will provide an optimised performance of the proposed PADC. It has evaluated that the PADC has approximately flat ENOB response for an RF input from 1 GHz up to 22 GHz. The proposed 8-Bit pipelined PADC performance in terms of ENOB is evaluated at 60 Gs/s which is about 4.1.

Different methods have been reported to implement PDACs, but the aim of reported method was to convert digital electrical signals to the corresponding analogue signal by assisting an optical technique. In the proposed BW-PDAC, optical digital signals

are fully optically converted to analogue signal. The SFDR at the output PDAC in a back-to-back setup of PADC and PDAC was 26.62 dBc.

3.12. References

[1] Arthur Gelb, and Wallace E. Vander Velde, Multiple-input describing functions and nonlinear system design, McGra-Hill, 1968.

[2] Ali Fard, Shalabh Gupta, and Bahram Jalali, "Digital Broadband Linearization Technique and its application to photonic time–stretch analog-to-digital converter", Optics Letters, vol. 36, No. 7, pp. 1077-1079, April 2011.

[3] R. H. Walden, "Analog-to-digital converter survey and analysis" , IEEE Journal of Selected Areas in Communications, vol. 17, no. 4, pp. 539-550, 1999.

[4] R. G. Vaughan, N. L. Scott, D. R. White, "The Theory of Bandpass Sampling", IEEE Transaction on Signal Processing, vol. 39, no. 9, pp.1973-1984, Sep. 1991.

[5] T. Li, M. Crisp, R. V. Penty, I. H. White, "Low Bit Rate Digital Radio over Fiber system", IEEE International Topical Meeting on Microwave Photonic, , pp. 1-4, 2009.

[6] S. Kuwano, Y. Suzuki, Y. Yamada, K. Watanabe, "Digitized Radio-over-Fiber (DRoF) System for Wide-Area Ubiquitous Wireless Network", IEEE International Topical Meeting on Microwave Photonic, pp. 1-4, 2006

[7] S. Kuwano, Y. Suzuki, Y. Yamada, Y. Fujinio, T. Fujiti, D. Uchida, K. Watanabe, "Diversity Techniques Employing Digitized Radio over Fiber Technology for Wide-Area Ubiquitious Network", IEEE Global Telecommunication Conference, (Globecom), pp. 1-5, Dec. 2008.

[8] C. Lim, A. Nirmalathas, M.Bakaul, P. Gamage, K. L. Lee, Y. Yang, D. Novak, R. Waterhouse , "Fiber-Wireless Networks and Subsystem Technologies", Journal of Lightwave Technology, vol. 28, no. 4, pp. 390-405, 2010.

[9] R. Stephens, "Jitter Analysis: The Dual-Dirac Model, RJ/DJ, and Q-sacle," Agilent Technical Note, Dec. 2004.

[10] Johnnie Hancock, " Jitter-Understanding it, Measuring it, Eliminating it, Part 1: Jitter Fundamentals" High Frequency Electronics, pp. 44-50, Summit Technical Media, LLC, April, 2004.

[11] G. C. Valley, "Photonic analog-to-digital converters," Optics Express, vol. 15, no. 5, pp. 1955-1982, 2007.

[12] J. Kim, M. J. Park, M. H. Perrott and F. Kartner, " Photonic subsampling analog-to-digital conversion of microwave signals at 40-GHz with higher than 7-ENOB resolution," Optics Express, vol. 16, no. 21, pp. 16509-16515, 2008.

[13] Walt Kester, Data Conversion Handbook, Elsevier, Analog Devices, 2005.

[14] Barry. L. Shoop, Photonic Analog-to-Digital Conversion, Springer, 2001.

[15] J. H. Reed, Software Radio: A Modern Approach to Radio Engineering. Upper Saddle River, NJ: Pearson Education, Inc., 2002.

[16] M. shinagawa, Y. Akazawa, and T. Wakimoto, "Jitter analysis of high-speed sampling system", IEEE Journal of Solid States Circuits and Systems, vol. 25, no. 1, pp. 220-224, Feb. 1990.

[17] Bin Le, Thomas w, Rondeau Jeffery H. Reed, and Charles. W. Bostion, " Analog-to-Digital Converters", IEEE Signal Processing Magazine, pp. 69-77, Nov. 2005.

[18] K. K. Markel and A. L. Wilson, "A survey of high performance analog-to digital converters for defence space applications", IEEE proceeding of Aerospace conference, vol. 5, pp. 2415-2427, March 2003.

[19] D. H. Auston, "Picosecond optoelectronic switching and gating in silicon," Applied Physics Letter 26, pp. 101-103,1975.

[20] R. A. Lawton and J. R. Andrews, "Optically strobed sampling oscilloscope," IEEE Trans. Instrum. Meas. 25, pp. 56-60, 1976.

[21] A. J. Low and J. E. Carroll, "10ps optoelectronic sampling system," Solid-State and Electron Devices 2, pp. 185- 190, 1978.

[22] C. H. Cox III, V. Diadiuk, I. Yao, F. J. Leonberger and R. C. Williamson, "InP optoelectronic switches and their high-speed signal-processing applications," Proc. SPIE 439, pp.164-168, 1983.

[23] C. K. Sun, C.-C. Wu, C. T. Chang, and W. H. McKnight, "A bridge type optoelectronic sample and hold circuit," Journal of Lightwave Technol. 9, pp.341-346, 1991.

[24] C. K. Sun, C. T. Chang, and W. H. McKnight, "A high-speed, high precision optically controlled sample and hold circuit for analog to digital conversion," Proc. SPIE 2051, pp. 758-767, 1993.

[25] C. K. Sun, D. T. Chang, G. A. Massey, T. Y. Lee, R. Yu, and D. J. Albares, "High energy and low jitter picosecond optical pulser for sample and hold," Proc. SPIE 3463, pp. 212-218, 1998.

[26] E. W. Jacobs, J.B. Sobti, V.F. Vella, R. Nguyen, D.J. Albares, R.B. Olsen, C.T. Chang, C.K. Sun, M.J. Choe, S. Beccue, R. Yu, J.P.A. van der Wagt, "Optically clocked track-and-hold for high-speed high-resolution analog-to-digital conversion," Technical Digest, IEEE International Topical Meeting on Microwave Photonics, pp. 190-192, 2004.

[27] R. Urata, R. Takahashi, V. A. Sabnis, D. A. B. Miller, and J. S. Harris, Jr., "Ultrafast differential sample and hold using low-temperature-grown GaAs MSM for photonic A/D conversion," IEEE Photonics Technology Letter, vol. 13, pp. 717-719, 2001.

[28] R. Urata, R. Takahashi, V. A. Sabnis, D. A. B. Miller, and J. S. Harris, Jr., "Ultrafast optoelectronic sample and hold using low-temperature-grown GaAs MSM," IEEE Photonics Technology Letter 15, pp.724-726, 2003.

[29] R. Urata, L. Y. Nathawad, R. Takahashi, K. Ma, D. A. B. Miller, B. A. Wooley, and J. S. Harris, Jr., "Photonic A/D conversion using low-temperature-grown GaAs MSM switches integrated with Si-CMOS," Journal of Lightwave Technology 21, pp.3104-3114, 2003.

[30] L. Y. Nathawad, R. Urata, B. A. Wooley, and D. A. B. Miller, "A 40-GHz-bandwidth, 4-bit, time-interleaved A/D converter using photoconductive sampling," IEEE Journal of Solid-State Circuits 38, pp. 2021-2030, 2003.

[31] K. Ma, R. Urata, D. A. B. Miller and J. S. Harris, Jr., "Low-temperature growth of GaAs on Si used for ultrafast photoconductive switches," IEEE Journal of Quantum Electronic, vol. 40, pp. 800-804, 2004.

[32] R. F. Pease, K. Ioakeimidi, R. Aldana, and R. Leheny, "Photoelectronic analog-to-digital conversion using miniature electron optics: Basic design considerations," J. Vac. Sci. Technol. 21, pp. 2826-2829, 2003.

[33] K. Ioakeimidi, R. F. Leheny, S. Gradinaru, P. R. Bolton, R. Aldana, K. Ma, J. E. Clendenin, J. S. Harris, Jr.,and R. F. W. Pease, "Photoelectronic analog-to-digital conversion: sampling and quantizing at 100 Gs/s," IEEE Trans. Microwave Theory and Tech., vol. 53, pp. 336-342, 2005.

[34] H. Zmuda and S. Hanna, "High-speed, high resolution optically assisted analog-to-digital conversion," Proc. SPIE 5435, pp. 153-163, 2004.

[35] H. Zmuda, S. Hanna, R. J. Bussjager, M. L. Fanto, M. J. Hayduk, S. T. Johns, J. E. Malowicki, and P. L. Repak, "Optically assisted high-speed, high resolution analog-to-digital conversion," Proc. SPIE 5814, pp. 51-61 , 2005.

[36] A. Johnstone, M. F. Lewis, and J. D. Hares "Optical replication technique for wideband transient waveform digitisation," Proc. SPIE 3285, pp. 209-216, 1998.

[37] A. Johnstone, M. F. Lewis, J. D. Hares, and P. A. Kellett, "High-speed opto-electronic transient waveform digitiser," 3rd International Conf. on Advanced

A/D and D/A Conversion Techniques and their Applications, no. 466, pp. 21-24, 1999.

[38] R. H. Walden, "Analog-to-digital converter survey and analysis," IEEE Journal of Selected. Areas Communication, 17, pp. 539-550, 1999.

[39] R. H. Walden, "Analog-to-digital conversion in the early 21st century," 2006.

[40] Y. Han, O. Boyraz, and B. Jalali, "Real-time A/D conversion at 480 GSample/s using the phase diversity photonic time-stretch system," Proc. Microwave Photonics 2004, pp. 186-189, 2004.

[41] J. Stigwall and S. Galt, "Signal reconstruction by phase retrieval and optical back-propagation in phasediverse photonic time-stretch systems," submitted to Journal of Lightwave Technology, 2006.

[42] Ali Fard, Shalabh Gupta, and Bahram Jalali, "Digital broadband linearization technique and its application to photonic time-stretch analog-to digital converter", Optics Letter, vol. 36, no. 7, pp. 1077-1079, April 2011.

[43] Ali Fard, Brandon Buckley, and Bahram Jalali, "Spectral Efficiency Improvement in Photonic Time-Stretch Analog-to-Digital Converter via Polarization Multiplexing", IEEE Photonics Technology Letters, vol. 23, no. 14, pp. 947-949, July 15, 2011.

[44] Rany R. Reibel Calvin C. Harrington, Jason R. Dahl, Charls, N. Ostrander, Peter A. Roos, R. Krishna Mohan, and Wm. Randall Rabitt, "Demonstration of Analog-to-Digital Conversion Using Spatial-Spectral Holography", OFC/NFOEC 2008, pp. 1-3, 2008.

[45] W. R. Rabbitt, M. A. Neifeld, and K. D. Merkel, " Broadband analog to digital conversion with spatial-spectral holography," Journal of Luminescence, vol. 127, pp. 152-157, 2007.

[46] Randy Ray Reibel1, Calvin Harrington1, Jason Dahl, Charles Ostrander, Peter Aaron Roos, Trenton Berg, R. Krishna Mohan1, Mark A. Neifeld, and Wm.

Randall Babbitt, "Demonstrations of analog-to-digital conversion using a frequency domain stretched processor", Optics Express, vol. 17, no. 14 , pp. 11281-11286, July 2009.

[47] C. H. Cox, III, Analog Optical Links, Cambridge University Press, Cambridge UK, 2004.

[48] G. P. Agrawal, Fiber-Optic Communication Systems, Wiley, New York, 336-343, 1997.

[49] R. Helkey, "Narrow-band optical A/D converter with suppressed second-order distortion," IEEE Photonics Technology Letters, vol. 11, pp. 599-601, 1999.

[50] J. C. Twichell, and R. Helkey, "Phase-encoded optical sampling for analog-to-digital converters," IEEE Photonic Technology Letters, vol. 12, pp. 1237-1239, 2000.

[51] D. Ralston, A. Metzger, Y. Kang, P. Asbeck and P. Yu, "Highly linear photoreceiver design for application to ultrahigh bandwidth photonic A/D converters," Proc. SPIE 4112, pp. 132-140, 2000.

[52] T. R. Clark, M. Currie, and P. J. Matthews, "Digitally linearized wide-band photonic link," Journal of Lightwave Technology, vol. 19, pp. 172-179, 2001.

[53] X. Meng, "Designing high dynamic range microwave photonic links for radio applications," Fiber and Integrated Optics 23, pp. 1-56, 2004.

[54] H. Zmuda, "Analog-to-digital conversion using high-speed photonic processing," Proc. SPIE 4490, pp. 84-95, 2001.

[55] H. Zmuda, E. N. Toughlian, G. Li and P. LiKamWa, "A photonic wideband analog-to-digital converter," IEEE Proceedings 2001 Aerospace Conference 3, 1461-1472, 2001.

[56] H. Zmuda, M. J. Hayduk, R. J. Bussjager, and E. N. Toughlian, "Wavelength-based analog-to-digital conversion," Proc. SPIE 4547, pp. 134-145, 2002.

[57] E. N. Toughlian and H. Zmuda, "A photonic wideband analog to digital converter," International Topical Meeting on Microwave Photonics 2000, Digest 248-250,2000.

[58] M. Johansson, B. Lofving, S. Hard, L. Thylen, M. Mokhtari, U. Westergren and C. Pala, "Study of an ultrafast analog-to-digital conversion scheme based on diffractive optics," Applied Optics, vol. 39, 2881-2887 (2000).

[59] C. Pala, L. Thylen, M. Mokhtari, and U. Westergren, "A high-speed electro-optical analog-to-digital converter principle," The 2001 IEEE International Symposium on Circuits and Systems, ISCAS 2001 1, pp. 432- 435, 2001.

[60] J. Stigwall and S. Galt, "Analysis of the resolution-bandwidth-noise trade-off in wavelength-based photonic analog-to-digital converters," Applied Optics, vol. 45, 4310-4318, 2006.

[61] J. Stigwall, "Photonic Analog-to-Digital Conversion," Thesis for the degree of licentiate of engineering, Chalmers University of Technology, Goteborg, Sweden, 2004.

[62] H. F. Taylor, "An optical analog-to-digital converter—design and analysis," IEEE Journal of Quantum Electron, vol. 15, pp. 210-216, 1979.

[63] H. F. Taylor, "An electro-optic analog-to-digital converter," Proc. IEEE 63, pp. 1524-1525, 1975.

[64] H. F. Taylor, H. F., M. J. Taylor, and P. W. Bauer, "Electro-optic analog-to-digital conversion using channel waveguide modulators," Applied Physics Letter, vol. 32, pp. 559-561, 1978.

[65] P. E. Pace and D. D. Styer, "High-resolution encoding process for an integrated optical analog-to-digital converter," Opt. Eng. 33, pp. 2638-2645, 1994.

[66] B. Jalali and Y. M. Xie, "Optical folding-flash analog-to-digital converter with analog encoding," Optics Letters, vol. 20, pp. 1901-1903, 1995.

[67] K. Ikeda, J. M. Abdul, S. Namiki, and K. Kitayama, "Optical quantizing and coding for ultrafast A/D conversion using nonlinear fiber-optic switches based on Sagnac interferometer," Optics Express 13, pp. 4296- 4302, 2005.

[68] K. Ikeda, J. M. Abdul, H. Tobioka, T. Inoue, S. Namiki, K. Kitayama, "Design considerations of all-optical A/D conversion: nonlinear fiber-optic sagnac-loop interferometer-based optical quantizing and coding," Journal of Lightwave Technology, vol. 24, pp. 2618-2628, 2006.

[69] Shuna Yang, Zhiguo Shi , Hao Chi a, Xianmin Zhang a, Shilie Zheng, Xiaofeng Jin, Jianping Yao "Photonic analog-to-digital conversion using multiple comparators and Mach-Zehnder modulators with identical half-wave voltages", Elsevier Optics Communications 282, pp. 504–507, 2009.

[70] B. Jalali and Y. M. Xie, "Optical folding-flash analog-to-digital converter with analog encoding", Optics Letters, vol. 20, no. 18, pp. 1901-1903, September 15, 1995.

[71] Marc Currie, "Optical Quantization of Microwave Signals Via Distributed Phase Modulation", Journal of Lightwave Technology, vol. 23, no. 2, pp. 827-833, February 2005.

[72] H. Chi, Z. Li, X. Zhang, S. Zheng, X. Jin, and J. P. Yao, "Proposal for photonic quantization with differential encoding using a phase modulator and delay-line interferometers", Optics Letters, vol. 36, no. 9, pp. May 1, 2011.

[73] Hao Chi, and Jianping Yao , "A photonic analog-to-digital conversion scheme using Mach-Zehnder modulators with identical half-wave voltages" Optics Express, vol. 16, no. 2, pp. 567-572, January 2008.

[74] Shuna Yang, Zhiguo Shi, Hao Chi, Xianmin Zhang, Shilie Zheng, Xiaofeng Jin, Jianping Yao, "Photonic analog-to-digital conversion using multiple comparators and Mach-Zehnder modulators with identical half-wave voltages",Elceveir Optics Communications 282, pp. 504–507, 2009.

[75] Henry F. Taylor, "An Optical Analog-to-Digital Converter-Design and Analysis", IEEE Journal of Quantum Electronics, vol. QE-15, no. 4, April 1979.

[76] Anatol Khilo et. Al, "Photonic ADC: overcoming the bottleneck of electronic jitter", Optics Express, vol. 20, no. 4, pp.445413-4469, Feb. 2012.

[77] S. Wright, I. M. Mason, M. G. F. Wilson, "High-speed electro-optic analogue-digital conversion," Electron. Lett. 10, pp. 508-509, 1974.

[78] Y. Tsunoda and J. W. Goodman, "Combined optical AD conversion and page composition for holographic memory applications," Applied Optics, vol. 16, pp. 2607-2609, 1977.

[79] Y. Li and Y. Zhang, "Optical analog-to-digital conversion using acousto-optic theta modulation and table lookup," Applied Optics, vol. 30, pp. 4368-4371, 1991.

[80] J. Stigwall and S. Galt, "Demonstration and analysis of a 40-Gigasample/s interferometric analog-to-digital converter," Journal of Lightwave Technology, vol. 24, pp. 1247-1256, 2006.

[81] J. Stigwall and S. Galt, "Analysis of the resolution-bandwidth-noise trade-off in wavelength-based photonic analog-to-digital converters," Applied Optics, vol. 45, pp. 4310-4318, 2006.

[82] Wangzhe Li, Hongming Zhang, Qingwei Wu, Zhuangqian Zhang, and Minyu Yao, "All-Optical Analog-to-Digital Conversion Based on Polarization-Differential Interference and Phase Modulation", IEEE Photonics Technology Letters, vol. 19, no. 8, pp. 625-627, April 15, 2007.

[83] Qingwei Wu, Hongming Zhang, Minyu Yao, and Wei Zhou, "All-Optical Analog-to-Digital Conversion Using Inherent Multiwavelength Phase Shift in LiNbO3 Phase Modulator", IEEE Photonics Technology Letters, vol. 20, no. 12, pp. 1036-1038, June 15, 2008.

[84] Qingwei Wu, Hongming Zhang, Yue Peng, Xin Fu and Minyu Yao, "40GS/s Optical analog-to-digital conversion system and its improvement", OPTICS EXPRES, vol. 17, no. 11, pp. 9252-9257, 25 May 2009.

[85] Yue Peng, Hongming Zhang, Qingwei Wu, Xin Fu, Yuancheng Zhang and Minyu Yao, "A Novel Proposal of All-Optical Analog-to-Digital Conversion with Unbalanced MZM and Filter Array", Proceedings of the 15th Asia-Pacific Conference on Communications (APCC 2009), no.115, pp. 485-486, 2009.

[86] Xin Fu, Hongming Zhang, Minyu Yao, "A New Proposal of Photonic Analog-to-Digital Conversion Based on Polarization Modulator and Polarizer", Proceedings of the 15th Asia-Pacific Conference on Communications (APCC 2009)-137, pp. 572-574, 2009.

[87] H. Chi, Z. Li, X. Zhang, S. Zheng, X. Jin, and J. P. Yao , "Proposal for photonic quantization with differential encoding using a phase modulator and delay-line interferometers", Optics Letters, vol. 36, no. 9, pp. 1629-1631, May 1, 2011.

[88] Yang Wang, Hongming Zhang, Qingwei Wu, and Minyu Yao, "Improvement of Photonic ADC Based on Phase-Shifted Optical Quantization by Using Additional Modulators" IEEE Photonics Technology Letters, vol. 24, no. 7, pp. 566-568, April 1, 2012.

[89] Marc Currie, Thomas R. Clark, and Paul J. Matthews, "Photonic Analog-to-Digital Conversion by Distributed Phase Modulation", IEEE Photonics Technology Letters, vol. 12, no. 12, pp.1689-169, Dec. 2000.

[90] Marc Currie, "Optical Quantization of Microwave Signals Via Distributed Phase Modulation", Journal of Lightwave Technology, vol. 23, no. 2, pp. 827-833, February 2005.

[91] Moshe Nazarathy and Oded Shaham, " Spatially distributed successive approximation register (SDSAR) photonic ADCs based on phase-domain quantization", Optics Express, vol. 20, no. 7, pp. 7833-7869, 26 March 2012.

[92] P. E. Pace, S. J. Ying, J. P. Powers, and R. J. Piepe, "Optical Sigma-Delta Modulation Using Fiber Lattice", The twenty-ninth conference on Asilomar , vol. 1, pp. 103-107, Feb., 1995.

[93] P. E. Pace, S. J. Ying, J. P. Powers, and R. J. Piepe , "Integrated optical sigma-delta modulators", Optical Engineering 35(07), pp. 1828-1836, July 1996.

[94] B. L. Shoop and J. W. Goodman, "Optical oversampled analog-to-digital conversion," Applied Optics, vol. 31, pp. 5654-5660, 1992.

[95] A. P. Willis, D. Griffiths, and P. B. Atanackovic, "The use of unipolar loop signals in the error diffusion modulator," IEEE Trans. Circuits and Syst. II 45, pp. 1597-1599, 1998.

[96] Qiao Yang and Xiaobo Wu, "Power Optimization for Pipeline ADC Via Systematic Automation Design" proceeding of the International Multi Conference of Engineers and Computer Scientists, vol. II, pp. 1-6, IMECS 2010.

[97] Fan Ye, Long Cheng, Kaihui Lin, and Junyan Ren, "An 80-MS/s 14-bit pipelined ADC featuring 83 dB SFDR", Springer Analog Integrated Circuits and Signal Processing, vol. 63, pp. 503-508, 2010.

[98] B. Jalali-Farahani and A. Meruva, "A 14-b 32 MS/s pipelined ADC with fast convergence comprehensive background calibration", Analog Integrated Circuits and Signal Processing, Springer, vol. 61, pp. 65-74, 2009.

[99] Orazio Svelto, "Principles of Lasers", 5th Edition, Springer, 2010.

[100] Govind P. Agrawal, "Nonlinear Fiber Optics", Academic Press, Third Edition, 2001.

[101] G. P. Agrawal, Fiber-optic communication systems, 3rd ed. New York: John Wiley & Sons, Inc., 2010.

[102] R. Paschotla, A. Schlatter, S.C. Zeller, H.R. Telle, and U. Keller ,"optical phase noise and carrier-envelope offset noise of mode-locked lasers", Journal of Applied Physics, B82, pp. 265-273, 2006.

[103] Ryan P. Scott, Theresa D. Mulder, Katherine A. Baker, and Brian H. Kolner, "Amplitude and Phase noise sensitivity of mode locked Ti: sapphire lasers in terms of complex noise transfer function", Optics Express, vol. 14, pp. 9090-9095, July. 2007.

[104] Johnnie Hancock, "Field Guide to Laser pulse Generation", SPIE press Bellingham WA, 2007.

[105] Chun-Ting Lin, Jason Chen, Sheng-Peng Dai, Peng-Chun Peng, and Sien Chi, " Impact of nonlinear transfer function and impact splitting ratio of MZM on optical up-conversion employing double sideband with carrier suppression modulation", Journal of Lightwave Technology, vol. 26, no. 15, pp. 2449-2459, Aug. 2008.

[106] B. G. Korenev, Bessel Functions and Their Applications, Taylor and Francis, 2002.

[107] R. C. Hollins, "Materials for optical limiters", Current Opinion in Solid State and Material Science, vol. 4, pp. 189-196, 1999.

[108] Y. P. Sun and J. E. Riggs, "Organic and inorganic optical limiting materials from fullerenes to nanoparticles", International Reviews in Physical Chemistry, Taylor & Francis, vol. 18, no. 1, pp.43-90, 1999.

[109] M. P. Joshi, J. Swiatkiewiez, F. Xu. P. N. Prasad, B. A. Reinhard, and R. Kannan, " Energy transfer coupling of two-photon absorption and reverse saturable absorption for enhanced optical power limiting", Optics Letters, vol. 23, Issue 22, pp. 1742-1744, 1998.

[110] F. E. Hernandez, S. Yang, E. W. Van Stryland, and D. J. Hagan, " High Dynamic range casecaded-focus optical limiter", Optics Letters, vol. 25, no. 16, Aug., 2000.

[111] Z. Jin. L. Huang, S. H. Gob, G. Xu and W. Ji, "Size dependent optical limiting behaviour of multi-walled carbon nanotubes", Chemical Physics Letters, vol. 352 pp. 328–333, 2002.

[112] Michael E. Derosa, and Stephan L. Logunov, "Fiber-Optic power limiter based on photothermal defocusing in an optical polymer", Applied Optics, vol. 42, no. 15, pp. May 2003.

[113] P. Wu. Reji Philip, R. B. Laghumavarapu, J. Devulapalli, D. V. G. Inrao, B. Kimball, M. Nkashima, and B. S. Decristafano, " Optical power limiting with photoinduced anisotropy of azobenzene films" Applied Optics, vol. 42, no. 22, pp. 4560-4565, Aug. 2003.

[114] George E. Dovgalenko, Mathew Klotz, and Gregory J. Salamo, Grary. L. Wood, "Optically induced birefringence in bacteriorhodospin as an optical limiter", Applied Physics Letters, vol. 68, issue 3, pp. 287-289, 1996.

[115] D. Narayana Rao, Chandra S. Yelleswarapu Sri-Rajasekhar Kothapalli and D. V. G. I. N Rao, "Self-Diffraction in bacteriorhodopsin films for low power optical limiting", Optics Express, vol. 11, no. 22, pp. 2848-2853, Nov. 2003.

[116] M Holtmannspoetter, and B. Schmauss, "All Optical Limiter Based on Self Phase Modulation and Dispersive Chirping", The European Conference on Lasers and Electro-Optics (CLEO/Europe), 2007.

[117] Hiroomi Goto, Tsuyoshi Konishi and Kazuyoshi Itoh, "An all-optical limiter with high-accuracy thresholding based on self-phase modulation assisted by preparatory waveform conversion" Journal of Optics A: Pure and Applied Optics, vol. 10, pp. 1-4, 2008.

[118] Lionel Provost, Christophe Finot, Periklis Petropoulos, Kazunori Mukasa, and David J. Richardson, "Design scaling rules for 2R-optical self-phase modulation-based regenerators", Optics Express, vol.15, no. 8, pp. 5100-5113, April 2007 .

[119] Lanlan Li, Jian Wu, Jifang Qiu, Bingbing Wu, Yan Li, Kun Xu, XiaoBing Hong, JinTong Lin, "Reconfigurable and Simultaneous Implementation of All-optical Logic Gate Using Four-Wave Mixing (FWM) in HNLF for NRZPolSK signal" 36th European Conference and Exhibition on Optical Communication (ECOC), pp. 1-3, 2010

[120] Fang Qiu , " Wavelength tolerance of an all-optical multi-logic gate based on XPM in a HNLF", 16th Optoelectronics and Communications Conference (OECC), pp. 573 – 574, 2011

[121] K. Sun, J. Qiu, M. Rochette, L. R. Chen , "All-Optical Logic Gates (XOR, AND, and OR) Based on Cross Phase Modulation in a Highly Nonlinear Fiber", 35th European Conference on Optical Communication, ECOC '09, pp. 1-2, 2009.

[122] Kristian E. Stubkjaer, "Semiconductor Optical Amplifier-Based All-Optical Gates for High-Speed Optical Processing", IEEE Journal on Selected Topics in Quantum Electronics, Vol. 6, No. 6, pp. 1428-1435, Nov. 2000.

[123] M. Currie and J.W. Lou, "Weighted, summing photonic digital-to-analogue converter", IEEE Electronics Letters, vol. 42, no. 1, pp.1-2, January 2006.

[124] A. Leven, Y. Yang, J. Lin1, P. Kondratko2, A. Tate, T. C. Hu, N. G. Weimann, Y. K. Chen, "High Speed Integrated InP Photonic Digital-to-Analog Converter", International Conference on Indium Phosphide and Related Materials Conference Proceedings, pp. 14-15, 2006.

[125] Yue Peng, Hongming Zhang, Yuancheng Zhang, and Minyu Yao, "Photonic digital-to-analog converter based on summing of serial weighted multiwavelength pulses", IEEE Photonics Technology Letters, vol. 20, no. 24, pp. 2135-2137, Dec., 2008.

[126] Yossef Ehrlichman, Ofer Amrani, and Shlomo Ruschin, "Improved Digital-to-Analog Conversion Using Multi-Electrode Mach–Zehnder Interferometer", IEEE Journal of Lightwave Technology, vol. 26, no. 21, pp. 3567-3575, Nov., 2008.

[127] Jinxin Liao, He Wen, Xiaoping Zheng, Hanyi Zhang, Yili Guo, and Bingkun Zhou, "Novel 2N bit bipolar photonic digital-to-analog converter based on optical DQPSK modulation coupled with differential detection" OPTICS LETTERS / Vol. 37, no. 9, pp. 1502-1504, May 2012.

[128] Ransom Stephens, "Analyzing Jitter at High Data Rates", IEEE Optical Communication, pp. 6-10 , Feb. 2004.

[129] Zhang Lixun*, Liu Yongzhi, Liu Yong , "A novel optical coding method for all-optical A/D Conversion usingnonlinear optical switches based on the Sagnac interferometer", Procceding of SPIE, vol. 6839, pp.1-6, 2008.

Chapter 4

Digital Optical Pulse Regeneration

4.1. Introduction

In today's and future telecommunication systems and networks, ultra-high speed digital data and signal processing are key challenges which are facing the following bottlenecks: the speed of processing hardware, cost, power consumption, and performance. Furthermore, high speed electronic systems and signal processors are subject to a variety of impairments, such as: relatively high power consumption, the impact of higher order parasitic components, and electromagnetic interference at high frequencies. Digital signal processing is more reliable, robust, convenient, and cost-effective than analog signal processing. Therefore, digital system applications have grown very fast and digital signal processing data rates have been experiencing similar growth up to hundreds of gigabits per second.

As well as analog systems in networks causing impairments, there are impairments in the networks digital data processing systems that have different undesired impacts on signals amplitude and phase, such as: fluctuation of the amplitude of the pulses, uncertainty in connection with zero crossing and pulses duration times, transmission line delay and inter-symbol interference. Therefore, data retiming and reshaping are important, unavoidable and essential tasks associated with all digital circuits and systems. In conventional digital electronic systems, data retiming and reshaping is known as bit synchronization and data recovery. The basic conceptual architecture of a data recovery system is shown in Figure 4-1.

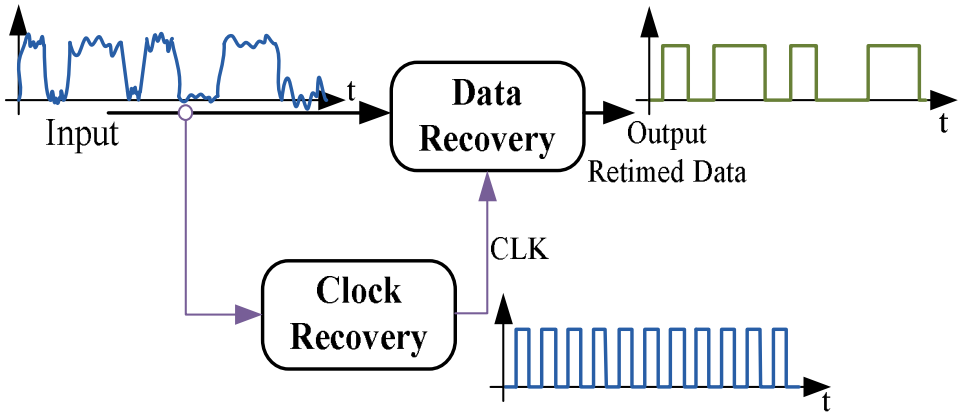

Figure 4-1: Basic architecture of data recovery.

This architecture includes two main subsystems: clock recovery and data recovery. In the process of clock recovery, the timing clock of random digital pulses will be recovered. In the process of data recovery, the recovered clock's phase is shifted so that it can be used for retiming the distorted digital data by sampling it in the midpoint of each bit interval. In this way, the retimed data is reshaped by the data recovery (DR) system.

When an optical data signal is transmitted, received, and recovered, it usually tolerates a number of inherent physical impairments induced by the link between the transmitter and the receiver. These physical impairments and noise cause different distortions of the signal's phase and amplitude. Consequently, the signal is degraded considerably during its propagation inside the fibre link. Optical amplifiers can be used to manage fibre losses, but they degrade the signal by adding amplified spontaneous emission (ASE) noise and timing jitter. These distortions of the phase and amplitude could be additive with the transmission distance and/or with a number of processes such as amplifying, multiplexing, demultiplexing, switching, etc. An optical regenerator transforms the degraded bit stream into its original form by performing three functions which are known as Reamplification, Reshaping, and Retiming. Such systems are referred to as "3R regenerators". The systems that perform only Reamplification and Reshaping are called "2R regenerators" and are important blocks of the modern optical communication system and network, while 3R regenerators a play key role when timing degradation of data is very high.

In this chapter, a photonic 3R regeneration system is proposed based on time stretching, optical sampling and optical hard limiting. System analysis and performance evaluation of the proposed system is discussed. Thus, the rest of this chapter is organized as follows: in section 4.2, all-optical 3R regeneration is described and its functional blocks are briefly discussed. The proposed system architecture is explained in section 4.3 which discusses the theoretical analysis of the proposed system, the modeling of the proposed system, and an investigation of its performance. Section 4.4 presents the conclusions.

4.2. All-Optical 3R Regeneration

There are different schemes for implementation of data recovery systems in electronic and photonic systems. In conventional implementation schemes for 3R regenerators, first the optical signal is converted to an electrical signal and clock recovery is applied followed by data retiming and reshaping in the electrical domain. Then, the recovered data is modulated onto an optical carrier. This process takes significant time in comparison with the bit time of the data traffic on a conventional optical network. Currently, data rates are growing very fast. Consequently, signal processing and conversion times: optical to electrical (O/E), electrical to optical (E/O) and signal processing in the electrical domain adds increasingly significant time delay. This delay causes data traffic congestion in the network.

Recent research has been highly focused on proposing cost-effective and applicable solutions that are based on fully optical 2R systems to mitigate the impact of congestion on network throughput. Many nonlinear techniques have been developed that make use of Self-Phase Modulation (SPM), Cross-Phase Modulation (XPM), and Four-Wave Mixing (FWM), and Stimulated Raman Scattering (SRS) [1].

All-optical 3R Regeneration is generally achieved using the scheme shown in Figure 4-2. In this scheme, the input (data) signal ($\lambda_{in}=\lambda_D$) follows two paths. In the top path, an optical clock signal is recovered (λ_c) using an optical clock recovery (OCR) system. In the bottom path, the clock and data signals are input into an

optical nonlinear medium, where the data (pump) signal intensity is used to optically gate the clock (probe) signal. Therefore, a high intensity probe signal opens the gate and a low intensity probe signal closes the gate. Throughout optical gating, intensity modulation on the data signal in the nonlinear medium is translated into the probe signal wavelength (λ_c). Therefore, an optical wavelength convertor is needed to transform the signal wavelength back to the original pump signal wavelength (λ_D).

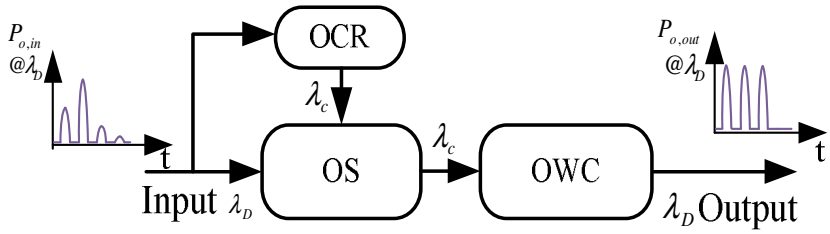

Figure 4-2: Generic architecture for all-optical 3R regeneration.

There are several methods available to perform Optical Sampling (OS), Optical Clock Recovery (OCR) and Optical Wavelength Conversion (OWC), which are presented in the following subsections.

4.2.1. Optical Sampling

There are different schemes for optical sampling such as: Cross-Absorption Modulation (XAM) [2-4], in this scheme the input high power pump signal is absorbed by the medium so that the gate can be opened or closed by the probe signal. XAM based sampling is sensitive to the input signal state of polarization [4], and wavelength [5][6]. Cross-Gain and Phase Modulation (XGM/XPM) is based on a combined effect of XGM and XPM. In this technique, a pump signal modulates the gain and phase of a probe signal in a medium such as a semiconductor optical amplifier (SOA) [7-13]. However, the long carrier recovery times of SOAs [14], additive amplified spontaneous emission (ASE) noise [15] and distortion of the regenerated signal caused by XGM, frequency chirp caused by XPM [16-18] and group velocity dispersion (GVD) [19] are important challenges of this scheme, as is the Four-Wave Mixing (FWM) that is caused by a nonlinear effect of third-order susceptibility in an optical medium. An optical fibre [20] or SOA can be used to

perform the optical sampling of the probe signal by using a pump signal. Because of ASE noise in SOAs, FWM efficiency in highly nonlinear fibre (HNLF) is significantly better than in a SOA medium [21-23]. However, in addition to the sensitivity of this scheme to the pump power that causes Self Phase Modulation (SPM) and XPM, the FWM is vulnerable to the input signal state of polarization, wavelength and power [24].

4.2.2. Optical Clock Recovery

There are different schemes of OCR system. The main challenges facing an all-optical clock recovery system are locking time, insensitivity to an absence of optical pulses, and the state of polarization.

Fabry-Perot Filters (FPFs) realize all-optical clock-recovery by optically filtering the clock harmonics of an input RZ signal. When the clock frequency component of an input signal coincides with one of the peaks in the transmission spectrum the clock frequency resonates in the FPF cavity [25]. Provided the free spectral range (FSR) is equal to the clock frequency of the input signal, the clock harmonic also resonates in the cavity. As a result, FPFs generate an optical clock signal oscillating at the clock frequency of the input signal. FPFs provide fast locking and release times [26]. The signal intensity fluctuation is caused by the exponential decay of resonant signals which occurs in the absence of clock signals, for example during a long 'zero' sequence. Since, FPFs with high finesse have longer decay times; they also exhibit less pattern effects. The tradeoff is that FPFs with higher finesse have a longer locking time, [27] and increasing sensitivity to variation in clock frequency [28]. FPFs with lower finesse have shorter locking and release times. However, they often suffer from intense pattern effects [29]. To compensate, amplitude equalization using an ultra-fast nonlinear interferometer (UNI) has been proposed, [27], but amplitude equalization increases FPFs complexity. Furthermore, FPFs are sensitive to the input signal wavelength. To satisfy the resonance condition, the input signal wavelength must be coincident with one of the transmission peaks. While the center frequency of the transmission peaks can be tuned by temperature the tuning range is often limited. In addition, FPFs are also sensitive to the input signal's state of

polarization [30]. Therefore, because of pattern effects and sensitivity to the input signal wavelength and state of polarization, FPFs are not the most suitable solution for OCR.

Several types of OCR system based on semiconductor laser based devices have been reported, such as mode-locked laser diodes (MLLDs), dual-mode Distributed Feedback Lasers (DFBLs) with two different sections (TS-DFBLs), amplified feedback DFB lasers (AFLs), and Self-Pulsating DFBLs (SP-DFBLs) [31-34][52]. Like FPFs, DFBLs have fast locking times. By stabilization of the clock signal amplitude the locking times of DFBLs based clock recovery systems have been demonstrated to be as short as FPFs locking times [35]. Fortunately, unlike FPFs, DFBLs do not exhibit pattern effects. DFBLs are capable of remaining synchronized to the clock frequency in the temporary absence an input signal, and over a wide range of input clock frequencies [36].

4.2.3. Optical Wavelength Conversion

All-optical wavelength converters (OWC) are considered key components in future wavelength division multiplexing (WDM) technique in optical networks due to their main advantages that comprise of enhancing the flexibility and capacity of these networks and facilitating their management. These systems can be implemented based on nonlinearity in any active or passive nonlinear medium such as SOA and HNLF, respectively. There are different realization methods for OWC implementation based on phase to amplitude modulation [48], and nonlinear optical signal processing such as XGM, XPM, and FWM [4][9][10][16][34]. XGM and XPM are polarization insensitive and have high efficiency while FWM is sensitive to signal polarization and power. The main features of the suitable techniques are polarization insensitivity, ease of implementation, low noise, low power cost, and integration potential with wavelength division multiplexing (WDM) systems [45][49-51].

4.3. System Architecture and Analysis

In this section, a photonic 3R regeneration system is proposed and system analysis and performance evaluation of the proposed system is discussed. The architecture of the proposed system is shown in Figure 4-3. In this system, suppose a sample random digital stream is fed to the 3R regenerator. The processing of the stream proceeds by performing the following key steps: a) time stretching of the input optical pulses, b) retiming of the pulses with reference sampling pulses, c) reshaping of the retimed the optical pulses.

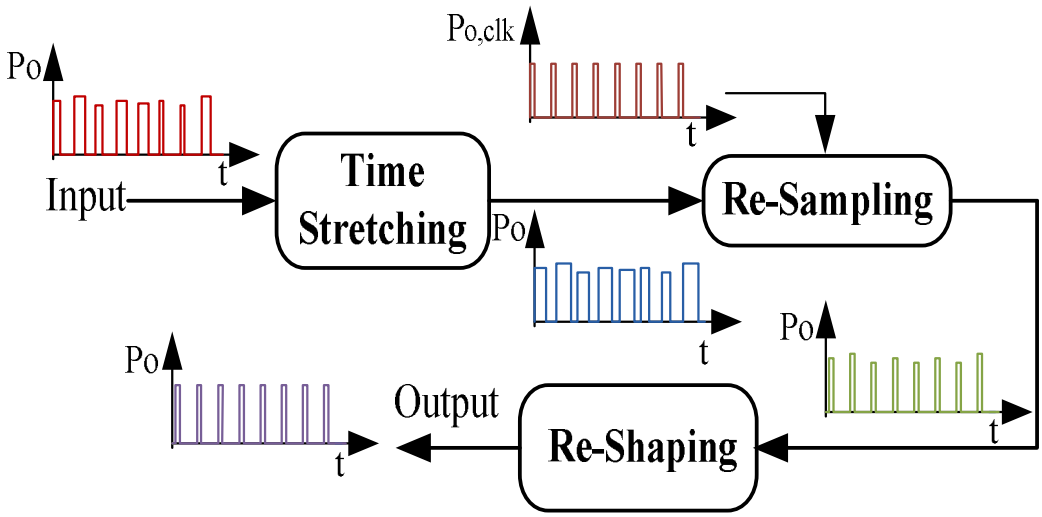

Figure 4-3: Proposed 3R regenerator architecture.

As shown in Figure 4-3, the ultra-short degraded optical pulses whose bit by bit time duration and intensity are not same have their time intervals broadened by the time stretching block. To rectify the variations in the pulses time duration and timing, the broadened optical pulses are fed to the resampling block to be retimed with recovered clock pulses. The duration of the retimed optical pulses is equal to the clock pulse width. The retimed optical pulses with different intensities are fed to the reshaping block to modify their amplitudes.

4.3.1 System Mathematical Theory

The mathematical model of the proposed 3R system is illustrated in Figure 4-4. In this analysis it is assumed that the power of a sample degraded optical pulse can be approximated as a Gaussian pulse:

$$P_D(t) = P_{D0} \exp(-\frac{t^2}{\tau^2}) \quad (4\text{-}1)$$

Where P_{D0} is the peak power and $\sqrt{2\ln(2\tau)}$ is the full wave half maximum (FWHM) time duration of the sample degraded optical pulse where $\ln(.)$ expresses the natural logarithm function. This signal is fed to the time stretching block.

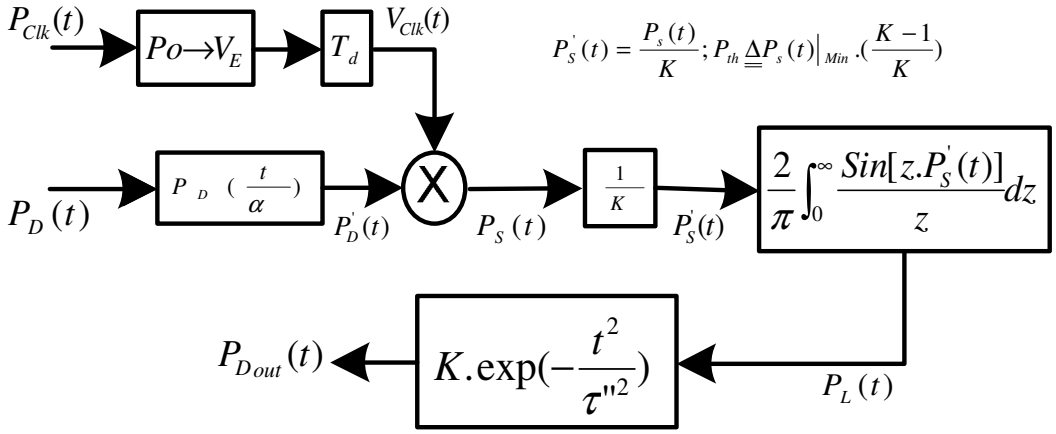

Figure 4-4: The proposed 3R data regeneration mathematical model.

The input degraded pulse τ value is stretched by $\Delta\tau = (a\text{-}1)\tau$ using dispersive fibre. Furthermore, the clock pulse is shifted to the middle of the bit interval by introducing a delay of about $T_d = T_s/2$ where $T_s \triangleq (\tau+\Delta\tau)$. Consequently, the time stretched Gaussian pulse is given by:

$$P_D^{'}(t) = P_{D0}^{'} \exp\left[-\left(\frac{t}{\tau+\Delta\tau}\right)^2\right] \quad (4\text{-}2)$$

The OCR system generates optical ultra-short clock pulses with low timing jitter that are given by:

$$P_{clk}(t) = P_{clk0} \exp(-\frac{t^2}{\tau'^2}) \quad (4\text{-}3)$$

Where $\tau' << \tau$ and is $\sqrt{2\ln(2\tau')}$ the FWHM of the clock pulse. The analytical calculation of the delay parameter T_d can be explained as follows: To perform proper sampling of a time stretched data pulse its time duration must be greater

than the recovered clock pulses width, $T_s > \tau'$. Furthermore, when the transmitted data rate B increases, the bit time $T_{bit} = 1/B$ of the transmitted data decreases accordingly. To prevent intersymbol interference the following inequality is enforced $T_s<T_{bit}$. Consequently, a suitable interval from which to choose a value for a is given by:

$$\frac{\tau'}{\tau} < \alpha < \frac{1}{B.\tau} \tag{4-4}$$

As $\tau' << \tau$, τ' is significantly less than T_s. Consequently, it is assumed that in the middle of a bit interval and for the time duration of the optical clock pulse, the amplitude of data power is approximately constant. Therefore, it is more likely to sample the correct value of the degraded signal. Furthermore, V_{clk} the corresponding voltage of the sampling clock pulse after detection by a photo diode is given by following equation:

$$V_{clk}(t) = V_{clk0} \exp(-\frac{t^2}{\tau'^2}) \tag{4-5}$$

Where V_{clk0} is the peak voltage. The electro-optical-modulator can be approximated as a multiplier according to the equation:

$$P_S(t) = \frac{\alpha_M . P_D^{'}(t)}{2} . \left[1 + \cos(\frac{\pi V_{clk}(t)}{V_\pi}) \right] \tag{4-6}$$

Where α_M is the insertion loss of the modulator [62]. If we define:

$$P_{clk}^{'}(t) \triangleq \cos(\frac{\pi V_{clk}(t)}{V_\pi}) \tag{4-7}$$

If we set $V_\pi = V_{clk0}$, $P'_{clk}(t)$ can be expressed as:

$$P_{clk}^{'}(t) = \cos(\pi \exp\left[-(\frac{t}{\tau'})^2 \right]) \tag{4-8}$$

Then by expressing the Taylor series of equation (4-8) around $t = T_d$ we get:

$$P_{clk}^{'}(t)=\cos(\pi\exp\left[-(\frac{T_d}{\tau'})^2\right])- \\ \frac{2\pi T_d}{\tau'^2}.\exp\left[-(\frac{T_d}{\tau'})^2\right].\sin(\pi\exp\left[-(\frac{T_d}{\tau'})^2\right])(t-T_d)+etc. \quad (4\text{-}9)$$

As the delay parameter T_d is significantly greater than the sampling clock pulse width τ', the ratio of $\frac{T_d}{\tau'}$ is very high. Therefore, the exponential term in equation (4-9) is very small. Consequently, the inside of the parentheses of the cosine function term of equation (4-9) can be approximated by 0. Therefore, this term is equal to 1. The term of the sine function is approximately equal to the term inside its parentheses. Therefore, equation (4-8) can be approximated as:

$$P_{clk}^{'}(t)=1-\frac{2\pi^2 T_d}{\tau'^2}.\exp\left[-2(\frac{T_d}{\tau'})^2\right](t-T_d) \quad (4\text{-}10)$$

Because of the very small impact of the higher order terms of equation (4-9), they are neglected in equation (4-10). Substituting equation (4-10) into equation (4-6) gives:

$$P_S(t)=\frac{\alpha_M.P_D^{'}(t)}{2}.\left[1+P_{clk}^{'}(t)\right] \\ =\alpha_M.P_D^{'}(t)-\frac{2\pi^2 T_d}{\tau'^2}.\exp\left[-2(\frac{T_d}{\tau'})^2\right](t-T_d).P_D^{'}(t) \quad (4\text{-}11)$$

From equation (4-11), the sampled signal power at $t=T_d$ is given by:

$$P_S(t)\Big|_{t=T_d}=\alpha_M.P_D^{'}(T_d) \quad (4\text{-}12)$$

Therefore, the effect of using an intensity electro-optical modulator, such as a Mach-Zehnder Modulator (MZM), can be approximated as that of a multiplier when the degraded data pulses power is sampled synchronously with ultra-short clock pulses. If we assume that the sampled signal $P_S(t)$ is attenuated with the rate K, $P'_S(t)$ can be approximated by:

$$P'_S(t)\approx P_S(t)-P_{th} \quad (4\text{-}13)$$

Where P_{th} is the attenuated power value from the $P_S(t)$ that can be expressed by:

$$P_S^{'}(t) = \frac{P_s(t)}{K} \tag{4-14}$$

$$P_{th} \triangleq \Delta P_s(t)\big|_{Min}.(\frac{K-1}{K}) \tag{4-15}$$

The signal $P_S^{'}(t)$ is fed to the reshaping block that consists of hard limiter and Gaussian filter blocks. At the hard limiter block, if the input sampled power is greater than a threshold value P_{th}, the output power value of the hard limiter, $P_L(t)$, is 'one' otherwise it is 'zero'.

$$P_L(t) = \frac{2}{\pi}\int_0^{\infty}\frac{\sin[z.P'_S(t)]}{z}dz = \begin{cases} 1 & if \;\; P_S(t) > P_{th} \\ 0 & if \;\; 0 < P_S(t) \le P_{th} \end{cases} \tag{4-16}$$

The digital values are passed through a Gaussian filter given by equation (4-17) to reshape them. The electrical field envelope, $E_L(t)$, of the hard limiter output is related to its output power, $P_L(t)$, and is given by:

$$E_L(t) = \sqrt{P_L(t)}\exp(j\omega_0 t) \tag{4-17}$$

Where ω_0 is the wave frequency. According to equation (4-16), if we suppose $P_L(t) \cong 1,\ 0 \le t \le T$, where T is the pulse width. The Fourier transform of the electrical field envelope of the hard limiter output is given by:

$$\tilde{E}_L(\omega) = 2\pi\delta(\omega - \omega_0) \tag{4-18}$$

Where $\delta(.)$ is the Dirac delta function and ω_0 is the optical carrier signal central frequency. The Fourier transform of the impulse response of a Gaussian filter which has a Gaussian transfer function is given by:

$$\tilde{H}_G(\omega) = \tau''\sqrt{\pi}\exp(-\frac{\tau''\omega^2}{4}) \tag{4-19}$$

Where $\sqrt{2\ln(2}\tau'')$ is the FWHM of the Gaussian filter impulse response. Therefore, the output field of the Gaussian filter block of the reshaping block can be expressed by:

$$\tilde{E}_{Dout}(\omega) = \tilde{E}_L(\omega).\tilde{H}_G(\omega)$$
$$= K.\exp(-\frac{\tau''(\omega-\omega_0)^2}{4}) \quad (4\text{-}20)$$

Where K is a constant. By taking the inverse Fourier transform of $\tilde{E}_{Dout}(\omega)$ given by equation (4-20), the field can be expressed by:

$$E_{Dout}(t) = K'.\exp(-\frac{t^2}{T'^2}).e^{j\omega_0 t} \quad (4\text{-}21)$$

Where K' is a constant and $\sqrt{2\ln(2T'})$ represents the FWHM of the filter output electrical field amplitude. Therefore, the output 3R regenerated pulse power is given by:

$$P_{Dout}(t) = K''.\exp(-\frac{t^2}{T^2}) \quad (4\text{-}22)$$

Where K'' is a constant and $\sqrt{2\ln(2T})$ is the FWHM time duration of the regenerated pulse.

4.3.2. Performance Evaluation and Analysis

To investigate the physical performance of the proposed architecture a model of the proposed system can be provided as follows: As shown in Figure 4-5 in the time stretching process by using a non-zero dispersion fibre length L1, the ultra-short distorted input optical pulses duration time is broadened. The clock is recovered using a coupled DFBL and Photo Diode (PD) pair and the delay block T_d is used to introduce a suitable delay of around half of a bit time on the clock signal and the delayed signal is fed to the RF input of a MZM to sample the input distorted optical pulses. The resulting retimed optical pulses are amplified by an Erbium Doped Fibre Amplifier (EDFA) G3 and fed into a optical power limiter [53-55] the output of

which is fed to an Optical Gaussian filter (OGF) to perform the pulse reshaping process. In this simulated model the splitter, Sp, is 50/50 and in Time Stretching block T_d is about 1.4 ps, the length of fibre L1 is about 100 m. The attenuation of fibre L1 is about 0.2 dB/km, its chromatic dispersion is about 16.75 ps/nm.km, its differential group delay is about 0.2 ps/km, and its polarization mode dispersion coefficient is about 0.5 ps/km$^{0.5}$. The bandwidth of OGF1 is 16nm. In the Retiming block the MZM extinction ratio is about 30 dB. The EDFA parameters are length 1m, core radius 2.2 um, Er doping radius 2.2 um, Er metastable lifetime 10 ms, numerical aperture 0.24, Er ion density 10e24 m-3, loss at 1550 nm 0.1 dB/km, loss at 980 nm about 0.15 dB/m, forward pump power 100 mW, forward pump wavelength 980nm, backward pump wavelength 980 nm, noise bandwidth 13 THz. Finally, for the Reshaping block the modeled power limiter threshold level is 1 mw and the OGF2 bandwidth is 20 nm.

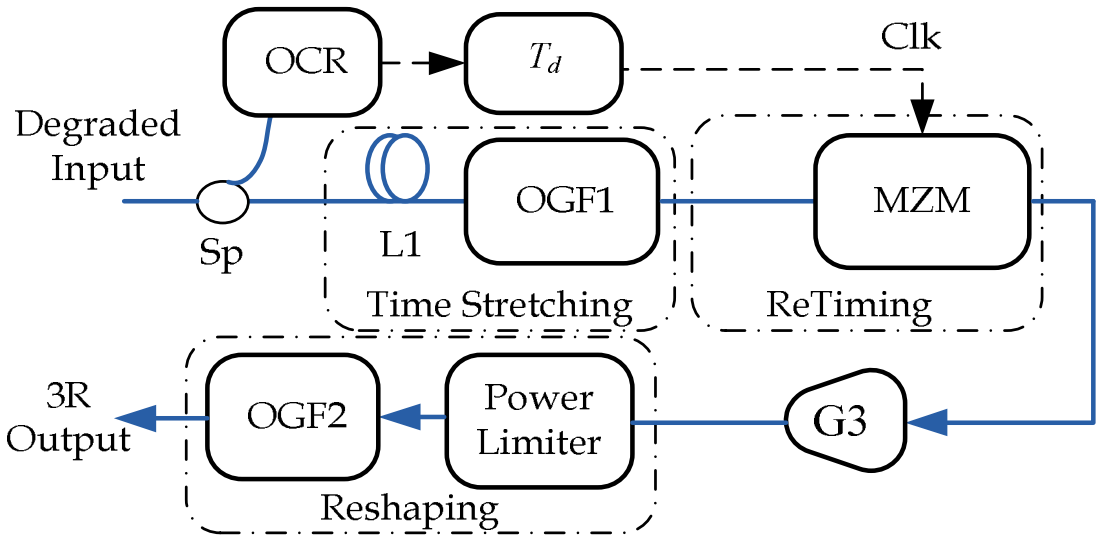

Figure 4-5: The simulated retiming and reshaping architecture.

To evaluate the proposed system's performance in conditions very close to those of a practical network, a random digital RZ data sequence is fed to a modeled degradation channel that adds phase and amplitude noise to the random RZ sequence that is shown in Figure 4-6. Pseudo random generator 1 (RN1) generates a sequence to model the RZ data. The random RZ data is passed through a Gaussian Low-Pass Filter (GLPF1) with 3-dB bandwidth equal to the digital input signal

bandwidth for Gaussian shaping of the transmitted RZ data. The output of GLPF1 is fed to an adder input where phase noise is added to the data signal. This added phase noise produces random and deterministic timing jitters on the zero crossing of the random data sequence [57-59]. Afterward, phase distorted random data is modulated onto an optical constant wave (CW) carrier using an intensity modulator (IM). The CW carrier is generated by a laser diode (LD) with 10 MHz linewidth, 1554 nm wavelength, 10 dBm power and optical signal to noise ratio (OSNR) of about 110 dB. The IM output is amplified by an optical amplifier (G1) with a gain of 10, and noise figure (NF) of about 4 dB. The OSNR at the output of G1 is about 19.7 dB. The amplitude noise is added to the modulated signal at this stage while the phase noise is added in electrical domain.

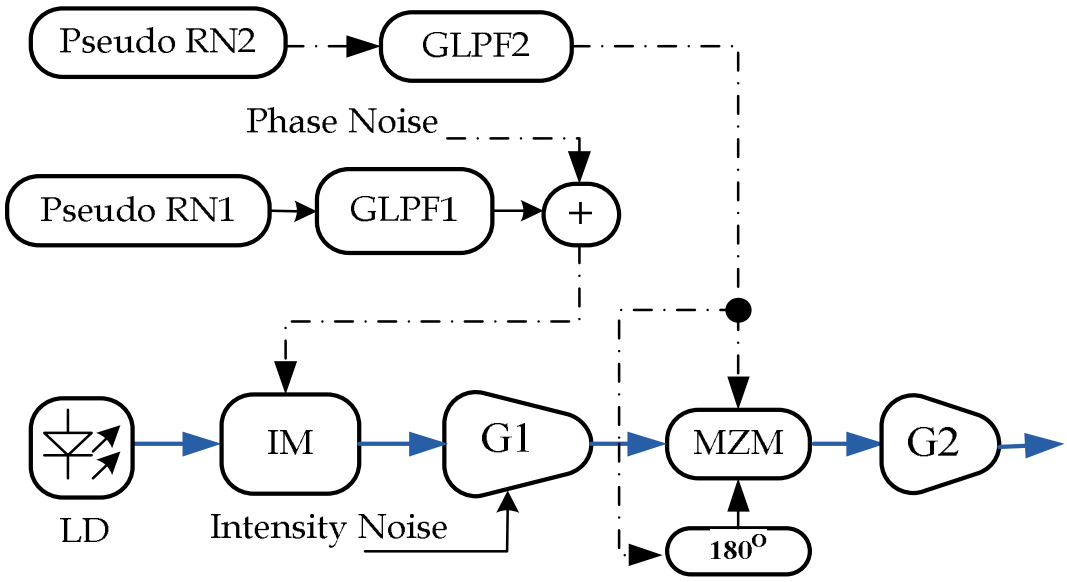

Figure 4-6: The simulation model for generating degraded optical pulses.

In addition, the AM noise will add some FM noise to the optical signal [56]. Furthermore, to model the intersymbol interference (ISI) throughout the data transmission in the link, a second pseudo random generator is used (RN2) that generates random data at a much lower rate than RN1. The output of RN2 is fed to GLPF2 to shape the signal. The output of GLPF2 is modulated onto the optical distorted data output from amplifier G1 with a 4 dB noise figure by using a dual driven MZM with a Vbis1 of about -2.8 V and a Vbis2 of about -1.1 V, and a

modulation voltage of about 0.6 V. The output signal of MZM is amplified using amplifier G2 which has a NF of about 4 dB and a gain of about 6 dB. The output of amplifier G2 as a degraded signal is fed to the 3R regeneration system shown in Figure 4-5. The OSNR at the output of G2 is about 16.8 dB.

To investigate the 3R regenerator's performance, the simulation model shown in Figure 4-7 was implemented. The model of receiver photo diode used is an avalanche photo diode (APD) with 2 dB gain, 1 A/W responsivity and 10 nA dark current.

The simulation model of Figure 4-7 is for investigation of the performance of the 3R regenerator against sampling clock pulses timing jitter. In this model, the degraded data is split into three parts. The first part is fed to the OCR block that generates a sampling clock pulse. The second part is connected to the time stretching block of the 3R regeneration system. The third part is fed to an attenuator followed by a photo diode to detect the degraded signal so its timing jitter and intensity fluctuation can be investigated for comparison with the corresponding parameters of the 3R regenerated signal.

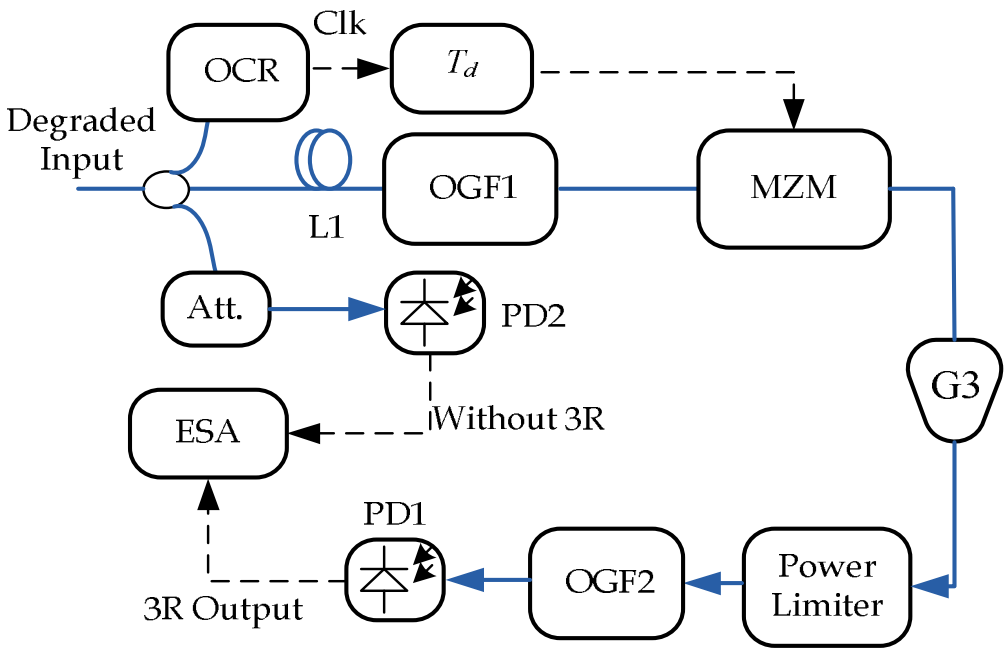

Figure 4-7: The simulation model for investigating the 3R regenerator's performance and measuring the rms timing jitter.

Figure 4-8 shows the eye diagram of the degraded signal, which has significant intensity fluctuation and timing jitter on the pulses zero crossing, and the eye diagram of the signal after 3R regeneration.

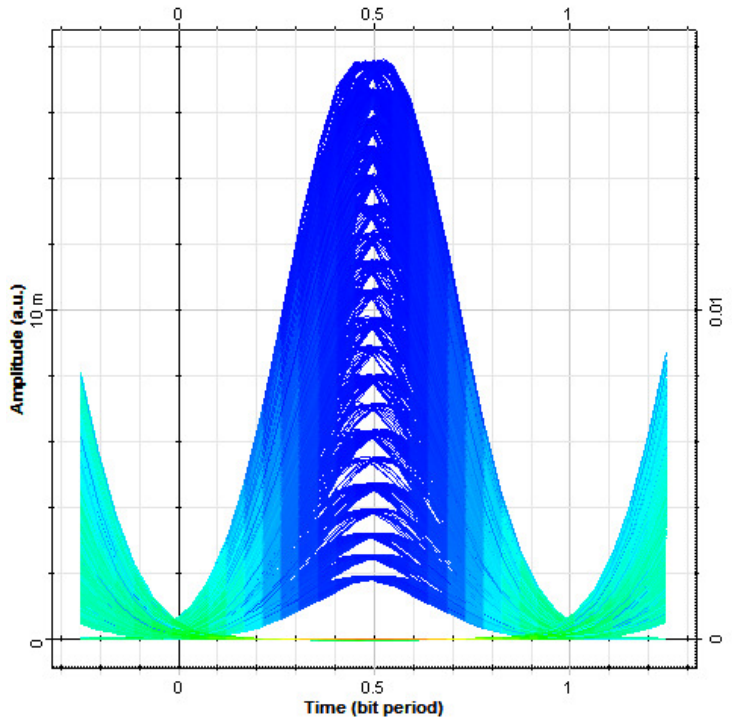

(a)

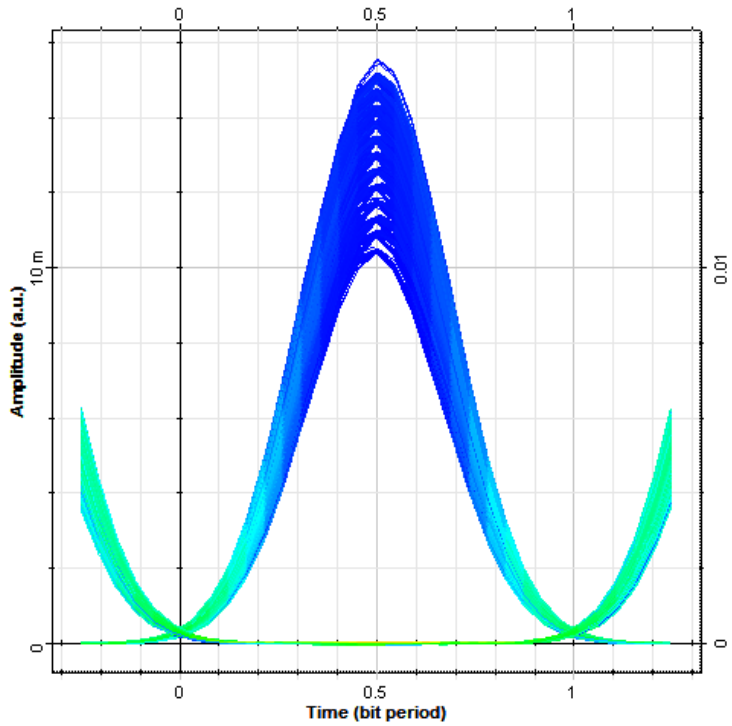

(b)

Figure 4-8: Eye diagram of signals: (a) Before 3R regeneration, (b) After 3R regeneration.

As shown in Figure 4-8 (a), the height of the eye opening of the degraded signal is about 10.08% of the signal intensity. The eye opening increases to 67.5% after the 3R regeneration process. Furthermore, the rms timing jitter of the degraded signal is about 823 fs at 65 Gbit/sec against the 87.9 fs rms timing jitter of the 3R regenerated signal. The rms jitter of the sampling clock was about 69.2 fs in this case. Therefore, it is clear that the 3R regenerator reduces the signal timing jitter by 91.5% and the height of the eye opening by 57.42%.

Figure 4-9 gives the 3R regenerated signal rms timing jitter versus the sampling clock pulse timing jitter for different degraded signal conditions. Figure 4-9 shows that the rms jitter of the output pulse of the regenerator is linearly related to the timing jitter of the sampling clock pulse and is independent of the degraded input pulse timing jitter. However, the timing jitter of the 3R regenerated signal is about 10 % of the input pulse rms timing jitter. Therefore, the timing jitter has been attenuated by 90% using the 3R regenerator.

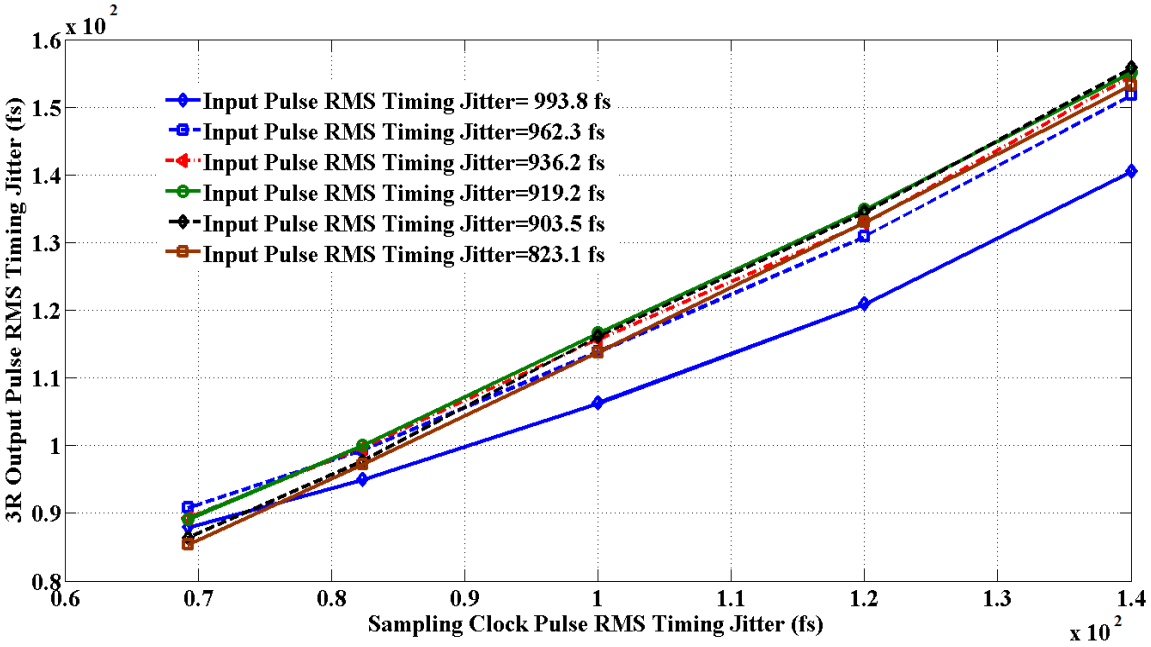

Figure 4-9: Comparison of the rms timing jitter of the 3R regenerated signal versus the sampling clock pulse rms timing jitter for different input degraded signals.

Figure 4-10 gives the height of the eye opening of the 3R regenerated signal versus the sampling clock pulse timing jitter for different degraded signal conditions. The input degraded signal eye opening height is about 10% of the input pulse rms timing

jitter. By using the proposed 3R regenerator the height of the eye opening is improved to at least 67.5% over the range of sampling clock pulse timing jitter considered. Therefore, the proposed 3R regenerator significantly reduces the ISI of the input degraded signal.

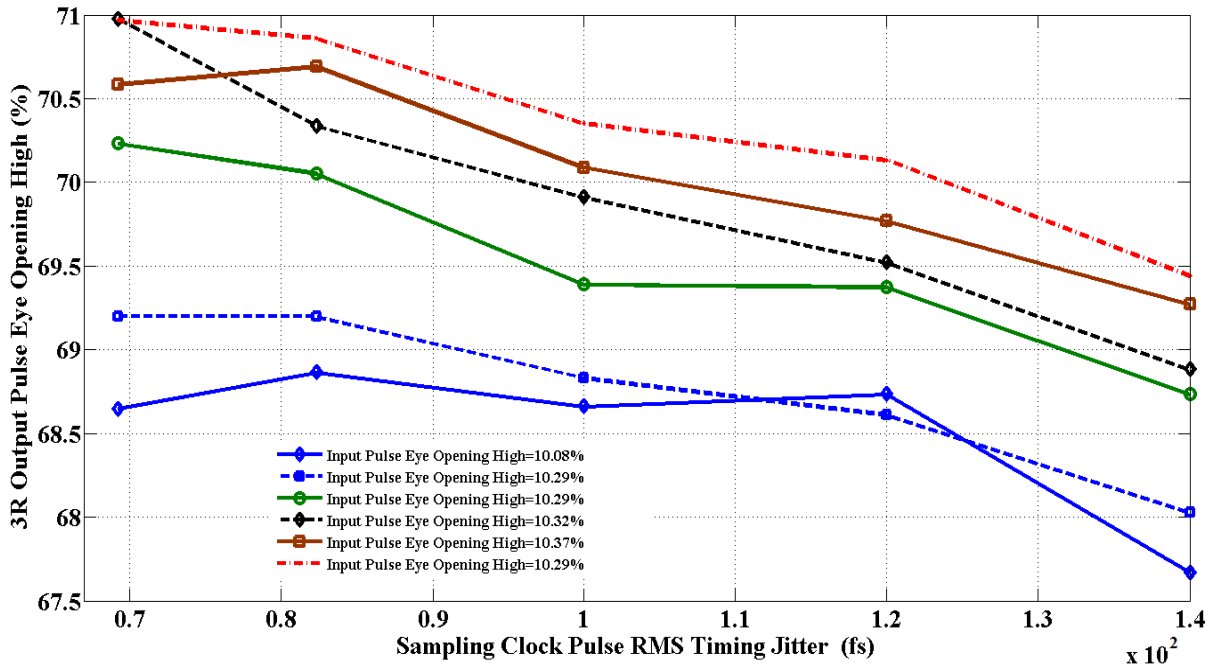

Figure 4-10: Comparison of eye opening height of a 3R regenerated signal versus the sampling clock pulse rms timing jitter for different degraded signals input.

As the input bandwidth of the Electrical Spectrum Analyzer (ESA) is limited, the impact of the input bandwidth of the ESA on the regenerated signal timing jitter and amplitude fluctuation needs to be investigated. The simulation model of Figure 4-11 was implemented to measure the performance variation of the proposed 3R regenerator for different GLPF bandwidths. The measurement results are shown in Figures 4-12 and 4-13.

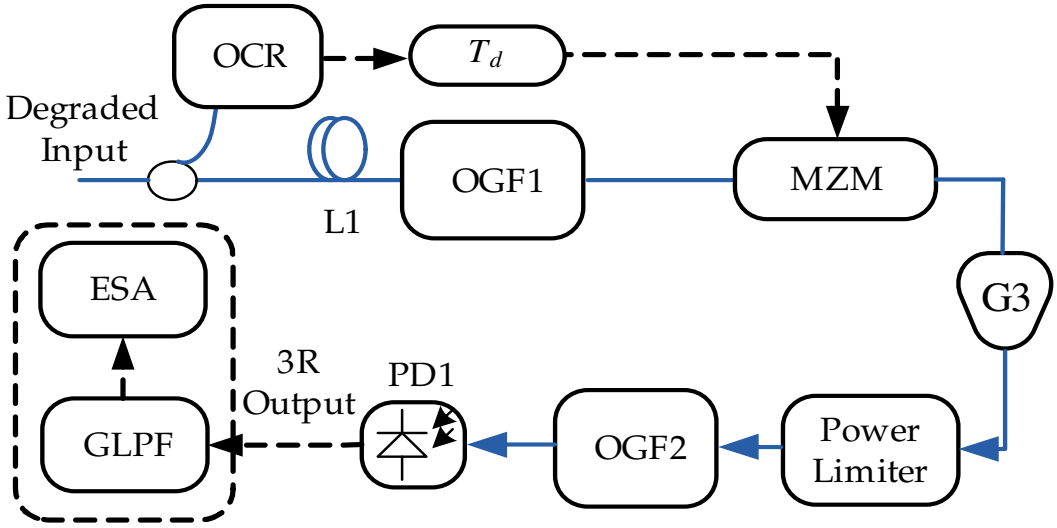

Figure 4- 11: The simulation model used to investigate the 3R regenerator's performance by measuring the rms timing jitter for different GLPF bandwidths.

The rms intensity variation per unit amplitude of the 3R regenerated output pulse versus the rms clock pulse timing jitter for different ESA input 3-dB bandwidths is shown in Figure 4-12.

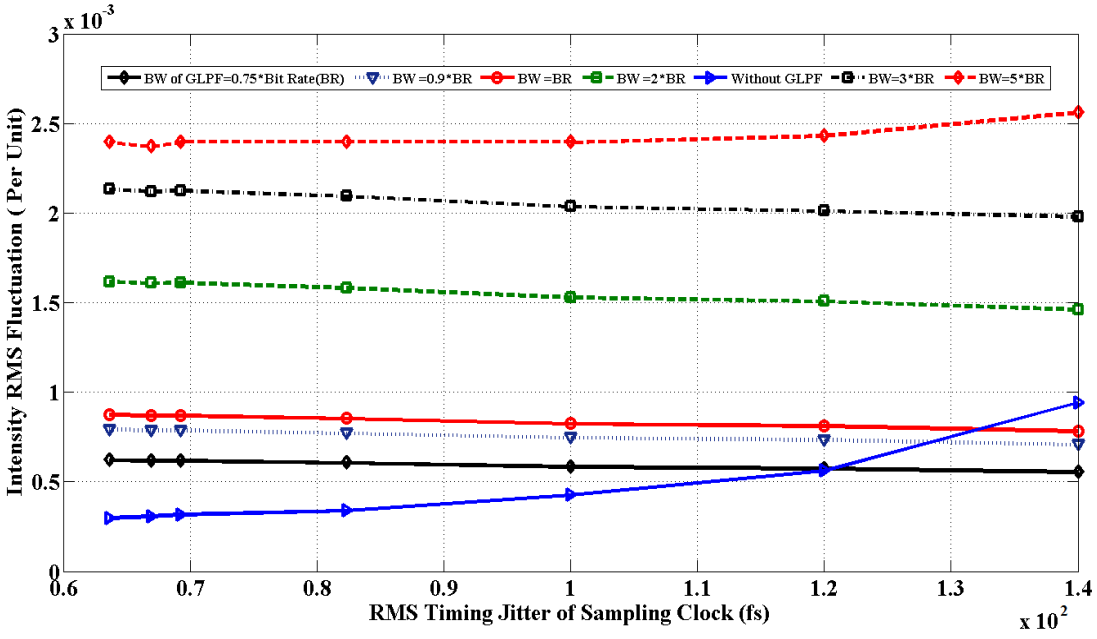

Figure 4-12: RMS intensity fluctuation of the 3R output versus the sampling clock pulse timing jitter for different output Gaussian LPF.

This figure shows that the ESA input filter bandwidth has a significant impact on the rms intensity fluctuation of the 3R regenerated pulse. It is clear that a broadband input bandwidth ESA has no degradation impact on the intensity fluctuation in

comparison with a limited input bandwidth ESA. However, considering the rms jitter in Figure 4-13, by increasing the ESA input bandwidth, the rms jitter decreases. However, around the bandwidth equal to the input signal bandwidth, the input bandwidth of the ESA does not have a significant impact on the rms jitter. The timing jitter of the 3R regenerated signal decreases when the input bandwidth of ESA is increased because of ISI added by deterministic jitter. However, for a bandwidth less than the input signal bandwidth, the expectation of increased timing jitter is not valid.

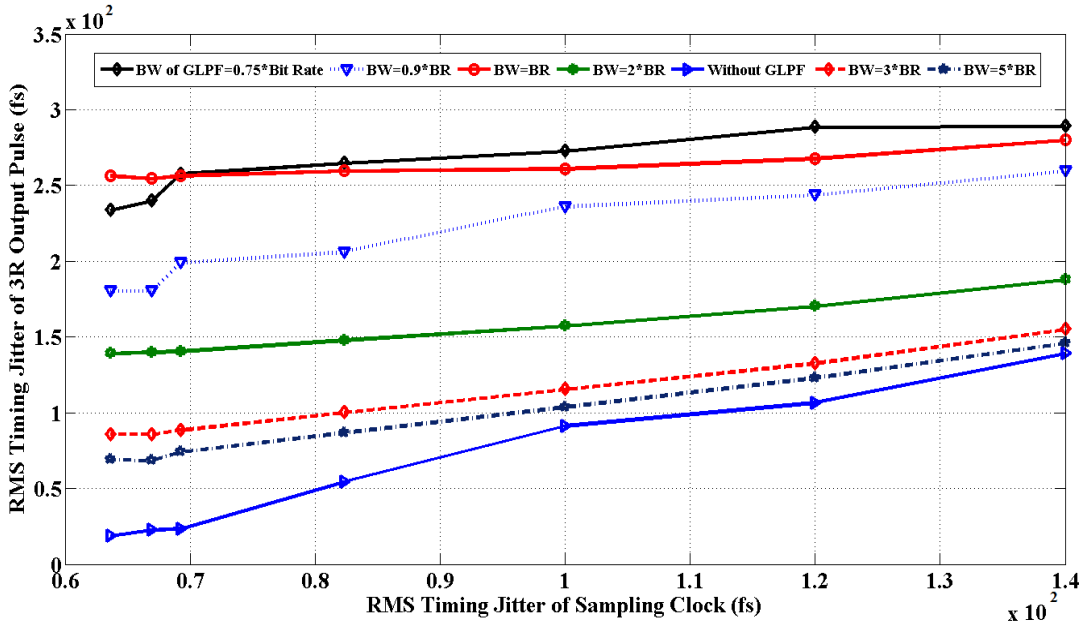

Figure 4-13: RMS timing jitter of the 3R regenerated pulse versus the timing jitter of the sampling clock pulse using ESA.

To investigate the link performance with 3R regeneration against the link performance without 3R regeneration, the simulation model shown in Figure 4-14 was implemented. In this simulation model, the pseudo random RZ data is generated and modulated onto optical carrier, degradation of the channel is considered by using the model that is illustrated in Figure 4-6. The degraded data signal is symmetrically split into two parts using 50/50 splitter. The first part is launched into a standard single mode fibre (SMF) with length L'1, chromatic dispersion compensation, and 0.2 ps/km polarization mode dispersion. The second output of the splitter is connected to the input of the 3R block. The 3R regenerated signal is launched into a SMF of length L'2 with chromatic dispersion compensation,

differential group delay of 0.2 ps/km and polarization mode dispersion coefficient of 0.5 ps/km$^{0.5}$. By using this model, the bit error rate (BER) of a sample link with and without 3R regeneration is simultaneously investigated. The transmitted sample random RZ data rate is 65 Gbit/s, the rms timing jitter of signal is about 1.1 ps at the output of degradation channel and the eye opening height of the degraded input signal is about 11.7%.

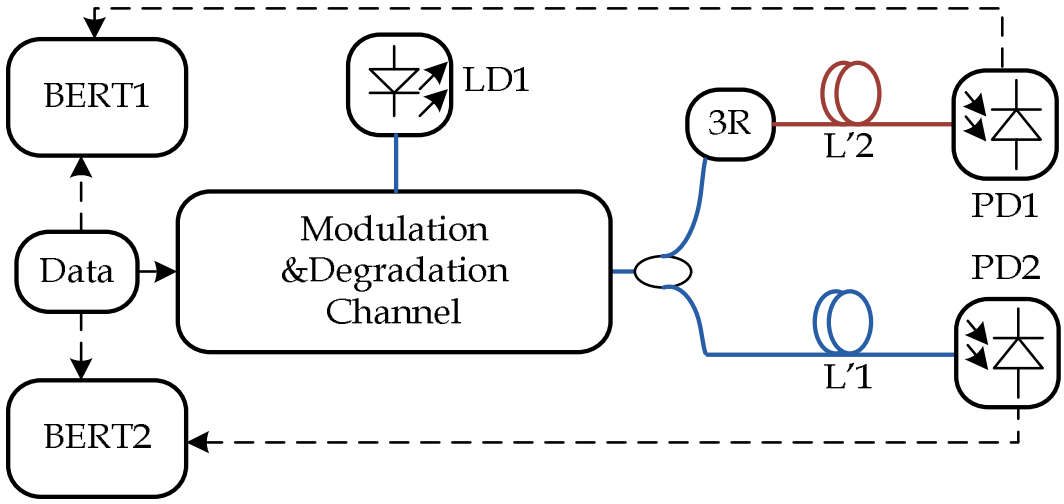

Figure 4- 14: The simulation model used to evaluate the 3R regenerator's performance by comparison with the system without 3R Regeneration.

The Q-Factor variation versus sampling clock timing jitter against the launched power into the standard SMF fibre at the output of 3R regenerator is depicted in Figure 4-15. As shown in this figure, the Q-factor is improved versus launched power while its quantity is decreased across the axis of ascending value of rms timing jitter of sampling clock pulse. However, the improvement obtained by increasing the launched power saturated at a higher launched power because of scattering nonlinearity throughout the fibre. The Q-Factor improvement at lower timing jitter is considerable but when the sampling clock pulse timing jitter is rising the impact of increasing launched power will be mitigated by a dominant timing jitter factor. However, in this evaluation the minimum magnitude of the sampling clock pulse rms timing jitter is above 66 femtosecond (fs). This is very high in comparison to reported MLL based sampling clock pulse timing jitter which is in the range of few fs or attosecond [60][61]. This means that the performance of the

proposed 3R regenerator has been assessed against 'worse case' sampling clock pulse jitter.

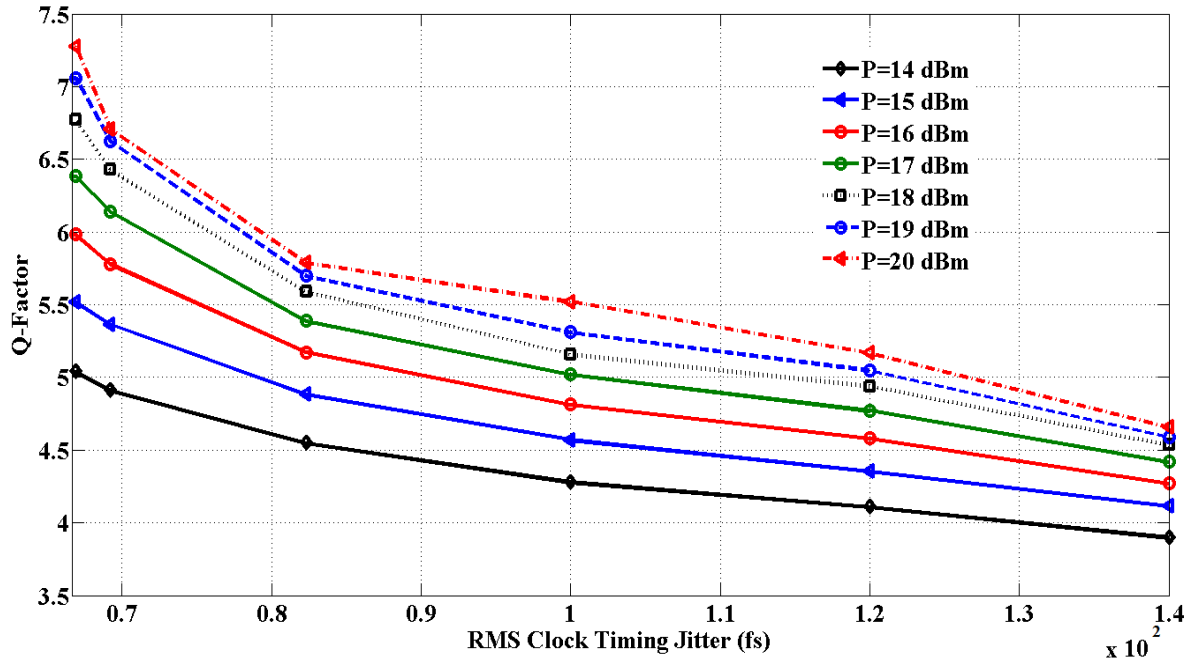

Figure 4-15: Q-Factor of the 40km link with 3R regeneration versus the sampling clock pulse rms timing jitter for different transmitted power.

The BER of the link with 3R regeneration versus sampling clock pulse rms timing jitter for different launched power into the 40 km of standard SMF is shown in Figure 4-16. As shown in this Figure, the BER of the link is related to the launched power into the link and the sampling clock pulse timing jitter. However, the impact of launched power above 18 dBm is saturated because of scattering in the fibre and will be mitigated at higher timing jitter. Figure 4-16 demonstrates that the dominant factor influencing the link performance is the sampling clock pulse jitter. While increasing the launched power has a slight impact on the link performance it is not significant compared to that of the sampling clock pulse timing jitter.

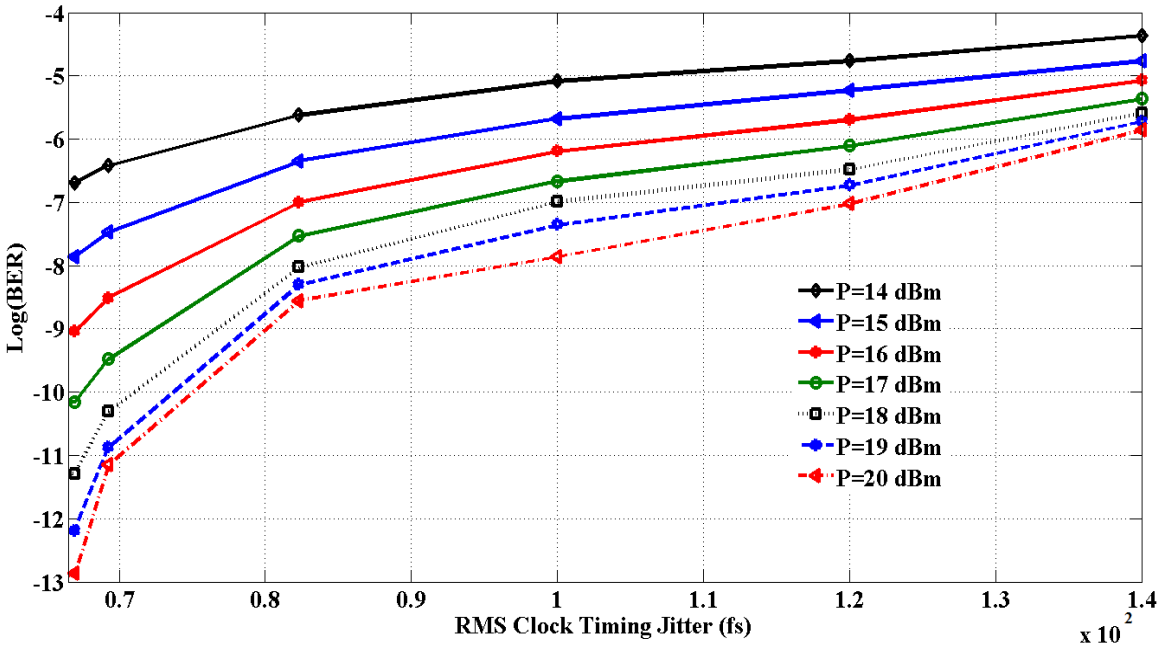

Figure 4-16: BER of the 40km link with 3R regeneration versus the sampling clock pulse rms timing jitter at different transmitted power without ESA input GLPF.

Figure 4-17 gives another view of the comparison of Figure 4-16 that shows that at high timing jitter increasing the transmitted power into the link will improve the BER slightly, illustrated in Figure 4-17 for rms jitter at and above 82.31 fs, while at lower jitter the impact of launched power into the link is more significant, as depicted for rms jitter below 82.31 fs. To investigate the link's performance verses launched power for different fibre lengths and compare the performance of the link with and without 3R regeneration the following conditions are assumed: a 26.2 fs standard deviation (rms) of the optical recovered clock timing jitter; 438.5 fs rms timing jitter of the input degraded signal; and an eye opening height of 10.48% of the input degraded pulses amplitude.

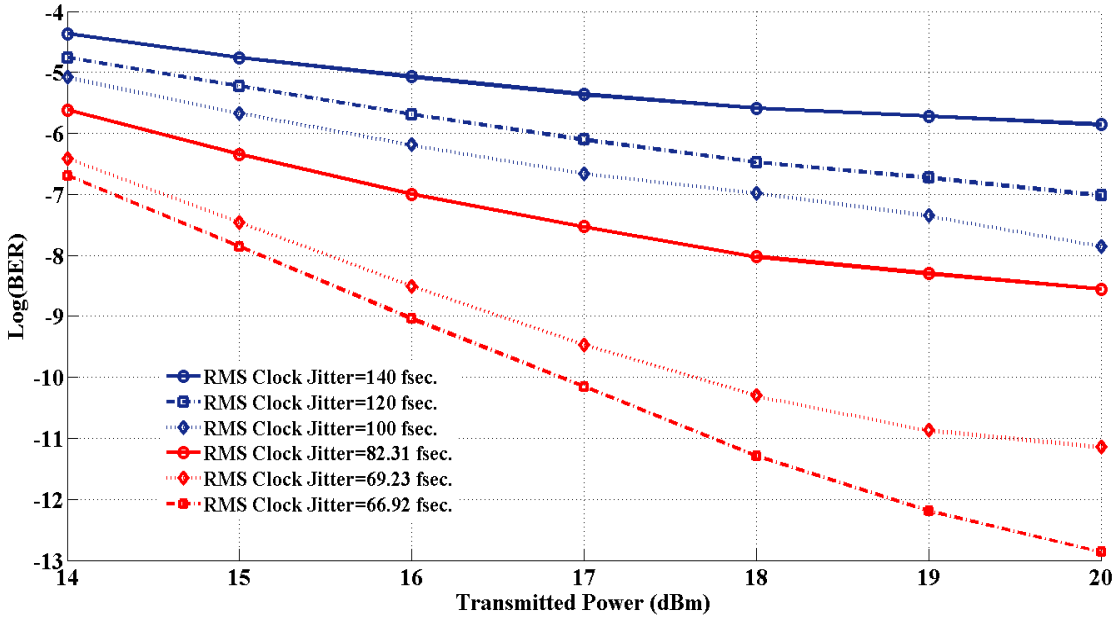

Figure 4-17: BER of 3R regeneration versus launched power onto 40km of SMF fibre for different sampling clock pulse jitter without ESA input GLPF.

The output regenerated pulses rms jitter is 109.2 fs and the pulses eye openings have a height of about 66.43% for a sample random 65 Gigabit/sec data sequence. These numerical results show the performance of the proposed 3R regenerator is acceptable and it reduces the input degraded optical pulses timing jitter and intensity fluctuation significantly.

Based on the simulation model of Figure 4-14, the simulation results shown in Figure 4-18 compare the BER of the system with 3R regeneration using different lengths of chromatic dispersion compensated standard SMF (DCSMF) with 0.2 ps/km polarization mode dispersion (different lengths of L'2) and a L'1=10 km DCSMF link without 3R regeneration against the launched power into the link. The results demonstrate that link performance is significantly improved by using a 3R regenerator. Furthermore, the BER of the link without a 3R regenerator is very significant for a 10 km DCSMF link and is independent of the launched power for powers less than 16 dBm. The simulation results also indicate that the BER of a 60 km DCSMF link with 3R regeneration is 7.1×10^3 times lower than that of a 10 km DCSMF link without 3R regeneration when 18 dBm of optical power is fed into the links. Figure 4-18 also indicates the performance of 40 and 50 km DCSMF links with

3R regeneration. The simulation results of Figure 4-18 indicate the improvement in link performance that can be obtained by 3R regeneration.

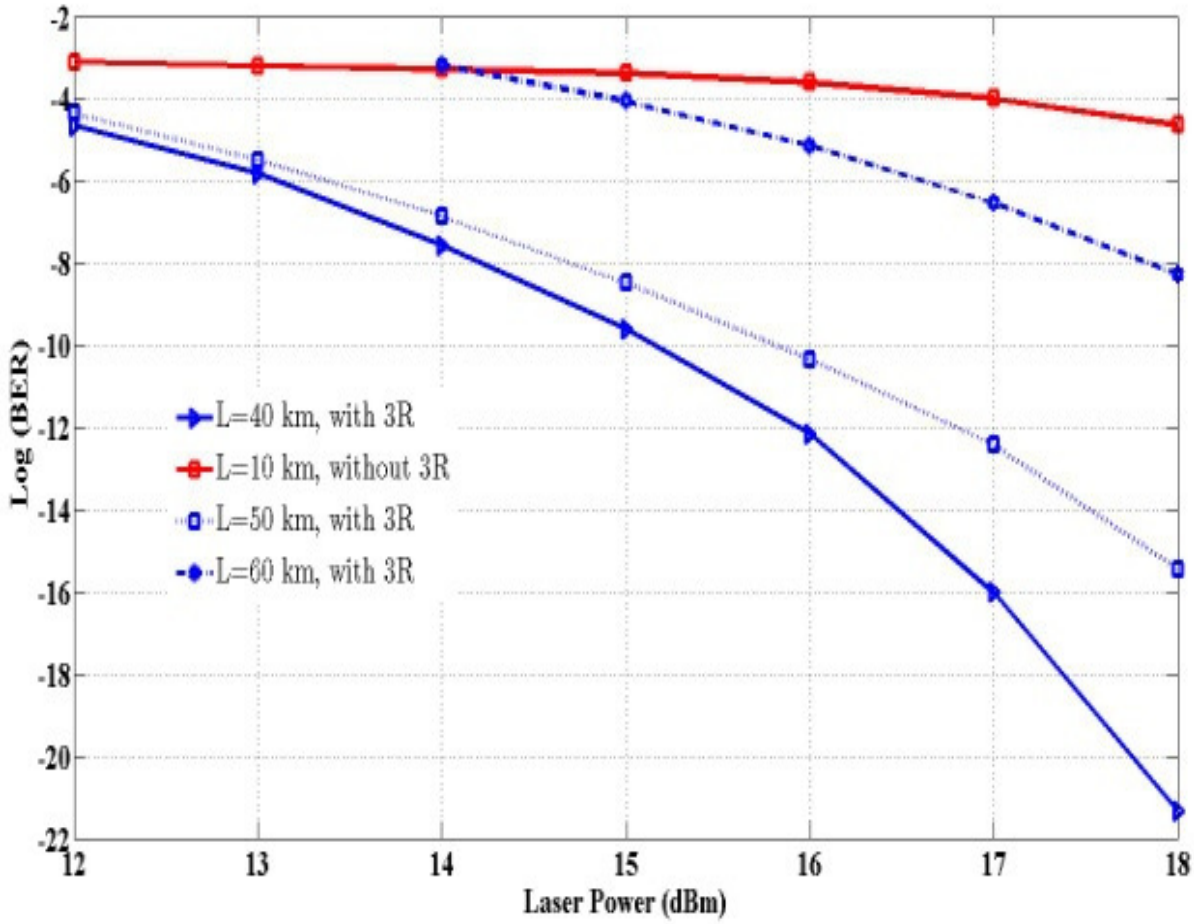

Figure 4-18: BER comparison of the link with and without 3R regeneration with ESA input GLPF with BW=Input RZ signal data rate.

A comparison of the BER of different lengths of DCSMF link with 3R regeneration is shown in Figure 4-19. As shown in this Figure and by comparison with Figure 4-18, for 10 km of DCSMF link, the power penalty of providing the link without 3R regeneration is clearly above 18 dBm for the same performance.

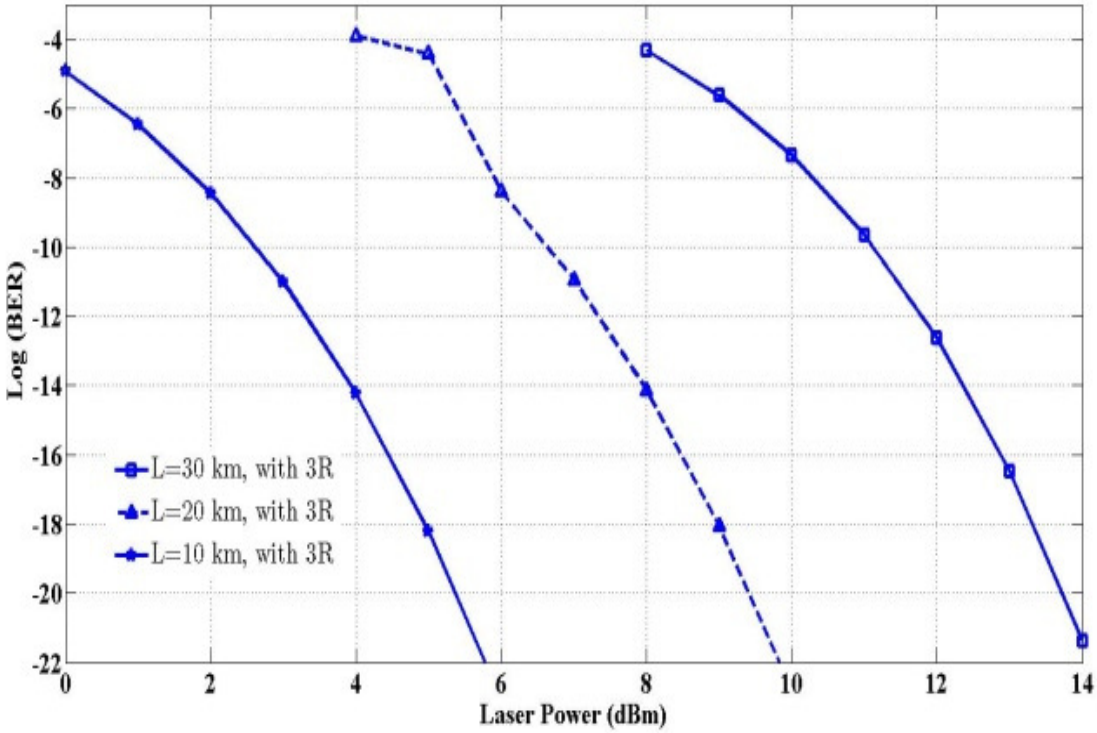

Figure 4-19: BER comparison of different lengths of link with 3R regeneration with ESA input GLPF with BW= Input RZ signal data rate.

4.4. Conclusion

In this chapter, an investigation of 3R regenerators is presented and a photonic 3R regeneration system is proposed. To evaluate the proposed system, its performance has been investigated against simulated amplitude and phase distortions and physical impairments caused by channel and physical components. Simulation results clearly show that the regenerated signal has significantly less phase noise and amplitude fluctuation than the degraded input signal. Furthermore, it is demonstrated that the link with 3R regeneration has significantly better performance and that 3R regeneration not only saves power but also improves the network's quality of service. Simulation results show that for an ultra-short RZ pulse with a 5% duty cycle at 65 Gbit/s using the proposed 3R regeneration system on a link reduces rms timing jitter by 90% while the regenerated pulse eye opening height is improved by 65%.

The dominant parameter influencing the 3R regeneration is sampling timing jitter. When the 3R system is applied on the link at lower timing jitter the amount of

launched power into the link has a significant impact on the link performance while at higher timing jitter its impact is mitigated by the timing jitter. The current 3R regeneration systems are based on analog signal processing the performance of which is directly affected by the tolerances of the physical components of the system. Furthermore, these components will be affected by environmental conditions. Nevertheless, the simulation results indicate the proposed system has sufficient promise to merit its physical implementation in order to properly assess its viability.

4.5. References

[1] T. Otani, T. Miyazaki, and S. Yamamoto, "40-Gb/s optical 3R regenerator using electroabsorption modulators for optical networks," IEEE Journal of Lightwave Technology, vol. 20, no. 2, pp. 195–200, Feb. 2002.

[2] H. F. Chou and J. E. Bowers, "Simplified optoelectronic 3R regenerator using nonlinear electro-optical transformation in an electroabsorption modulator," Optic Express, vol. 13, no. 7, pp. 2742–2746, Apr. 2005.

[3] L. Huo, Y. Yang, Y. Nan, C. Lou, and Y. Gao, "A study on the wavelength conversion and all-optical 3R regeneration using cross-absorption modulation in a bulk electroabsorption modulator," IEEE Journal of Lightwave Technology, vol. 24, no. 8, pp. 3035–3044, Aug. 2006

[4] S. Høfeldt, S. Bischoff, and J. Mørk, "All-optical wavelength conversion and signal regeneration using an electroabsorption modulator," IEEE Journal of Lightwave Technology, vol. 18, no. 8, pp. 195–200, Aug. 2000.

[5] K. Nishimura, R. Inohara, M. Usami, and S. Akiba, "All-optical wavelength conversion by electroabsorption modulator," IEEE Journal of Select. Topics of Quantum Electronic, vol. 11, no. 1, pp. 278–284, Jan.-Feb. 2005.

[6] L. Billes, J. C. Simon, B. Kowalski, M. Henry, G. Michaud, P. Lamouler, and F. Alard, "20 Gbit/s optical 3R regenerator using SOA based Mach-Zehnder interferometer gate," in Proc. Eur. Conf. Optical Communications (ECOC), pp. 269–272, 1997.

[7] B. Lavigne, D. Chiaroni, P. Guerber, L. Hamon, and A. Jourdan, "Improvement of regeneration capabilities in semiconductor optical amplifier-based 3R regenerator," in Proc. Optical Fiber Communication Conf. (OFC), pp. 128–130, 1999.

[8] A. E. Kelly, I. D. Phillips, R. J. Manning, A. D. Ellis, D. Nesset, D. G. Moodie, and R. Kashyap, "80 Gbit/s all-optical regenerative wavelength conversion using semiconductor optical amplifier based interferometer," Electronic Lett., vol. 35, no. 17, pp. 1477–1478, Aug. 1999.

[9] D. Wolfson, A. Kloch, T. Fjelde, C. Janz, B. Dagens, and M. Renaud, "40- Gb/s all-optical wavelength conversion, regeneration, and demultiplexing in an SOA-based all-active Mach-Zehnder interferometer," IEEE Photon. Tech. Lett., vol. 12, no. 3, pp. 332–334, Mar. 2000.

[10] J. Leuthold, B. Mikkelsen, R. E. Behringer, G. Raybon, C. H. Joyner, and P. A. Besse, "Novel 3R regenerator based on semiconductor optical amplifier delayed interference configuration," IEEE Photonics Technology Letters, vol. 13, no. 8, pp. 860–862, Aug. 2001.

[11] Y. Ueno, S. Nakamura, and K. Tajima, "Penalty-free error-free all-optical data pulse regeneration at 84 Gb/s by using a symmetric-Mach-Zehnder-type semiconductor regenerator," IEEE Photonics Technology Letters, vol. 13, no. 5, pp. 469– 471, May 2001.

[12] R. J. Essiambre, B. Mikkelsen, and G. Raybon, "Semiconductor-based all-optical 3R regenerator demonstrated at 40 Gbit/s," Electronic Lett., vol. 40, no. 3, pp. 192–194, Feb. 2004.

[13] Y. A. Leem, D. C. Kim, E. Sim, S. B. Kim, H. Ko, K. H. Park, D. S. Yee, J. O. Oh, S. H. Lee, and M. Y. Jeon, "The characterization of all-optical 3R regeneration based on InP-related semiconductor optical devices," IEEE J. Select. Topics Quantum Electron., vol. 12, no. 4, pp. 726–735, July-Aug. 2006.

[14] J. L. Pleumeekers, M. Kauer, K. Dreyer, C. Burrus, A. G. Dentai, S. Shunk, J. Leuthold, and C. H. Joyner, "Analysis and optimization of SPM-based 2R signal

regeneration at 40 Gb/s," IEEE Photonics Technology Letters., vol. 14, no. 1, pp. 12–14, 2002.

[15] K. Obermann, S. Kindt, D. Breuer, K. Petermann, C. Schmidt, S. Diez, and H. G. Weber, "Noise characteristics of semiconductor-optical amplifiers used for wavelength conversion via cross-gain and cross-phase modulation," IEEE Photonics Technology Letters, vol. 9, no. 3, pp. 312–314, Mar. 1997.

[16] T. Durhuus, B. Mikkelsen, C. Joergensen, S. L. Danielsen, and K. E. Stubkjaer, "All-optical wavelength conversion by semiconductor optical amplifiers," IEEE Journal of Lightwave Technology, vol. 14, pp. 942 – 954, Jun. 1996.

[17] P. S. Cho, D. Mahgerefteh, J. Goldhar, L. G. Joneckis, and G. L. Burdge, "High performance non-interferometric semiconductor-optical-amplifier/fibre bragg grating wavelength converter," Electronic Lett., vol. 34, no. 4, pp. 371– 373, Feb. 1998.

[18] H. Lee, H. Yoon, Y. Kim, and J. Jeong, "Theoretical study of frequency chirping and extinction ratio of wavelength-converted optical signals by XGM and XPM using SOAs," IEEE J. Quantum Electron., vol. 35, no. 8, pp. 1213–1219, Aug. 1999.

[19] G. P. Agrawal, Fiber-optic communication systems, 3rd ed. New York: John Wiley & Sons, Inc., 2010.

[20] G. P. Agrawal, Nonlinear fiber optics, 4th ed. San Diego: Academic Press, Inc., 2007.

[21] K. Inoue, "Optical nonlinearity in optical fibers and semiconductor optical amplifiers," in Proc. Conf. Lasers and Electro-Optics (CLEO), pp. 1089–1090,1999.

[22] A. Reale, P. Lugli, and S. Betti, "Format conversion of optical data using four-wave mixing in semiconductor optical amplifiers," IEEE J. Select. Topics Quantum Electron., vol. 7, no. 4, pp. 703–709, July-Sept. 2001.

[23] C. Politi, D. Klonidis, and M. J. O'Mahony, "Waveband converters based on four-wave mixing in SOAs," IEEE Journal of Lightwave Technology, vol. 21, no. 3, pp. 1203–1217, Mar. 2006.

[24] S. Song, C. T. Allen, K. R. Demarest, and R. Hui, "Intensity-dependent phasematching effects on four-wave mixing in optical fibers," IEEE Journal of Lightwave Technology, vol. 17, no. 11, pp. 2285–2290, Nov. 1999.

[25] M. Jinno and T. Matsumoto, "Optical tank circuits used for all-optical timing recovery," IEEE J. Quantum Electron., vol. 28, no. 4, pp. 895–900, Apr. 2002.

[26] C. Ito and J. C. Cartledge, "Polarization independent all-optical 3R regeneration of optical packets based on the Kerr effect and offset spectral slicing," in Proc. Eur. Conf. Optical Communications (ECOC) (accepted), 2007.

[27] C. Bintjas, K. Yiannopoulos, N. Pleros, G. Theophilopoulos, M. Kalyvas, H. Avramopoulos, and G. Guekos, "Clock recovery circuit for optical packets," IEEE Photonics Technology Letters, vol. 14, no. 9, pp. 1363–1365, Sep. 2002.

[28] E. Kehayas, L. Stampoulidis, H. Avramopoulos, Y. Liu, E. Tangdiongga, and H. Dorren, "40 Gb/s all-optical packet clock recovery with ultrafast lock-in time and low inter-packet guard bands," Optic Express, vol. 13, no. 2, pp. 475–480, Jan. 2005.

[29] X. Zhou, C. Lu, P. Shum, H. H. M. Shalaby, T. H. Cheng, and Y. Peida, "A performance analysis of an all-optical clock extraction circuit based on Fabry-P´erot filter," IEEE Journal of Lightwave Technology, vol. 19, no. 5, pp. 603–613, 2001.

[30] Z. Zhu, M. Funabashi, P. Zhong, L. Paraschis, D. L. Harris, and S. J. B. Yoo, "High-performance optical 3R regeneration for scalable fiber transmission system applications," IEEE Journal of Lightwave Technology, vol. 25, no. 2, pp. 504–511, 2007.

[31] S. Bauer, C. Bornholdt, O. Brox, D. Hoffmann, M. Möhrle, G. Sahin, B. Sartorius, and S. Schelhase, "Ultrafast locking optical clock for IP packet switching applications," in Proc. Optical Fiber Communication Conf. (OFC), 2000, pp. 78–80.

[32] B. Sartorius, C. Bornholdt, O. Brox, H. J. Ehrke, D. Hoffmann, R. Ludwig, and M. Möhrle, "All-optical clock recovery module based on self-pulsating DFB laser," Electronic Lett., vol. 34, no. 17, pp. 1664–1665, Aug. 1998.

[33] S. Fischer, M. Dulk, E. Gamper, W. Vogt, E. Gini, H. Melchior, W. Hunziker, D. Nesset, and A. D. Ellis, "Optical 3R regenerator for 40 Gbit/s networks," Electronic Lett., vol. 35, no. 23, pp. 2047–2049, Nov. 1999.

[34] J. Wiesenfeld, "Wavelength conversion techniques in optical networks," in Proc. LEOS Annual Meeting, 1997, p. ThB4.

[35] T. Ito, N. Yoshimoto, K. Magari, and H. Sugiura, "Wide-band polarization independent tensile-strained InGaAs MQW-SOA gate," IEEE Photonics Technology Letters, vol. 10, no. 5, pp. 657–659, May 1998.

[36] A. Bogris and D. Syvridis, "Regenerative properties of a pump-modulated fourwave mixing scheme in dispersion-shifted fibers," IEEE Journal of Lightwave Technology, vol. 21, no. 9, pp. 1892–1902, Sep. 2003.

[37] C. Ito, I. Monfils, and J. C. Cartledge, "All-optical 3R regeneration using higher order four-wave mixing with a clock-modulated optical pump signal," in Proc. LEOS Annual Meeting, 2006, pp. 223–224.

[38] C. Yu, T. Luo, B. Zhang, Z. Pan, M. Adler, Y. Wang, J. E. McGeehan, and A. E. Willner, "Wavelength-shift-free 3R regenerator for 40-Gb/s RZ system by optical parametric amplification in fiber," IEEE Photonics Technology Letters, vol. 18, no. 24, pp. 2569–2571, Dec. 2006.

[39] E. Ciaramella and S. Trillo, "All-optical signal reshaping via four-wave mixing in optical fibers," IEEE Photonics Technology Letters, vol. 12, no. 7, pp. 849–851, Jul. 2000.

[40] K. Inoue, "Suppression of level fluctuation without extinction ratio degradation based on output saturation in higher order optical parametric interaction in fiber," IEEE Photonics Technology Letters, vol. 13, no. 4, pp. 338–340, Apr. 2001.

[41] Y. Chen and A. W. Snyder, "Four-photon parametric mixing in optical fibers: effect of pump depletion," Opt. Lett., vol. 14, no. 1, pp. 87–89, Jan. 1989.

[42] T. Torounidis, M. Karlsson, and P. A. Andrekson, "Fiber optical parametric amplifier pulse source: theory and experiments," IEEE Journal of Lightwave Technology, vol. 23, no. 12, pp. 4067–4073, Dec. 2005.

[43] D. Dahan, E. Shumakher, and G. Eisenstein;, "A multiwavelength short pulse source based on saturated optical fiber parametric amplification," IEEE Photonics Technology Letters, vol. 18, no. 4, pp. 592–594, Feb. 2006.

[44] T. Yamamoto and M. Nakazawa, "Active optical pulse compression with a gain of 29.0 dB by using four-wave mixing in an optical fiber," IEEE Photonics Technology Letters, vol. 9, no. 12, pp. 1595–1597, Dec. 1997.

[45] K. Inoue and H. Toba, "Wavelength conversion experiment using fiber four-wave mixing," IEEE Photonics Technology Letters, vol. 4, no. 1, pp. 69–72, Jan. 1992.

[46] K. Inoue and T. Mukai, "Signal wavelength dependence of gain saturation in a fiber optical parametric amplifier," Opt. Lett., vol. 26, no. 1, pp. 10–12, Jan. 2001.

[47] K. K. Chow, C. Shu, C. Lin, and A. Bjarklev, "Polarization-insensitive widely tunable wavelength converter based on four-wave mixing in a dispersion flattened nonlinear photonic crystal fiber," IEEE Photonics Technology Letters, vol. 17, no. 3, pp. 624–626, Mar. 2005.

[48] T. Durhuus, C. Joergensen, B. Mikkelsen, R.J.S. Pedersen, and K.E. Stubkjaer, "All Optical Wavelength Conversion by SOA' s in a Mach-Zehnder Configuration, " IEEE Photonics Technology Letters, vol.6, no. 1, pp. 53-55, Jan. 1994.

[49] Kristian E. Stubkjaer, "Semiconductor Optical Amplifier-Based All-Optical Gates for High-Speed Optical Processing," IEEE Journal on Selected Topics in Quantum Electronics, vol. 6, no. 6, pp. 1428-1434, Nov. 2000

[50] K. Vyrsokinos, L. Stampoulidis, F. Gomez-Agis, K. Voigt, L. Zimmermann, T. Wahlbrink, Z. Sheng, D. V. Thourhout and H. J. S. Dorren, "Ultra-high Speed, All-optical Wavelength Converters Using Single SOA and SOI Photonic Integrated Circuits," IEEE Photonics Society Winter Topicals Meeting Series (WTM), WC2.3, pp. 113-114, 2010.

[51] Bimberg, D.; Meuer, C.; Laemmlin, M.; Liebich, S.; Kim, J.; Eisenstein, G., Kovsh, A.R., "Quantum Dot Semiconductor Optical Amplifiers for Wavelength Conversion Using Cross-Gain Modulation," IEEE 10th Anniversary International Conference on Transparent Optical Networks (ICTON 2008), pp. 141-144, 2008.

[52] Yu Sun, Jiao Qing Pan, Ling Juan Zhao, Weixi Chen, Wei Wang, Li Wang, Xiao Fan Zhao, and Cai Yun Lou, "All-Optical Clock Recovery for 20 Gb/s Using an Amplified Feedback DFB Laser," Journal of Lightwave Technology, vol. 28, no. 17, Sep. 1, pp. 2521-2525, 2010.

[53] Holtmannspoetter, M. and Schmauss, B. , "All Optical Limiter Based on Self Phase Modulation and Dispersive Chirping," International European Conference on Lasers and Electro-Optics Quantum Electronics Conference, pp. 1-1, CLEOE-IQEC 2007.

[54] N. Pleros, G. T. Kanellos, C. Bintjas, A. Hatziefremidis, and H. Avramopoulos , "Optical Power Limiter Using a Saturated SOA-Based Interferometric Switch," IEEE Photonics Technology Letters, vol. 16, no. 10, pp.2350-2352 Oct. 2004.

[55] Lukasz Brzozowski and Edward H. (Ted) Sargent, " All-Optical Analog-to-Digital Converters, Hardlimiters, and Logic Gates," IEEE Journal of Lightwave Technology, vol. 19, no. 1, PP. 114-119, Jan. 2001

[56] Ryan P. Scott, Theresa D. Mulder, Katherine A. Baker, and Brian H. Kolner, " Amplitude and Phase noise sensitivity of modelocked Ti:sapphire lasers in terms

of complex noise transfer function", Optics Express, vol. 14, pp. 9090-9095, July. 2007.

[57] Johnnie Hancock, " Jitter-Understanding it, Measuring it, Eliminating it, Part 1: Jitter Fundamentals" High Frequency Electronics, pp. 44-50, Summit Technical Media, LLC, April, 2004.

[58] Ransom Stephens, "Analyzing Jitter at High Data Rates", IEEE Optical Communication, pp. 6-10 , Feb. 2004.

[59] Ransom Stephens "Jitter Analysis: The Dual-Dirac Model, RJ/DJ, and Q-sacle", Agilent Technical Note, Dec. 2004.

[60] Junqwon Kim, Jeff Chen, Jonathan Cox, and Franz X. Kartnr, "Attosecond-Resolution Timing Jitter Characterization of Free-Running Mode-Locked lasers", Optics Letters, vol. 32, pp. 3519-3521, 2007.

[61] A. Bartels, S. A. Diddams, T. M. Ramond, and L. Holberg, " Mode-locked laser pulse trains with subfemtosecond timing jitter synchronized to an optical reference oscillator", Optic Letters, vol. 28, pp. 663-665, 2003.

[62] Charles H. Cox, III, Analog Optical Links Theory and Practice Cambridge University press, 2004.

Chapter 5

Fully-Photonic Digital Radio over Fibre (FP-DROF) Network

5.1. Introduction

Fully-Photonic Digital Radio over Fibre (FP-DROF) system deployment aims to strengthen merging wireless and photonic technologies for future super-broadband access network application. In this system, the digital information packets which are transported from Wide Area Networks (WANs), mobile or fixed Internet Services Providers (ISPs), mobile operators, and digital multimedia broadcasting organizations through conventional metropolitan network to a central station (CS). The digital information from wireless and mobile service providers is modulated onto RF carriers. The modulated RF carriers could be delivered based on different wireless and mobile telecommunication standards by service providers such as: 3G, WiMAX, LTE, WiFi, and DVB2.

In the proposed FP-DRoF system, the RF signals can be digitized optically whereas modulated onto an optical carrier for distribution to Remote Base Stations (RBS) at the end-users premises. At the remote base station, the optical digital data from CS converted back to an analogue optical signal and transmitted over last meters of fibre links to radiate and distribute using Photonic Distributed Antenna Systems (PDASs). Furthermore, digital multimedia broadcasting organizations can transparently transport digital information to the RBS and convey to wired and wireless end-users simultaneously. Therefore, it could be an integrated photonic system with digital signal conversions at CS and RBS. The analogue RF signal transceiver at PDASs can transport and handover different wireless and mobile services standard signals. Furthermore, digital baseband information can be delivered via Baseband over Fibre

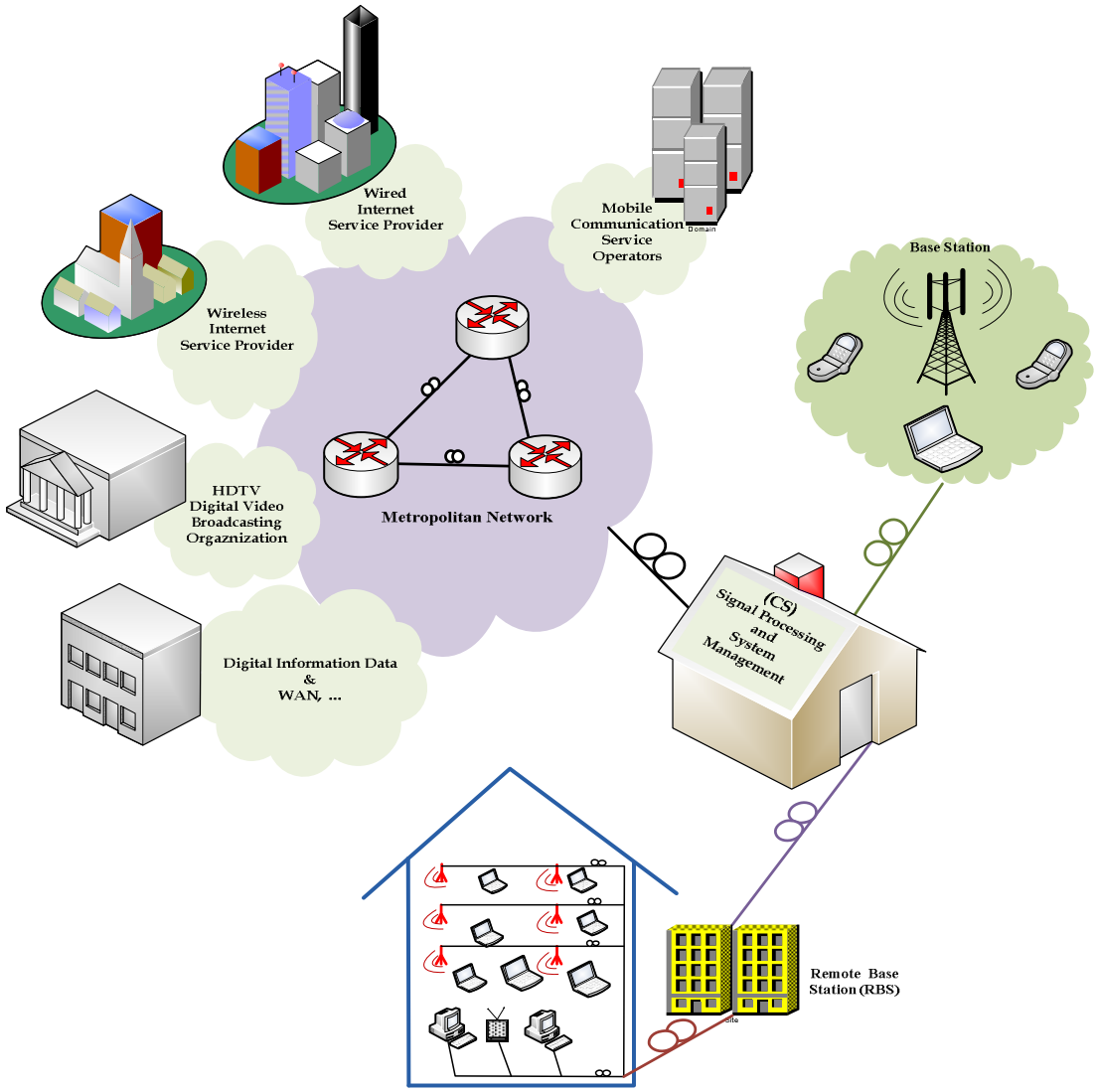

Figure 5-1: Architecture of radio over fibre system.

(BoF) network based on wired IP services for providing interactive multimedia services such as high definition multimedia (HDTV or UHDTV with 3D) as well as wireless network data traffics using the common infrastructure, is shown in Figure 5-1.

In the following of the design of two key all-optical data converters in chapter 3, in this chapter, a Fully-photonic Digital Radio over Fibre (FP-DRoF) architecture is proposed. The FP-DRoF system performance is evaluated in different channel conditions for demonstrate its functionality to transport a sample 5 GHz RF signal. The proposed link's performance is investigated in the presence of other channels interference and the physical impairments of communication link and individual

components. The simulation results are compared with an Analogue Radio over Fibre (ARoF) communication link. Furthermore, the results illustrate that the proposed FP-DRoF is a suitable candidate for very high sampling rate of the digital optical links and is more robust against channel interferences than Analogue Radio over Fibre (ARoF).

This proposed system will provide the following potential advantages: 1) the ability to support a broad range of services. 2) Presenting competition by flexibility. 3) Protection of previous and future investments. 4) Reliability and low maintenance costs. 5) Seamless upgrade of existing access networks. Therefore, future wireless networks are likely to be integrated with existing optical networks that reduce the future super-broadband mm-wave access network system implementation and service cost overhead. By implementing this scheme, it is possible to use free spectrum capacity of metro and access networks for transporting all broadband system traffics such as ARoF and BoF and any digital information traffics.

This chapter is organized as follows: In Section 5.2. the FP-DRoF architecture is presented and the link sub-subsystems are described accordingly. Section 5.3. presents an investigation on the FP-DRoF and ARoF links performance and the comparison of their Bit Eror Rate (BER), for a shared and individual fibre links. The evaluation of the FP-DRoF system performance for different schemes of uniform and non-uniform wavelength allocation is presented in Section 5.4. Concluding remarks are given in Section 5.5. and finally, the references are given in Section 5.5.

5.2. FP-DROF Architecture

The proposed FP-DRoF architecture is illustrated in Figure 5-2. This system includes three building blocks 1) Central Station (CS) 2) Remote Base Station (RBS) 3) Photonic Distributed Antenna System (PDAS). The central station is centralizing and setting up the exclusive and complex signal processing, management and monitoring tasks. This sets up the network more cost-effective and integrated. The system includes transceivers, signal processing systems and control and monitoring subsystems. The downlink transmitter includes a digital baseband signal processing

system that performs some tasks such as reframing the packets and demultiplexing digital information data that are transmitted from metro network. The system transports each type of user's data traffic to perform individual modulation schemes regarding to the particular standard. Finally, the modulated symbols could be transmitted by individual optical transmitters such as RF, mm-wave and digital baseband data over fibre.

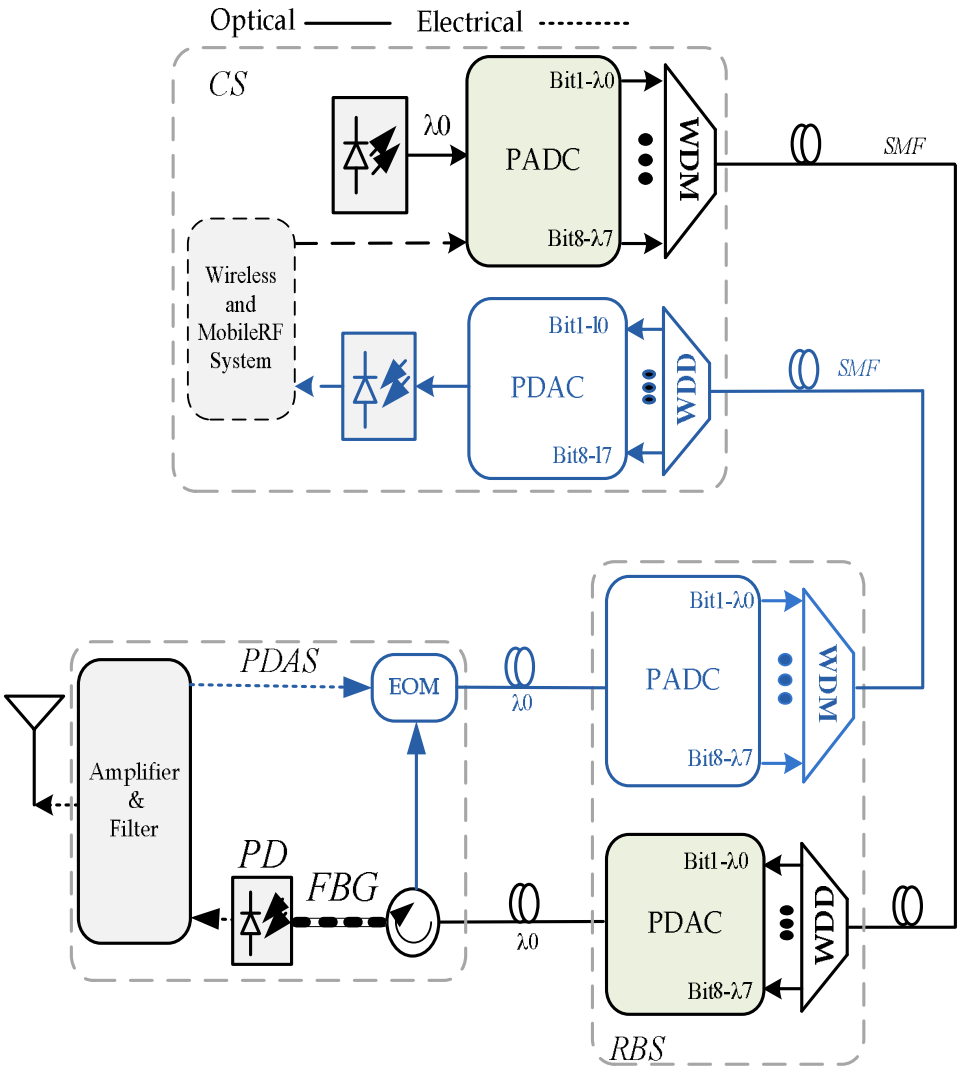

Figure 5-2: The FP-DRoF architecture.

To deploy FP-DRoF for downlink communication, RF signal is sampled using optical pulses train and modulated optical carrier by a mode-locked laser. The optical power of sampled pulses is quantized in PADC. By using WDM the generated digital

traffics at different wavelengths are transmitted through the Single Mode Fibre (SMF) to the Wavelength Division Demultiplexer (WDD) of PDAC at the RBS.

The uplink subsystem receives optical signals from RBS, the digital optical data come from PADC at RBS to CS over different wavelength using WDM. It converts digital optical signal to the corresponding analogue signal and detects an RF or mm-wave signals to perform the following processes: filtering, amplification, down conversion, detection, demodulation, demapping the symbols, and multiplexing digital information data to send the digital data stream to the service provider.

Remote Base Station: The RBS is located nearside the indoor's end-users. It is a two way signal converter that includes PADC and PDAC. This system designed to improve quality of the transported signal, wavelength multiplexing and demultiplexing, wavelength conversion, distributing and collecting of the optical signal from or to the uplink and downlink PDASs' subsystem or baseband wired optical access network systems. Furthermore, the RBS will relay the digital baseband data from CS to wired network devices in the end-user premise and vice versa using BoF technique.

Distributed Antenna Unit: The Distributed Antenna System (DAS) is simple photonic-wireless integrated transceiver that includes the following blocks: uplink and downlink blocks that receive and transmit the wireless signal from and to the mobile or wireless users. RoF technology makes a DAS further cost effective and reliable. There have been recently many attempts to centralize the light source at the CS and reuse the optical carrier of the downlink signal at the RBS for uplink transmission [1-3]. Therefore, the proposed system cost and circuit's complexity are reduced by reusing the optical carrier at Photonic DASs (PDASs).

The photonic digital waveform is converted to the analogue signal using PDAC which is fed to the PDAS. Prior to detection of the analogue signal, an optical circulator is cascaded with a FBG filter to deploy a system for reusing the MLL pulses for uplink RF signal sampling and modulation by an EOM. This technique reduces the system implementation cost and complexity, whereas, the need for an

additional optical source as a carrier and sampling pulse has been satisfied in the PDASs. The analogue optical signal at the output of FBG filter is detected using a photo diode. The recovered electrical discrete samples are filtered out to generate RF carrier. The recovered RF signal is amplified and is fed to an antenna to propagate through the air which is detected by end-users wireless and mobile devices. In the uplink data transportation, the same technique has been implemented.

5.3. System Analysis and Discussion

In this section, the simulation and discussion for performance evaluation of the FP-DRoF architecture are presented. For assessment of the proposed FP-DRoF's performance, a sample network concept is proposed in Figure 5-3, which integrates the photonic systems with RF transceiver at RAP, for transporting the ARoF and DRoF and Baseband over Fibre (BoF) traffics using a common fibre infrastructure. In this architecture, all types of signals are simultaneously transported through access networks using WDM technique.

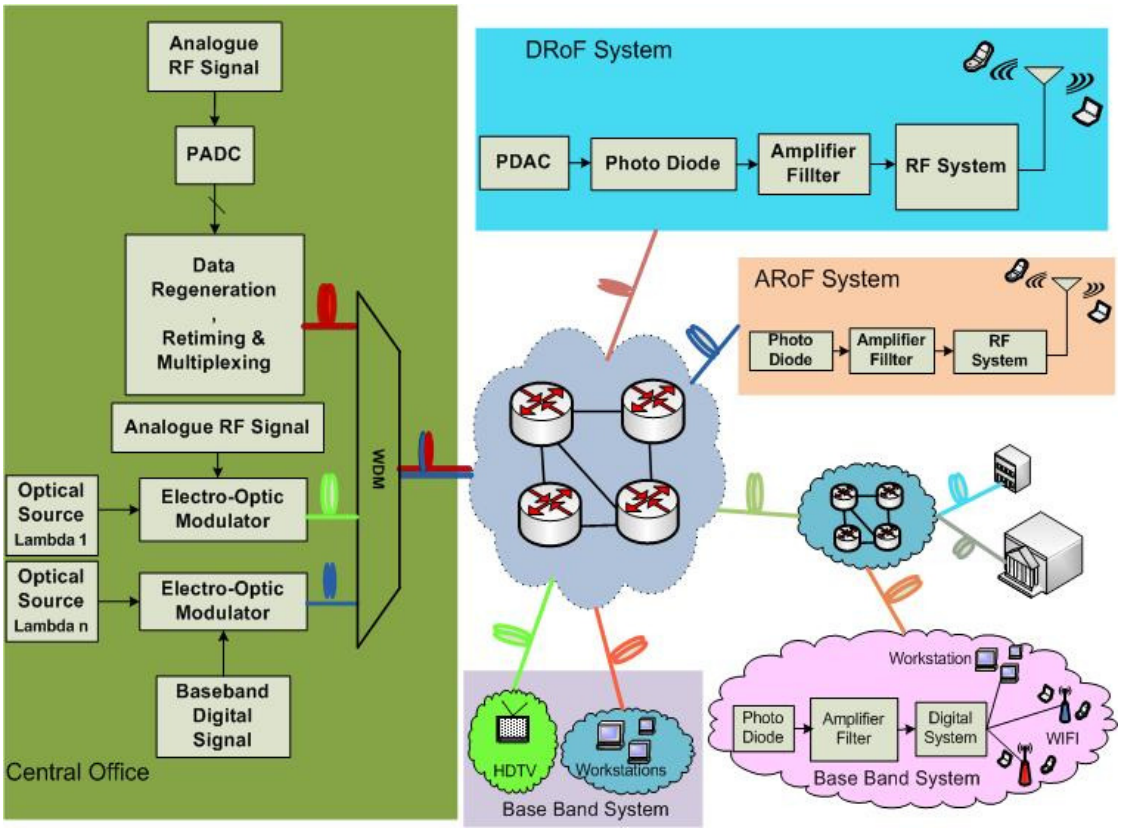

Figure 5-3: An integrated architecture of DRoF, BoF and ARoF techniques.

By deployment of this proposed system the following features could be realized. It is possible to use un-occupied channels capacity of implemented network for transporting the broadband wired and wireless data traffic. This technique can integrate the RoF system with Fibre-To-The-Home (FTTH) Passive Optical Network (PON). Therefore, by upgrading conventional Optical Line Terminal (OLT) and Optical Network Unit (ONU) the possibility to more centralize the signal processing, system management, and monitoring processes is achievable. Therefore, wireless networks can be integrated with existing optical networks to reduce the future super-broadband access network implementations and cost overheads for the wired, wireless and mobile service providers and eventually the service cost to the end-users with guaranteed Quality of Transmission (QoT).

Therefore, according to the proposed architecture in Figure 5-3, the model of Figure 5-4 is simulated to evaluate the system performance and to assess the system functionality.

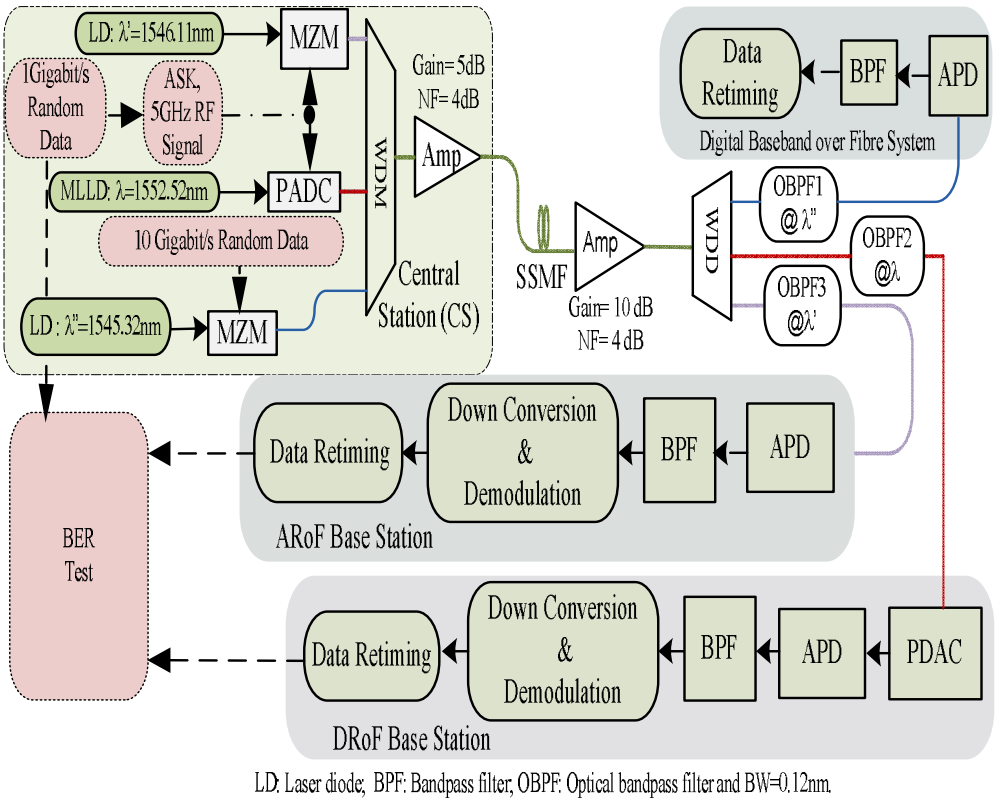

Figure 5-4: The simulated model of an integrated link.

In this simulation model, a sample 1 Gbps NRZ pseudo-random data is generated which is ASK modulated onto a 5 GHz carrier. To investigation each link's performance individually and independently, the laser source of the link under investigation was powered on while the other optical source was powered off, during performance investigation of the desired link. Figure 5-5 illustrates a Bit Error Rate (BER) performance comparison of the two FP-DRoF and ARoF links. These results are generated based on independently investigation of the two links for the length of 15 km of Standard Single Mode Fibre (SSMF) versus the received power level at the RBS. The link performance is investigated for compensated 17 ps/nm.km chromatic dispersion of SSMF, whereas the link Polarization Mode Dispersion (PMD) is not mitigated. Furthermore, the MLL timing jitter is modelled in worst case for FP-DRoF link. The overall phase and amplitude noise impacts on the laser pulse provide the MLL pulse with 29.42 dB Optical Signal to Noise Ratio (OSNR) with modelled 192.7 femtosecond random rms and 808 femtosecond deterministic jitters at 15 Gigasample/s.

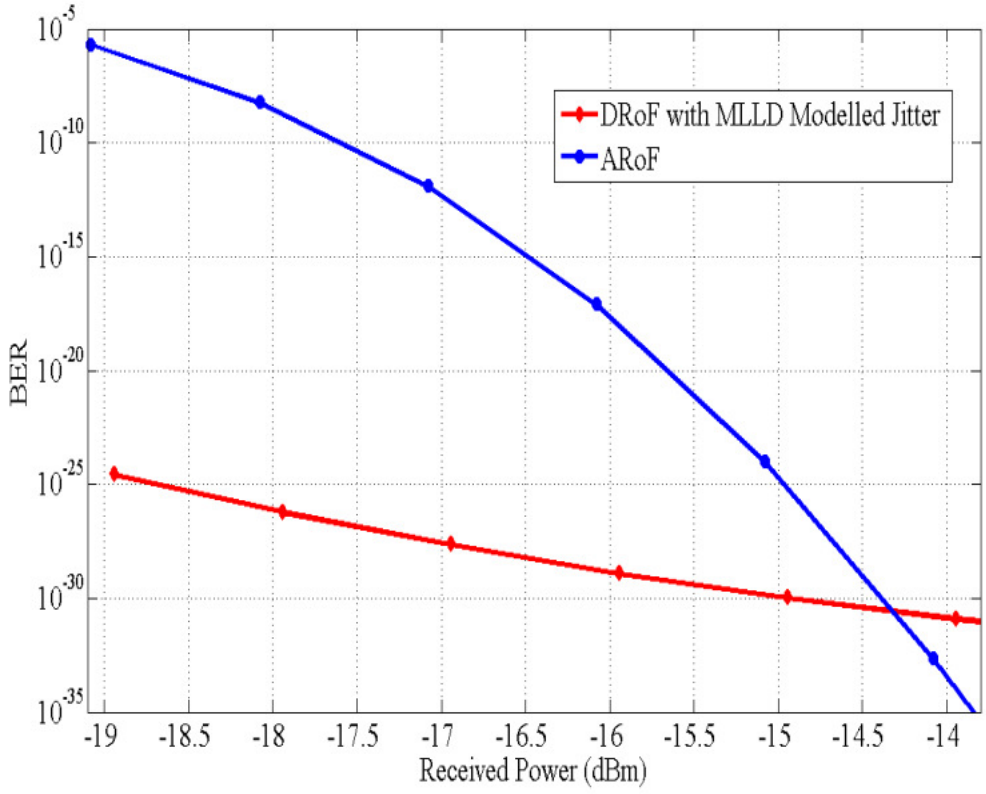

Figure 5-5: BER of the ARoF and the FP-DRoF links vs. received power at BS over dedicated 15 km dispersion compensated SSMF.

However, by increasing the ARoF link's power, at about -14.4 dBm, the ARoF link's BER performance exceed the BER's of FP-DRoF. However, the simulation results show that in low level of Signal to Noise Ratio (SNR), in comparison with ARoF through a dedicated fibre link, the DRoF has better BER performance than ARoF in the order of 10^{-20}. Furthermore, to realize BER about 10^{-25} the power penalty for ARoF is about 4 dBm. The simulation results demonstrate that by considering 0.2 dB/km attenuation of a SSMF, the dedicated fibre length for the FP-DRoF link could be increased about 20 km than ARoF link. Figure 5-6 illustrated the MLLD pulses's jitter histograms that the Jitter measurement is performed after detection by an APD with an OSNR=29.42 dB at the input of the APD.

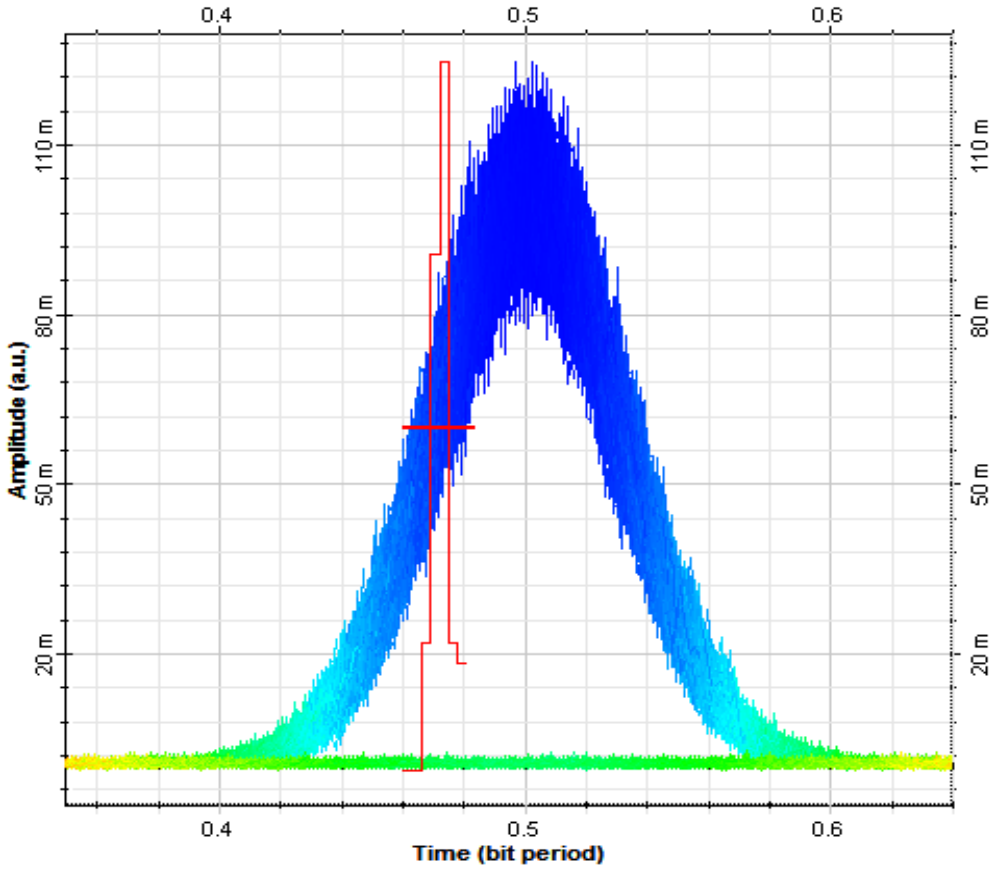

Figure 5-6: Mode-locked laser diode pulses' jitter histograms.

Furthermore, for accommodating the interference impacts of other channels on the both FP-DRoF and ARoF systems, the investigation is performed on a shared optical fibre link that both the DRoF and the ARoF signals are simultaneously transported

through the integrated link in the presence of third baseband digital random traffic (BoF).

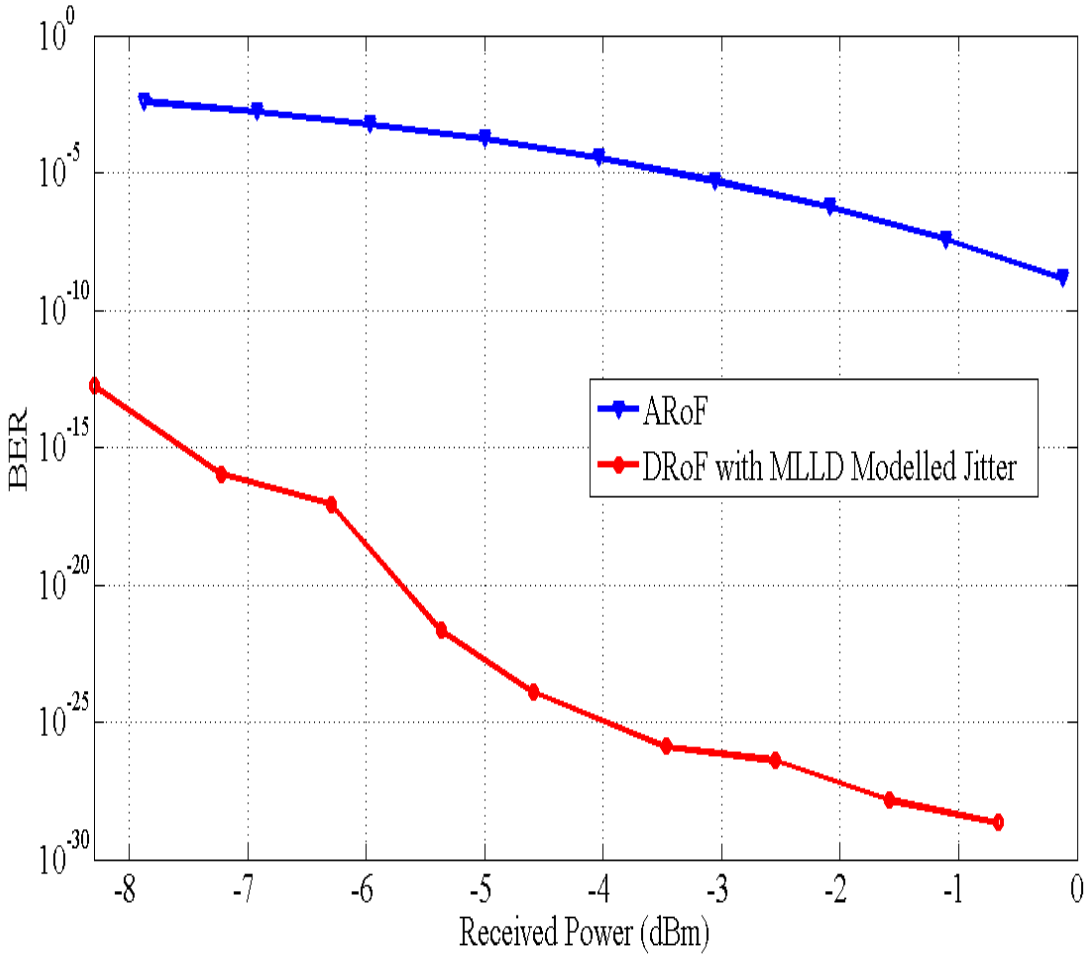

Figure 5-7: BER of the ARoF and the FP-DRoF vs. simultaneously received power at the BS over integrated 15 km dispersion compensated SSMF.

Figure 5-7 shows the system performance in terms of the BER of the received signals over integrated fibre link. This figure gives a comparison of the BER performance of the received signals using the FP-DRoF and the ARoF systems over 15 kilometres of the SSMF fibre length against the received power level in the presence of the third (BoF) baseband digital optical traffic over the network. For the shared fibre link, the BER of the FP-DRoF link is about 10^{-10} times less than the ARoF link for -19 dBm lunched power into the fibre and the power penalty of the ARoF system is more than 10 dBm which is significant to increase the fibre link's length of the FP-DRoF access network using common infrastructure. By comparing the illustrated BER results in Figure 5-5 and Figure 5-7, it can be observed that the BER of the FP-DRoF is more independent of the launched power and consequently the fibre length and in the

shared like it is demonstrated that the interferences of other channels, significantly affect on the ARoF link performance whereas the FP-DRoF is more robust against interferences. In Figure 5-8, the eye diagrams of the ARoF and FP-DRoF are illustrated at -3 dBm and -5 dBm received power, respectively. As shown in this figure, the eye opening high in diagram of the ARoF link of the Figure 5-8 (a) is smaller than the eye opening height of the FP-DRoF link about 27% and the timing jitter of the FP-DRoF is significantly less than ARoF link. Therefore, these results demonstrate that the FP-DRoF link is more robust than the ARoF link.

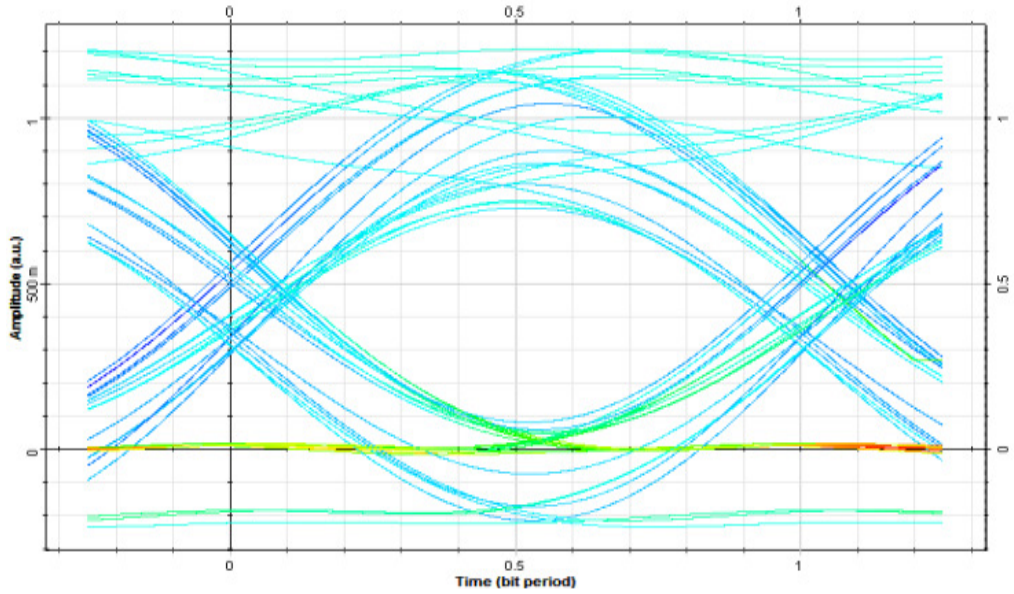

(a)

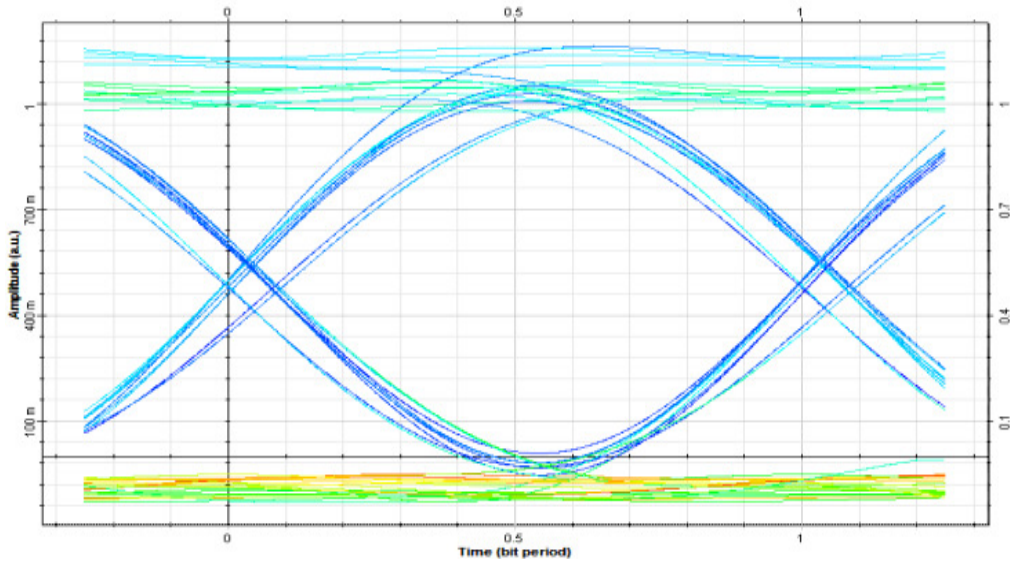

(b)

Figure 5-8: Eye diagram of 1 Gbps ASK modulated signal with 5 GHz carrier for 15 km length of dispersion compensated SSMF: (a) ARoF (b) FP-DRoF.

According to simulation results, it is demonstrated that DRoF is more independent on fibre network impairments and the proposed all-photonic DRoF architecture by gaining photonic sampling pulses in comparison with high-speed electronic circuits and systems signal conversion and processing limitation, can support digitized RF signal transmission for delivering the future super-broadband traffics to the remote distributed wired and wireless access networks. Consequently, by deploying FP-DRoF system it will be achievable to use the present digital optical communication infrastructures and decrease the number of CS by increasing the length of fibre link between the CS and RBS. It will decrease the service provider and operators cost overhead per bit will keep the service quality, which reduces the service cost to the end-users.

5.4. Wavelength Allocation Scheme

Four-Wave Mixing (FWM) is a nonlinear phenomenon in the optical communication system that introduces undesired interferences on a wavelength division multiplexing (WDM) application for RoF broadband access networks. This impairment significantly degrades the RoF system's performance. In this section, the proposed FP-DRoF system's performance is investigated with utilizing different uniform and non-uniform WDM schemes to assess the FWM impact on the link performance.

In a WDM system, the FWM phenomenon happens for every possible choice of three channel waves that co propagating through a medium that is described in chapter 2. FWM is worse for equally spaced wavelength allocation in a WDM system and at high launched power. In a conventional WDM, the channel space is uniformly divided between several channels. However, the probability of FWM is not completely prevented in the uniform channel allocation, even increasing the channel space. Figure 5-9, shows the FWM in the uniform spaced WDM channels. As shown in this figure, the f_{223}, f_{132} and f_{221} are the mixed products that are overlapped with the fundamental channels completely. Therefore, they cause significant interchannel interferences. Consequently, by allocating more space between the channels its impact cannot be mitigated even by proper filtering.

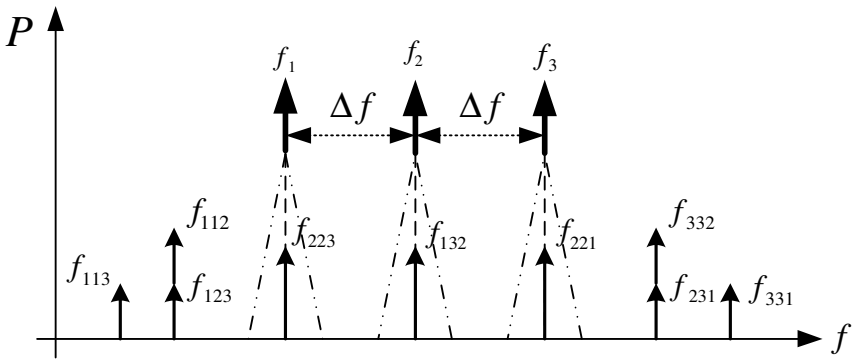

Figure 5-9: The FWM effects in uniform wavelength allocation.

The solution for minimizing FWM is to use unequal channel spacing. In this scheme, the desired channels' mixed products do not interfere with the fundamental signal channels. The new algorithm of non-uniform channel allocation which is proposed in [4] based on Optical Golomb Ruler (OGR) to reduce the FWM effect as well as improve the WDM system performance without inducing additional cost, in terms of bandwidth. Figure 5-10 shows the FWM effects in non-uniform wavelength allocation. As illustrated, in this scheme the mixed product channels can be filtered out by proper filtering without significant interference on the fundamental channels. Therefore, the FWM impact on the channels interfering is mitigated, significantly.

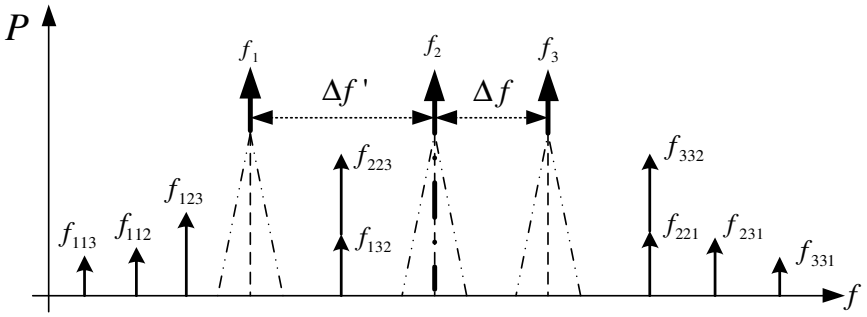

Figure 5-10: The FWM effects in non-uniform wavelength allocation.

For investigation of the FP-DRoF system's performance for two wavelength allocation scheme, a sample ASK modulated, 1 Gbps NRZ pseudo-random data with 5 GHz RF carrier is transported through the optical link. In the simulated model of the system, the chromatic dispersion of the single mode fibre is assumed about 17 ps/(nm.km) which is compensated using a dispersion compensation fibre whereas the 0.2 ps/km PMD is not compensated. Figure 5-11 shows the DRoF transmission systems performance with eye diagrams of the received signal with implementing

uniform and non-uniform OGR WDM schemes. As shown in this figure, the eye opening height in the FP-DRoF link with uniform WDM schem is 30 % smaller than the eye opening hieght in the link with non-uniform WDM scheme. Furthermore, the timing jitter of the received signal in the FP-DRoF link with uniform WDM is significantly higher than the FP-DRoF link with non-uniform WDM scheme.

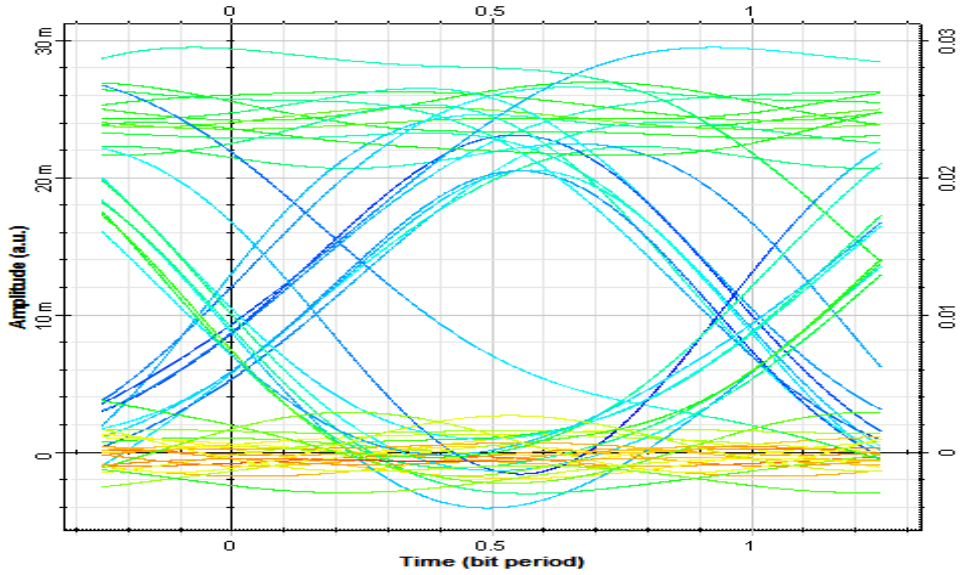

(a)

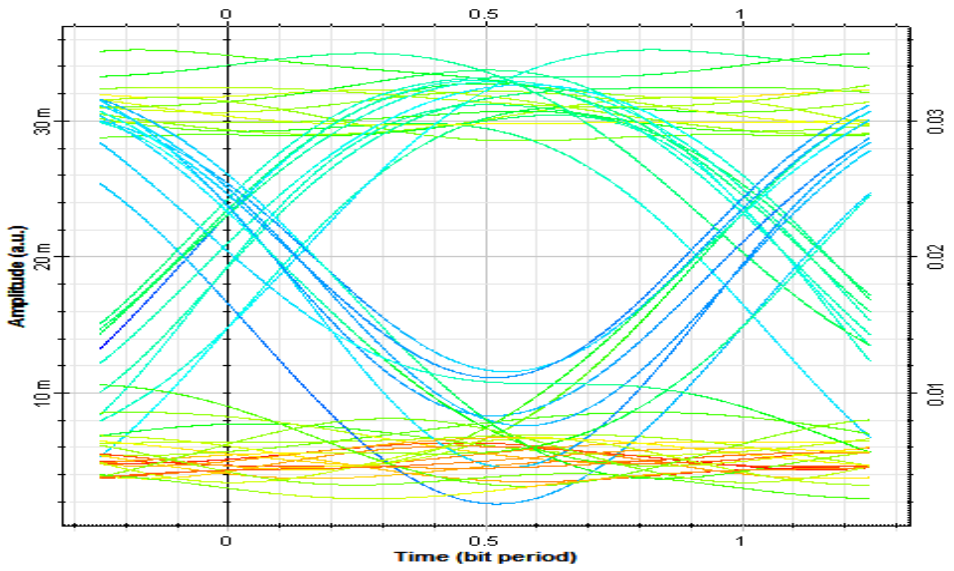

(b)

Figure 5-11: Eye diagram of the FP-DRoF for 1 Gbps ASK modulated signal with 5 GHz carrier over 31 km of SSMF with (a) uniform WDM technique (b) non-uniform OGR WDM technique.

In this figure, the performance of the received signal for FP-DRoF link with uniform WDM is assessed at 1.15 dBm launched power at the CS into the SSMF and the BER

was about4.48×10^{-10}. The FP-DRoF link's performance with OGR non-uniform WDM system is evaluated with about 0.7 dBm launched power into the SSMF where the received signal BER was about 5.78×10^{-12} over a 31 kilometres length of the fibre. The simulation results show that using the OGR WDM technique for FP-DRoF, the system is more robust against the FWM impairment than FP-DRoF system with applying uniform WDM.

Figure 5-12 shows the BER comparison of the two WDM schemes implementation of the FP-DRoF links. As shown in this figure, the FP-DRoF with non-uniform WDM has better performance in comparison with the link with uniform space wavelength allocation. Furthermore, it is demonstrated that power penalty at CS for FP-DRoF link with uniform WDM technique is about 2 dBm higher than OGR non-uniform technique for the BER about 10^{-15} whereas more bandwidth is required in uniform scheme. Therefore, the FP-DRoF in non-uniform wavelength allocation scheme can save more power than uniform WDM scheme.

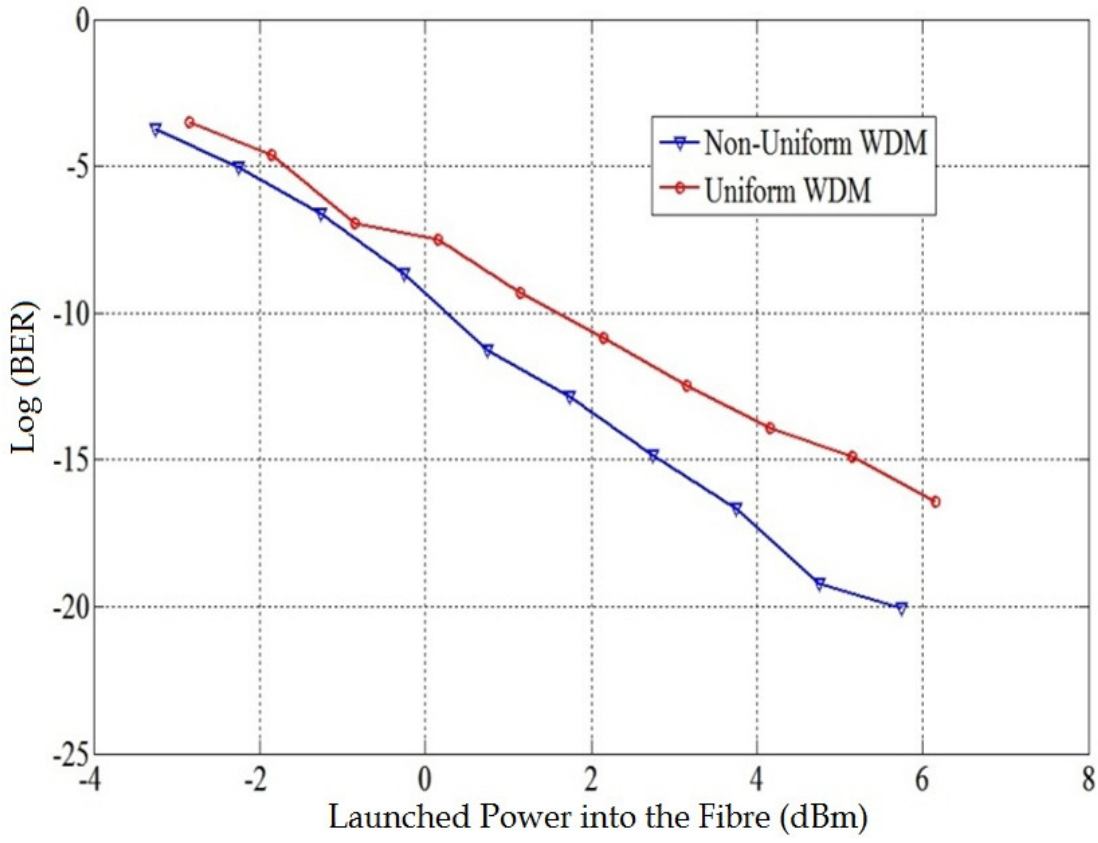

Figure 5-12: BER of the FP-DRoF vs. launched power at the CS over 31 km of dispersion compensated SSMF.

5.5. Conclusions

In this chapter, a Fully Photonic DRoF (FP-DRoF) is proposed and its performance is evaluated through a sample dedicated and a shared fibre networks, individually. The proposed model is simulated using Optiwave-Optisystem and Matlab simulation tools. This has been gained the inherent low phase noise photonic sampling pulses and high speed signal conversion rate of optical system in comparison with high-speed electronic circuits. The proposed FP-DRoF system can be used to transport a digitized RF signal for delivering future super-broadband traffics to the remote distributed wired and wireless access networks. It is observed that the interferences of other channels, nonlinearity and noise significantly affect the ARoF link performance while FP-DRoF is more robust against interference of other channels.

Furthermore, simulation results demonstrated that the FP-DRoF with non-uniform WDM is more robust against FWM impairment than the conventional WDM technique with uniform wavelength allocation and has better performance in terms of BER. It is clearly verified that the lunched power penalty at CS for FP-DRoF link with uniform WDM techniques is about 2 dB higher than non-uniform technique while uniform WDM method requires more bandwidth than non-uniform scheme.

This technique can centralise the signal processing, system management, and monitoring processes more than a conventional ARoF by increasing the length of fibre. Therefore, wireless network could be integrated with existing optical networks that reduce the future super-broadband access-network-system implementation overheads and service costs. By realizing the implementation of this scheme in integration with the digital baseband communication system, it is achievable to use free spectrum of present infrastructure networks for transporting the broadband wireless and wireline data traffic over longer distances. Consequently, the number of CS will decrease and which is reducing the service provider and operators cost overhead per bit/sec.

5.6. References

[1] Michael Sauer, Andrey Kobyakov, Jacob George, "Radio Over Fiber for Picocellular Network Architectures", Journal of Lightwave Technology, vol. 25, no. 11, pp. 3301-3320, 2007.

[2] H-C Ji, H. Kim, and Y. C. Chung, " Full-duplex radio-over-fiber system using phase-modulated downlink and intensity-modulated uplink", IEEE Photonics Technology Letters, vol. 21, no. 1, pp. 9-11, Jan. 2009.

[3] C. Lim, A. Nirmalathas, M. Bakaul, P. Gamage, K. L. Lee, Y. Yang, D. Novak and R. Waterhouse, " Fiber-Wireless Networks and Subsystem Technologies," Journal of Lightwave Technology, vol. 28, no. 4, pp. 390-405, 2010.

[4] Rajneesh Randhawa, J. S. Sohalb and R. S. Kaler, "Optimum algorithm for WDM channel allocation for reducing four-wave mixing effects", International Journal for Light and Electron Optics (Elseiver), vol. 120, Issue 17, pp. 898-904, Nov. 2009.

Chapter 6

Conclusion and Future Works

6.1. Conclusion

Mobile and wireless networks generated traffic rates are growing very fast and are expected to double each year. The expectation is for delivering several Giga bit per second (Gbps) multi-services traffic to each end-user in the near future for personal and multimedia communication services. Therefore, deploying super-broadband networks will be essential for service providers and operators. Analogue Radio-over-Fibre (ARoF) is a solution for deploying wireless access to broadband and super-broadband seamlessly. It can provide dynamic allocation of resources and can be realised with simple and small BSs with centralized operations. However, Digital Radio over Fibre (DRoF) is more independent of the fibre network impairments and length than ARoF link. In this dissertation, a Fully-Photonic DRoF (FP-DRoF) technique is proposed for deploying of future super-broadband access networks.

In the proposed FP-DRoF, the two key data conversion components are designed fully optical and their performance and physical functionality are evaluated accordingly. The system simulation results show that the Photonic Analogue to Digital Converter (PADC) has 10 GHz bandwidth around 60 GHz of sampling rate. Furthermore, by changing the bandwidth of the Optical Bandpass Filter (OBPF) switching to another band of sampling frequency provides optimised condition to have a suitable performance of the PADC. It has evaluated that the PADC has approximately smooth ENOB response for RF input up from 1 to 22 GHz for 60 GHz sampling frequency. The proposed 8-Bit pipelined PADC performance in terms of ENOB is evaluated at 60 Gigasample/s about 4.1.

Recently, different methods have been reported to implement Photonic Digital to Analogue Converters (PDACs), but the aim of reported methods was convert digital

electrical signals to the corresponding analogue signal by assisting an optical technique. In the proposed Binary Weighted PDAC (BW-PDAC), optical digital signals are fully optically converted to an analogue signal. According to the system evaluation procedure, the Spurious Free Dynamic Range (SFDR) was 26.62 dBc at the output of the PDAC in a back-to-back deployment of the PADC and the PDAC. To improve the system performance of proposed system a Retiming, Reshaping and Reamplifying (3R) regeneration system is proposed and the simulation results show that for an ultra-short RZ pulse with a 5% duty cycle at 65 Gigabit/s using the proposed 3R regeneration system on a link reduces rms timing jitter by 90% while the regenerated pulse eye opening height is improved by 65%.

Finally, the proposed FP-DRoF functionality is evaluated. Its performance is investigated individually through a dedicated and shared fibre networks. The simulation results show in case of low level Signal to Noise Ratio (SNR), the FP-DRoF has better BER performance than the ARoF in the order of 10^{-20} throught a dedicated fibre link. Furthermore, to realize the BER about 10^{-25} power penalty for ARoF is about 4 dBm higher than the FP-DRoF. The simulation results demonstrate that by considering 0.2 dB/km attenuation of a standard Single Mode Fibre (SMF), the dedicated fibre length for FP-DRoF link could be increased about 20 km more than the ARoF link.

For shared fibre link, the BER of FP-DRoF link is about 10^{-10} of magnitude less than the ARoF link for -19 dBm launched power into the fibre and the power penalty of the ARoF system is more than 10 dBm in comparison with the FP-DRoF. This is significant in order to increase the fibre link's length of the FP-DRoF access network using common infrastructure. It can be observed that the interferences of other channels, nonlinearity and noise significantly affect the ARoF link performance while the FP-DRoF is more robust against interference of other channels than the ARoF. By realizing the implementation of this technique, it will be achievable to centralize signal processing, system management, and monitoring processes more than a conventional ARoF system. Therefore, wireless networks can be integrated with existing digital optical communication network infrastructures to reduce the

future super-broadband access network implementations and cost overheads for the wired, wireless and mobile services.

Simulation results demonstrate that the FP-DRoF with non-uniform WDM is more robust against FWM impairment than the conventional WDM scheme with uniform wavelength allocation and it has better performance in terms of BER. It is clearly verified that the launched power penalty at CS for the FP-DRoF link with uniform WDM technique is about 2 dB higher than non-uniform technique for a BER about 10^{-15}. Furthermore, the uniform WDM method requires more bandwidth than non-uniform scheme.

6.2. Future Works

In the following of this research the below works can be performed as future works:

1) Multi-Radio signal transmission over the FP-DRoF link and assess the performance of the link in comparison with the ARoF link.
2) Design a dynamic wavelength allocation system and investigate the impact of Orthogonal Wavelength Division Multiplexing (OWDM) technique on the FP-DRoF system performance and spectrum efficiency.
3) Investigate different technique of chromatic dispersion compensation technique and evaluate the FP-DRoF link performance in different conditions.
4) Compensate the polarization mode dispersion of the link and evaluate the FP-DRoF system performance against a conventional ARoF system. Furthermore, investigate the performance of system with optical coherent detecting scheme.
5) Design and implementation of a photonic transceiver with integrated antenna system for a distributed antenna system application. This system receives the signal optically and transmits it wirelessly and vice versa. Moreover it could be implemented in integration with an optical transmitter and receiver with a patch multiband antenna.
6) Developing all-optical signal processing and implementation of the system. Investigation on the design and implementation of fully photonic logical and mathematical operations. In this work the following goals are targeted: to

optimise the performance, power consumption, cost overhead and packaging size of circuits and systems for higher integrity scale at lower cost with suitable performance.

Appendix A:

Table A-1: The typical loss of optical components

Component	Insertion loss (dB)	Wavelength Dependent Loss (dB)	Polarization Dependent Loss (dB)
Mux & Demux	5	<1	0.1
2X2 Add & Drop Switch	1.2	0.2	0.1
Coupler 2X2	3	-	-
Filter	1	0.1	
Interleaver	2-3	-	-
OXC	3	0.4	0.1

Table A-2: Power Penalty Requirement

Item	Loss Margin (dB)
Fibre Chromatic Dispersion	1
SPM	0.5
XPM	0.5
Dispersion Compensation Unit	6
FWM	0.5
SRS/SBS	0.5
PDL	0.3
PMD	0.5
Amplifier Gain Tilt (due to nonflat gain spectra)	3
Receiver Sensitivity Tilt (Wavelength dependence of PMD)	0.5
Transmitter Chirp	0.5
Fibre Connector	0.5

Publications

1. S. R. Abdollahi, H.S. Al-Raweshidy, S. Mehdi Fakhraie, and R. Nilavalan, "Full Duplex 60 GHz Millimeter Wave Transmission over Multi-Mode Fiber ", IEEE ICUFN 2010, South Korea, June 2010.
2. S. R. Abdollahi, H.S. Al-Raweshidy, S. Mehdi Fakhraie, and R. Nilavalan, " Digital Radio over Fibre for Future Broadband Wireless Access Network Solution ", IEEE ICWMC 2010, Spain, Sep. 2010.
3. S. R. Abdollahi, H.S. Al-Raweshidy, R. Nilavalan, and Abolgasem Darzi, " Future Broadband Access Network Challenges ", IEEE WOCN 2010, Sri Lanka, Sep. 2010.
4. S. R. Abdollahi, H.S. Al-Raweshidy, S. Mehdi Fakhraie, and R. Nilavalan, "All Photonic Analogue to Digital and Digital to analogue conversion techniques for digital Radio over Fiber system applications", ITU-T Kaleidoscope Event, Beyond the Internet ?: Innovation for future networks and services, India, Dec 2010.
5. S. R. Abdollahi, H.S. Al-Raweshidy, and R. Nilavalan, "Wavelength Allocation Schemes Impact on All-Photonic Digitized-Radio over Fibre Access Network", 2011 Advanced Photonics Congress, Optical Socity America, June 2011 Toronto, Canada.
6. S. R. Abdollahi, H.S. Al-Raweshidy, and R. Nilavalan, "An Integrated Transportation System for Baseband Data, Digital and Analogue Radio Signals over Fibre Network", IEEE IWCMC 2011, Turkey, July 2011.
7. S. R. Abdollahi, H.S. Al-Raweshidy, and R. Nilavalan, "Fully-Photonic Analogue-to-Digital Conversion Technique for Super-Broadband Digitized-Radio over Fibre Link", NOC2011, UK, July 2011.
8. S. R. Abdollahi, H.S. Al-Raweshidy, and R. Nilavalan "Non-Uniform Wavelength Allocation in All-Photonic Digitized-Radio over Fibre Access Network", IEEE WPMC11 France, Sep 2011.
9. S. R. Abdollahi, H.S. Al-Raweshidy, and R. Nilavalan, "Pipeline Time-Interleaved All-photonic Sampling and Quantization Analogue-to-Digital Converter", IEEE International Congress on Ultra Modern Telecommunications and Control Systems (ICUMT), 2011.
10. M. Behjati, S. R. Abdollahi, and H.S. Al-Raweshidy, "Photonic Sampled and Electronically Quantized Analogue to Digital Conversion in Access Networks", IEEE International Congress on Ultra Modern Telecommunications and Control Systems (ICUMT), 2011.
11. S. R. Abdollahi, H.S. Al-Raweshidy, A. Ahmadinia, and R. Nilavalan, "An All-photonic Digital Radio over Fiber architecture," IEEE Swedish Communication Technologies Workshop (Swe-CTW), 2011.

12. S. R. Abdollahi, H.S. Al-Raweshidy, and Thomas Owens, "Data Regeneration in Communication Networks" IEEE International Conference on Ubiquitous and Future Networks, ICUFN 2012.

Book Chapter:

Book Chapter "Super-Broadband Wireless Access Network" @ Wireless Communication Network- Recent Advances, Published in http://www.intechopen.com/books/wireless-communications-and-networks-recent-advances/super-broadband-wireless-access-network- April 2012.

Under Reviews and Submited Papers:

1) S. R. Abdollahi, and H.S. Al-Raweshidy, and Thomas Owens, "Digital Pulse Regeneration in Optical Networks", Submitted to IEEE Journal of Optical Communications and Networking.
2) S. R. Abdollahi, and H.S. Al-Raweshidy, and Thomas Owens, "Binary-Weighted Photonic Digital-to-Analogue Converter", Submitted to IEEE Journal of Lightwave Technology.
3) S. R. Abdollahi, and H.S. Al-Raweshidy, and Thomas Owens, "Pipelined Photonic Analogue to Digital Converter", Submitted to IEEE Journal of Lightwave Technology.
4) S. R. Abdollahi S. R. Abdollahi, and H.S. Al-Raweshidy, and Thomas Owens, "8-Bit Fully Photonic Analogue to Digital Converter", Submitted to Optical Socity of America, Journal of Optics Express.